The Pennsylvania State University

The Graduate School

Department of Materials Science and Engineering

MODELING OF HEAT TRANSFER AND FLUID FLOW IN KEYHOLE MODE WELDING

A Dissertation in

Materials Science and Engineering

by

Rohit Rai

Submitted in Partial Fulfillment
of the Requirements
for the Degree of

Doctor of Philosophy

December 2008

The dissertation of Rohit Rai was reviewed and approved* by the following:

Tarasankar DebRoy
Professor of Materials Science and Engineering
Dissertation Advisor
Chair of Committee

Ivica Smid
Associate Professor of Engineering Science and Mechanics

Long-Qing Chen
Professor of Materials Science and Engineering

Suzanne Mohney
Professor of Materials Science and Engineering

Todd Palmer
Research Associate and
Assistant Professor of Materials Science and Engineering
Special Member

Gary L. Messing
Professor of Ceramic Science and Engineering
Head of the Department of Materials Science and Engineering

*Signatures are on file in the Graduate School

ABSTRACT

Since deep penetration welds can be made with keyhole mode laser and electron beam welding, they are widely used for joining thick sheets of metals and alloys. The weld geometry and microstructure depend on the temperature distribution and the cooling rates. Experimental determination of temperatures in the work-piece through the use of thermocouples, can provide data for a limited number of points and is time consuming and expensive. Numerical modeling of heat transfer and fluid flow in high energy density laser and electron beam welding can provide previously unavailable information about the temperature distribution and thermal cycles at all points in the computational domain in a relatively short time and at low cost. A critical review of the available literature indicates the following problems with the numerical models of keyhole mode welding. (1) There is no comprehensive three dimensional model of keyhole mode electron beam welding (EBW) available in literature. (2) While comprehensive models of keyhole mode laser beam welding (LBW) have been proposed, none has been tested for the welding of various materials under different process conditions. (3) None of the existing models of keyhole mode laser or electron beam welding contains a structural component designed to provide good agreement between the computed and experimental results. (4) None of the existing models can work backwards, i.e. provide a set of welding process variables that will result in desired weld characteristics. The goal of this thesis is to address these important issues.

In this work, computationally efficient numerical models have been developed for linear keyhole mode LBW and EBW processes. The models combine an energy balance based model for keyhole geometry calculation with a well tested 3D heat transfer and fluid flow model. For LBW, keyhole wall temperatures are assumed to be equal to the boiling point of the alloy at 1 atm pressure. Keyhole wall temperatures in EBW are calculated from the equilibrium vapor pressure versus temperature relation for the work-piece material. The vapor pressure is, in turn, calculated from a force balance at the keyhole walls between the surface tension, vapor pressure and hydrostatic forces. A turbulence model is used to estimate the effective values of viscosity and thermal

conductivity to account for the enhanced heat and mass transport in the turbulent weld pool due to the fluctuating components of velocities in both LBW and EBW. The proposed model for LBW has been tested for materials with wide ranging thermo-physical properties under varying input powers and welding speeds covering both partial and full penetration welds. The tested materials include Al 5754 alloy, A131 steel, 304L stainless steel, Ti-6Al-4V, tantalum, and vanadium. These materials vary significantly in their thermo-physical properties, including boiling point, thermal conductivity, and specific heat. The EBW model was tested for 21Cr-6Ni-9Mn steel, 304L stainless steel, and Ti-6Al-4V for different input powers and power density distributions. To improve the agreement between the calculated and experimental results, a methodology is presented to estimate the values of uncertain input parameters like absorption coefficient and beam radius using a genetic algorithm with the numerical model and limited amount of experimental data. Finally, a genetic algorithm is used with the numerical model to prescribe welding conditions that would result in a desired weld attribute.

The computed weld cross-sectional geometries and thermal cycles agreed reasonably well with the experimental observations. The weld pool shapes depended on the convective heat transport within the weld pool. Convective heat transfer was more important for materials with low thermal diffusivity. The calculated solidification parameters showed that criterion for plane front stability was not satisfied for the alloys and the range of welding conditions considered in this work. Higher peak temperatures were found in the EBW of Ti-6Al-4V welds compared to similar locations in 21Cr-6Ni-9Mn stainless steel welds due to the higher boiling point and lower solid state thermal conductivity of the former. Non-dimensional analysis showed that convective heat transfer was very significant and Lorentz force was small compared to Marangoni force. Comparison of calculated weld geometries for electron beam and laser beam welds for similar process parameters showed that lower keyhole wall temperatures in EBW tend to make the welds deeper and narrower compared to laser beam welds. A genetic algorithm was used to optimize the values of absorption coefficient and beam radius based on limited volume of experimental data for 5182 Al-Mg alloy welds. The weld geometry calculated using the optimized values of absorption coefficient and beam radius was in

good agreement with experimental observations. The optimized values of absorption coefficient and beam radius were then used to prescribe sets of welding conditions to obtain specified weld geometry. These sets of welding conditions differed significantly but resulted in the same weld geometry.

The results show that a widely applicable and computationally efficient 3D model of heat transfer and fluid flow can be developed by combining an energy balance based keyhole calculation sub model with a 3D convective heat transfer model. The modeling results can improve the understanding of the keyhole mode welding process. The results also show that by combining numerical models with an optimizing algorithm, the model results can be made more reliable. Finally, systematic tailoring of weld attributes via multiple pathways, each representing alternative welding parameter sets, is possible based on scientific principles.

TABLE OF CONTENTS

LIST OF FIGURES

LIST OF TABLES

ACKNOWLEDGEMENTS

Many people have helped me in my doctoral research over the course of the last four years. I would first like to express my sincere gratitude and appreciation for my advisor Professor Tarasankar DebRoy whose guidance was indispensable for my doctoral research. I am grateful to him for his constant encouragement, guidance and support for my research as well as my professional development.

I would like to acknowledge Drs. Long-Qing Chen, Suzanne Mohney, Ivica Smid and Todd Palmer for serving on my thesis committee. I greatly appreciate their taking the time to critically review this doctoral dissertation.

I would like to thank Drs. Thomas J. Lienert, Paul Burgadt, John O. Milewski at Los Alamos National Laboratory, Dr. John W. Elmer at Lawrence Livermore National Laboratory, and Drs. Richard Martukanitz and Shawn Kelly, for providing the experimental data. I would also like to thank Dr Thomas J. Lienert and Dr. John W. Elmer for their valuable suggestions during my thesis research.

I am very grateful to my colleagues Dr. Saurabh Mishra, Dr. Amit Kumar, Dr. Xiuli He, Dr. Gour Gopal Roy, Rituraj Nandan, Amit Arora and Brandon Ribic for their help during my research and for making my stay at Penn State a memorable one.

I am grateful to my family and friends for their support. I would especially like to thank my parents whose support was vital for my success at every stage in life.

Finally, I would like to acknowledge a grant from the U.S. Department of Energy, Office of Basic Energy Sciences, Division of Materials Sciences, for supporting this research work, under grant number DE-FGO2-01ER45900.

Chapter 1

Introduction

1.1 Keyhole mode welding

Laser and electron beam welding are widely used as joining techniques for wide ranging applications. At energy densities above 10^9 W/m^2, strong evaporation results in the formation of a deep and narrow vapor cavity called keyhole [1]. Keyhole mode laser welding involves the interaction of a number of complex physical processes which include multiple reflections of the energy beam within the keyhole [2-8], attenuation of the beam by the vapors and ions present in the keyhole due to absorption and scattering [9-12], absorption of energy at keyhole walls and transfer of heat into the liquid metal pool that surrounds the keyhole through conduction and convection.

Properties of the welded joint depend on its geometry and microstructure which are determined by the temperature distribution and thermal cycles in the work-piece. The experimental measurement of temperatures involves placing thermocouples in the work-piece which is very cumbersome, expensive, and time consuming. Moreover, only a limited number of thermocouples can be placed in the work-piece. Furthermore, due to the small fusion zone, and very high temperatures and temperature gradients, accurate determination of temperatures in the weld pool is very difficult. Numerical modeling of heat and mass transport in the work-piece can therefore be used to supplement the experimental studies. Once validated with experiments, the numerical models can save time and costs by reducing the need for additional experiments. They can also provide great insight by providing temperatures and thermal cycles at all points in the calculation domain.

Numerical studies of keyhole mode welding available in the literature (discussed in Chapter 2) have been limited to selected materials and welding conditions. Moreover, to make the computations tractable, the numerical models often make simplifications like

assuming a pre-defined axisymmetric keyhole shape or constant keyhole wall temperature, neglecting convection as a mode of heat transfer, or performing a two dimensional analysis of a three dimensional (3D) problem. These simplifications limit the applicability of a model to specific process parameters (e.g. low welding speed) or to materials with a specific range of thermo-physical properties (e.g. high thermal conductivity). For example, the models that ignore fluid flow in the weld pool cannot be applied to low thermal conductivity alloys like steel where convective heat transfer in the weld pool is likely to play a very strong role. Furthermore, since the variation of keyhole wall temperatures with depth in electron beam welding (EBW) can be significant (see Appendix A) and can therefore affect the heat transfer and fluid flow in the weld pool, numerical models that assume a constant temperature on the keyhole walls [3, 8, 13-15] cannot be applied to EBW. 3D models of heat transfer and fluid flow for keyhole mode EBW have not been reported in peer reviewed journals. Finally, comprehensive models of keyhole mode laser welding require transient tracking of various gas/liquid free surfaces and the resulting fluid flow in the both the molten weld pool and the two-phase solid and liquid regions surrounding it. Consideration of these physical processes makes the computational task very time consuming.

In short, existing numerical models of keyhole mode welding are either limited in their applicability to a few materials and/or welding speeds or are computationally intensive. Therefore, well tested computationally efficient phenomenological models for keyhole mode laser and electron beam welding that can be applied to metals and alloys with widely different thermo-physical properties and for a wide range of welding conditions are needed. The model predictions like fusion zone geometry, cooling rates, and thermal cycles should agree reasonably with the experimental observations.

Sometimes errors in the input data provided to the model may arise from uncertainties in the values of material properties (e.g. absorption coefficient of the beam energy, thermal conductivity values at elevated temperatures) or process parameters (e.g. measured beam radius at the focal plane). As a result, the model predictions may not always agree with the corresponding experimental data even if the model adequately represents the important physical phenomena involved in a process. That is, the model

predictions may not always be reliable. The current models of keyhole mode welding do not have a structural component to ensure closure with experimental data. Therefore, a procedure is needed for estimating such uncertain input parameters involved in the welding process so that the model predictions can be made more reliable.

Another problem with the numerical heat transfer and fluid flow models of welding processes is that they are usually designed to calculate weld characteristics from the welding variables and lack the much needed ability to go backwards and prescribe a set of welding process conditions to attain a particular set of weld characteristics (weld geometry, cooling rate). Moreover, since the keyhole mode welding process is very complicated and involves non-linear interactions of several welding variables, a particular weld attribute may be obtained via multiple sets of welding variables like the input power, welding speed, beam defocusing, etc. The unidirectional numerical models of keyhole mode welding cannot prescribe these multiple sets of welding variables. Therefore, a procedure is needed for using the numerical models to determine the various choices of welding conditions each of which would result in a desired set of weld attributes.

1.2 Objectives

The objectives of this work are three-fold:

1. To develop computationally efficient numerical heat transfer and fluid flow models for keyhole mode laser and electron beam welding that are widely applicable for:
    a. Materials with wide ranging thermo-physical properties.
    b. A wide range of welding process variables like input power, welding speed, etc.
2. To improve the reliability of the model by improving the accuracy of the input parameters.

3. To tailor weld geometry by recommending welding conditions to achieve desired weld attributes.

1.3 Thesis structure

This thesis is divided into six chapters. Chapter 1 explains the motivation, objectives and the structure of the thesis. In Chapter 2, previous work related to the physical processes involved in laser and electron beam welding and their numerical modeling are critically reviewed to identify important unsolved problems in the field.

Chapters 3 and 4 describe the proposed mathematical models and the modeling results for LBW and EBW, respectively. The model is validated by comparing the calculated weld geometries and thermal cycles with experimental observations. The modeling results are explained in the light of material properties. Study of dimensionless numbers is undertaken to understand the significance of various physical processes. Plots of effective viscosity show that turbulence was limited to regions close to the top surface of the weld pool. Furthermore, calculated solidification parameters and cooling rates are used to understand the expected scale of solidification microstructure in partial and full penetration welds. The deformation of the free surface of the weld pool under the combined effects of the recoil pressure of the metal vapors, the surface tension force, and the hydrostatic force is calculated for laser welding.

In Chapter 5, a genetic algorithm is combined with 3D heat transfer model of keyhole mode LBW to improve the reliability of the model predictions and to tailor the weld geometry. In order to make the model more reliable, the absorption coefficient and laser beam radius at focal spot are optimized to reduce the error between the experimental and calculated results for a limited volume of experimental data. Using these optimized values of absorption coefficient and beam radius, the GA is then used to find multiple sets of process parameters that will result in desired weld geometry.

Chapter 6 provides the summary and conclusions. Appendix A explains the reason why there is significant variation of keyhole wall temperature in EBW even though the variation is relatively small for LBW. The calculation of recoil pressure of

metal vapors is given in Appendix B. Appendix C explains the GA and the Parent Centric Cross-Over operator used in this study.

1.4 References

[1] Rai R, Elmer JW, Palmer TA, DebRoy T. Heat transfer and fluid flow during keyhole mode laser welding of tantalum, Ti-6Al-4V, 304L stainless steel and vanadium. J. Phys. D-Appl. Phys. 2007;40:5753.
[2] Wang SC, Wei PS. Energy-Beam Redistribution and Absorption in a Drilling or Welding Cavity. Metallurgical Transactions B-Process Metallurgy 1992;23:505.
[3] Kaplan A. A Model of Deep Penetration Laser-Welding Based on Calculation of the Keyhole Profile. J. Phys. D-Appl. Phys. 1994;27:1805.
[4] Milewski J, Sklar E. Modelling and validation of multiple reflections for enhanced laser welding. Modelling and Simulation in Materials Science and Engineering 1996;4:305.
[5] Ho CY, Wei PS. Energy absorption in a conical cavity truncated by spherical cap subject to a focused high-intensity beam. International Journal of Heat and Mass Transfer 1997;40:1895.
[6] Solana P, Negro G. A study of the effect of multiple reflections on the shape of the keyhole in the laser processing of materials. J. Phys. D-Appl. Phys. 1997;30:3216.
[7] Ki H, Mohanty PS, Mazumder J. Multiple reflection and its influence on keyhole evolution. J. Laser Appl. 2002;14:39.
[8] Zhao H, DebRoy T. Macroporosity free aluminum alloy weldments through numerical simulation of keyhole mode laser welding. J. Appl. Phys. 2003;93:10089.
[9] Yilbas BS, Yilbas Z, Akcakoyun N. Investigation into absorption of the incident laser beam during Nd:YAG laser processing of metals. Optics and Laser Technology 1996;28:503.
[10] Tu JF, Inoue T, Miyamoto I. Quantitative characterization of keyhole absorption mechanisms in 20 kW-class CO2 laser welding processes. J. Phys. D-Appl. Phys. 2003;36:192.
[11] Lacroix D, Jeandel G. Spectroscopic characterization of laser-induced plasma created during welding with a pulsed Nd:YAG laser. J. Appl. Phys. 1997;81:6599.
[12] Chen X, Wang HX. Prediction of the laser-induced plasma characteristics in laser welding: a new modelling approach including a simplified keyhole model. J. Phys. D-Appl. Phys. 2003;36:1634.
[13] Matsunawa A, Semak V. The simulation of front keyhole wall dynamics during laser welding. J. Phys. D-Appl. Phys. 1997;30:798.
[14] Dowden J, Postacioglu N, Davis M, Kapadia P. A Keyhole Model in Penetration Welding with a Laser. J. Phys. D-Appl. Phys. 1987;20:36.
[15] Ye XH, Chen X. Three-dimensional modelling of heat transfer and fluid flow in laser full-penetration welding. J. Phys. D-Appl. Phys. 2002;35:1049.

Chapter 2

Background

2.1 Physical processes during keyhole mode welding

2.1.1 Plasma attenuation of high energy beams

When a high energy density laser or electron beam impinges on a work-piece surface, the material vaporizes resulting in the formation of a deep and narrow cavity called a keyhole. The keyhole is filled with metal vapors and ions and is surrounded by the weld pool. As the laser or electron beam traverses the plasma, the beam intensity decreases due to absorption and scattering by the atoms and ions present in the keyhole. The attenuation of the beam intensity depends on the nature of the beam and the plasma.

2.1.1.1 Laser beam

The incident laser beam is absorbed by the plasma through electron-atom and electron ion collisions, inverse Bremsstrahlung, and photo-ionization processes [1-4]. Classical descriptions of laser beam absorption assume that the kinetic energy gained by the electrons in the plasma through acceleration by the electromagnetic field of the laser is dissipated through ohmic heating. The extent of absorption of laser by the plasma depends on the elements present and the nature of the incident beam. For example, because of its higher wavelength, the CO_2 laser (10.6 μm) is more strongly absorbed through inverse Bremsstrahlung absorption mechanism as compared to Nd-YAG laser (1.06 μm) [5]. The absorption of the CO_2 laser by the plasma plume is stronger for

argon compared to helium as the shielding gas [3]. Yilbas et al. [1] experimentally and theoretically studied the absorption of Nd:YAG laser by the plasma due to electron-ion, electron-atom collisions, photo-ionization and inverse Bremmstrahlung processes. About 13 % of the laser beam was absorbed at a plane 2.6 mm above the work-piece surface, with the absorption being highest near the center of the beam and lowest near the periphery. Modeling of the physical processes in the keyhole plasma can give a quantitative measure of the extent of radiation absorbed by the plasma [6-9]. Absorption of laser by plasma depends on the degree of ionization as well as the density of the gas. As the temperature of the plasma increases from the edge of the plasma towards the center, degree of ionization increases. Thus, absorption coefficient of the plasma for the laser beam increases. At high powers and near the center of the plasma, the density of gas may decrease significantly, resulting in a decrease in the absorption of the laser radiation by the plasma. Klemens [10] modeled the absorption of laser by plasma using non-zero absorption coefficient between two critical temperatures and zero absorption otherwise. Assuming uniform electron temperature distribution, Matsunawa and Semak [11] calculated the plasma absorption coefficient from the relation given in Eq. **2.1** based on an expression for the density of metal vapors:

$$\mu(l) = \mu_{max} \sin\left(\frac{\pi}{2}\frac{l}{d}\right) + \mu_s \qquad (\mathbf{2.1})$$

where μ is the plasma absorption coefficient, l is the local depth, d is the keyhole depth, and subscripts *max* and *s* represent the values at keyhole bottom and keyhole exit, respectively.

Kaplan [12] calculated the plasma absorption coefficient for CO_2 lasers and iron plasma through inverse Bremmstrahlung mechanism by first calculating the degree of ionization as a function of temperature using Saha's equation. His results showed that the plasma absorption coefficient first increases with temperature due to increasing ionization and then decreases due to the reduction in density of plasma. As shown in Figure **2.1**, the calculated plasma absorption coefficient increased from less than 50 m^{-1} near the keyhole walls to 200 m^{-1} before decreasing near the core. The power loss due to plasma absorption was only 10 % and an average location independent value of 100 m^{-1}

was recommended. Solana and Ocana [13] calculated the inverse Bremmstrahlung absorption coefficient for 4-10 kW CO_2 lasers to be 100-185 m^{-1} in the range of 2-6 m/min (33.3 – 99.9 mm/s) welding speed. The value is likely to differ with the process parameters and the material. Miller and DebRoy [14] calculated inverse Bremmstrahlung absorption coefficient at various distances from the top surface of the weld pool by first calculating the electron temperatures and number density of electrons. The inverse Bremmstrahlung absorption coefficient was strongly dependent on the electron density and varied from 0.3 m^{-1} at a distance of 1.6 mm from the top surface of the weld pool to 1128.5 m^{-1} at a distance of 0.1 mm. Amount of absorption decreased with the increase in the shielding gas flow rate due to a decrease in the plasma volume.

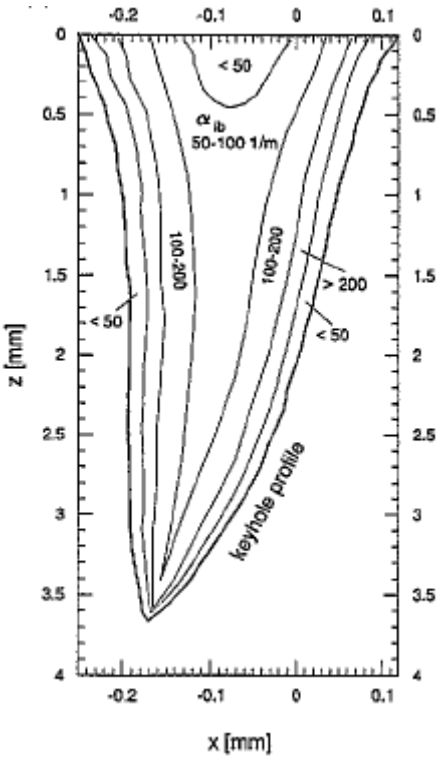

Figure **2.1**: Spatial variation of plasma absorption coefficient in the plasma as calculated by Kaplan [12].

In addition to the absorption mechanisms, scattering of the beam by metal vapors and clusters can also result in attenuation of the beam [2, 3, 15]. Rayleigh scattering of

the laser beam by ultra fine particles is more significant for the shorter wavelength Nd:YAG laser compared to CO_2 laser [3, 15]. The experimental and theoretical studies have provided insight into the attenuation of laser beam due to absorption and scattering. Based on these studies, many researchers have used an average absorption coefficient in the modeling of keyhole mode welding, independent of depth and location in a horizontal plane using the Beer-Lambert law for the absorption of beam as it traverses a unit distance in the plasma [16, 17]. Mazumder and Steen [16] used a value of 800 m^{-1} for the absorption of CO_2 lasers by iron plasma in the range of 1000 W to 2000 W input power and 5-25 mm/s welding speed. For absorption of CO_2 lasers by aluminum vapors at 50 % ionization, Klemens [10] used a plasma absorption coefficient of 600 m^{-1}. Fabbro and Chouf [17] used a range of 100-200 m^{-1} for absorption of 5-10 kW CO_2 laser by the iron plasma at a welding speed of 200 mm/s.

2.1.1.2 Electron beam

When an electron beam strikes a work-piece surface, it gives off its energy to the atoms and molecules in the work-piece through elastic and inelastic collisions which alter the trajectory of the electron. Because of the small size of electrons compared to the atoms and molecules, only a portion of the electron energy is released by each collision. Therefore, before releasing all its energy, the electron undergoes a large number of collisions. The distance from the surface that the electrons travel before losing all of their energy is called the electron range (ER). The electron range depends solely on the energy of the electrons and the density of matter [18]. Furthermore, mass traversed by an electron per unit area (= density X electron range) is independent of the state of the material (solid/liquid/vapor). In other words, the electron range is inversely proportional to the density. This fact can be used to estimate the extent of absorption of electrons in the keyhole plasma. For example, for electrons with energies in the range of 10-150 keV, the typical electron range in liquid or solid iron, ER_{solid} is about 0.04 mm [10]. Taking a value of $\rho_s/\rho_v = 2 \times 10^4$ for iron vapor at its boiling point, Klemens [10] estimated the

electron range in iron vapor to be about 80 mm(= ρ_s/ρ_v X ER_{solid}) making the absorption of electrons in the vapor rather unimportant.

Scattering of the electron beam in the plasma can play a significant role in electron beam welding (EBW). Increase in scattering at higher pressures can lead to a decrease in keyhole depth [18]. Since the pressure in the keyhole increases with depth, scattering is expected to be higher near the keyhole bottom than the top. Scattering can also increase the beam radius. Radius of the scattered beam increases with increase in the molecular weight of the scattering gas and with decrease in the accelerating voltage [18]. Scattering of electrons at large angles, or backscattering, by the plasma can also result in loss of power.

2.1.2 Absorption by material

2.1.2.1 Laser-material interaction

The absorption coefficient for clean flat surfaces and normal incidence can be estimated from the following relation based on the assumption that energy absorption is due to a photon–electron interaction [19]:

$$\alpha = 0.365\left(\frac{\rho}{\lambda}\right)^{1/2} - 0.0667\left(\frac{\rho}{\lambda}\right) + 0.006\left(\frac{\rho}{\lambda}\right)^{3/2} \qquad (\mathbf{2.2})$$

where ρ is the electrical resistivity (ohm-cm) of the liquid metal at the boiling point and λ is the wavelength (cm) of the incident laser beam. However, the estimated absorption coefficient may differ from the actual value owing to surface imperfections. As shown in Eq. **2.2**, the absorption coefficient depends on the wavelength of the laser beam. CO_2 laser (10.6 μm) is absorbed less efficiently than Nd:YAG laser (1.06 μm) [5]. For example, the absorption coefficient for CO_2 laser - steel interaction is much smaller (~0.15) compared to that for Nd:YAG laser – steel interaction (~0.3). The absorption coefficient also varies with the angle of incidence [11, 20, 21] and the angle of

polarization of the laser beam [21]. Matsunawa and Semak [11] used the following expression to simulate the angular dependence of absorption coefficient:

$$\alpha(\theta) = \alpha_0 \cos^K(\theta) \qquad (\mathbf{2.3})$$

where α is the absorption coefficient, α_0 is the absorption coefficient for normal incidence, θ is the angle between the laser beam and the surface normal, and the exponent K is a constant depending on the particular material. Value of K was taken to be equal to 0.2 to simulate the experimental results for steel [11]. Figure **2.2** illustrates the angular dependence of absorption coefficient when α_0 = 0.3. At large angles of incidence, the absorption coefficient may be much lower than its value for normal incidence.

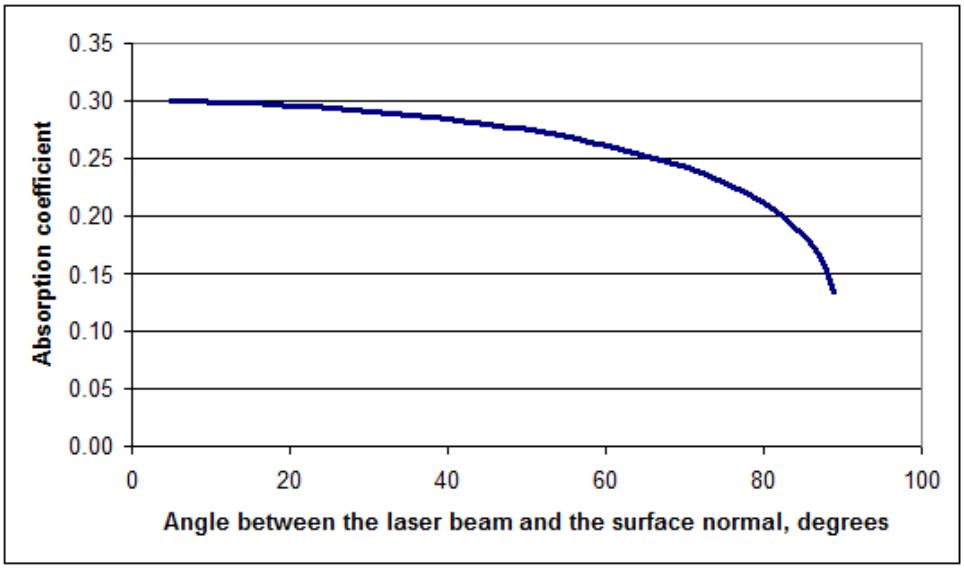

Figure **2.2**: Angular dependence of absorption coefficient for Nd:YAG laser–steel interaction.

2.1.2.2 Electron beam - material interaction

An electron beam accelerated under a voltage V_B gains a kinetic energy equal to eV_B, where 'e' is the Coulombic charge of the electron. When an electron beam strikes

the surface of the material, some of the electrons are back-scattered while the rest are stopped by the material within a small distance from the surface [18]. The kinetic energy of the electrons is converted into heat and/or excitation (atomic or molecular) energy. In addition, X-rays and secondary electrons may be produced as a result of secondary processes.

The fraction of electron beam that is backscattered is independent of the incident beam energy [18] but increases with increasing atomic number. The fraction of the electron beam that is backscattered also increases as the angle between the normal to the surface and the electron beam increases [18]. For electron beam incident on the keyhole walls at small angles of incidence, only a small portion of the beam is absorbed while the rest is back-scattered.

2.1.3 Beam divergence and defocus

A laser or an electron beam increases in size, and decreases in intensity, as the distance from the focal plane increases [18, 22]. Since the divergence of the beam with distance can affect the keyhole geometry, this behavior should be taken into account in the modeling of the keyhole. Furthermore, defocusing of the laser or electron beam can affect the keyhole depth. For positive defocusing, i.e. when the focal plane of the beam lies above the surface of the work-piece, beam spot size at and below the work-piece surface is higher than the focal spot radius. Therefore, the intensity of the beam is lower at and below the work-piece surface resulting in decreased penetration. On the other hand, when the beam is focused below the surface of the work-piece, i.e. for negative defocusing, the penetration may first increase and then decrease with increase in the magnitude of defocus. The effect of beam defocus on keyhole porosity has been discussed by Zhao and DebRoy [22]. They found that porosity is more likely in a transition range where the welding process is neither completely keyhole mode nor completely conduction mode. The transition of welding mode between conduction and keyhole can result in trapped gases or porosity.

A laser beam may be focused by the operator intentionally above or below the work-piece surface as part of the experimental set up. Alternatively, a beam may be defocused due to manual error in focusing of the beam [23]. Palmer and Elmer [23] used the Enhanced Modified Faraday cup (EMFC) electron beam diagnostic tool to determine the sharp focus condition of electron beams. Even a sharply focused electron or laser beam may get defocused during the welding process as a result of the depression of the melt pool surface under the effect of recoil pressure. Finally, plasma present above the keyhole during the welding process acts as a refracting lens and re-focuses the energy beam [3].

The variation of the electron beam profile with distance can be expressed by Eq. **2.4** [18] :

$$d_F^2(z) = d_F^2(z=0) + 4a_B^2 z^2 \qquad (\mathbf{2.4})$$

where d_F is the beam diameter at distance 'z' from the focal spot and a_B is the beam aperture in radians. The divergence of beam decreases with increase in the distance between the focusing lens and the work-piece. Therefore, for large distances and small keyhole depths, the location of the focal plane affects the keyhole depth to a lesser degree [18]. The electron beam size is also affected by ion-compensation, self magnetic field and scattering of the electron beam. Dilthey et al. [24] simulated the effects of these factors on the variation of beam size with distance by comparing the calculated beam profile with the experimental measurements. They concluded that for the conditions of their experiments, the influence of the self-magnetic field was secondary to the aberration of the beam forming system and that the space charge of electron beam was completely compensated by the ions.

2.1.4 Multiple reflections in keyhole

When a laser or an electron beam is incident on the keyhole walls, only a fraction of energy is absorbed. The reflected beam is again intercepted by the keyhole walls and

undergoes further absorption. Thus, multiple reflections of the beam within the keyhole result in enhanced absorption which is considered in numerical models in one of the following ways. First, the keyhole is assumed to be a black body that absorbs all incident energy. In other words, the absorption coefficient is considered to be unity when the work-piece temperature becomes equal to the boiling point of the alloy [25]. This method is very simple to implement. However, it does not consider the effect of keyhole geometry and the Fresnel absorption coefficient. For example, for the interaction of CO_2 laser with aluminum alloys, the Fresnel absorption coefficient is 0.1, which means that complete absorption of the beam energy may not take place for a keyhole with low depth to width ratio. Second, a location independent effective absorption coefficient for the laser-material interaction is calculated based on the keyhole geometry and the Fresnel absorption coefficient [12, 22]. If the laser beam undergoes 'n' reflections on the keyhole walls before exiting, the effective absorption coefficient α_{eff} is given by:

$$\alpha_{eff} = 1-(1-\alpha)^n \qquad (\mathbf{2.5})$$

where α is the singe incidence absorption coefficient [12, 22]. The average number of reflections, and hence the absorption due to multiple reflections, can be related to the mean angle of the keyhole as shown in Figure **2.3** [12]. As the keyhole angle becomes smaller, the number of reflections, and hence the energy utilization, increase. Third, detailed ray tracing method [17, 26-28] is used to estimate the absorption of energy beam at any location within the keyhole considering both the keyhole geometry and the Fresnel absorption coefficient.

Solana and Negro [29] investigated the effects of inverse Bremsstrahlung absorption and multiple reflections on the keyhole penetration. The intensity distributions due to multiple reflections were similar for different laser input profiles like Gaussian and uniform top-hat profile, and multiple reflections resulted in increased penetration over that achieved with only a single reflection. Consideration of inverse Bremsstrahlung absorption resulted in shallower keyholes.

Ho and Wen [30] investigated the distribution of laser energy on a hemispherical cavity using a Monte Carlo method and an analytical method. They considered both

specular and diffuse reflections of laser considering the dependence of absorptivity on angle of incidence and the polarization of the beam. They found that the beam intensity at the bottom of a hemispherical cavity is markedly increased due to multiple reflections on cavity walls. Ki et al. [31] studied the effect of multiple reflections on the keyhole geometry by using a ray tracing procedure. They showed that the reflections in the keyhole are highly dependent on geometry making a predefined keyhole shape. For example, a paraboloid of revolution is not a good choice for a keyhole shape because of its particular focusing properties.

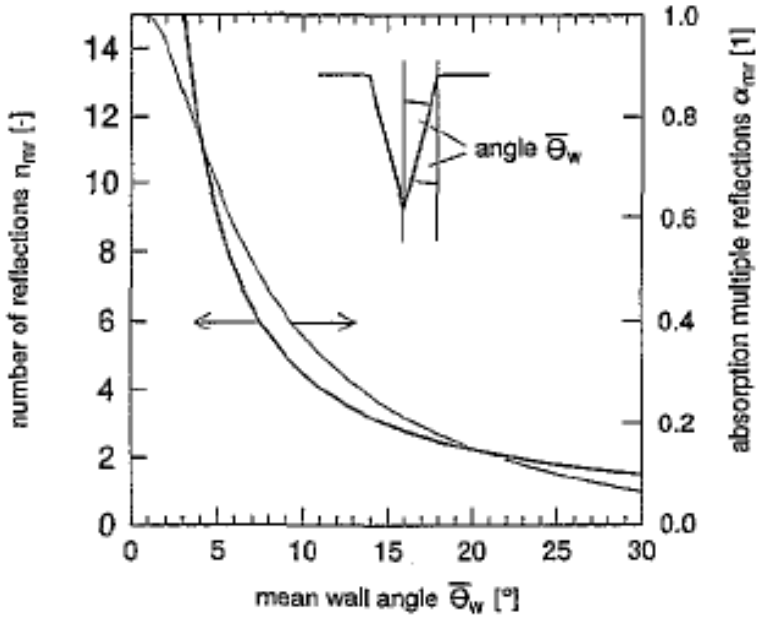

Figure **2.3**: Plot of average number of reflections and the absorption due to multiple reflections as a function of mean keyhole wall angle [12].

2.1.5 Pressure balance and keyhole wall temperatures

The surface tension force at the liquid-vapor interface and the hydrostatic force of the liquid metal tend to close the keyhole [10]. The vapor pressure of the metal vapors within the keyhole provides the balancing force that keeps the keyhole open. With an

increase in distance from the weld pool surface, the radius of curvature of the keyhole decreases, thus increasing the surface tension force. Thus, a larger vapor pressure is needed in the keyhole at a greater distance from the top surface to balance the higher surface tension force. The temperatures on the keyhole walls can be calculated from the equilibrium temperature versus pressure relation for the given alloy. As the vapor pressure within the keyhole increases from the keyhole top to the bottom, the equilibrium wall temperatures increase from the top to the bottom of the keyhole. The keyhole wall temperatures in laser beam welding (LBW) are often assumed to be equal to the boiling point of the alloy at all locations [11, 12, 22, 32, 33]. Trappe et al. [34] modeled the keyhole in LBW considering heat conduction and pressure balance at keyhole walls and found the calculated wall temperatures to be nearly constant. However for EBW, the variation of wall temperatures is expected to be significant (see Appendix A). The difference in variation of wall temperatures with depth between EBW and LBW is discussed in Appendix A.

2.1.6 Weld pool turbulence

The temperature gradient on the weld pool surface in high energy density welding can be very high. The resulting high surface tension gradients on the weld pool surface cause very high fluid velocities and the weld pool is often turbulent [35]. The enhanced rates of heat, mass, and momentum transport caused by the presence of turbulence can be taken into account by using effective viscosity and thermal conductivity values [36-38] for heat transfer and fluid flow calculations. These effective values are calculated by enhancing the molecular values at all locations within the weld pool by a certain factor based on prior experimental and theoretical work.

Alternatively, an appropriate turbulence model can be used to estimate the location dependent turbulent viscosity and thermal conductivity within the weld pool [35, 39]. In theory, the turbulent flows can be modeled through solution of the Navier-Stokes equation. However, since the length scale for turbulence is very small, this approach will

be very expensive in terms of storage space and computational time [40]. Therefore, time averaged models of turbulence are required. Launder and Spalding [40] classified the existing turbulence models into three categories:

1. Algebraic models: Effective turbulent properties like viscosity are given in terms of the local fluid properties.
2. Differential models: Prescription of effective turbulent properties requires solution of one or more differential equations.
3. Stress transport models: Instead of providing values of turbulent properties, these models provide equations for turbulent fluxes directly.

Prandtl's mixing length hypothesis forms the basis of several algebraic and differential models. The basic statement of the hypothesis can be expressed as [40]:

$$\mu_t = \rho l_m v_m \qquad (\mathbf{2.6})$$

where μ_t is the turbulent viscosity, ρ is the density of the fluid, l_m is the characteristic length, and v_m is the characteristic velocity. The characteristic velocity can be calculated in several ways. For example, it can be expressed as the product of the characteristic length, l_m and the local velocity gradient, $\left|\frac{\partial u}{\partial y}\right|$. That is,

$$\mu_t = \rho l_m v_m = \rho l_m^2 \left|\frac{\partial u}{\partial y}\right| \qquad (\mathbf{2.7})$$

Or, the characteristic velocity can be taken as the square-root of the turbulent kinetic energy per unit mass, K_e [40].

$$\mu_t = \rho l_m K_e^{1/2} \qquad (\mathbf{2.8})$$

K_e can be calculated from differential equations. The characteristic length scale can be calculated either by using the distance from the solid boundary or from differential equations. In a simple approach, the characteristic length can be considered to be proportional to the distance from the solid boundary [40].

Kumar and DebRoy [41] used a vorticity based model for turbulent viscosity using van Driest model to calculate the characteristic length based on the distance from the solid boundary and the local velocity gradient. If K_e is calculated from the solution of a differential equation and l_m is prescribed directly, the resulting model will be a one-equation turbulence model. If both K_e and l_m are calculated from differential equations, the model will be called a two-equation turbulence model. Specific studies for turbulence in weld pools are not readily available in literature. Since these models involve constants which depend on the particular type of flow, the increased complexity of a model does not necessarily mean that the model is more accurate for application to weld pool turbulence. Therefore, it might be reasonable to opt for a computationally simpler approach.

2.1.7 Surface deformation

In keyhole mode laser or electron beam welding, the weld pool surface reaches very high temperatures in a very short time. The material evaporates and the metal vapors leaving the surface exert a recoil pressure on the weld pool surface forming a deep and narrow vapor cavity or keyhole. If no material is added to the weld pool, the volume change should be zero provided the average densities of the initial and the final phases are similar. Under these conditions, therefore, the top surface deformation in partial penetration welds is expected to be small. In full penetration welds, the bottom surface of the weld pool can deform under the influence of the vapor pressure and the weight of the liquid metal even when the total volume change is zero. However, some top surface deformation is often observed even for partial penetration welds without material addition to the weld pool. This deformation could be due to the volume expansion during melting followed by rapid freezing. Postacioglu et al. [42] found that the top surface deformation for low welding speeds could be represented by a simple shape, such as a circular arc, of equal area. Deformation of the free surface of the weld pool involves work done in, or against, the direction of surface tension and gravity. The configuration

of the free surface can be calculated by either minimizing the energy associated with the surface deformation or performing a force balance for the free surface [43].

2.2 Numerical models of keyhole mode welding

2.2.1 Laser beam welding

To appreciate the complexity of the simultaneous physical processes involved in keyhole mode laser welding and how the solution of such a complex problem has evolved in recent decades, a brief survey of previous work is undertaken. Swift-Hook and Gick [44] formulated an analytical model considering a line source going into the work-piece. Andrews and Atthey [25] calculated the keyhole shape for semi-infinite weld pool assuming that all the input power was absorbed and used to evaporate the surface, and that the pressure anywhere inside the keyhole was 1 atm. They used an analytical model to calculate the penetration depth in the absence of surface tension but had to resort to numerical techniques when surface tension was included. Keyhole profiles calculated without considering surface tension had a cusp (point formed by intersection of two curves) at the bottom. They found that the consideration of surface tension reduced the calculated keyhole depth by a factor of three, and smoothed the cusp formed at the keyhole bottom.

Figure **2.4** (a) and (b) show the variation of calculated penetration depth with power density and beam radius, respectively. The process was controlled by dimensionless power and dimensionless surface tension parameters. Figures **2.4** (a) and (b) show two regimes in which the slope of the curve is distinctly different. Since the input power was constant at 5 kW, higher beam radius corresponds to lower power density. At low beam radius, or high power density, the keyhole depth is directly proportional to $(W/a)^{2/3}$. At high beam radius, or low power density, the keyhole depth

varies as $(W/a^2)^2$. As shown in Figure **2.4**, the calculated keyhole depth decreases by several factors as the surface tension is increased.

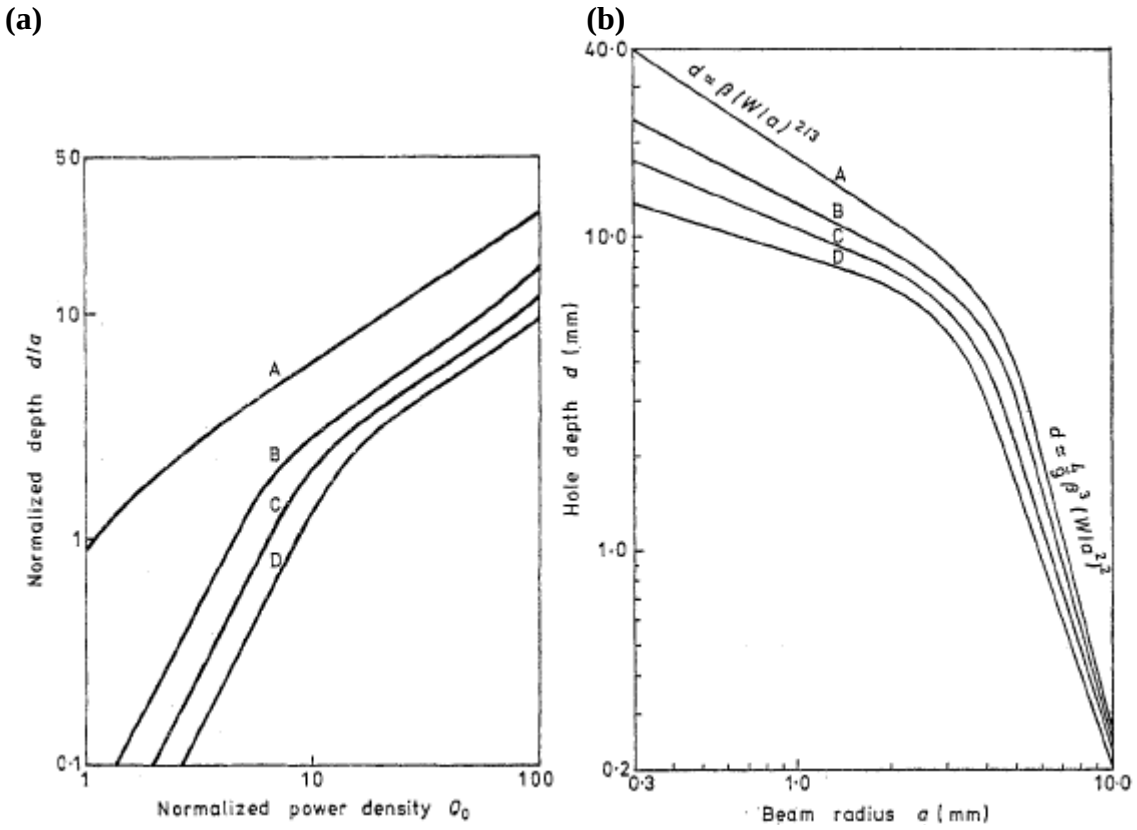

Figure **2.4**: (a) Variation of normalized keyhole depth, d/a (where'd' is the keyhole depth and 'a' is the beam radius), with normalized power density Q_0 for various values of the normalized (dimensionless) surface tension coefficient τ. A, $\tau = 0$ (no surface tension); B, $\tau = 20$; C, $\tau = 50$; D, $\tau = 100$. $Q_0 = q/(g\rho\rho_g h^2 a)^{1/2}$, where q is the energy flux density, g is the acceleration due to gravity, ρ is the density of liquid, ρ_g is the density of metal vapors, h is the heat of vaporization per unit mass. $\tau = T/\rho g a^2$ where T is the surface tension. (b) Variation of keyhole depth with beam radius for various values of surface tension coefficient T. Beam power W is 5 kW, and the value of constant β $(= 9/(4\pi^2 h^2 g\rho\rho_g)^{1/3})$ is $6.09 \times 10^{-7} m^{5/3} W^{-2/3}$. A, T = 0 (no surface tension); B, T = 0.4 N m^{-1}; C, T = 0.9 N m^{-1}; D, T = 1.8 N m^{-1} [25].

Klemens [10] calculated the keyhole radius by balancing vapor pressure in the cavity, the hydrostatic pressure, and the surface tension:

$$p_0(z) = \frac{\sigma}{r(z)} + \rho g z \qquad (\mathbf{2.9})$$

where p_0 is the excess pressure above the ambient gas pressure, σ is the surface tension, r(z) is the keyhole radius at distance z below the top surface, and ρ is the density.

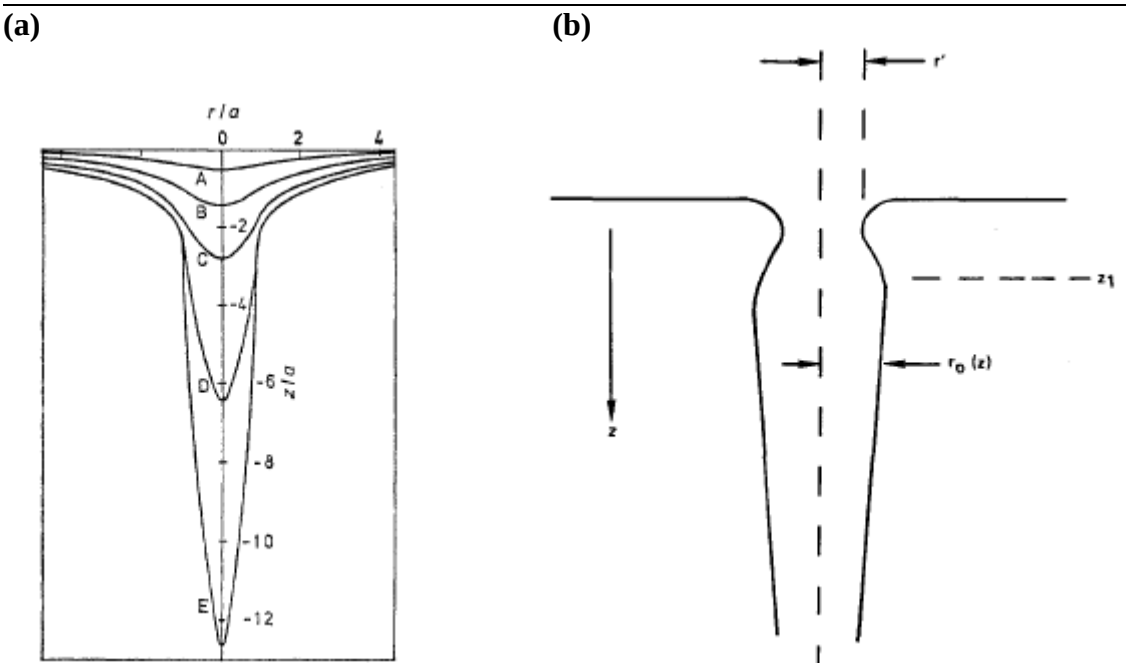

Figure **2.5**: Keyhole shapes showing a (a) flare [25], or (b) constriction [10], near the entrance.

Since there is a flow of metal vapors, a pressure gradient builds up along the keyhole depth. The vapor pressure in the keyhole can be given as the sum of ambient pressure and the pressures due to surface tension and hydrostatic forces. At the top of the keyhole, the hydrostatic force is zero. So the vapor pressure in the keyhole right at the top surface should be equal to the sum of ambient pressure and the pressure due to surface tension. But just outside the keyhole, the pressure is equal to the ambient pressure. Therefore, continuity of pressure near the keyhole entrance requires that the pressure due to surface tension vanishes at the entrance. Since the pressure due to surface tension is proportional to the curvature of the keyhole, the curvature should vanish at the interface. This may happen if the keyhole has a trumpet-like flare near the entrance as shown in Figure **2.5** (a) [25], or if the keyhole profile is constricted near the top, as shown in Figure **2.5** (b) [10]. Neglecting Marangoni convection, Postacioglu et al. [42]

calculated the configuration of the top surface for low process Pecelt number which is defined as:

$$Pe = \frac{Ua}{\kappa} \qquad (\mathbf{2.10})$$

where U is the welding speed, 'a' is the keyhole radius, and κ is the thermal diffusivity. They assumed circular keyhole and liquid regions. They calculated the vapor pressure in the keyhole by adding the pressure due to surface tension to the pressure in the liquid assuming that the pressure due to evaporation particles was small in comparison. Taking the value of surface tension at the boiling point of the material to be half of its value at the melting point, they estimated the vapor pressure in the keyhole to be about 5 % of the ambient pressure.

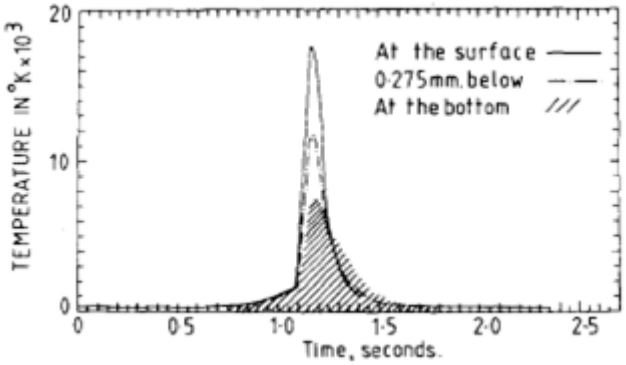

Figure **2.6**: Thermal cycles calculated for Ti-6Al-4V keyhole welds made at 2 mm/s [16].

Mazumder and Steen [16] numerically modeled the three-dimensional (3D) heat conduction in surface hardening, laser glazing and welding assuming zero reflectivity in the keyhole region. The plasma absorption was calculated using the Beer-Lambert law with a location independent absorption coefficient (= 800 m^{-1}). Figure **2.6** [16] shows the calculated thermal cycle for keyhole mode welds made on Ti-6Al-4V alloy. Cooling rates at the top surface were found to be about 8000 K/s. This cooling rate is much higher than the values typically experienced during arc welding where the heat source is much more diffuse [45].

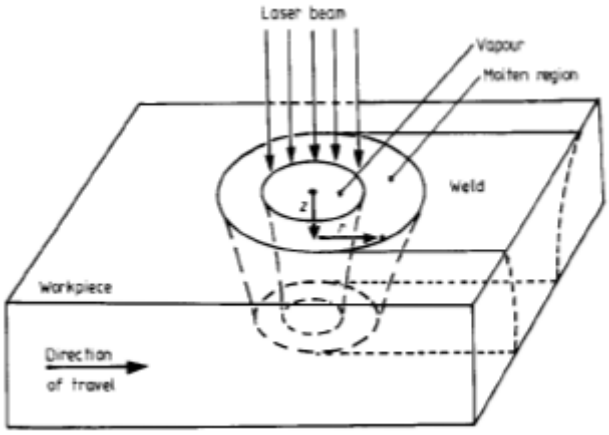

Figure **2.7**: Axi-symmetric keyhole and weld pool assumed by Dowden et al. [32].

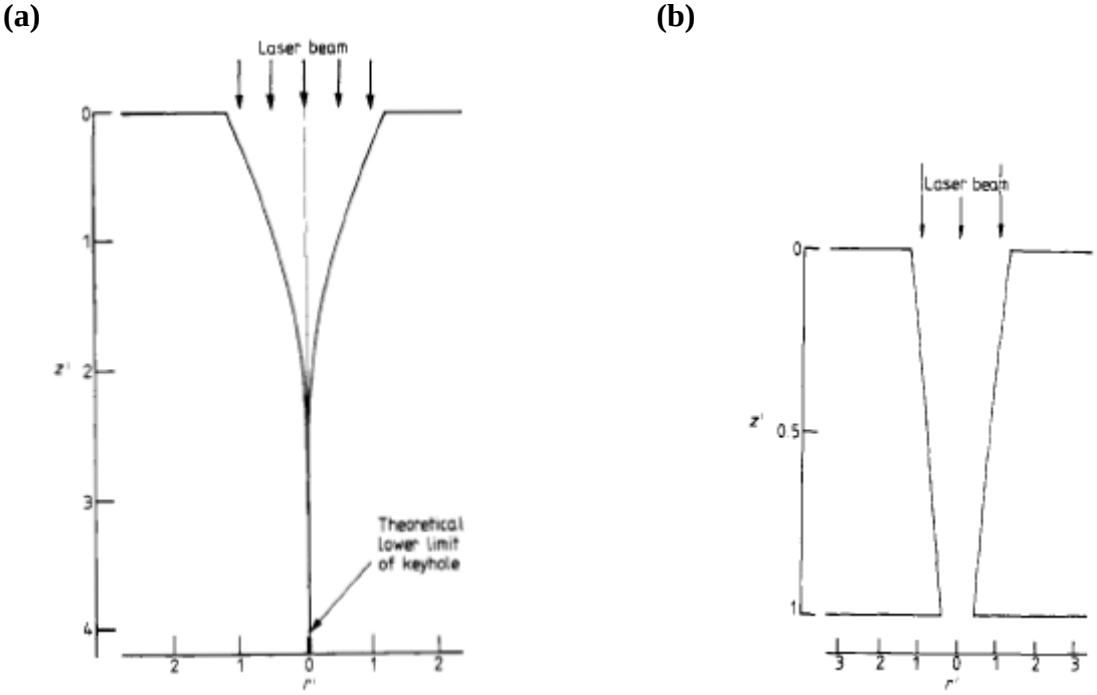

Figure **2.8**: Partial and full penetration keyholes calculated by Dowden et al. [32].

Dowden et al. [32, 46] assumed a keyhole, shown in Figure **2.7**, with circular horizontal sections of radius varying with depth to model the physical processes in the vapor and molten regions. Incident radiation was assumed to be uniformly absorbed over each cross-section, and the keyhole walls were assumed to be at boiling point

temperature. The temperature inside the keyhole was assumed to have a quadratic variation with radial distance. They further assumed all conditions in both the keyhole and weld pool region to be axi-symmetric. Since the motion of the heat source imparts a directional dependence to the distribution of variables (for example, elongation of the weld pool in the welding direction), this assumption limits the application of the model to low welding speeds.

Figure **2.8** shows the keyhole shapes for partial and full penetration cases calculated by Dowden et al. [32]. The pressure in the keyhole was found to be determined by the surface tension and radius of the keyhole. As the keyhole radius decreased with depth, the pressure in the keyhole increased. Dowden et al. [32], however, recommended a detailed 3D heat transfer and fluid flow analysis for a better description of the weld pool.

Kroos et al. [47] studied the stability of a cylindrical keyhole concentric with the laser beam by balancing the forces and energy flux on the keyhole walls. Figure **2.9** shows the variation of normalized evaporation and normalized surface tension pressure at keyhole walls as a function of normalized keyhole radius. The temperature was calculated by balancing the absorbed energy flux density, Q_{abs}, which is the sum of the conduction losses, Q_{λ}, and evaporation, Q_{evap} at the keyhole walls:

$$Q_{abs} = Q_{\lambda} + Q_{evap} \qquad (\mathbf{2.11})$$

The energy flux density absorbed by the keyhole depends on the input power, P and the keyhole radius, a:

$$Q_{abs} = f_1(P, a) \qquad (\mathbf{2.12})$$

For Peclet number, Pe less than 0.2, the keyhole wall temperature can be given as a function of heat flux density at the circumference of the keyhole, Q_{λ} and Pe. That is,

$$T_s = f_2(Q_{\lambda}, a). \qquad (\mathbf{2.13})$$

The flux density due to evaporation can be given as a function of surface temperature, T_s, and ambient pressure, p_0:

$$Q_{evap} = f_3(T_s, p_0) \quad \textbf{(2.14)}$$

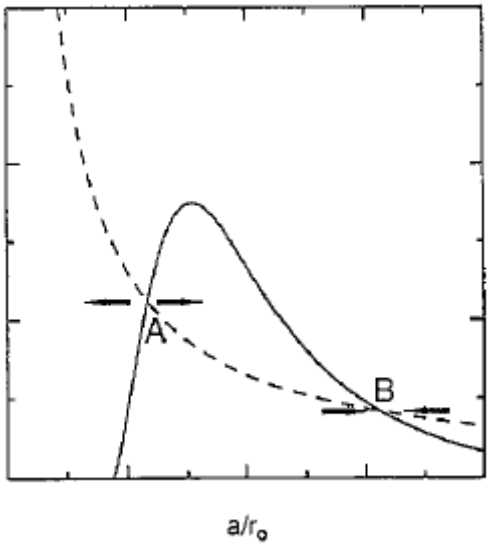

Figure **2.9**: Variation of vapor pressure (——) and surface tension (- - -) with keyhole radius. r_0 is the laser beam radius [47].

With p_0 and P known, substituting Eqs. **2.12** through **2.14** into Eq. **2.11** gives the surface temperature, T_s as a function of keyhole radius, 'a'. Thus, the vapor pressure due to evaporation can be given as a function of keyhole radius, 'a'. An increase in keyhole radius results in increase in the power entering the keyhole up to a certain value and then saturates at a value equal to the total beam power. Therefore, the flux of absorbed energy first increases and then decreases with increasing keyhole radius. This explains the maxima in variation of vapor pressure with keyhole radius. Surface tension pressure (= σ/a, where σ is the surface tension and 'a' is the keyhole radius) was assumed to be dependent only on the keyhole radius and not on the temperature. The intersections of the two curves mark the keyhole radii for which force balance is satisfied. The keyhole will collapse if the keyhole radius is to the left of point A in Figure **2.9**, since the surface tension is greater than vapor pressure. On the other hand, the keyhole radius will expand to point B if the keyhole radius is between points A and B since the vapor pressure is greater than the surface tension pressure. Finally, if the keyhole radius is to the right of

B, the keyhole radius will return to point B because the surface tension force exceeds the vapor pressure. Therefore, point A is unstable whereas point B is stable [47]. This analysis, though, neglected the pressure built up in the keyhole due to flow of metal vapors.

Kroos et al. [48] then studied the dynamic behavior of the keyhole when the laser power is suddenly shut off by analyzing the balance between the surface tension and the vapor pressure for a cylindrical keyhole surrounded by a cylindrical weld pool. From a perturbation analysis, they concluded that the keyhole is expected to undergo radial oscillations with a characteristic frequency that varied with the input power per unit thickness and the welding speed. Klein et al. [49] theoretically studied the characteristic frequencies, damping rates and stability of radial, azimuthal, and axial oscillations (Figure **2.10**) of a cylindrical keyhole surrounded by cylindrical melt pool in laser welding. In addition to the vapor pressure considered by Kroos et al. [48], they also considered the excess pressure built up in the keyhole due to metal vapor flow, δp which is given as [49]:

$$\delta p = \frac{1}{3} m n_g u_g^2 \left(\frac{d}{a} \right)^2 \qquad (\mathbf{2.15})$$

where m is the mass of ablating particles, n_g is the density, u_g is the vapor velocity, d is the keyhole depth, and a is the keyhole radius. Large amplitudes of oscillations may result in the keyhole radius becoming smaller than the unstable keyhole radius (point A in Figure **2.9**) and the keyhole may collapse. Since the separation between the unstable and the stable keyhole radius is smaller at lower absorbed power per unit thickness until it becomes zero at a threshold value, even small perturbations may result in the collapse of the keyhole at lower absorbed powers. Therefore, the stability of the keyhole increases with increase in absorbed laser power.

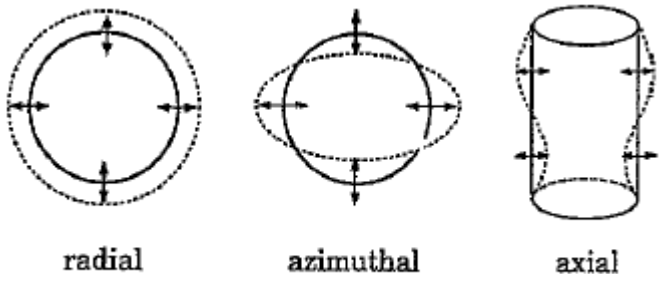

Figure **2.10**: Radial, azimuthal, and axial oscillations of the keyhole [49].

Trappe et al. [34] calculated the keyhole geometry through a two dimensional (2D) finite element model assuming a prescribed heat flux and found that the keyhole wall temperatures were nearly constant. Kaplan [12] predicted asymmetric keyhole shapes by energy balance on keyhole walls which enabled prediction of weld geometry for high welding speeds, but neglected fluid flow. Assuming the keyhole walls to be at the boiling point of the work-piece material and planar heat conduction, he modeled the heat conduction in the plasma and the liquid melt pool. The degree of ionization of the metal vapors was calculated as a function of temperature using Saha's equation. Local thermodynamic equilibrium was assumed, i.e. both the electron and heavy particles were at same temperature. The inverse Bremmstrahlung absorption coefficient was calculated based on the degree of ionization. The model was applied to a wide range of welding speeds (10 to 150 mm/s).

Sudnik et al. [38] calculated the pressure in the keyhole by balancing the vapor pressure, surface tension and hydrostatic forces on the keyhole walls and used the equilibrium pressure versus temperature relation to assign keyhole wall temperatures. Thus, they considered the variation of temperature on keyhole walls. However, the 3D fluid flow in the weld pool was approximated with 2D flow in the horizontal and vertical sections. They used effective turbulent thermal conductivity by enhancing the molecular values by a factor and ignored the convective heat flow. Due to these simplifications, the model could be run in a very short time. Matsunawa and Semak [11] simulated the dynamics of the front keyhole wall through a hydrodynamic model assuming that all of the laser beam fell on the front keyhole wall. They considered angular dependence of

absorption coefficient and also a used a location dependent plasma absorption coefficient. Starting with an assumed shape of the front keyhole wall, they calculated its transient behavior. They found that the spatial frequency of humps at the top surface increases with welding speed and finally the humps disappear.

Solana and Ocana [13] modeled the keyhole geometry and the weld pool for the laser welding process through energy and pressure balances. They also calculated the electron densities in the plasma and the absorption coefficient for the inverse Bremsstrahlung absorption of laser beam by the plasma. They reduced the 3D heat conduction equations for the plasma and the liquid region to 2D by assuming the temperature gradient in the vertical direction to be a constant. The value of the constant was guessed initially and iterated until convergence was obtained. Their work focused mainly on the calculation of the keyhole geometry. Therefore, they made simplifications to the analysis of the liquid and the solid regions. For example, they neglected the fluid flow, the phase changes, the associated enthalpy change, and assumed the same thermo-physical properties for solid and liquid irrespective of the temperature.

Amara and Bendib [26] proposed a 2D finite element model of the vapor flow in the keyhole and considered the effect of multiple reflections of the laser beam in the keyhole by using a ray-tracing procedure. Dowden [50] studied the role of viscous drag from the flow of vapor on the interaction between the keyhole and the weld pool. Ki et al. [31, 51, 52] calculated free surface evolution by tracking gas/fluid interface considering recoil pressure, fluid flow, and multiple reflections. To track the vapor/liquid interface, they used the narrow band level set method which transforms the problem to a partial differential equation and simplifies the calculations of the curvature of the surface and the unit vector normal to the surface. The calculation of surface normal through level set method was used to track the rays during multiple reflections within the keyhole. The convergence criterion for the governing equations required the time step to be less than 10^{-6} s. Therefore, the code was parallelized and optimized on a supercomputer to make the computations manageable.

Table **2.1**: Dimensionless numbers in heat transfer and fluid flow analysis.

Dimensionless Number	Definition	Remarks
Peclet number, Pe	Ua/α	Ratio of heat transfer through convection to heat transfer through conduction
Prandtl number, Pr	ν/α	Ratio of kinematic viscosity to thermal diffusivity
Reynolds number, Re	$a\rho U/\mu$	Ratio of inertial force to viscous force
Marangoni number, Ma	$-(d\gamma/dT)(T_b-T_0)a/\mu\alpha$	Represents the effects of surface tension gradient on fluid flow and heat transfer
Stefan number, Ste	$C(T_b-T_0)/L$	Represents the effect of latent heat of fusion on heat transfer
Grashof number, Gr	$g\beta(T_b-T_0)a^3/\nu^2$	Ratio of buoyancy force to viscous force
Nusselt number, Nu	$aQ_{av}/((T_b-T_0)\,k)$	Ratio of heat transfer through convection to heat transfer through conduction across a boundary
Temperature, T	$(T-T_0)/(T_b-T_0)$	Dimensionless temperature
Height, H	h/a	Dimensionless height

Ye and Chen [33] assumed a cylindrical keyhole and solved dimensionless Navier-Stokes equations. They compared the results of 2D and 3D modeling of full penetration laser welds to demonstrate that even for the welding of thin plates, the 2D modeling approach was not satisfactory. The calculations of the 3D model for full penetration weld considering Marangoni convection at the top and bottom surfaces of the full penetration welds resulted in hour-glass shaped weld pool. They studied the dimensionless numbers to understand the significance of various parameters involved in a process. The various dimensionless numbers involved in this study are defined in Table **2.1**. U is the welding speed, 'a' is the radius of the cylindrical keyhole, α is the thermal diffusivity, ν ($=\mu/\rho$) is the kinematic viscosity, μ is the viscosity, ρ is the density, T_b is the boiling point, T_0 is the ambient temperature, C is a constant, 'g' is the acceleration due to gravity, β is the coefficient of volumetric expansion, and Q_{av} is the average heat flux density at the liquid/vapor interface. Typical values of the

dimensionless parameters for full penetration welding on thin plates are: Pr = 0.01 to 0.1, Ste = 1 to 10, Ma = 100 to 10000, Gr = 10 to 1000, and Pe = 1 to 10 [33]. Low value of Prandtl number means that heat diffuses quickly compared to velocity. High value of Marangoni number means that surface tension gradient has a strong effect on the heat transfer and fluid flow. Since the Grashof number is much higher than one, the buoyancy force is much stronger than the viscous force. High Peclet numbers indicate that convection is typically very important for heat transfer in the weld pool.

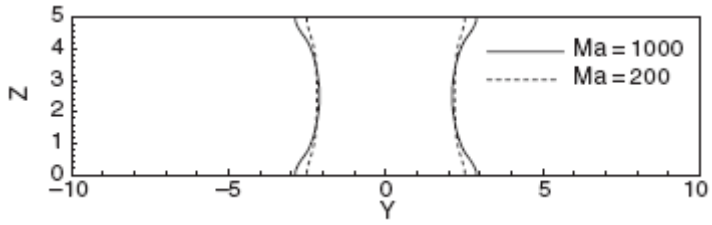

Figure **2.11**: Computed weld profile in the vertical plane perpendicular to welding direction for two different Marangoni numbers. Pe = 1, Pr = 0.1, Ste = 5.0, H = 5, T_m = 0.5, and Gr= 0 [33].

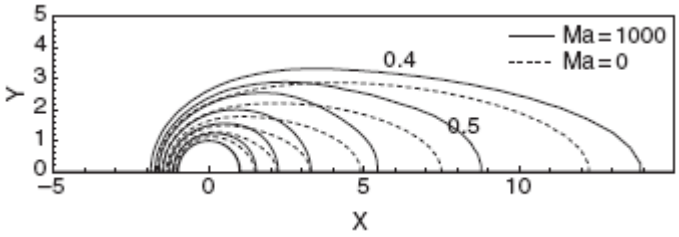

Figure **2.12**: Computed weld pool shape at the top surface for two different Marangoni numbers. Pe = 1, Pr = 0.1, Ste = 5.0, H = 5, T_m = 0.5, and Gr= 0 [33].

Figure **2.11** shows the calculated weld cross-sections for a full penetration weld for two different Marangoni numbers. The welding condition in terms of dimensionless numbers was Pe = 1, Pr = 0.1, melting point, T_m = 0.5, Gr = 0, Ste = 5.0, and the dimensionless thickness, H = 5.0. The dimensionless thickness of 5.0 corresponded to a plate 1.35 mm thick for a keyhole radius of 0.27 mm. Since the keyhole was assumed to be cylindrical and the effect of buoyancy was neglected (Gr = 0), the weld pool was

symmetrical with respect to the horizontal plane at mid-thickness of the work-piece. The weld pool was wider at the top and bottom surfaces compared to the middle plane and the widening at the free surfaces is greater at higher Marangoni number.

Figure **2.12** shows the comparison of isotherms for welds calculated considering Marangoni convection (Ma = 1000) and ignoring Marangoni convection (Ma = 0). The welding condition was defined in terms of dimensionless numbers as Pe = 1, Pr = 0.1, T_m = 0.5, Gr = 0, Ste = 5.0, and, H = 5. The isotherms are marked for T = 0.4 to T = 1.0 at intervals of 0.1. The figure shows that Marangoni convection can appreciably affect the weld results even for small plate thickness of 1.35 mm.

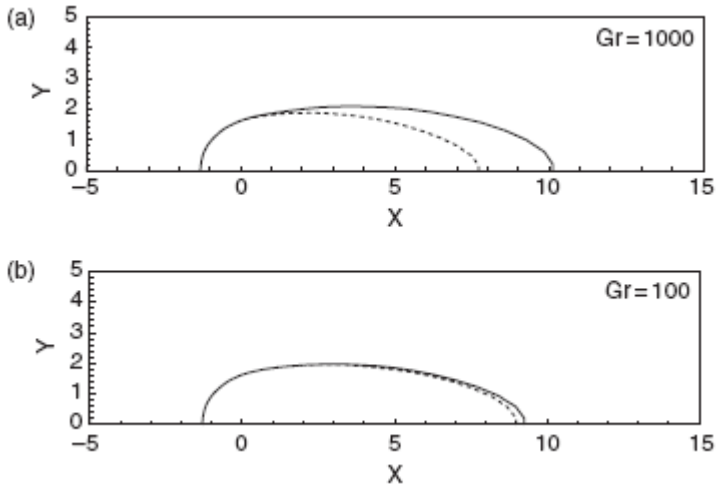

Figure **2.13**: Comparison of calculated weld pool shape at top (——) and bottom (·····) surfaces for a full penetration weld made on thin plate (plate thickness = 1.35 mm). (a) Gr = 1000, and (b) Gr = 100. Pe = 2, Pr = 0.1, Ste = 5.0, H = 5, T_m = 0.5, and Ma = 200 [33].

Figure **2.13** compares the calculated weld pool shapes at the top and the bottom surfaces for two different Grashof numbers, i.e. for different significance of buoyancy. The welding condition in terms of dimensionless numbers was Pe = 2, Ma = 200, T_m = 0.5, Pr = 0.1, Ste = 5.0 and H = 5. Due to buoyancy, the weld pool becomes asymmetric about the middle plane at Gr = 1000. The weld pool is wider at the top surface compared to the weld pool at the bottom surface. At Gr = 100, the shapes of weld pool at the top

and bottom surfaces were similar. Therefore, at low values of Gr, the convection due to variation of variation of density can be neglected.

The net power absorbed by the work-piece with thickness 'h' can be given by Eq. **2.16**:

$$P = 2\pi hk(T_b - T_0)Nu \qquad (\mathbf{2.16})$$

That is, higher Nusselt number means more heat is absorbed by the work-piece. Total power absorbed by the work-piece can be given by integrating the local energy flux density over the keyhole surface:

$$P = -k(T_b - T_0)\int_0^H d\bar{z}\int_0^{2\pi}\frac{d\overline{T}}{d\bar{r}}d\theta \qquad (\mathbf{2.17})$$

The average Nusselt number, Nu can be calculated from Eqs. **2.16** and **2.17** as:

$$Nu = -\frac{1}{2\pi H}\int_0^H d\bar{z}\int_0^{2\pi}\frac{d\overline{T}}{d\bar{r}}d\theta \qquad (\mathbf{2.18})$$

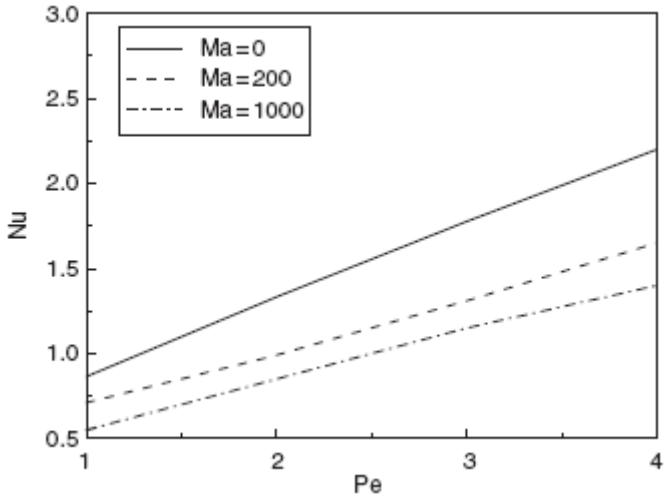

Figure **2.14**: Variation of computed Nusselt number with Peclet number for three different Marangoni numbers. $T_m = 0.5$, Pr = 0.1, Ste = 5.0, Gr = 0, and H = 5 [33].

Figure **2.14** shows the variation of the calculated Nusselt number with variation in Peclet number at three different Marangoni numbers. Nu increases with increasing Pe (or

welding speed) and decreases with increasing Ma. Eq. **2.16** implies that more laser energy is required for full penetration welding when Nu is high. Since Pe and Ma depend on the welding speed and material properties ($d\gamma/dt$, T_b, μ, and α), the amount of laser energy required to form a full penetration weld can be related to these parameters. For fixed laser energy absorbed by the work-piece (and consequently, Nu), Pe is higher at higher Ma. Recall that, $Pe = Ua/\alpha$. If, then, both the welding speed and the laser energy absorbed by the work-piece are fixed, higher Ma will result in higher keyhole radius.

Lee et al. [27] studied the mechanism of keyhole formation and stability in stationary laser welding of mild steel by assuming an axisymmetric keyhole profile and using volume of fluid method. Figure **2.15** shows the evolution of the keyhole and the weld pool with time for a mild steel weld made with 2 kW CO_2 laser. The recoil pressure of evaporating material induces an upward flow of molten material and causes the formation of a convex profile at the top surface. The convex profile causes a downward flow due to hydrostatic pressure and surface tension. The collision of the upward and downward flow causes the formation of a protrusion on the keyhole wall at 5.4 ms. The protrusion blocks the laser beam energy which causes evaporation of the upper surface of the protrusion. The recoil pressure of the evaporating particles pushes the protrusion downwards. As a result, a void is formed at 5.5 ms.

Zhao et al. [22] studied the effect of beam defocusing on keyhole porosity by considering 3D conduction heat transfer. The model was used to predict the transition from conduction to keyhole mode welding. The occurrence of macroporosity is more likely in the transition regime compared to both conduction and keyhole mode regimes. Tsirkas et al. [53] calculated the distortion in LBW by using a 3D heat transfer finite element model that considered metallurgical transformations. Du et al. [54] modeled the fluid flow in full penetration welds using non-staggered grids with a momentum interpolation scheme to reduce the required storage space. Wang et al. [55] assumed a laminar flow and a double ellipsoid heat source to model the heat transfer and fluid flow in laser welding through control volume method.

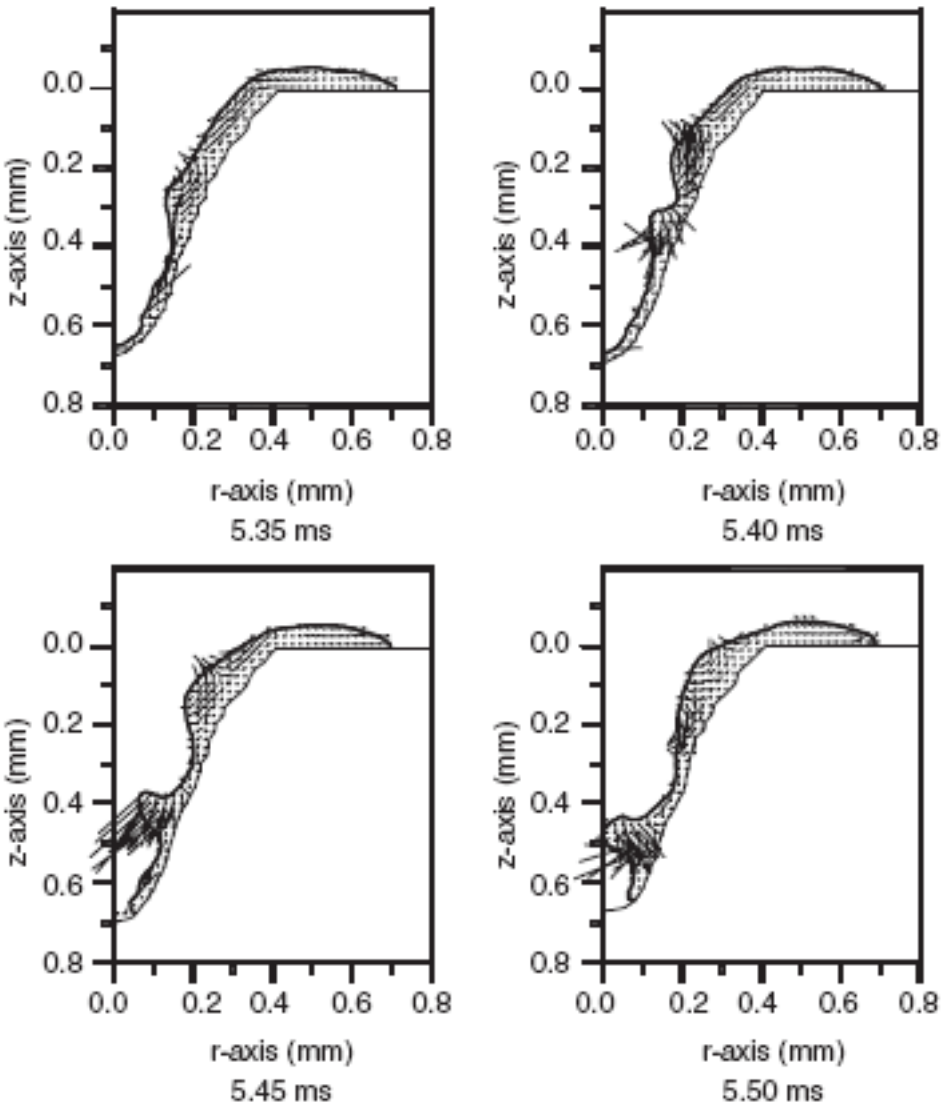

Figure **2.15**: Flow pattern in the weld pool of mild steel around a stationary keyhole for 2kW CO_2 laser [27].

Zhou et al. [56, 57] modeled the keyhole dynamics and the plasma zone during pulsed laser welding using the volume of fluid method for tracking free surface. They attributed void formation to rapid solidification after the laser pulse was shut off and proposed controlling the pulse shape to reduce porosity. Lines (a), (b) and (c) in Figure **2.16** show three different laser pulse profile for generating a thick weld pool, for generating a thin weld pool, and for preventing porosity, respectively. As opposed to laser pulses (a) and (b), input power is not switched off suddenly in pulse (c). Instead,

the input power is reduced to 0.6 kW and maintained at that level for 5 ms before switching off the power. The resulting sequence of fluid flow is given in Figure **2.17**. After the laser power is reduced to 0.6 kW at 14 ms, the weld pool continues to be heated. Therefore, the liquid metal which is at high temperature has low viscosity and has enough time to fill the vapor cavity completely before solidifying. As a result, the occurrence of porosity is reduced.

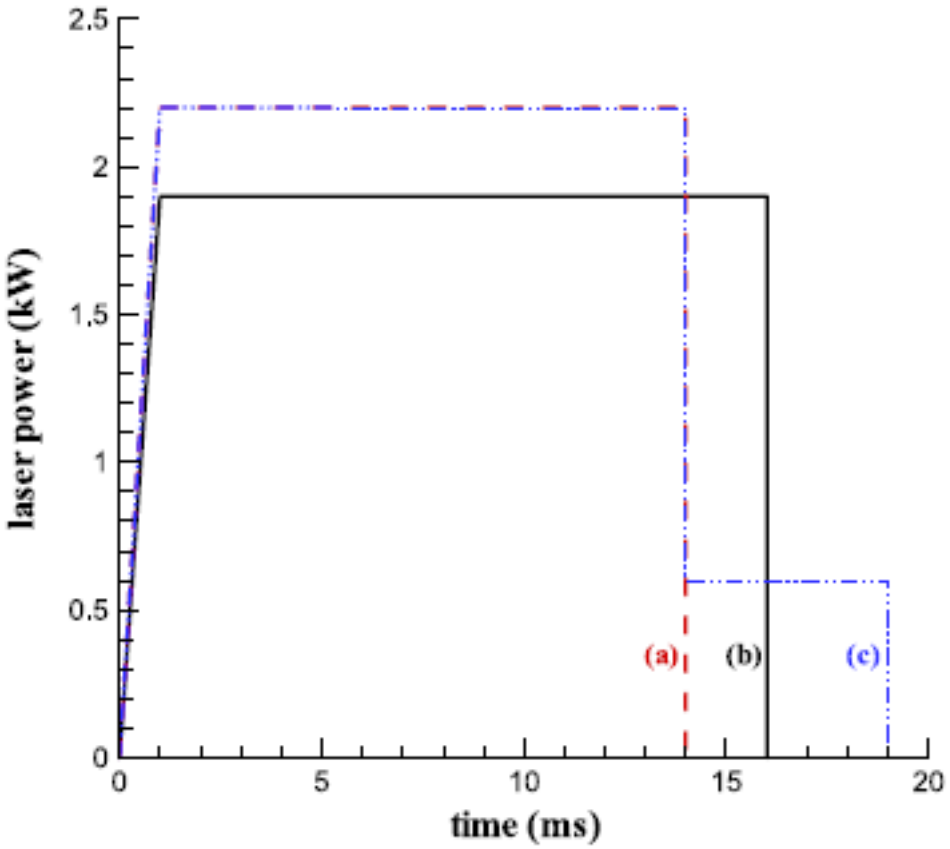

Figure **2.16**: Laser pulse for (a) generating a thick weld pool, (b) generating a thin weld pool, and (c) preventing porosity [56].

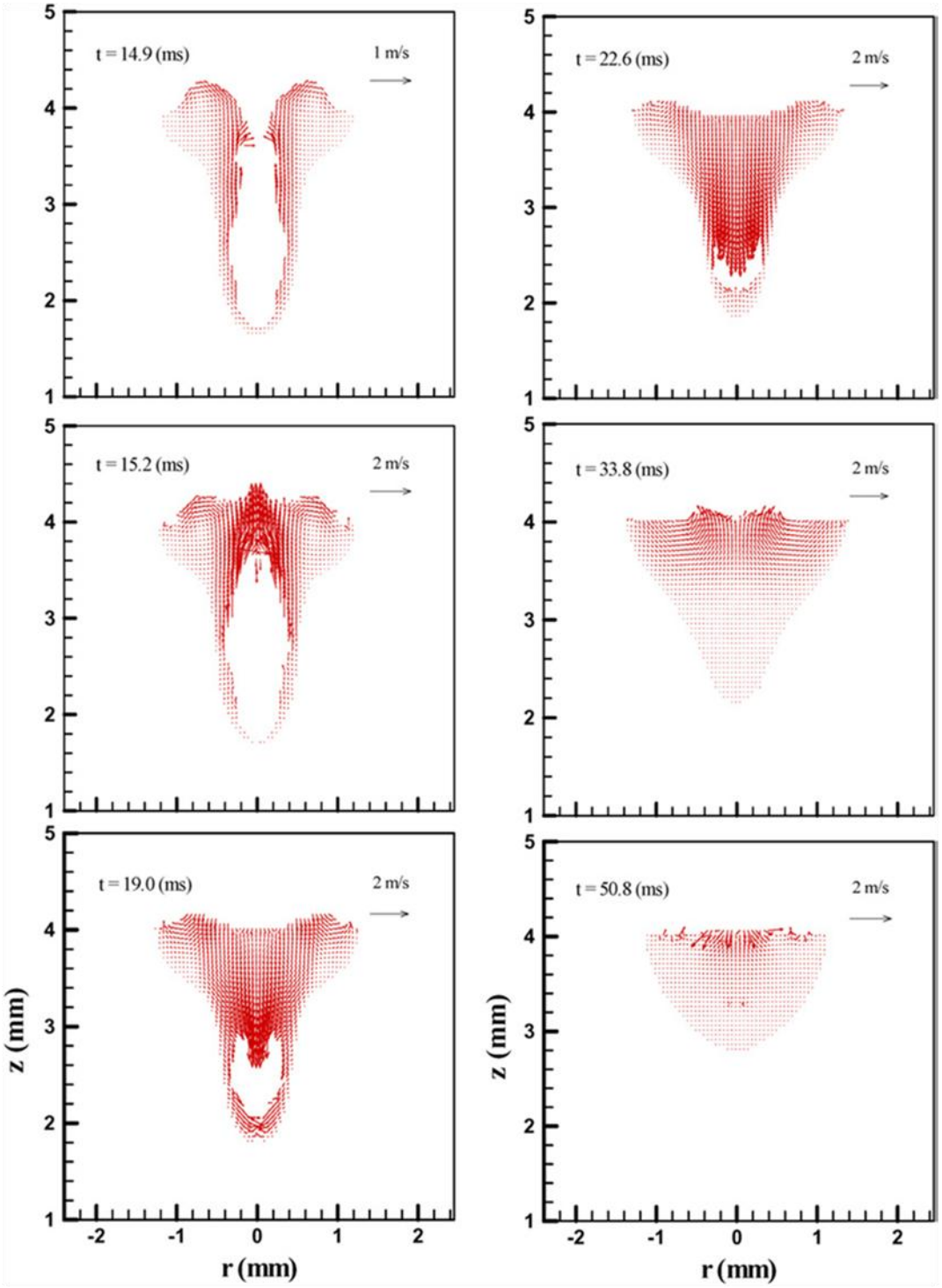

Figure **2.17**: Fluid flow during the collapse of a stationary keyhole after the laser power is shut off [56].

In short, the available numerical models for keyhole mode laser welding often make simplifying assumptions. For example, some of the models assume a particular shape for the keyhole. Other models neglect convective heat transfer and consider only conduction heat transfer for the calculation of temperature fields. Some models perform only a 2D heat transfer analysis on the 3D problem while still others simplify the fluid flow analysis into 2D analysis of flow in horizontal and vertical planes. These assumptions simplify the computations but limit the application of these models to selected process parameters and the materials.

Models that consider only heat transfer through conduction cannot be applied to high Peclet number systems, i.e. conditions under which heat transfer through convection is very significant. Such conditions include welding of low thermal conductivity alloys like steel, vanadium, and Ti-6Al-4V alloy. Since these are important engineering materials, it is important that the numerical model of keyhole mode welding is applicable to these alloys.

On the other hand, comprehensive 3D models of heat transfer and fluid flow in keyhole mode welding that consider physical processes like transient tracking of the liquid/vapor and solid/liquid interfaces are computationally very intensive. Therefore, there is a need of a computationally efficient model of keyhole mode welding that can be applied to a range of welding conditions and for materials with very different thermo-physical properties. A widely applicable model must consider fluid flow as well as heat transfer in three dimensions, but computational tasks can be reduced by making appropriate simplifications.

2.2.2 Electron beam welding

While many numerical models for heat transfer and fluid flow have been developed for keyhole mode laser welding [4, 10-13, 16, 17, 20, 25-27, 29, 31-34, 38, 42, 44, 46-53, 55-68], very few models are dedicated to the calculation of heat transfer and fluid flow for EBW [10, 69-74]. Klemens [10] calculated the electron beam penetration

using energy balance on keyhole walls. He assumed that the absorption of electrons by the plasma was small, that the electrons were completely absorbed once they reached the keyhole wall, and that the keyhole walls were at the boiling point of the alloy. Elmer et al. [71] proposed three heat conduction models for EBW based on distributed, point or line heat sources, depending on the power densities and compared calculated and measured weld geometries. Point energy source model predicts an aspect ratio of 1. Aspect ratio less than 1 implies that the heat is distributed at the top surface and correspondingly, a distributed heat source model is used. For aspect ratios much higher than 1, depth is very large compared to the half-width of the weld pool and a line source model is used in such cases. To prescribe the regimes for which each of the above heat source model was applicable, Elmer et al. [71] identified the parameter average energy density, $\bar{E}_0$ (=P/vd). Here 'P' is the input power, 'v' is the welding speed, and 'd' is the beam diameter. Figure **2.18** [71] shows the variation of weld aspect ratio (depth divided by half-width of weld pool) with average energy density, $\bar{E}_0$, for three input power levels for 304 stainless steel welds. Based on the discussion on the typical aspect ratios of weld pool calculated from different types of heat source models, it can be seen that for energy densities higher than $\bar{E}_0^*$, and high input powers, when depth is higher than width, a line source model should be used. For energy densities higher than $\bar{E}_0^*$ and low input powers, when aspect ratio is close to 1, a point source model should be used. Finally, for energy densities lower than $\bar{E}_0^*$, a distributed heat source model should be used to obtain low depth to width ratio.

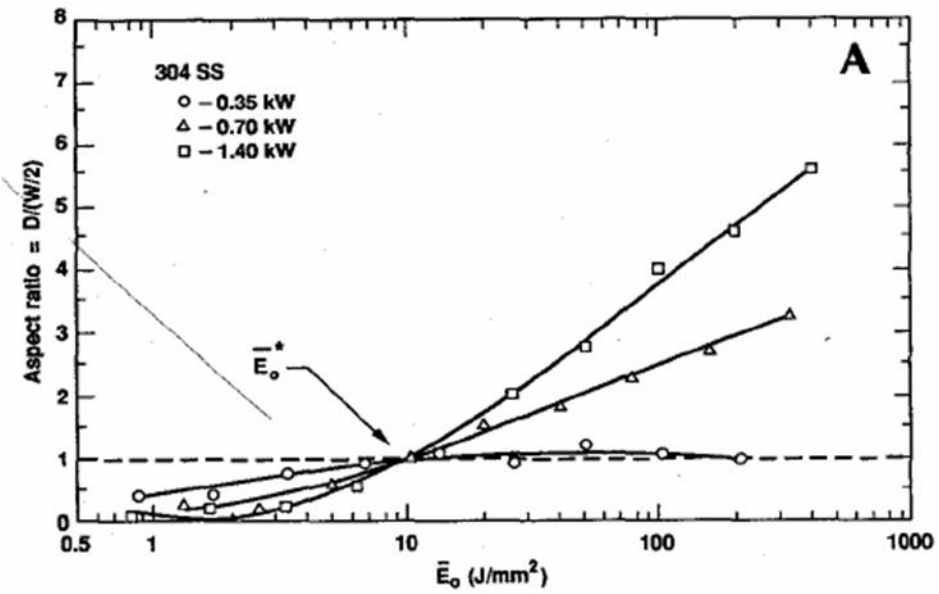

Figure **2.18**: Weld aspect ratio versus average energy density [71].

Hemmer and Grong [72] used an analytical heat conduction model and predicted keyhole penetration assuming a cylindrical keyhole shape with a predefined surface temperature. Wei and Chow [73] studied the effect of beam focusing and alloying elements on the shape of the electron beam keyhole. Any horizontal cross-section of the keyhole was assumed to be a circle and the variation of wall temperature on the circumference at any depth was assumed to be small compared to the surface temperature and was neglected. They further neglected latent heat due to melting and evaporation, radiative loss, and convection in melt pool. Balance between surface tension and vapor pressure was done to obtain the keyhole surface temperatures. Figure **2.19** shows the variation of keyhole wall temperatures with depth for the welding of Al 1100 alloy at 4.34 kW input power and 8 mm/s welding speed. The calculated values are given by the solid line. The corresponding keyhole wall temperatures measured by Schauer and Giedt [75] using a narrow band infrared pyrometer are given by the dotted line. The computed keyhole surface temperatures for Al 1100 alloy varied with depth by as much as 600 K which was similar to the variation in measured values.

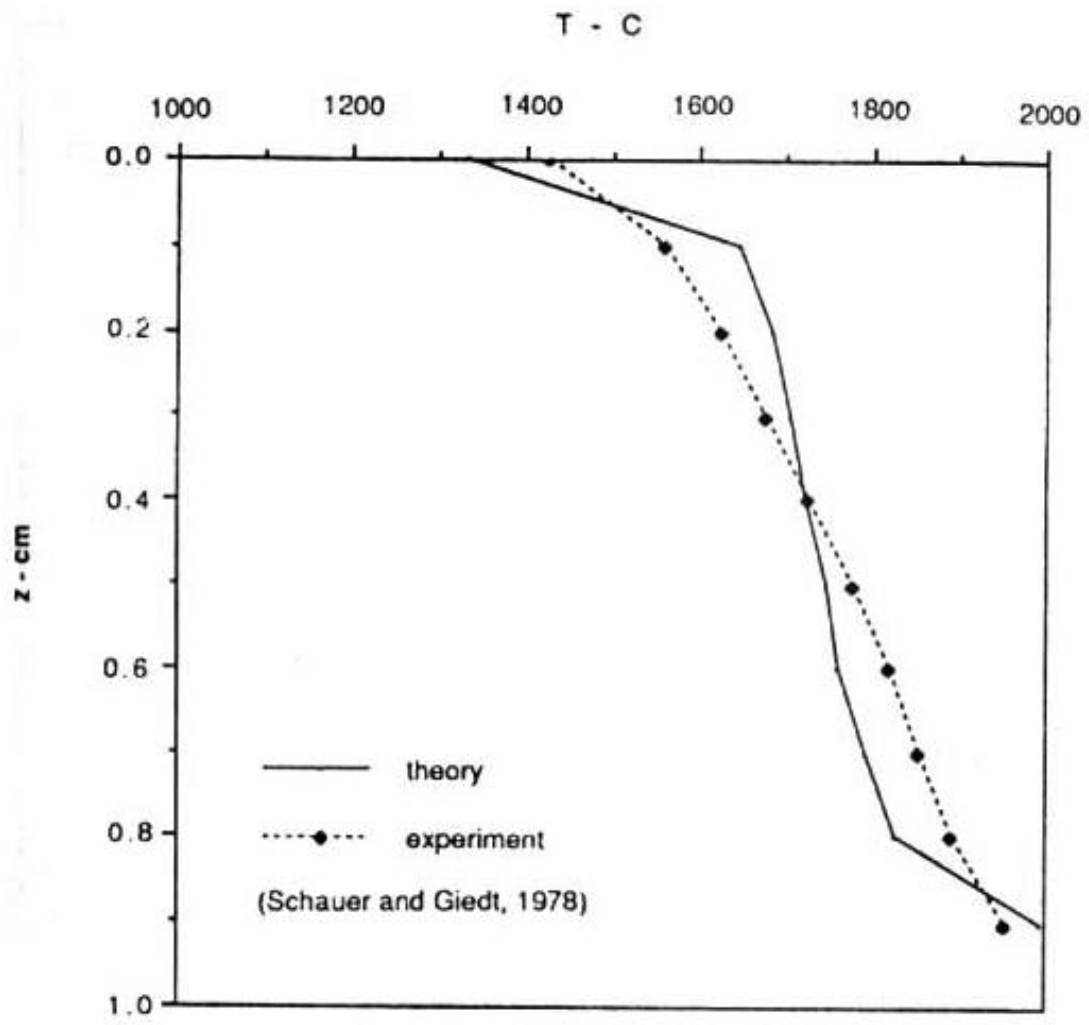

Figure **2.19**: Variation of keyhole wall temperatures for Al 1100 alloy at 4.34 kW input power, 8 mm/s welding speed, 0.005 rad divergence, -4 mm defocus, and 0.7 mm focal spot size [73].

The effect of small additions of volatile alloying elements on the keyhole wall temperatures is shown in Figure **2.20**. The computed keyhole wall temperature at the bottom was about 2300 K for pure Aluminum which was close to the value obtained from experimental observations by Schauer and Giedt [75]. Addition of small amounts (0.1 wt %) of volatile alloying element (Zinc) to pure Aluminum resulted in significant drop in calculated keyhole surface temperatures (~400 K) and a consequent increase in penetration depth. The keyhole wall temperatures are calculated through a balance

between the vapor pressure, which increases strongly with increase in temperature, and the surface tension. The total vapor pressure is significantly increased in the presence of volatile alloying elements. Therefore, the total vapor pressure becomes high enough to balance the surface tension at lower temperatures compared to when no volatile alloying elements are present. In other words, the equilibrium keyhole wall temperatures are lowered. As can be seen from Figure **2.20**, the reduction in keyhole wall temperatures is lower when the alloying element content is increased from 0.1 to 0.2 % compared to the increase from 0 to 0.1 %. Because of the lower keyhole wall temperatures (or boiling temperatures) required, the penetration depth is increased.

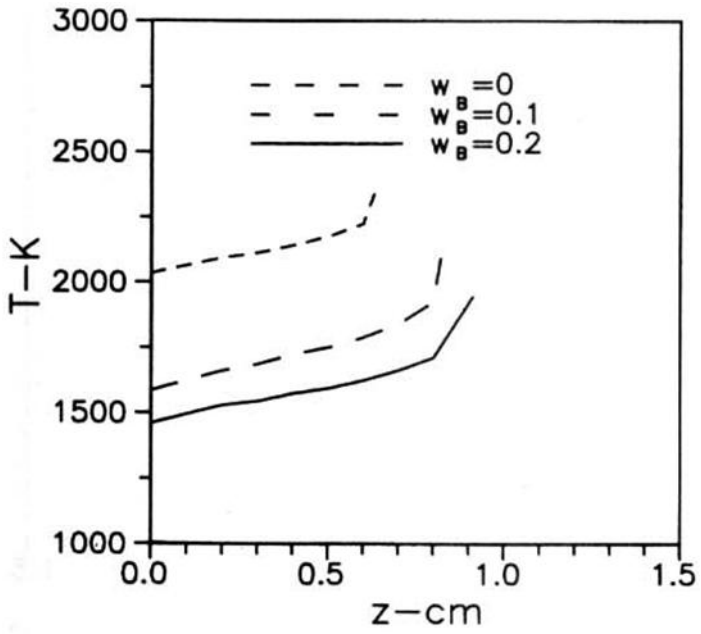

Figure **2.20**: Effect of volatile alloying elements on computed keyhole wall temperatures for aluminum with different weight percents of alloying elements at 3 kW input power, 20 mm/s welding speed, 0 mm defocus, and 0 rad divergence [73]. w_B is the weight percent of Zn.

Wei and Giedt [74] proposed a 2D heat transfer and fluid flow model and computed the free surface temperature, liquid layer thickness and tangential free surface fluid velocities assuming that the surface tension gradient is the main driving force for the fluid flow. They studied the effect of Reynold's number, surface tension, convection and

conduction on the surface temperatures, the liquid layer thickness and the surface velocity and found that the effect of conduction in the flow direction on the surface temperatures and liquid layer thickness was relatively unimportant. Assuming any horizontal cross-section of the keyhole to be circular, Wei, Wu, and Chow [76] calculated keyhole shape and wall temperatures through energy and force balance at keyhole walls.

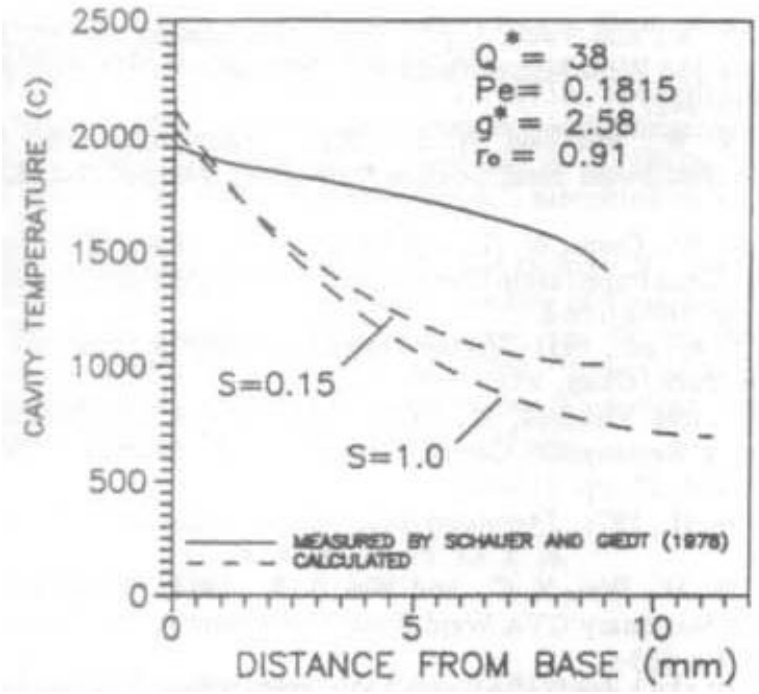

Figure **2.21**: Variation of measured and computed keyhole wall temperatures with depth for welding of Al 1100 alloy [77]. $S = \alpha/\alpha_{enh}$, where α is the thermal diffusivity and α_{enh} is the enhanced thermal diffusivity of liquid. $Q^* = Q/(k_l\sigma(T_m-T_0))$ where Q is the input power, k_l is the thermal conductivity of liquid, σ is a dimensional energy distribution parameter (units of length), T_m is the melting temperature, and T_0 is the ambient temperature. $Pe = U\sigma/\alpha$, where U is the welding speed. $g^* = Ug/2\alpha$, where g is the work- piece thickness. $r_0 = r/\sigma$, where r is the cavity opening radius.

Assuming the vapor cavity to be a paraboloid of revolution, Wei and Shian [77] calculated penetration depth and surface temperatures using an analytical 3D heat conduction model. To account for the convective heat transfer, thermal diffusivity in the flow direction was enhanced by a factor of five. The cavity opening radius, beam power, Peclet number, and a parameter approximating convection, S ($=\alpha/\alpha_{enh}$, where α_{enh} is the

enhanced thermal diffusivity) were specified for the calculations. By comparing the temperatures calculated in the liquid and the heat affected zone with the experimental observations of Schauer and Giedt [75], they showed that using point and line heat source solutions for high energy density was not accurate. Figure **2.21** shows the comparison between the calculated keyhole wall temperatures and the values measured by Schauer and Giedt [75]. The keyhole wall temperature at the base calculated using the 3D analytical model was found to be similar to the measured value. However, the variation of keyhole wall temperatures with depth was significantly different from the experimental measurements of Schauer and Giedt [75]. This difference was attributed primarily to the deviation of the keyhole shape from the assumed paraboloid of revolution.

Ho, Wen and Lee [78] calculated the keyhole wall temperatures using a 3D analytical model assuming the keyhole shape to be a paraboloid of revolution. They neglected fluid flow calculations and instead enhanced the thermal diffusivity five times the molecular value to account for convective heat transfer.

The survey of available literature shows that a comprehensive 3D numerical model of heat transfer and fluid flow in keyhole mode EBW is not available. Conduction heat transfer models of keyhole mode EBW are clearly limited in their applicability to low Peclet number situations where convection plays only a minor role in the heat transfer. Some models consider convective heat transfer by enhancing the thermal diffusivity by a constant multiple. Such an approach may give reasonable results when the focus is on a particular region in the keyhole (e.g. when calculating keyhole wall temperatures). However, since the contribution of convection depends on the local fluid velocities and therefore varies with location, this approach may not be accurate when the temperature distribution in the entire weld pool is needed. Furthermore, the multiple by which thermal diffusivity should be enhanced will depend on the work-piece material and the process conditions. Therefore, it will have to be determined separately for different welding conditions. Other models that simplify the fluid flow in the weld pool to a 2D problem in the horizontal plane are likely to give results differing from experimental observations. This is specifically true in light of the surface tension driven convection in

the axial direction due to significant difference in keyhole wall temperatures along the depth as discussed previously.

As evident from the results of numerical studies discussed earlier, the keyhole wall temperatures in EBW done under near vacuum conditions can vary significantly with depth. The corresponding variation in LBW is smaller (Appendix A) and is often neglected in numerical models. The variation of keyhole wall temperatures with depth can affect the heat balance at keyhole walls significantly and also result in surface tension gradient driven axial flow at the keyhole walls thereby affecting the calculated keyhole geometry. Numerical models of keyhole mode welding that do not consider this variation of keyhole wall temperature along the depth cannot be applied to EBW. Therefore, a numerical model for keyhole mode EBW should, in addition to addressing the need for computational efficiency and consideration of 3D fluid flow and heat transfer mentioned in section **2.2.1**, also calculate the variable keyhole wall temperatures at various depths and its effect on fluid flow and heat transfer.

2.3 Important unanswered questions

(A) Numerical models of keyhole mode welding often make simplifications that limit their applicability in terms of range of welding conditions. On the other hand, there are models that make detailed calculations of transient processes in keyhole mode welding which make the calculations very time consuming. Is there a middle path that reduces the required computational time for the model but does not limit the applicability of the model? Can a model obtained following such a middle path be applicable to materials with wide ranging material thermo-physical properties and under wide ranging process conditions involving both high and low Peclet number conditions?

In this work, numerical models have been proposed for keyhole mode laser and electron beam welding with these goals in mind. The models separate the keyhole geometry calculation, which is done based on energy balance, from 3D heat transfer and fluid flow. This approach reduces the computational task

while still maintaining the applicability of the model to both high and low Peclet number conditions.

(B) The material properties affect the heat transfer and fluid flow in the weld pool which in turn determine the temperature distribution and the cooling rates in the work-piece. The structure and integrity of the welded joint depend on the temperature distribution and cooling rates, and therefore, the material properties. The heat transfer and fluid flow model need to be used to answer the following important questions: (1) How do the material properties affect the heat transfer and hence the weld characteristics like geometry and thermal cycles? (2) How important is convective heat transfer in determining the weld characteristics and how does its significance change with material properties? (3) How do the solidification parameters vary with process conditions? (4) How do the temperature fields and cooling rates differ in partial and full penetration welds? (5) How does the temperature variation on the keyhole walls in EBW affect the weld geometry?

(C) Since the model results depend on the input parameters, can the accuracy of model predictions be improved by using a methodology to better estimate the values of input parameters whose values are not accurately known? Can the welds be tailored to obtain specific weld characteristics?

The goal of the research reported in this thesis is to address these important unsolved problems.

2.4 References

[1] Yilbas BS, Yilbas Z, Akcakoyun N. Investigation into absorption of the incident laser beam during Nd:YAG laser processing of metals. Optics and Laser Technology 1996;28:503.

[2] Tu JF, Inoue T, Miyamoto I. Quantitative characterization of keyhole absorption mechanisms in 20 kW-class CO2 laser welding processes. J. Phys. D-Appl. Phys. 2003;36:192.

[3] Lacroix D, Jeandel G. Spectroscopic characterization of laser-induced plasma created during welding with a pulsed Nd:YAG laser. J. Appl. Phys. 1997;81:6599.

[4] Chen X, Wang HX. Prediction of the laser-induced plasma characteristics in laser welding: a new modelling approach including a simplified keyhole model. J. Phys. D-Appl. Phys. 2003;36:1634.
[5] Debroy T, David SA. Physical Processes in Fusion-Welding. Reviews of Modern Physics 1995;67:85.
[6] Tix C, Simon G. A Transport Theoretical-Model of the Keyhole Plasma in Penetration Laser-Welding. J. Phys. D-Appl. Phys. 1993;26:2066.
[7] Wang HX, Chen X. Three-dimensional modelling of the laser-induced plasma plume characteristics in laser welding. J. Phys. D-Appl. Phys. 2003;36:628.
[8] Moscicki T, Hoffman J, Szymanski Z. Modelling of plasma plume induced during laser welding. J. Phys. D-Appl. Phys. 2006;39:685.
[9] Dilthey U, Goumeniouk A, Lopota V, Turichin G. Kinetic description of keyhole plasma in laser welding. J. Phys. D-Appl. Phys. 2000;33:2747.
[10] Klemens PG. Heat Balance and Flow Conditions for Electron-Beam and Laser-Welding. J. Appl. Phys. 1976;47:2165.
[11] Matsunawa A, Semak V. The simulation of front keyhole wall dynamics during laser welding. J. Phys. D-Appl. Phys. 1997;30:798.
[12] Kaplan A. A Model of Deep Penetration Laser-Welding Based on Calculation of the Keyhole Profile. J. Phys. D-Appl. Phys. 1994;27:1805.
[13] Solana P, Ocana JL. A mathematical model for penetration laser welding as a free-boundary problem. J. Phys. D-Appl. Phys. 1997;30:1300.
[14] Miller R, Debroy T. Energy-Absorption by Metal-Vapor-Dominated Plasma During Carbon-Dioxide Laser-Welding of Steels. J. Appl. Phys. 1990;68:2045.
[15] Greses J, Hilton PA, Barlow PA, Steen WM. Plume attenuation under high power Nd : yttritium-aluminum-garnet laser welding. J. Laser Appl. 2004;16:9.
[16] Mazumder J, Steen WM. Heat-Transfer Model for Cw Laser Material Processing. J. Appl. Phys. 1980;51:941.
[17] Fabbro R, Chouf K. Keyhole modeling during laser welding. J. Appl. Phys. 2000;87:4075.
[18] Schiller S, Heisig U, Panzer S. Electron Beam Technology. Berlin: John Wiley and Sons, 1982.
[19] Bramson MA. Infrared Radiation: A Handbook for Applications New York: Plenum, 1968.
[20] Cho JH, Na SJ. Implementation of real-time multiple reflection and Fresnel absorption of laser beam in keyhole. J. Phys. D-Appl. Phys. 2006;39:5372.
[21] Pierron N, Sallamand P, Jouvard JM, Cicala E, Mattei S. Determination of an empirical law of aluminium and magnesium alloys absorption coefficient during Nd : YAG laser interaction. J. Phys. D-Appl. Phys. 2007;40:2096.
[22] Zhao H, DebRoy T. Macroporosity free aluminum alloy weldments through numerical simulation of keyhole mode laser welding. J. Appl. Phys. 2003;93:10089.
[23] Palmer TA, Elmer JW. Characterisation of electron beams at different focus settings and work distances in multiple welders using the enhanced modified Faraday cup. Science and Technology of Welding and Joining 2007;12:161.

[24] Dilthey U, Goumeniouk A, Nazarenko OK, Akopjantz KS. Mathematical simulation of the influence of ion-compensation, self-magnetic field and scattering on an electron beam during welding. Vacuum 2001;62:87.
[25] Andrews JG, Atthey DR. Hydrodynamic Limit to Penetration of a Material by a High-Power Beam. J. Phys. D-Appl. Phys. 1976;9:2181.
[26] Amara EH, Bendib A. Modelling of vapour flow in deep penetration laser welding. J. Phys. D-Appl. Phys. 2002;35:272.
[27] Lee JY, Ko SH, Farson DF, Yoo CD. Mechanism of keyhole formation and stability in stationary laser welding. J. Phys. D-Appl. Phys. 2002;35:1570.
[28] Milewski J, Sklar E. Modelling and validation of multiple reflections for enhanced laser welding. Modelling and Simulation in Materials Science and Engineering 1996;4:305.
[29] Solana P, Negro G. A study of the effect of multiple reflections on the shape of the keyhole in the laser processing of materials. J. Phys. D-Appl. Phys. 1997;30:3216.
[30] Ho CY, Wen MY. Distribution of the intensity absorbed by the keyhole wall in laser processing. Journal of Materials Processing Technology 2004;145:303.
[31] Ki H, Mohanty PS, Mazumder J. Multiple reflection and its influence on keyhole evolution. J. Laser Appl. 2002;14:39.
[32] Dowden J, Postacioglu N, Davis M, Kapadia P. A Keyhole Model in Penetration Welding with a Laser. J. Phys. D-Appl. Phys. 1987;20:36.
[33] Ye XH, Chen X. Three-dimensional modelling of heat transfer and fluid flow in laser full-penetration welding. J. Phys. D-Appl. Phys. 2002;35:1049.
[34] Trappe J, Kroos J, Tix C, Simon G. On the Shape and Location of the Keyhole in Penetration Laser-Welding. J. Phys. D-Appl. Phys. 1994;27:2152.
[35] Kumar A, Debroy T. Tailoring complex weld geometry through reliable heat-transfer and fluid-flow calculations and a genetic algorithm. Metallurgical and Materials Transactions a-Physical Metallurgy and Materials Science 2005;36A:2725.
[36] He X, Norris JT, Fuerschbach PW, DebRoy T. Liquid metal expulsion during laser spot welding of 304 stainless steel. J. Phys. D-Appl. Phys. 2006;39:525.
[37] De A, DebRoy T. Improving reliability of heat and fluid flow calculation during conduction mode laser spot welding by multivariable optimisation. Science and Technology of Welding and Joining 2006;11:143.
[38] Sudnik W, Radaj D, Erofeew W. Computerized simulation of laser beam welding, modelling and verification. J. Phys. D-Appl. Phys. 1996;29:2811.
[39] Yang Z, Debroy T. Modeling macro-and microstructures of gas-metal-arc welded HSLA-100 steel. Metallurgical and Materials Transactions B-Process Metallurgy and Materials Processing Science 1999;30:483.
[40] Launder BE, Spalding DE. Lectures in Mathematical Models of Turbulence. NY: Academic Press, 1972.
[41] Kumar A, DebRoy T. Improving reliability of modelling heat and fluid flow in complex gas metal arc fillet welds - part II: application to welding of steel. J. Phys. D-Appl. Phys. 2005;38:127.
[42] Postacioglu N, Kapadia P, Davis M, Dowden J. Upwelling in the Liquid Region Surrounding the Keyhole in Penetration Welding with a Laser. J. Phys. D-Appl. Phys. 1987;20:340.

[43] Kumar A, Zhang W, DebRoy T. Improving reliability of modelling heat and fluid flow in complex gas metal arc fillet welds - part I: an engineering physics model. J. Phys. D-Appl. Phys. 2005;38:119.
[44] Swift-Hook DE, Gick AEF. Penetration Welding with Lasers. Weld. J. 1973;52:S492.
[45] Zhang W, Roy GG, Elmer JW, DebRoy T. Modeling of heat transfer and fluid flow during gas tungsten arc spot welding of low carbon steel. J. Appl. Phys. 2003;93:3022.
[46] Dowden J, Davis M, Kapadia P. Some Aspects of the Fluid-Dynamics of Laser-Welding. Journal of Fluid Mechanics 1983;126:123.
[47] Kroos J, Gratzke U, Simon G. Towards a Self-Consistent Model of the Keyhole in Penetration Laser-Beam Welding. J. Phys. D-Appl. Phys. 1993;26:474.
[48] Kroos J, Gratzke U, Vicanek M, Simon G. Dynamic Behavior of the Keyhole in Laser-Welding. J. Phys. D-Appl. Phys. 1993;26:481.
[49] Klein T, Vicanek M, Kroos J, Decker I, Simon G. Oscillations of the Keyhole in Penetration Laser-Beam Welding. J. Phys. D-Appl. Phys. 1994;27:2023.
[50] Dowden J. Interaction of the keyhole and weld pool in laser keyhole welding. J. Laser Appl. 2002;14:204.
[51] Ki H, Mohanty PS, Mazumder J. Modeling of laser keyhole welding: Part I. Mathematical modeling, numerical methodology, role of recoil pressure, multiple reflections, and free surface evolution. Metallurgical and Materials Transactions a-Physical Metallurgy and Materials Science 2002;33:1817.
[52] Ki H, Mohanty PS, Mazumder J. Modeling of laser keyhole welding: Part II. Simulation of keyhole evolution, velocity, temperature profile, and experimental verification. Metallurgical and Materials Transactions a-Physical Metallurgy and Materials Science 2002;33:1831.
[53] Tsirkas SA, Papanikos P, Kermanidis T. Numerical simulation of the laser welding process in butt-joint specimens. Journal of Materials Processing Technology 2003;134:59.
[54] Du HB, Hu LJ, Liu JH, Hu XY. A study on the metal flow in full penetration laser beam welding for titanium alloy. Computational Materials Science 2004;29:419.
[55] Wang H, Shi YW, Gong SL. Numerical simulation of laser keyhole welding processes based on control volume methods. J. Phys. D-Appl. Phys. 2006;39:4722.
[56] Zhou J, Tsai HL, Lehnhoff TF. Investigation of transport phenomena and defect formation in pulsed laser keyhole welding of zinc-coated steels. J. Phys. D-Appl. Phys. 2006;39:5338.
[57] Zhou J, Tsai HL, Wang PC. Transport phenomena and keyhole dynamics during pulsed laser welding. Journal of Heat Transfer-Transactions of the ASME 2006;128:680.
[58] Amara EH, Fabbro R. Modelling of gas jet effect on the melt pool movements during deep penetration laser welding. J. Phys. D-Appl. Phys. 2008;41.
[59] Amara EH, Fabbro R, Hamadi F. Modeling of the melted bath movement induced by the vapor flow in deep penetration laser welding. J. Laser Appl. 2006;18:2.
[60] Dowden J, Davis M, Kapadia P. The Flow of Heat and the Motion of the Weld Pool in Penetration Welding with a Laser. J. Appl. Phys. 1985;57:4474.

[61] Fabbro R, Chouf K. Dynamical description of the keyhole in deep penetration laser welding. J. Laser Appl. 2000;12:142.
[62] Fabbro R, Slimani S, Coste F, Briand F. Study of keyhole behaviour for full penetration Nd-Yag CW laser welding. J. Phys. D-Appl. Phys. 2005;38:1881.
[63] Klein T, Vicanek M, Simon G. Forced oscillations of the keyhole in penetration laser beam welding. J. Phys. D-Appl. Phys. 1996;29:322.
[64] Matsunawa A. Problems and solutions in deep penetration laser welding. Science and Technology of Welding and Joining 2001;6:351.
[65] Matsunawa A, Kim JD, Seto N, Mizutani M, Katayama S. Dynamics of keyhole and molten pool in laser welding. J. Laser Appl. 1998;10:247.
[66] Mohanty PS, Kar A, Mazumder J. A modeling study on the influence of pulse shaping on keyhole laser welding. J. Laser Appl. 1996;8:291.
[67] Steen WM, Dowden J, Davis M, Kapadia P. A Point and Line Source Model of Laser Keyhole Welding. J. Phys. D-Appl. Phys. 1988;21:1255.
[68] Sudnik W, Radaj D, Breitschwerdt S, Erofeew W. Numerical simulation of weld pool geometry in laser beam welding. J. Phys. D-Appl. Phys. 2000;33:662.
[69] Andrews JG, Atthey DR. Motion of an Intensely Heated Evaporating Boundary. Journal of the Institute of Mathematics and Its Applications 1975;15:59.
[70] Klemens PG. Mechanism of Cavity Formation in Electron-Beam and Laser-Welding. Bulletin of the American Physical Society 1976;21:591.
[71] Elmer JW, Giedt WH, Eagar TW. The Transition from Shallow to Deep Penetration During Electron-Beam Welding. Weld. J. 1990;69:S167.
[72] Hemmer H, Grong O. Prediction of penetration depths during electron beam welding. Science and Technology of Welding and Joining 1999;4:219.
[73] Wei PS, Chow YT. Beam Focusing Characteristics and Alloying Element Effects on High-Intensity Electron-Beam Welding. Metallurgical Transactions B-Process Metallurgy 1992;23:81.
[74] Wei PS, Giedt WH. Surface-Tension Gradient-Driven Flow around an Electron-Beam Welding Cavity. Weld. J. 1985;64:S251.
[75] Schauer DA, Giedt WH, Shintaku SM. Electron-Beam Welding Cavity Temperature Distributions in Pure Metals and Alloys. Weld. J. 1978;57:S127.
[76] Wei PS, Wu TH, Chow YT. Investigation of High-Intensity Beam Characteristics on Welding Cavity Shape and Temperature Distribution. Journal of Heat Transfer-Transactions of the ASME 1990;112:163.
[77] Wei PS, Shian MD. 3-Dimensional Analytical Temperature-Field around the Welding Cavity Produced by a Moving Distributed High-Intensity Beam. Journal of Heat Transfer-Transactions of the ASME 1993;115:848.
[78] Ho CY, Wen MY, Lee YC. Analytical solution for three-dimensional model predicting temperature in the welding cavity of electron beam. Vacuum 2007;82:316.

Chapter 3

Heat Transfer and Fluid Flow in Laser Beam Welding

3.1 Introduction

As discussed in Chapter 2, numerical models of keyhole mode laser welding that are available in literature are often applicable to a limited range of welding parameters and/or materials. These limitations are due to simplifications in the calculation scheme such as assumption of symmetrical keyhole and/or weld pool shapes, neglect of convective fluid flow, and two dimensional (2D) analysis of a three-dimensional (3D) problem [1-11]. The comprehensive models of keyhole mode laser welding, on the other hand, are computationally intensive because of transient calculations that consider tracking of liquid/vapor interface, multiple reflections, etc. [12-17]. Therefore, there is a need for a fluid flow and heat transfer model for keyhole mode laser welding that is applicable to a wide range of work-piece materials and welding conditions and is also computationally efficient so that it can be run in a small amount of time. In this work, a 3D numerical model of keyhole mode heat transfer and fluid flow is developed and tested. The model considers the important physical processes involved in laser welding while making simplifications to make the computational task tractable. It has been tested for a wide range of materials and welding conditions including partial and full penetration welds. Calculations of the numerical model show distinct differences in the weld geometries of high and low thermal diffusivity materials. The role of convective heat transfer in determining the weld geometry is further demonstrated through calculation of dimensionless numbers. The numerical model has been used to calculate solidification parameters at the trailing edge of the weld pool and relate them to expected solidification microstructure. It has also been used to illustrate the difference between partial and full penetration welds in terms of weld characteristics like fusion zone geometry and cooling rates.

3.2 Experiments

For validating the three dimensional heat transfer and fluid flow model for LBW, several welds were made at Applied Research Laboratory (ARL) at The Pennsylvania State University, and Lawrence Livermore National Laboratory (LLNL).

3.2.1 A131 welds made at ARL

Autogenous laser welds were made on A131 grade EH-36 steel (composition given in Table **3.1**) using a 14 kW maximum power continuous wave CO_2 laser (UTIL SM-21-14) at the ARL. The raw laser beam, a 63.5 mm annulus, is focused onto the work-piece using a 330.2 mm focal length lens. The focal spot in the absence of plasma is approximately 1.0 mm in diameter. Laser power was measured at the work-piece prior to welding using a laser power probe. Power incident on the work-piece was varied from 3.3 to 9.6 kW and the welding speed varied from 12.7 to 31.8 mm/s. Table **3.2** lists the welding parameters used for these experiments. The laser was focused on the surface of the plate and plasma suppression was provided by a helium shielding nozzle with a gas flow rate of 1.57×10^{-3} m^3/s. Samples were 10 mm thick, 51 mm wide and 152 mm in length. The 127 mm long autogenous welds were centered on the plate. The top surface of the plate was ground to remove primer prior to welding. Selected welds were sectioned, polished, etched and photographed to reveal the weld fusion zone profile and microstructure.

Table **3.1**: Specified Composition (max %) of ASTM A131 grade EH-and DH-36 Steels

C	Mn	Si	P	S	Al	Nb	V	Ti	Cu	Cr	Ni	Mo
0.18	1.6	0.5	0.035	0.035	0.015	0.05	0.10	0.02	0.35	0.2	0.4	0.08

Table **3.2**: Welding variables for experiments.

Data set	Power (kW)	Welding speed (mm/s)	Energy/length (J/mm)
(a)	3.3	12.7	260
(b)	5.0	12.7	371
(c)	6.8	12.7	505
(d)	9.6	12.7	713
(e)	5.1	19.05	268
(f)	4.9	25.4	193
(g)	5.0	31.75	157

3.2.2 304L stainless steel, Ti-6Al-4V, Tantalum, and Vanadium welds at LLNL

A second set of welds was made using a Rofin Sinar DY-022 diode pumped continuous wave Nd:YAG laser at LLNL [18] with a maximum power output of 2200 W. The laser beam is delivered from the power supply to a Class 1 laser workstation using a 30 m long 300 μm diameter fiber optic cable. Within the workstation, the beam passes through a set of 1:1 focusing optics, consisting of a 160 mm collimator and a 160 mm focal length lens. The actual power output of the laser system at the exit of the optics assembly was measured using a water-cooled Coherent power meter, which has a rated measurement accuracy of ±1 % and a calibration uncertainty of ±2 %. Table **3.3** compares the power levels measured at the exit of the laser optics to the range of machine settings using the 300 μm diameter fiber. The % values given in Table **3.3** are calculated as hundred times the difference between the machine power setting and the measured output at the end of fiber optics divided by the machine power setting. Overall, the laser power measurements displayed losses of approximately 10 % of the machine setting as the laser beam passed through the fiber optics.

Table **3.3**: Summary of machine power settings and measured output power.

Machine Power Setting (W)	Measured Output (W)	% loss
220	202	8.2
440	396	10.0
660	588	10.9
880	779	11.5
1100	973	11.5
1320	1160	12.1
1540	1340	13.0
1760	1550	11.9
1980	1770	10.6
2200	1980	10.0

Autogenous bead on plate laser welds, 50 mm in length, were made on flat plates of vanadium, Ti-6Al-4V, 304L stainless steel, and tantalum. The chemical compositions of the four materials are given in Table **3.4**. The sample thickness for each of these materials varied, from 3.2 mm for the vanadium samples, to 6.0 mm for the tantalum samples, to 9.5 mm for the 304L stainless steel, and 12.7 mm for the Ti-6Al-4V samples. Table **3.5** provides a summary of the work-piece dimensions for all the materials used. It should also be noted that unlike the samples used for the other materials examined here, the tantalum samples contain a machined step-shaped butt joint.

All welds were made at sharp focus, with the beam focus set at the surface of the weld sample. During welding, argon shielding gas was supplied through a 4.0 mm diameter nozzle with a gas pressure of 5.51×10^5 Pa placed approximately 25.0 mm from the laser beam impingement area. Welds in the 304L stainless steel, Ti-6Al-4V, and tantalum samples are made with the laser beam oriented normal to the weld sample. In the welding of the vanadium samples, the laser head was tilted at an angle of 5º normal to the sample surface and towards the leading edge of the weld and along the direction of welding to avoid any damage to the laser optics from potential back-reflection.

The welding experiments performed on each material system have utilized different ranges of welding parameters, which are summarized in Table **3.5**. In the first set of experiments, the effects of changes in the input power, from approximately 615 W through 1980 W, at a constant travel speed have been analyzed on the vanadium, 304L

stainless steel, and the Ti-6Al-4V samples. The travel speeds were 16.9 mm/s, 19.1 mm/s, and 25.4 mm/s for Ti-6Al-4V, 304L stainless steel samples, and vanadium samples respectively. The second set of experiments compared the effects of changing travel speeds at a constant input power for both tantalum and 304L stainless steel samples. For the tantalum samples, the travel speeds varied between 0.85 mm/s to 12.7 mm/s at a fixed input power of 1900 W, while those for the 304L stainless steel varied between 6.4 mm/s and 16.9 mm/s at a fixed input power of 1980 W.

After welding, a section of the weld comprising approximately 6.4 mm of the weld length was removed from a location near the middle of each weld. This sample was mounted in cross section, polished, and etched to reveal both the microstructure and the resulting weld fusion zone boundary, which defines its shape and size. Each metal/alloy required a different etchant to reveal the microstructure effectively. The 304L stainless steel samples were etched with an electrolytic oxalic acid etch commonly used with stainless steels. Krolls etchant was used to reveal the fusion zone boundary in the Ti-6Al-4V sample. An etchant composed of 20 mL ethylene glycol, 10 mL HNO_3, and 10 mL HF was used for the vanadium samples. Finally an aqueous chemical etchant consisting of 30 grams of ammonium bifluoride, 20 ml water, and 50 ml nitric acid was used on the tantalum samples.

A digital micrograph of each weld cross-section was taken using a conventional optical microscope. From this micrograph, the weld width at the top surface and the weld depth below the surface of the plate were measured using a commercially available image analysis software package (Adobe Photoshop 7.0). For each weld, measurements of the weld depth along the centerline of the weld cross section and the weld width along the surface of the sample have been made.

Table **3.4**: Composition of Vanadium, Ta, 304L stainless steel, and Ti-6Al-4V alloy.

Material	Element	Weight %
Vanadium	Si	0.034
	C	0.0052
	H	0.0004
	N	0.017
	O	0.01
Ta	Commercially pure	
304L SS	Cr	18.2
	Ni	8.6
	Mn	1.7
	Mo	0.47
	Co	0.14
	Cu	0.35
	Si	0.44
	C	0.02
	N	0.082
	P	0.03
	S	0.0004
	Fe	Balance
Ti-6Al-4V	Al	6.09
	V	4.02
	C	0.01
	H	0.0022
	Fe	0.25
	N	0.007
	O	0.117
	Ti	Balance

Table **3.5**: Welding conditions. All welds were made using a 300μ diameter fiber with argon shielding gas.

Material	Power, W	Welding Speed, mm/s	Weld Depth, mm	Weld Width, mm
Vanadium	664		0.91	1.12
	887		1.22	1.32
	1109		1.51	1.52
3.2 mm X 152.4 mm X 25.4 mm	1332	25.4	1.66	1.65
	1777		2.18	1.9
	1980		2.28	2.13
304 SS	664		1.92	1.3
	887		2.31	1.66
	1109		2.64	1.79
9.5 mm X 152.4 mm	1332	19.1	2.81	1.79
X 25.4 mm	1554		3.1	1.93
	1777		3.41	2.22
	1980		3.58	2.19
Ti-6Al-4V	615		1.623	1.854
	720		1.93	2.108
	783		2.057	2.184
	875		2.21	2.337
12.7 mm X 152.4 mm X 76.2 mm	980	16.9	2.464	2.464
	1055		2.54	2.642
	1234		2.692	2.743
	1400		3.023	2.896
Tantalum		0.85	2.9	4.4
		1.7	2.7	3.5
	1900	2.54	2.5	3.7
6 mm X 150 mm X 25 mm		3.81	2.3	3.1
		6.4	2.2	2.6
		12.7	2.0	2.2
304 SS		6.4	4.48	4.48
		8.5	4.16	4.08
		10.6	4.06	3.61
9.5 mm X 152.4 mm X 25.4 mm	1980	12.7	3.65	3.3
		14.8	3.51	3.23
		16.9	3.41	3.1

3.3 Mathematical Model

Linear keyhole mode laser welding is assumed to be a quasi-steady state process, i.e. temperature fields are independent of time when viewed from a co-ordinate system fixed to the heat source. Among other factors, the transient fluctuations of the keyhole due to fluid flow, irregularities in the material, and slight variations in process parameters, have been neglected.

3.3.1 Co-ordinate system

A rectangular co-ordinate system has been used for the 3D fluid flow and heat transfer calculation. Different grids have been used for scalar and vector variables, as explained elsewhere [19]. Non-uniform grids, with a finer mesh near heat source and coarser mesh far away from the heat source, have been used for computational efficiency. Welding direction is opposite to the x-axis. Y-axis is perpendicular to the welding direction with $y = 0$ at the weld center line. Z-axis is the vertical direction with $z = 0$ at the bottom of the work-piece.

3.3.2 Keyhole profile calculation

The keyhole geometry is calculated using a methodology similar to Kaplan's model [7, 11] that considers energy balance on a liquid-vapor interface assuming boiling point at the keyhole walls and constant absorption coefficients. The boiling point of the alloy was taken to be a temperature where the sum of the equilibrium vapor pressures of all alloying elements over the alloy is 1 atmosphere. Since the orientation of keyhole is almost vertical and the keyhole walls have a constant temperature at all depths, the heat transfer takes place mainly along the horizontal plane. The keyhole geometry calculation considers enhanced absorption of laser beam due to multiple reflections within the keyhole. The number of reflections of the laser within the keyhole depends on the

keyhole geometry which is iteratively determined. During calculation of the asymmetric geometry of the keyhole, all temperatures inside the keyhole were assigned the boiling temperature of the alloy for the identification of the keyhole. The temperature distribution from the keyhole model is then stored in a data file, which is then read into the thermo-fluid model. At each horizontal *xy* plane, the keyhole boundary was identified by both a minimum and a maximum *x* value for each *y* value. The energy balance model for calculation of keyhole geometry is described in greater detail in Chapter 5.

3.3.3 Fluid flow and heat transfer calculation

After calculating the keyhole profile, the equations of conservation of mass, momentum, and energy are solved in 3D to model the fluid flow and heat transfer in the weld pool. The heat source is assumed to be moving in the negative x-direction. Density of the molten metal is assumed to be constant except when calculating buoyancy force according to Boussinesq approximation. The momentum conservation equations in 3D, for the liquid metal flow in the weld pool can be expressed as [19, 20]:

$$\rho\frac{\partial u_j}{\partial t}+\rho\frac{\partial\left(u_i u_j\right)}{\partial x_i}=\frac{\partial}{\partial x_i}\left(\mu\frac{\partial u_j}{\partial x_i}\right)+\rho g_j\beta\left(T-T_{ref}\right)+S_j \qquad (\mathbf{3.1})$$

where ρ is the density, t is the time, x_i is the distance along the i^{th} (i = 1, 2 and 3) orthogonal direction, u_j is the velocity component along the j direction, μ is the effective viscosity, β is the coefficient of volume expansion, g_j is the acceleration due to gravity, and T_{ref} is the reference temperature. The second term on the right hand side is the buoyancy source term [21-25]. The source term for the j^{th} momentum equation, S_j is given by (Eq. **3.2**):

$$S_j=-\frac{\partial p}{\partial x_j}+\frac{\partial}{\partial x_i}\left(\mu\frac{\partial u_i}{\partial x_j}\right)-C\left(\frac{(1-f_L)^2}{{f_L}^3+A}\right)u_j-\rho U\frac{\partial u_j}{\partial x_1}+\varepsilon_{jkl}J_k B_l \qquad (\mathbf{3.2})$$

where ‘p’ represents pressure, U is the welding velocity, and ε_{jkl} is the alternating tensor. ε_{jkl} = 1, if the indices are in cyclic order, and ε_{jkl} = -1 if the indices are in anti-cyclic order. It is equal to 0 if any two indices are equal. The third term represents the frictional dissipation in the mushy zone according to the Carman-Kozeny equation for flow through a porous media [26, 27], where f_L is the liquid fraction, A is very small computational constant introduced to avoid division by zero, and C is a constant accounting for the mushy zone morphology (a value of 1.6×10^4 was used in the present study [27]). The fourth term accounts for the relative motion between the laser source and the work-piece [21]. The fifth term is due to electromagnetic force [25].

The following continuity equation is solved in conjunction with the momentum equation to obtain the pressure field:

$$\frac{\partial(\rho u_i)}{\partial x_i} = 0 \qquad \textbf{(3.3)}$$

In order to trace the phase change at the liquid/solid interface, the total enthalpy H is represented by a sum of sensible heat ‘h’ and latent heat content ΔH, i.e., $H = h + \Delta H$ [21]. The sensible heat ‘h’ is expressed as $h = \int C_p dT$, where C_p is the specific heat, and T is the temperature. The latent heat content ΔH is given as $\Delta H = f_L L$, where L is the latent heat of fusion. The liquid fraction f_L is assumed to vary linearly with temperature for simplicity [21]:

$$f_L = \begin{cases} 1 & T > T_L \\ \dfrac{T - T_S}{T_L - T_S} & T_S \le T \le T_L \\ 0 & T < T_S \end{cases} \qquad \textbf{(3.4)}$$

where T_L and T_S are the liquidus and solidus temperatures, respectively. Thus, the thermal energy transportation in the weld work-piece can be expressed by the following modified energy equation:

$$\rho\frac{\partial h}{\partial t} + \rho\frac{\partial(u_i h)}{\partial x_i} = \frac{\partial}{\partial x_i}\left(\frac{k}{C_p}\frac{\partial h}{\partial x_i}\right) + S_h \qquad \textbf{(3.5)}$$

where k is the thermal conductivity. The source term S_h is due to the latent heat content and is given as:

$$S_h = -\rho\frac{\partial(\Delta H)}{\partial t} - \rho\frac{\partial(u_i \Delta H)}{\partial x_i} - \rho U\frac{\partial h}{\partial x_1} - \rho U\frac{\partial \Delta H}{\partial x_1} \qquad \textbf{(3.6)}$$

The heat transfer and fluid flow equations were solved for the complete work-piece. For the region inside the keyhole, the coefficients and source terms in the equations were adjusted to obtain boiling point temperature and zero fluid velocities.

A 3D Cartesian coordinate system is used in the calculation. Only half of the work-piece is considered since the weld is symmetrical about the weld center line. The boundary conditions are shown in Figure **3.1**.

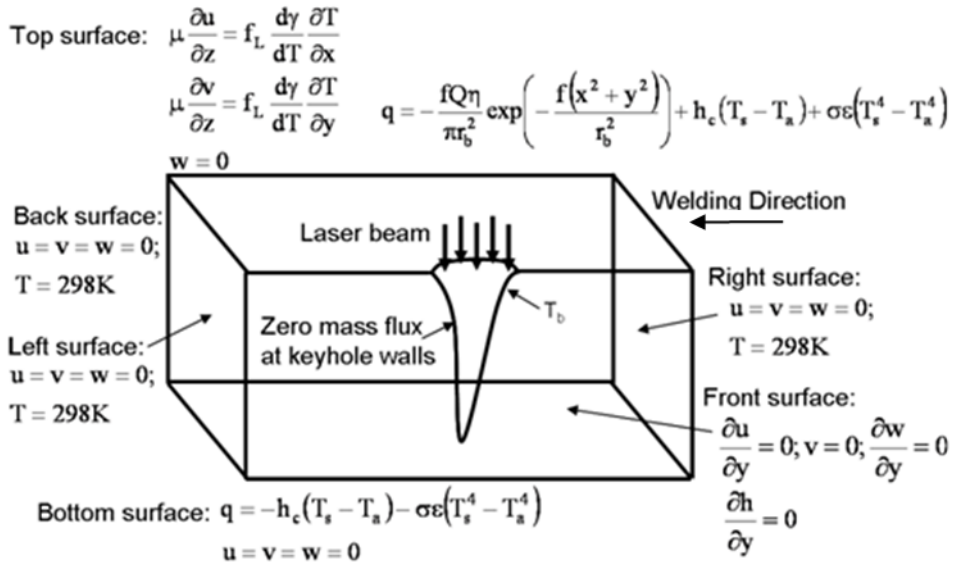

Figure **3.1**: Schematic of the boundary conditions.

3.3.3.1 Top surface

The weld top surface outside the keyhole region is assumed to be flat. The velocity boundary condition is given as [28-32]:

$$\mu\frac{\partial u}{\partial z} = f_L\frac{d\gamma}{dT}\frac{\partial T}{\partial x}$$
$$\mu\frac{\partial v}{\partial z} = f_L\frac{d\gamma}{dT}\frac{\partial T}{\partial y} \qquad (\mathbf{3.7})$$
$$w = 0$$

where u, v, and w are the velocity components along the x, y, and z directions, respectively, and $d\gamma/dT$ is the temperature coefficient of surface tension. As shown in this equation, the u and v velocities are determined from the Marangoni effect [28-32]. The w velocity is equal to zero since there is no outward flow at the pool top surface. The heat flux at the top surface is given as:

$$k\frac{\partial T}{\partial z}\bigg|_{top} = \frac{fQ\eta}{\pi {r_b}^2}\exp\left(-\frac{f(x^2+y^2)}{{r_b}^2}\right) - \sigma\varepsilon\left(T^4 - {T_a}^4\right) - h_c(T - T_a) \qquad (\mathbf{3.8})$$

where r_b is the beam radius, f is the power distribution factor, Q is the total laser power, η is the absorptivity, σ is the Stefan-Boltzmann constant, h_c is the heat transfer coefficient, and T_a is the ambient temperature. In Eq. **3.8**, the first term on the right hand side is the heat input from the heat source, defined by a Gaussian heat distribution. The second and third terms represent the heat loss by radiation, and convection, respectively.

3.3.3.2 Symmetric plane

Zero flux boundary condition is applied for momentum and enthalpy at the symmetric plane, i.e., the vertical plane containing the welding direction, as:

$$\frac{\partial u}{\partial y} = 0, \quad v = 0, \quad \frac{\partial w}{\partial y} = 0 \qquad (\mathbf{3.9})$$

$$\frac{\partial h}{\partial y} = 0 \qquad (\mathbf{3.10})$$

3.3.3.3 Keyhole surface

The temperature everywhere at the keyhole surface is fixed at the boiling point of the alloy by assigning a constant enthalpy value at all points on the keyhole surface:

$$h = h_{boil} \tag{3.11}$$

h_{boil} is the enthalpy of the liquid metal/alloy at its boiling point. Thus, the keyhole wall temperature is fixed at the boiling temperature of the alloy. The velocity component perpendicular to keyhole surface is assigned a value of zero to represent no mass flux due to convection.

3.3.3.4 Bottom surface

A convective heat transfer boundary condition with a given heat transfer coefficient is specified for the bottom surface. For partial penetration welds, fluid velocities are zero at the bottom surface. For full penetration welds, a flat bottom surface was assumed for the fluid flow and heat transfer calculations. However, free surface deformation was calculated, based on minimization of surface energy, after the temperature fields were computed. Marangoni force driven velocity boundary conditions were assumed at the bottom surface of the weld pool:

$$\begin{aligned} \mu\frac{\partial u}{\partial z} &= -f_L\frac{d\gamma}{dT}\frac{dT}{dx} \\ \mu\frac{\partial v}{\partial z} &= -f_L\frac{d\gamma}{dT}\frac{dT}{dy} \\ w &= 0 \end{aligned} \tag{3.12}$$

3.3.3.5 Solid Surfaces

At solid surfaces far away from the heat source, temperatures are set at ambient temperature (T_a) and the fluid velocities are set to be zero.

3.3.4 Turbulence model

In high energy density welding, turbulence in the weld pool may result in enhanced rates of heat, mass and momentum transport due to fluctuating components of velocity. To estimate this enhanced transport phenomenon, often an appropriate turbulence model is used that provides a systematic framework for calculating effective viscosity and thermal conductivities [33, 34]. The values of these properties vary with the location in the weld pool and depend on the local characteristics of the fluid flow.

In this work, a turbulence model based on Prandtl's mixing length hypothesis (see Chapter 2) is used to estimate the turbulent viscosity [33]:

$$\mu_t = \rho l_m v_t \qquad (\mathbf{3.13})$$

where μ_t is the turbulent viscosity, l_m is the mixing length, and v_t is the turbulence velocity. The mixing length at any location within the weld pool is the distance traveled by an eddy before its decay and is often taken as the distance from the nearest wall [34]. The extent of computed turbulent kinetic energy was found to be about 10 % of the mean kinetic energy [35] in a controlled numerical study of re-circulating flows in a small square cavity. Yang and DebRoy [36] computed mean velocity and turbulent energy fields during GMA welding of HSLA 100 steel using a two equation k-ε model. Their results also show that the turbulent kinetic energy was of the order of 10 % of the mean kinetic energy. The turbulent velocity v_t can therefore be expressed as:

$$v_t = (0.1v^2)^{1/2} \qquad (\mathbf{3.14})$$

$$\mu_t = 0.3\ \rho l_m v \qquad (\mathbf{3.15})$$

Effective viscosity at a particular point is the sum of the turbulent (μ_t) and laminar (μ_l) viscosities, i.e.

$$\mu = \mu_t + \mu_l \qquad (\mathbf{3.16})$$

The corresponding local turbulent thermal conductivities are calculated by using the turbulent Prandtl number, which is defined in the following relationship:

$$\mathrm{Pr} = \frac{\mu_t c_p}{k_t} \qquad (\mathbf{3.17})$$

Based on previous modeling work [30, 34] the turbulent Prandtl number is set to a value of 0.9 for the calculations described here.

3.3.5 Free Surface Calculation

When no backing plate is present at the bottom surface of a full penetration weld, the surface deforms due to the weight of the liquid metal and the recoil pressure of the evaporating metal resulting in the formation of a hump. This deformation of the bottom surface can be calculated based on constrained minimization of energy considering contributions from the gravitational energy, surface tension and the recoil pressure of the metal vapors. Since this requires knowledge of the weld pool geometry and the temperature distribution on the weld pool surface, the free surface calculation is done after the heat transfer and fluid flow calculations have been completed. The calculation of free surface neglects the effect of non-zero z-direction fluid velocities.

The equations governing the top and the bottom free surface are given as [21, 22]:

$$P_{rec} + \lambda + \gamma \frac{\left(1+\phi_y^2\right)\phi_{xx} - 2\phi_x\phi_y\phi_{xy} + \left(1+\phi_x^2\right)\phi_{yy}}{\left(1+\phi_x^2+\phi_y^2\right)^{3/2}} = \rho g \phi \qquad (\mathbf{3.18})$$

$$\lambda - \gamma \frac{\left(1+\psi_y^2\right)\psi_{xx} - 2\psi_x\psi_y\psi_{xy} + \left(1+\psi_x^2\right)\psi_{yy}}{\left(1+\psi_x^2+\psi_y^2\right)^{3/2}} = \rho g\left(\psi + L\right) \qquad (\mathbf{3.19})$$

where P_{rec} is the recoil pressure, λ is the Lagrangian multiplier [37], γ is the surface tension, $\phi_x = \partial\phi/\partial x$, $\phi_y = \partial\phi/\partial y$, and $\phi_{xy} = \partial\phi/\partial x\,\partial y$. The symbols ϕ and ψ represent the depression of the top and bottom surfaces, respectively. The calculation of recoil pressure is described in Appendix B. The Lagrangian multiplier method [37] is used for the solution of a set of equations with constraints such as volume conservation. Different

values of the Lagrangian multiplier, λ, result in different surface configurations. The correct value of λ is determined from the volume conservation.

Volume conservation for partial penetration welds gives the following constraint equation:

$$\iint \phi dxdy = 0 \qquad (\mathbf{3.20})$$

Volume conservation for full penetration welds gives the following constraint equation:

$$\iint \phi dxdy = \iint \psi dxdy \qquad (\mathbf{3.21})$$

3.3.6 Calculation methodology

1) The keyhole geometry is calculated prior to starting the heat transfer and fluid transport calculations. The procedure for the calculations is available in the literature [7, 11] and is described in greater detail in Chapter 5.
2) The computed keyhole geometry is mapped into the co-ordinate system of the thermo-fluid model, i.e., all grid points in the interior of the keyhole are identified.
3) Momentum and energy balance equations, given by Eq. **3.1, 3.3,** and **3.5,** are solved assuming boiling temperature at the keyhole surface and no heat or mass flux across it. Velocities and temperature inside the keyhole are fixed at zero and boiling point, respectively, by adjusting the source term coefficients using the control volume technique. The fluid velocities at the keyhole surface adjust accordingly so that there is zero mass flux across the keyhole walls.
4) During calculations, the viscosities and thermal conductivities are updated at all locations in the liquid phase based on the turbulence model.
5) Deformation of the bottom surface of the full penetration weld is calculated using the temperature data from the thermo-fluid calculations.

3.4 Computational time

A desktop computer with 3.2 GHz Pentium 4 processor and 1 GB Ram was used for the execution of the computer program. The computational time for convergence ranged between 7 to 20 minutes depending mainly on the number of control volumes and the number of iterations. For example, for the welding of 304L stainless steel with 1980 W input power at 19.1 mm/s welding speed, 1.09 million grid points (172 X 102 X 62) were used and 1500 iterations were necessary for convergence. The time taken for this run was 11 min 6 s. Since the momentum conservation equations are solved only in the weld pool region, the computational time depended not only on the total number of grid points and the number of iterations, but also on the size of the weld pool. The extent of imbalance of enthalpy and velocities in the computational domain was used to determine convergence. For example, when the absolute values of enthalpy imbalance divided by the enthalpy were added over all the enthalpy control volumes and the sum was less than 0.01 %, enthalpy values were assumed to have converged. The same convergence criterion was used for the each of the three velocity components.

Non-uniform grids are used with a finer spacing at locations near the heat source compared to the locations farther away from heat source. Grid dependence of the model results was tested for the welding of Ti-6Al-4V alloy at 1000 W input power at 16.9 mm/s welding speed using different number of grid spacing. With an increase in the number of grids points, the weld pool length at the top surface, width pool width at the top surface, and weld depth were not significantly affected. As shown in Table **3.6**, increasing the number of grid points by about 138 % (from 142 X 57 X 77 to 180 X 77 X 107) resulted in less than 3 % variation in the calculated weld dimensions. Table **3.6** also shows the computational time required on a computer with 1 GB RAM using Intel Fortran Compiler 9.5 to complete 3000 iterations for each grid system. Since the model results are not greatly affected by an increase in the number of grid points in this range, the coarser of the two grid systems may be chosen to reduce computational time.

Table **3.6**: Grid dependence of model results.

Mesh	Time taken	Half-width (mm)	Length (mm)	Depth (mm)
142 X 57 X 77	20 m 56 s	1.22	4.47	3.56
162 X 57 X 77	24 m 52 s	1.22	4.48	3.56
180 X 57 X 87	29 m 32 s	1.23	4.54	3.63
180 X 77 X 87	37 m 57 s	1.21	4.48	3.63
180 X 77 X 107	46 m 21 s	1.24	4.60	3.63

3.5 Results and Discussion

3.5.1 Model Validation: Weld geometry

The fluid flow and heat transfer model was used to calculate the temperature fields, flow velocities, weld geometries and solidification parameters for the keyhole mode laser welding of A131 steel, vanadium, Ti-6Al-4V, 304L stainless steel (SS), and tantalum. These metals and alloys differ significantly in density, 4000 kg/m^3 to 15000 kg/m^3, solid thermal conductivity, 20 W/m-K to 57 W/m-K, boiling point, 3100 K to 5643 K, and other properties. Particular attention is paid to the effects of variations in welding power and travel speed. The model predictions of weld pool shape and size are then compared with the corresponding experimental results. The results obtained from the current model reasonably predict the weld characteristics for a range of welding conditions and material properties by considering 3D fluid flow in the weld pool, while avoiding the computationally intensive task of vapor-liquid interface tracking. Data used for the calculations is given in Tables **3.7** and **3.8**.

Table **3.7**: Data used for keyhole calculations.

Physical Property	A131 steel	V	304L SS	Ti-6Al-4V	Ta
Boiling point, (K) [38, 39]	3100	3683	3100	3560	5643
Density of liquid at boiling point, (kg/m^3) [38-41]	5800	5200	5800	3780	15000
Specific heat of liquid at boiling point, (J/kg K) [28, 38, 40, 42, 43]	800	907	800	730	231
Thermal conductivity of liquid at boiling point, (W/m-K) [40, 44-47]	29	50	29	30	67
Absorption coefficient, η	0.16 (CO_2 laser)	0.28	0.30	0.30	0.32
Heat of evaporation, x 10^6 , (J/kg) [38, 39]	6.52	8.98	6.52 (Fe) 6.21 (Cr)	1.03 (Ti)	4.1 (Ta)
Plasma attenuation coefficient, (m^{-1})	100	100	100	100	100

Table **3.8**: Data used for fluid flow calculations.

Physical Property	A131 steel	V	304L SS	Ti-6Al-4V	Ta
Solidus temperature, (K) [28, 38, 48]	1745	2175	1697	1878	3288
Liquidus temperature, (K) [28, 38, 48]	1785	2175	1727	1928	3288
Density of liquid (kg/m^3) [38-41, 48]	7000	5500	7000	4000	15000
Specific heat of solid, (J/kg K) [28, 38, 48]	706	730	712	610	190
Specific heat of liquid, (J/kg K) [38, 40, 42, 43, 48]	810	780	800	700	231
Thermal conductivity of liquid, (W/m-K) [40, 44-47]	21	50	29	30	67
Thermal conductivity of solid, (W/m-K) [40, 44-47]	21	30	27	21	55
Viscosity, (Pa-s) [48, 49]	0.007	0.005	0.007	0.005	0.01
Coefficient of thermal expansion, x 10^{-5} (1/K) [38]	1.0	1.0	1.96	0.8	0.66
Temperature coefficient of surface tension, x10^{-3} (N/mK) [38]	-0.49	0.31	-0.49	-0.26	-0.25
Enthalpy of solid at melting point, x 10^6 (J/kg) [28, 38]	1.20	1.25	1.20	1.12	0.52
Enthalpy of liquid at melting point, x 10^6 (J/kg) [28, 38]	1.26	1.58	1.26	1.49	0.68

3.5.1.1 Variation of input power

Figures **3.2** to **3.5** show the comparison of experimental and calculated weld pool cross-sections for A131 structural steel, 304L stainless steel, Ti-6Al-4V alloy, and vanadium, respectively. Figure **3.2** shows the variation of calculated weld cross-sections for A131 structural steel welds made using a continuous wave CO_2 laser at a welding speed of 12.7 mm/s and input powers ranging from 3.3 kW to 9.6 kW. The three lines in the computed left side of the figures indicate the solidus temperature (1745 K), the boiling point temperature (3100 K), and the A1 line temperature for the A131 alloy (1000 K). The boiling point contour marks the cross-sectional geometry of the keyhole, the solidus temperature contour marks the weld pool boundary, and the A1 line contour

approximately marks the HAZ region of the welded section. The solid line on the experimental weld cross-section, shown in the right side of each figure, marks the boundary between the fusion zone and the heat affected zone. The slight deformation of the top surface was used as a guide to determine the fusion zone boundary. The highest power level of 9.6 kW resulted in a full penetration weld while the lower power levels produced partial penetration welds. The calculated weld cross-sections agree reasonably well with the experimental observations. The deviation of the simulated weld pool geometry from the experimental results falls within the variation of the weld geometry under seemingly identical experimental conditions. The weld pool geometry is clearly affected by the convective heat transfer, as evidenced by the widening of the pool near the top surface where fluid velocities are highest. For the full penetration case, the weld pool widens near the bottom as well as near the top due to Marangoni convection resulting in an "hour-glass" shape. The weld geometry shows that for the welding conditions used, convective heat transfer plays an important role.

For 304L stainless steel, Ti-6Al-4V alloy, and vanadium welds shown in Figures **3.3** to **3.5**, the dotted lines and the solid lines mark the experimentally observed fusion zone boundary and the calculated weld pool boundary (as defined by the solidus temperatures), respectively. The dashed lines show the keyhole geometry as defined by the boiling points of various materials. As shown in Figure **3.3**, there is good agreement between the calculated and experimental weld pool cross-sections of the 304L stainless steel welds for the three different input powers. The agreement seems to be better at lower input powers than at higher powers. The calculated weld pool cross-sectional shapes for Ti-6Al-4V agree with the experimental weld pool shapes as shown in Figure **3.4**. It should be noted that it is often difficult to discern the exact fusion zone boundary in Ti-6Al-4V welds because of grain growth in the heat affected zone. Since the top surface deformation was small, it could not be used as a guide to determine the fusion zone boundary which is expected to be somewhere in the light etching region towards the boundary between the dark and the light etching regions. The dotted line in Figure **3.4** marks the boundary between the dark and the light etching regions. For the vanadium welds shown in Figure **3.5**, the calculated weld cross-sections agree with the

experimental observations. The calculations show less spread in the weld pool width at the top surface than the experimental results. Each of these welds shows a cross-section with a wide upper part and a narrow lower part with nearly parallel sides. The calculated weld cross-sections also show a widening at the top with a narrower lower part. However, the lower parts of the calculated weld cross-sections are tapered toward the bottom rather than having parallel sides.

Near the lower part of the weld pool, the small fluid velocities indicate that convection plays a very small role in heat transfer. Since conduction is the main mechanism of heat transfer, and the temperature at the keyhole wall is constant (equal to the boiling point of the alloy) at all depths, the temperature contours are governed by the shape of the keyhole which is tapered towards the bottom. However, during experiments it is likely that the keyhole wall temperatures are slightly higher near the bottom because of the higher pressures and the focusing of laser beam near the keyhole bottom due to reflections at the keyhole walls. The increase in keyhole wall temperatures with depth can result in a weld cross-section with parallel sides. Figures **3.6**, **3.7**, and **3.8** show that there is good agreement between the computed and experimental weld pool depths for the power variation study on 304L stainless steel, Ti-6Al-4V, and vanadium welds, respectively. The experimental weld depths were measured for these four materials using commercial image analysis software. Since similar measurements were not made for the A131 steel welds, only a comparison of weld cross-sections is reported here.

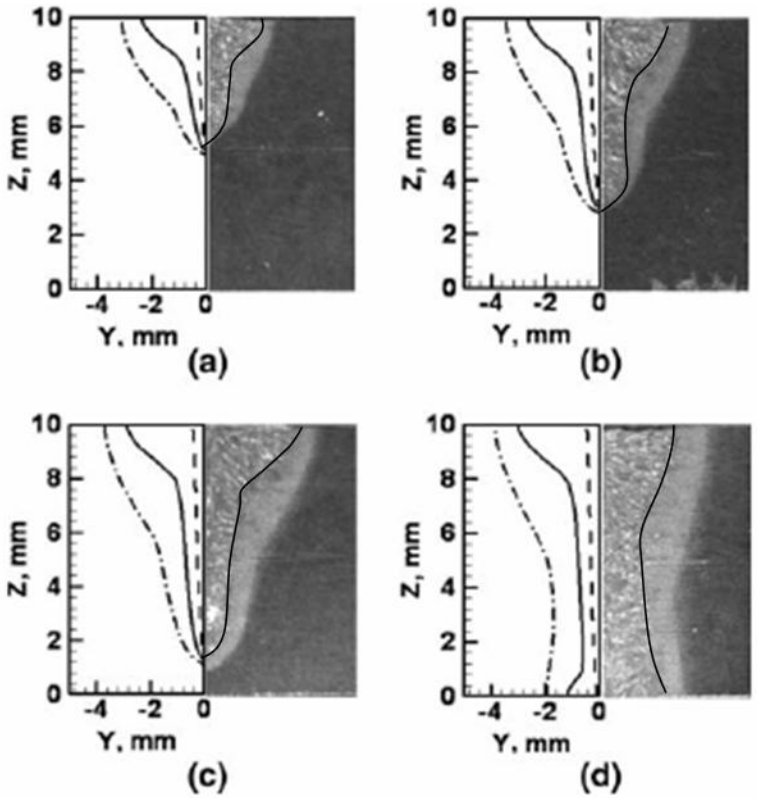

Figure **3.2**: Comparison of experimental and simulated weld cross-sections for the A131 steel for a welding speed of 12.7 mm/s and powers of a) 3.3 kW, b) 5.0 kW, c) 6.8 kW, and d) 9.6 kW.

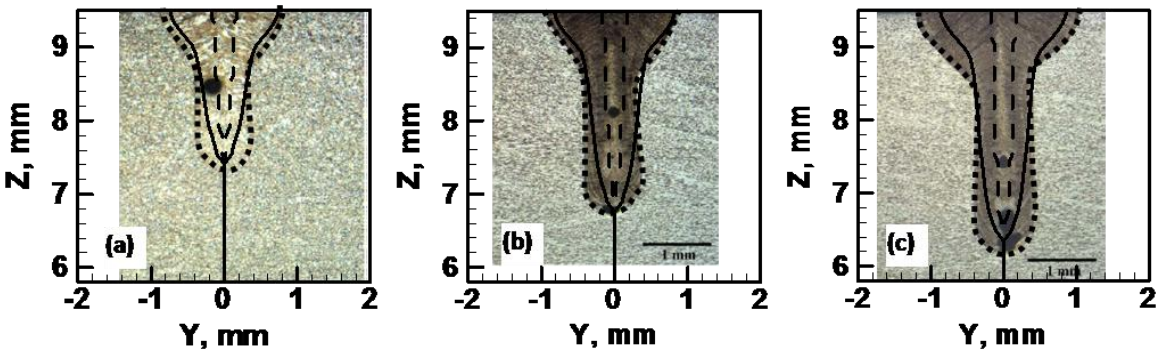

Figure **3.3**: Comparison of calculated and experimental weld geometry for 304L stainless steel welds made at 19.1 mm/s welding speed with input laser powers (a) 887 W, (b) 1332 W, and (c) 1777 W. The solid line represents the solidus and the dashed line represents the keyhole marked by boiling point temperature. The dotted line shows the experimentally observed weld pool boundary.

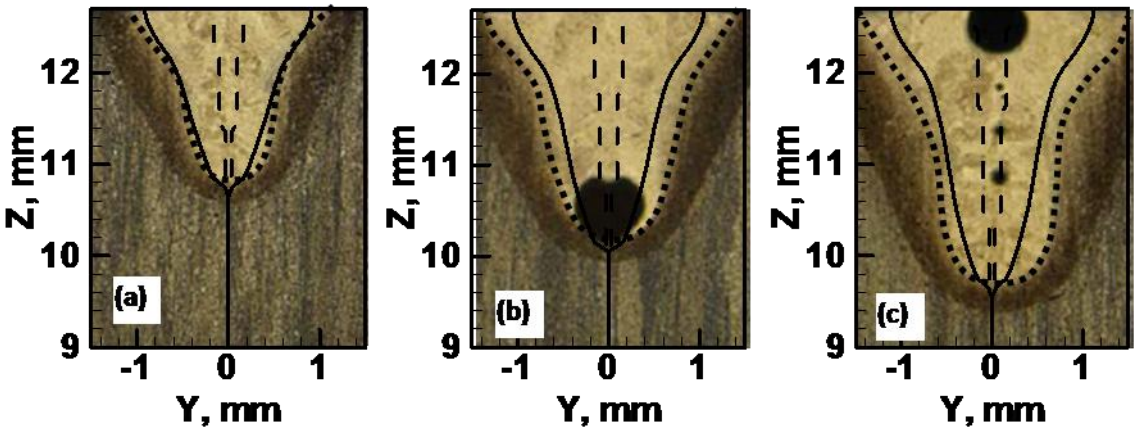

Figure **3.4**: Comparison of calculated and experimental weld geometry for Ti-6Al-4V alloy welds made at 16.9 mm/s welding speed with input laser power (a) 720 W, (b) 1100 W, (c) 1400 W. The solid line represents the solidus and the dashed line represents the keyhole marked by boiling point temperature. The dotted line shows the boundary between the dark and the light etching regions.

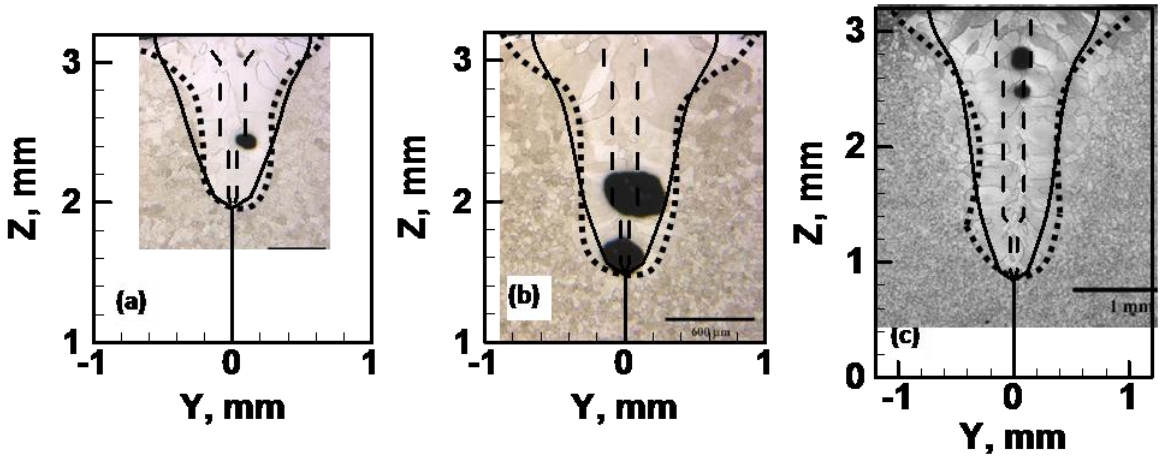

Figure **3.5**: Comparison of calculated and experimental weld geometry for vanadium welds made at 25.4 mm/s welding speed with input laser powers (a) 887 W, (b) 1332 W, and (c) 1777 W. The solid line represents the solidus and the dashed line represents the keyhole marked by boiling point temperature. The dotted line shows the experimentally observed weld pool boundary.

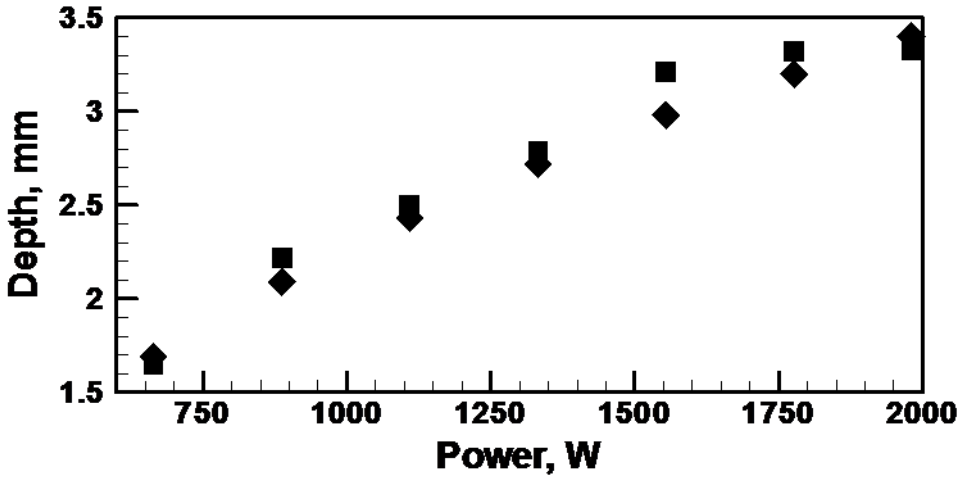

Figure **3.6**: Experimental and calculated weld dimensions of 304L stainless steel welds made with different input laser powers at 19.1 mm/s welding speed. Square: experimental value, diamond: calculated value.

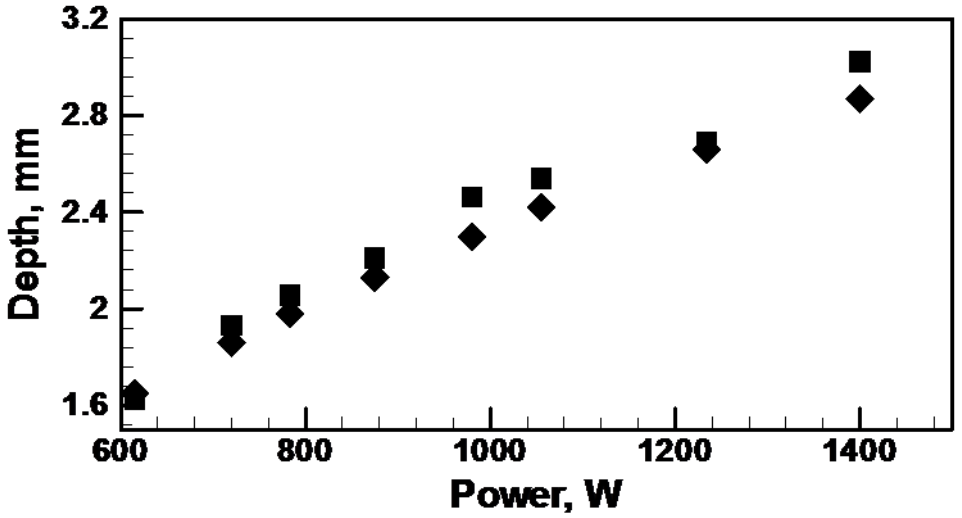

Figure **3.7**: Experimental and calculated weld dimensions of Ti-6Al-4V alloy welds made with different input laser powers at 16.9 mm/s welding speed. Square: experimental value, diamond: calculated value.

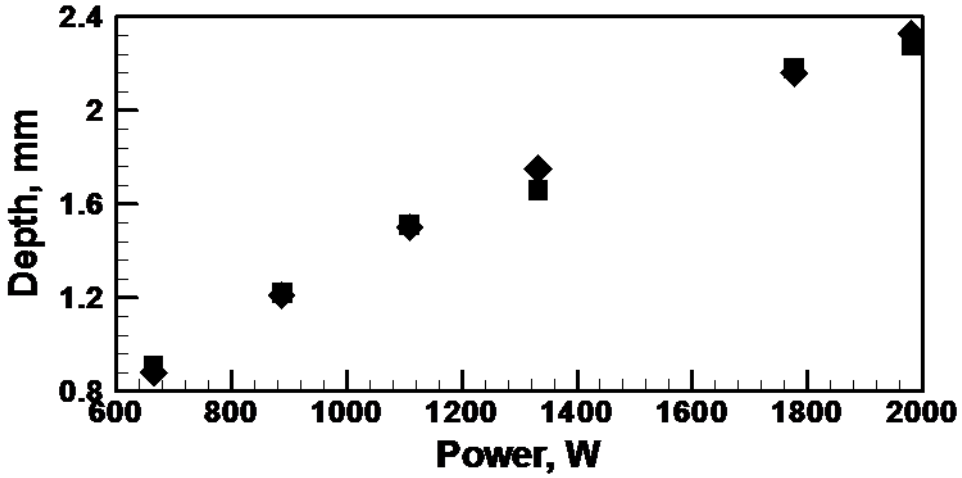

Figure **3.8**: Experimental and calculated weld dimensions of vanadium welds made with different input laser powers at 25.4 mm/s welding speed. Square: experimental value, diamond: calculated value.

3.5.1.2 Variation of welding speed

Figures **3.9** to **3.11** show the comparison of experimental and calculated weld cross-sections for A131 structural steel, tantalum and 304L stainless steel welds made with fixed input power at different travel speeds. The solid line on the experimental weld cross-section, shown in the right part of Figures **3.9** (a) – (d), marks the boundary between the fusion zone and the heat affected zone. The slight deformation of the top surface was used as a guide to determine the fusion zone boundary.

As shown in Figure **3.9,** the calculated weld cross-sections for A131 structural steel, including the fusion zone and the heat affected zone, agree reasonably well with the experimentally observations. For tantalum welds shown in Figure **3.10**, the agreement between the experimental and calculated weld pool cross-sections is better at higher welding speeds than at lower welding speeds. The experimental weld cross-sections, especially at lower welding speeds, exhibit a wide spread in the weld pool very close to the top surface. The calculated weld pool shapes, however, show a gradual change in weld pool cross-sectional width with depth because the heat transfer is mainly governed by conduction. The agreement between the calculated and experimental weld cross-sections for 304L stainless steel, shown in Figure **3.11**, is better at higher welding speeds, or at lower heat input per unit length. The weld dimensions were measured for tantalum and 304L stainless steel using image analysis software. Figures **3.12** and **3.13** show good agreement between the computed and experimental weld pool depths for the welding speed variation study on tantalum and 304L stainless steel, respectively. The decrease in penetration depth with increasing weld speed is greater at lower welding speeds than at higher welding speeds, especially for tantalum for which the welding.

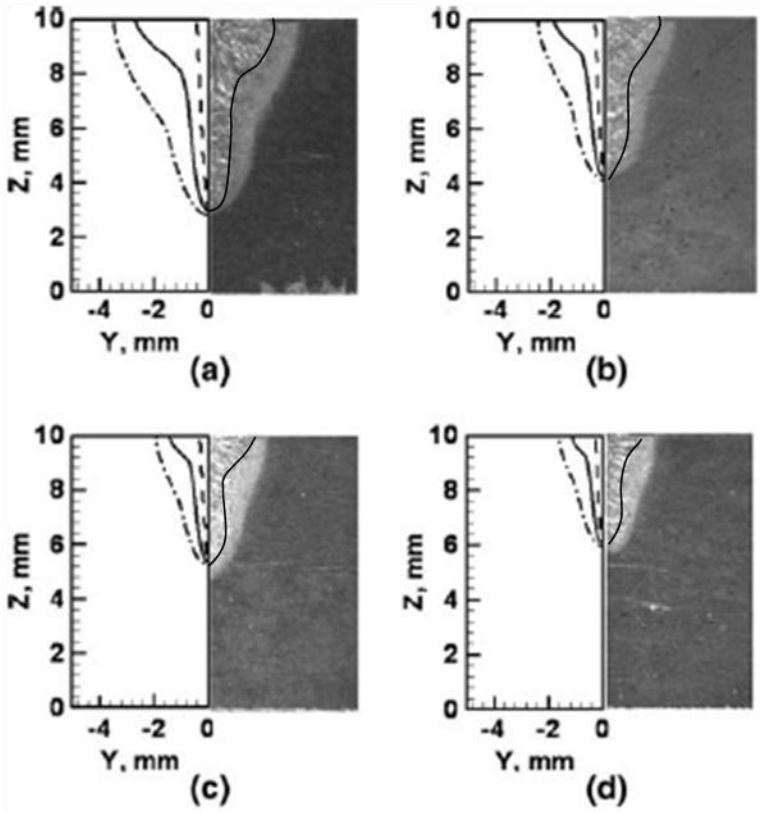

Figure **3.9**: Comparison of experimental and simulated weld cross-sections for the A131 steel for a power of about 5.0 kW and welding speeds of a) 12.7 mm/s, b) 19.1 mm/s, c) 25.4 mm/s, and d) 31.8 mm/s.

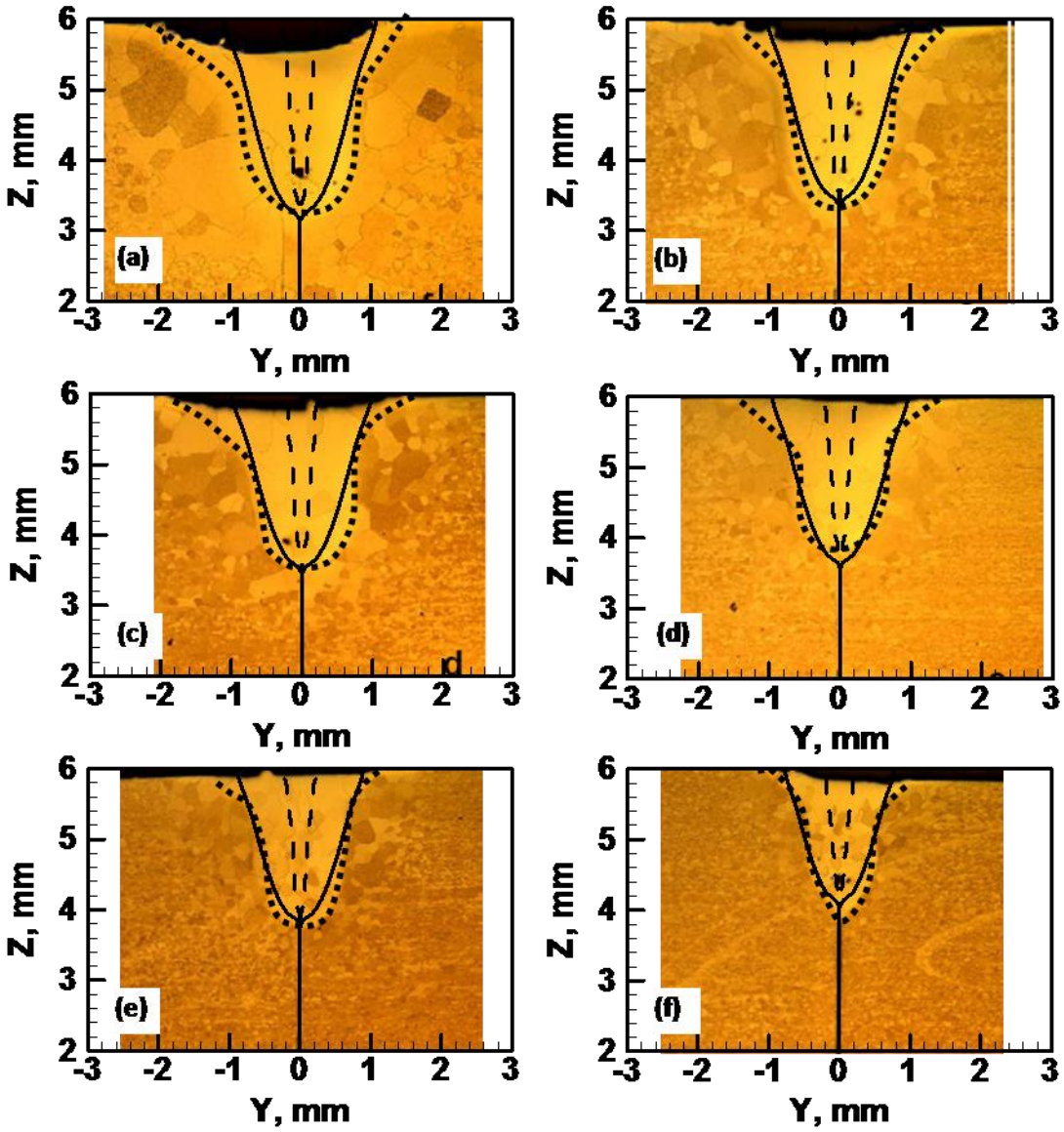

Figure **3.10**: Comparison of calculated and experimental weld geometry for tantalum welds made with 1900 W input laser power at welding speeds (a) 0.85 mm/s, (b) 1.7 mm/s, (c) 2.54 mm/s, (d) 3.81 mm/s, (e) 6.4 mm/s, and (f) 12.7 mm/s. The solid line represents the solidus and the dashed line represents the keyhole marked by boiling point temperature. The dotted line shows the experimentally observed weld pool boundary.

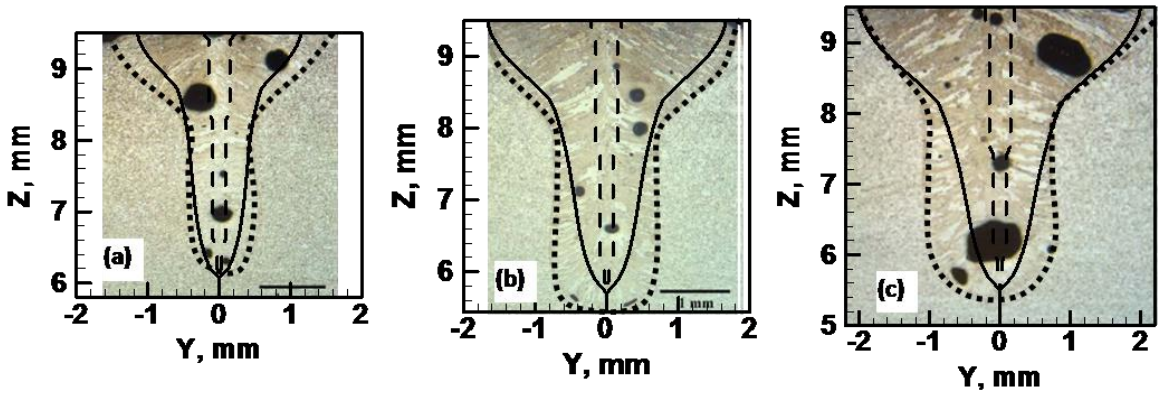

Figure **3.11**: Comparison of calculated and experimental weld geometry for 304L stainless steel welds made with 1980 W input laser power at welding speeds (a) 16.9 mm/s, (b) 10.6 mm/s, and (c) 8.5 mm/s. The solid line represents the solidus and the dashed line represents the keyhole marked by boiling point temperature. The dotted line shows the experimentally observed weld pool boundary.

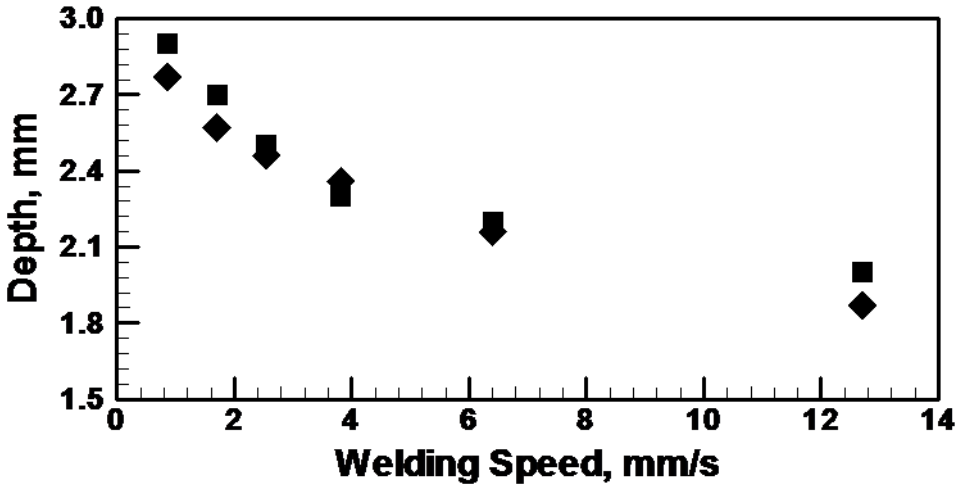

Figure **3.12**: Experimental and calculated weld dimensions of tantalum welds made with 1900 W input laser power at different welding speeds. Square: experimental value, diamond: calculated value.

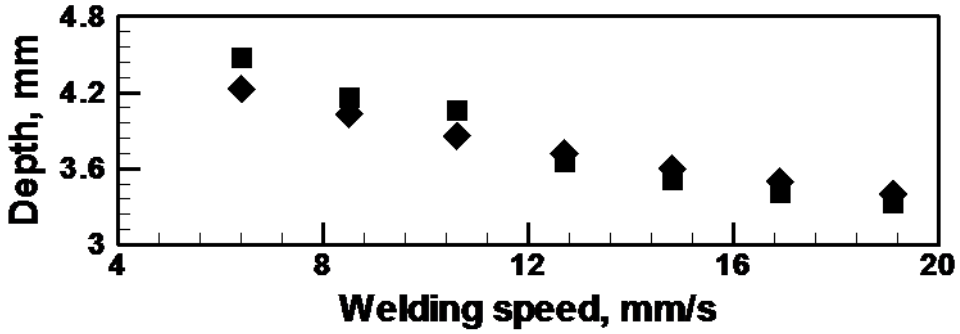

Figure **3.13**: Experimental and calculated weld dimensions of 304L stainless steel welds made with 1980 W input laser power at different welding speeds. Square: experimental value, diamond: calculated value.

3.5.2 Convective heat transfer and weld geometry

3.5.2.1 Weld geometry

The weld geometry depends on heat transfer and fluid flow in the weld pool. To illustrate the significance of the predominant mode of heat transfer (convective versus conductive) on weld geometry, weld cross-sections for high thermal conductivity Al 5754 alloy were compared with the weld cross-sections for low thermal conductivity 304L stainless steel. Figure **3.14** shows the calculated weld cross-sections superimposed over the experimentally observed weld cross-section for Al 5754 alloy (thermal conductivity ~138 W/m-K) for a fixed input power and varying welding speeds. The fusion zone is wide and shows a gradual decrease as the distance from the top surface increases. Contrast this to the weld cross-sections shown in Figure **3.15** for the lower thermal conductivity (29 W/m-K) 304L stainless steel alloy. The stainless steel welds are narrow through the majority of the weld depth, with a sharp increase in the weld depth near the top surface of the weld giving the partial penetration welds a characteristics ‘nail-head’ shape. Full penetration welds with a free surface at the bottom of the work-piece can

take what was previously referred to as an ‘hour-glass’ shape, similar to that shown in Figure **3.2** (d).

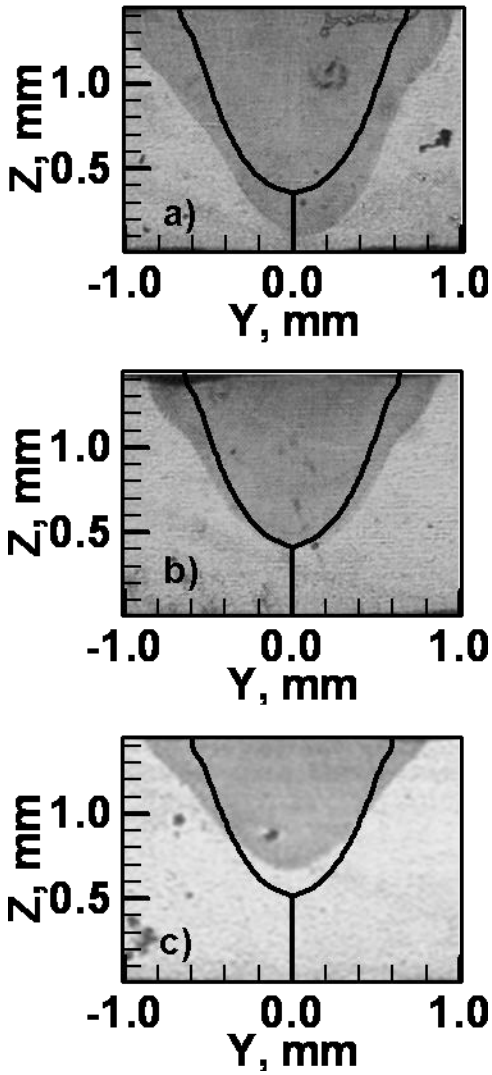

Figure **3.14**: Comparison of weld pool cross-section with simulated weld pool cross-section for Al 5754 alloy for laser power of 2600 W and welding velocity a) 74.1 mm/s b) 84.7 mm/s and c) 10.6 mm/s.

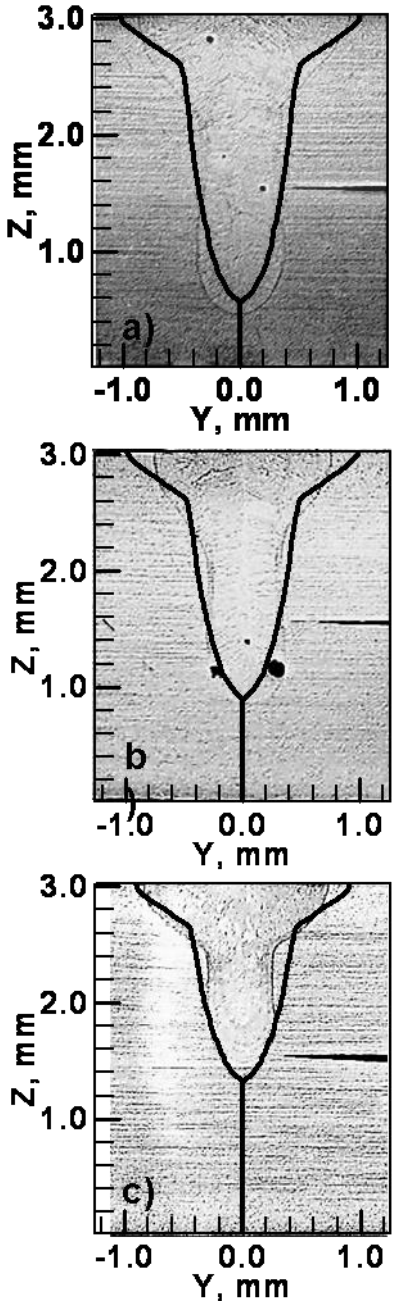

Figure **3.15**: Comparison of weld pool cross-section with simulated weld pool cross-section of 304L stainless steel at 19 mm/s welding speed and input power of a) 1250 W b) 1000 W and c) 750 W.

3.5.2.2 Fluid flow

Figure **3.16** shows the computed fluid flow and temperature fields along the symmetric plane and the top surface. The conical region with no velocity vectors is the keyhole. Due to the temperature gradients at the top surface of the weld pool, surface tension gradients are generated. These gradients lead to Marangoni convection which drives the flow of hot molten material outwards from the location of heat source, resulting in enhanced heat transfer and elongation and widening of the weld pool near the top surface. At a distance far away from the top surface, the fluid velocities are dampened, and the role of convective heat transfer is diminished.

The weld pool size depends on the Peclet number. For low Peclet number near the bottom of the weld pool, the contribution of convection to heat transfer is very small, thus decreasing the weld pool width. The difference between the weld pool shapes of the two alloys also arises from the relative role of convective heat transfer in the weld pool. Because of the lower thermal conductivity of 304L stainless steel, convective heat transfer is more important relative to the conductive heat transfer in 304L stainless steel than in Al5754 alloy. In the 304L stainless steel weld, the temperature contours are very strongly affected by the fluid flow. Thus, the temperature contours are widely spaced near the top surface where the fluid flow plays the role of diffusing the heat flux from the keyhole walls. Slightly below the top surface, where the fluid flow is radially inwards and towards the keyhole, the flow of heat from the keyhole region is diminished, resulting in compressed temperature contours. Still further down, the velocities diminish in magnitude and therefore the temperature contours widen again and then converge to the bottom of the keyhole because the heat transfer in the region is influenced by conduction. For Al 5754 alloy, the temperature contours do not strictly follow the fluid flow patterns because significant heat transfer takes place through conduction.

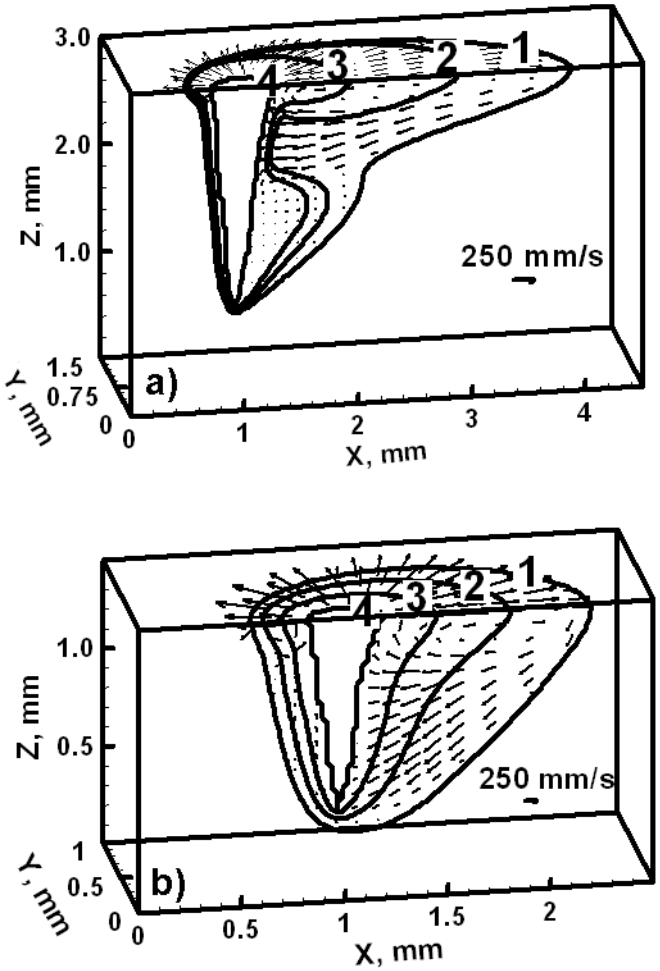

Figure **3.16**: Computed temperature and flow field for a) SS 304L, 1000W, 19 mm/s; b) Al 5754, 2600 W, 74.1 mm/s. For SS 304L levels 1, 2, 3 and 4 correspond to 1697 K, 1900 K, 2100 K and 3100 K, respectively. For Al 5754 K levels 1, 2, 3 and 4 correspond to 880 K, 1100 K, 1400 K and 2035 K, respectively.

The weld pool shape may be further explained by Figure **3.17** (a) and (b) that show the computed temperature contours and fluid velocities on horizontal planes (x-y planes) at different elevations for the stainless steel and the aluminum alloy, respectively. It may be observed that in all x-y planes the contours are compressed in front of the heat source and expanded behind it because heat is transferred towards a colder region in front of heat source. It may be clearly observed that in case of steel weld (Figure **3.17** (a)) the solidus contour shrinks rapidly with increase in depth from top. In contrast, Figure **3.17**

(b) for the aluminum alloy shows that the solidus contour on the horizontal xy-planes shrinks gradually from top to bottom.

The computed half cross-sections in a y-z vertical plane containing the heat source for the welding of 304L stainless steel and 5754 aluminum alloy are shown on the left side of Figure **3.18** (a) and (b), respectively. The experimentally observed weld cross-section is shown on the right side of the figures. The velocity vectors and temperature contours are superimposed on the computed half cross section. However, please note that the computed sections at the heat source location that is shown in Figure **3.18** are not the computed weld cross-sections. Rather, the weld cross-section is represented by the outer boundary of the projection of computed 3D solidus contours on the plane perpendicular to welding direction, and was shown previously in Figure **3.15**. Figure **3.18** qualitatively shows the weld pool boundary and explains the effect of fluid flow pattern on the weld cross section. The temperature contours for stainless steel more closely follow the re-circulatory fluid flow pattern that is set up at the top surface of the liquid due to Marangoni convection. In contrast, the temperature contours do not strictly follow the re-circulating flow in case of aluminum alloy because significant heat flow takes place by heat conduction.

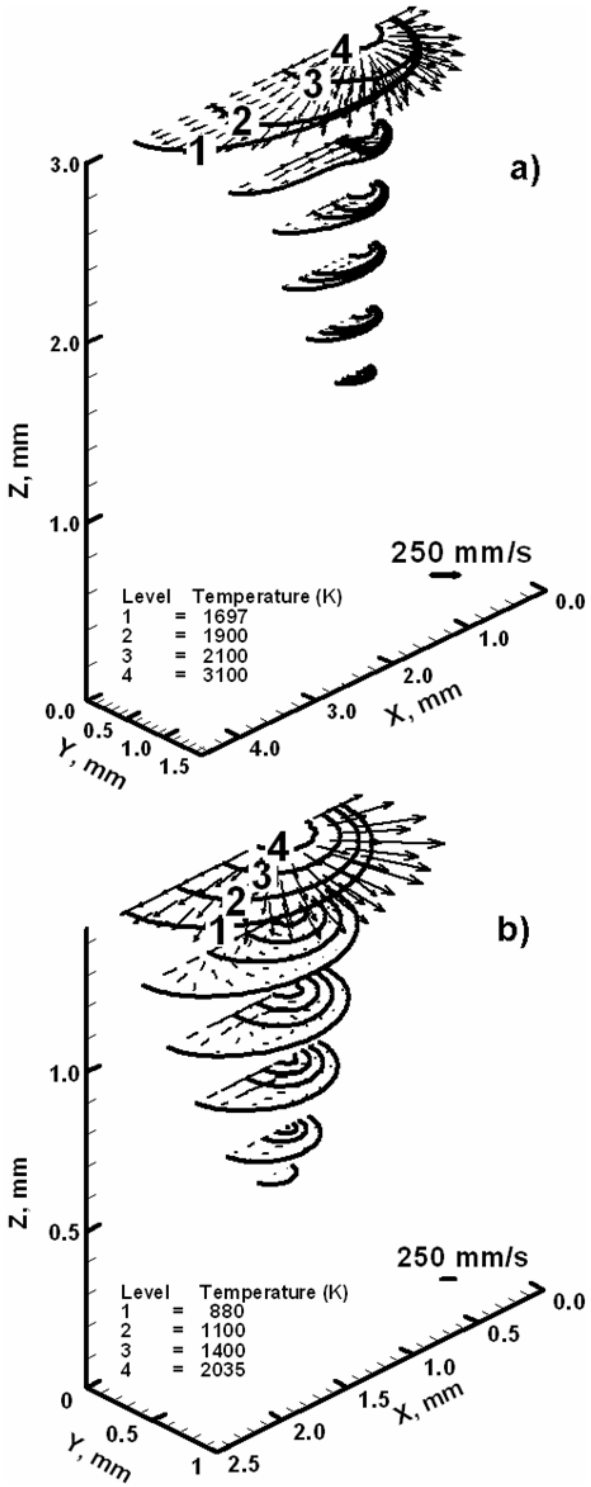

Figure **3.17**: Computed fluid flow and temperature profile for different z-sections for a) SS 304L, 1000 W, 19 mm/s b) 5754 Al alloy, 2600 W, 74.1 mm/s.

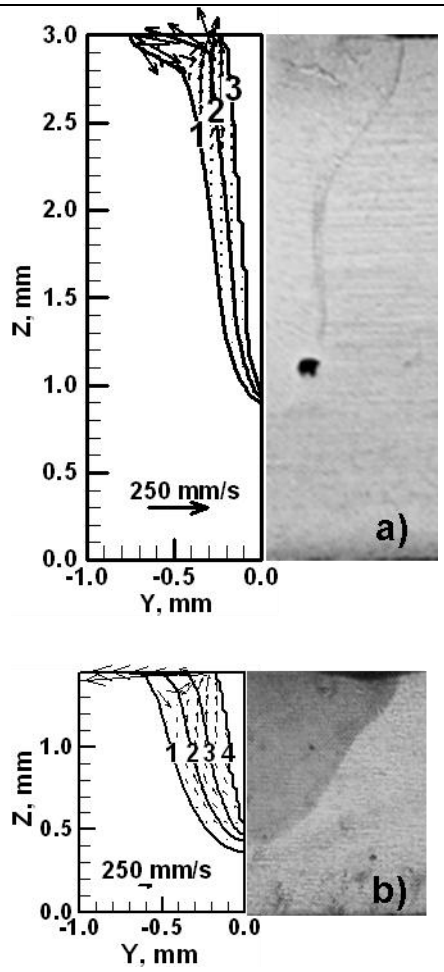

Figure **3.18**: Experimental and calculated y-z cross-sections for plane near laser source, for a) SS 304L, 1000W, 19 mm/s, b) Al 5754, 2600 W, 74.1 mm/s. For SS 304L levels 1, 2 and 3 correspond to 1697 K, 2300 K and 3100 K, respectively. For Al 5754 K levels 1, 2, 3 and 4 correspond to 880 K, 1100 K, 1400 K and 2035 K, respectively.

Figure **3.19** shows the computed 3D temperature contours and fluid flow patterns for 304L stainless steel, Ti-6Al-4V, vanadium, and tantalum for an input laser power of 1900 W at a welding speed of 12.7 mm/s. Since surface tension depends on temperature, the large temperature gradients on the weld pool surface result in large surface tension gradients. As a result, liquid metal flows from near the keyhole to the edge of the weld pool owing to surface tension induced Marangoni convection, thereby enhancing the heat transfer. The radial heat transfer results in wider and longer weld pools. The velocities on the weld pool surface decay near the edge of the weld pool.

Depending on the extent of convective heat transfer and how it varies with depth, the weld pool may either have a spread near the top (as in Figure **3.19** (a) – (c)) or a cross-section with a gradual change in width from top to bottom (as in Figure **3.19** (d)). The 3D views of weld pools in Figure **3.19** show elongated weld pool shapes in the 304L stainless steel, Ti-6Al-4V alloy and vanadium samples as a result of the prominence of the Marangoni convection. In the tantalum weld, shown in Figure **3.19** (d), the effect of Marangoni convection on the weld pool shape is less explicit. The high boiling point and density of tantalum results in lower weld penetration than other materials.

In high thermal conductivity solids, efficient dissipation of energy from the weld pool into the solid region makes the weld pool relatively small. On the other hand, in low thermal conductivity materials, more heat is available for melting because of slow dissipation of heat into the solid region. As a result, the weld pool tends to be relatively large. High boiling and melting points, along with high thermal conductivity of solid tantalum result in relatively small weld pool depth and width compared with other materials under similar welding conditions (Figure **3.19**).

The importance of convective heat transfer relative to conductive heat transfer can be determined by calculating the Peclet number, Pe, which is defined in the relationship shown below:

$$\mathrm{Pe} = \frac{\text{Heat transfer by convection}}{\text{Heat transfer by conduction}} = \frac{u\rho C_p \Delta T}{k\Delta T / L_R} = \frac{u\rho C_p L_R}{k} \qquad (\mathbf{3.22})$$

where u is the characteristic velocity, ρ is the density, C_p is the specific heat at constant pressure, L_R is the characteristic length, and k is the thermal conductivity. With a higher Peclet number, the contribution of convection to heat transfer is increased. It should be noted that the Peclet number varies with location within the weld pool. Thus, the high velocity region near the weld pool surface will have a higher Peclet number than the low velocity regions in the interior of the weld pool. Even in systems where convection is the dominant mechanism of heat transfer, the Peclet number values near a solid-liquid boundary will be very low due to small local fluid velocities. For a weld pool where conduction is the dominant heat transfer mechanism, the Peclet number values in most locations should be significantly lower than 1.

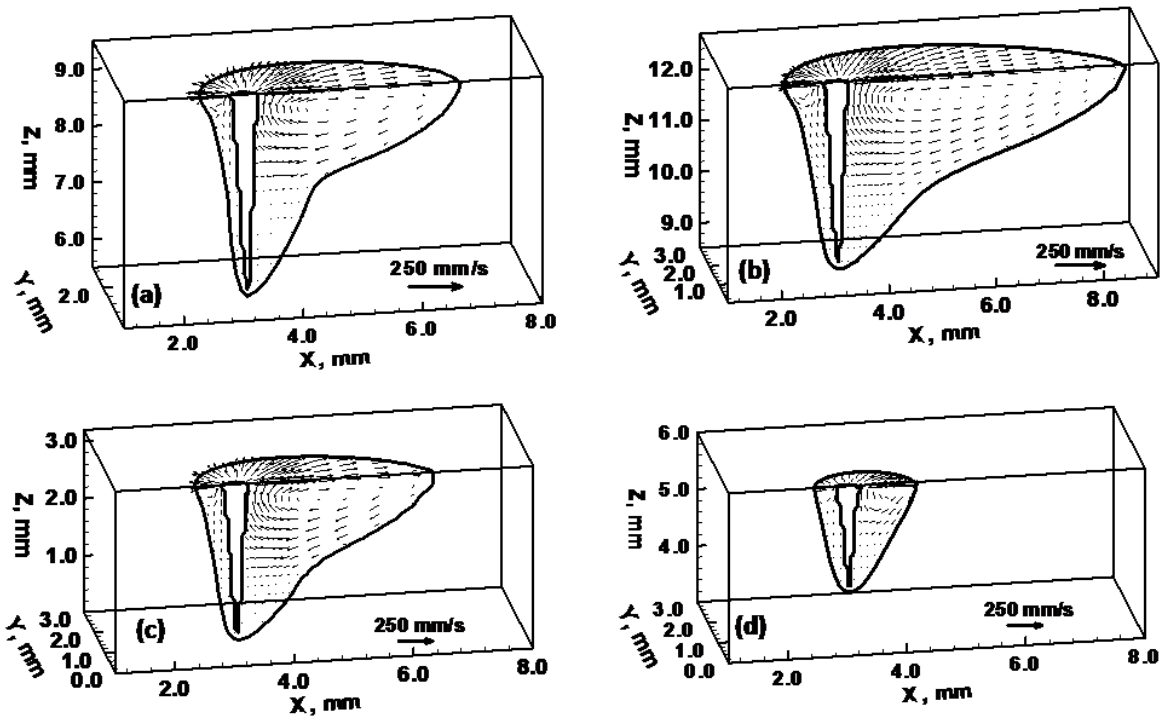

Figure **3.19**: 3D weld pool shape and fluid flow for welds made with 1900 W laser power at 12.7 mm/s welding speed. a) 304L Stainless Steel, (b) Ti-6Al-4V, (c) Vanadium, and (d) Tantalum.

Table **3.9**: Peclet number for various welding systems.

Material	U (m/s)	ρ (kg/m^3)	Cp (J/kg-K)	L (m)	k (W/m-K)	Thermal diffusivity m^2/s	Pe
SS 304L	0.1	7000	800	0.001	29	5.18×10^{-6}	19.3
Ti-6Al-4V	0.1	4000	700	0.001	30	1.07×10^{-5}	9.3
V	0.1	5500	780	0.001	50	1.17×10^{-5}	8.6
Ta	0.1	15000	231	0.001	67	1.94×10^{-5}	5.1
Al	0.1	2300	1250	0.001	138	4.8×10^{-5}	2.1

Table **3.9** lists the thermal diffusivity and Peclet numbers calculated for 304L stainless steel, Ti-6Al-4V, vanadium, tantalum, and aluminum alloy welds. Of the five materials, tantalum and 304L stainless steel display the highest and the lowest values of

thermal diffusivity, respectively. The computed values of Pe show that convection is very important for heat transfer in the welding of all five materials. However, the ratio of heat transported by convection and conduction is highest for stainless steel and lowest for aluminum alloy.

3.5.3 Partial and full penetration welds

Partial and full penetration welds were made on A131 steel samples. Detailed description of the experiment is given in section **3.2.1** and the input process parameters are given in Tables **3.7** and **3.8**.

3.5.3.1 Fluid flow

Figure **3.20** (a) and (b) show the temperature contours and fluid flow for the symmetry plane and the top plane for a partial penetration and a full penetration weld, respectively. The temperature contours follow the fluid flow pattern. At the top plane, the liquid metal flows outward from the keyhole and carries heat away from the center. Thus a wide and elongated weld pool is obtained. The weld pool length decreases with distance from the top surface due to viscous effects and the weld pool is increasingly influenced by conduction heat transfer. Due to the effect of the moving heat source, the temperature contours are compressed in the front of the heat source and elongated behind it. For the full penetration weld, the flow pattern at the top surface is similar to that in a partial penetration weld. However, since the weld pool extends to the bottom surface of the work-piece, surface tension driven Marangoni convective currents are present at the bottom surface which elongate and widen the weld-pool. Thus, the weld pool is spread near the top and bottom surfaces and is columnar in between. The resulting weld cross-section has an ‘hour-glass’ shape as shown in Figure **3.2** (d).

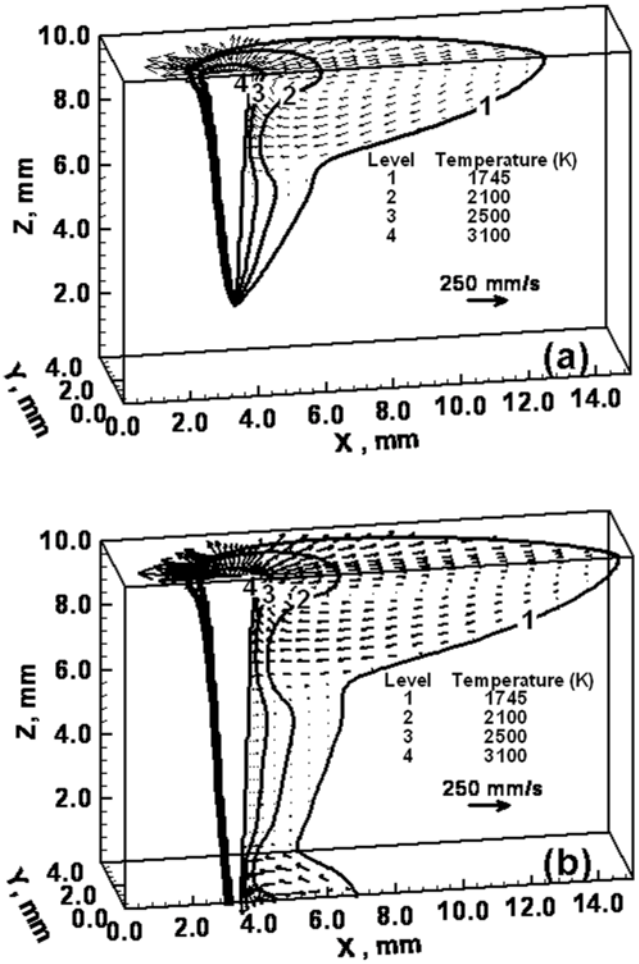

Figure **3.20**: Top surface and symmetry plane of A131 steel weld pool with temperature contours and velocity vectors for a) v = 12.7 mm/s, 5.0 kW, and b) v =12.7 mm/s, 9.6 kW.

Figure **3.21** shows various temperature contours and velocity vectors for various transverse y-z cross-sections of the weld pool for partial penetration welding of A131 steel at 5.0 kW laser power and 12.7 mm/s welding speed. The effect of Marangoni convection on the weld pool size and shape is clearly visible. The circulation currents formed due to Marangoni convection take heat from the center, thus resulting in a wide pool. The highest weld pool depth is obtained for a cross-section slightly behind the laser source. For different z levels, maximum weld pool widths are obtained at different x-locations. Figure **3.22** shows the temperature contours and velocity vectors for various transverse sections of the melted region for full penetration welding of A131 steel at 9.6

kW laser power and 12.7 mm/s welding speed. Marangoni convection currents are seen at the top and bottom surfaces resulting in enhanced heat transfer resulting in weld pool which is wider at the top and bottom surfaces and narrower in the middle. The weld pool transverse cross-section is obtained by the superimposition of solidus contours on all y-z melted sections.

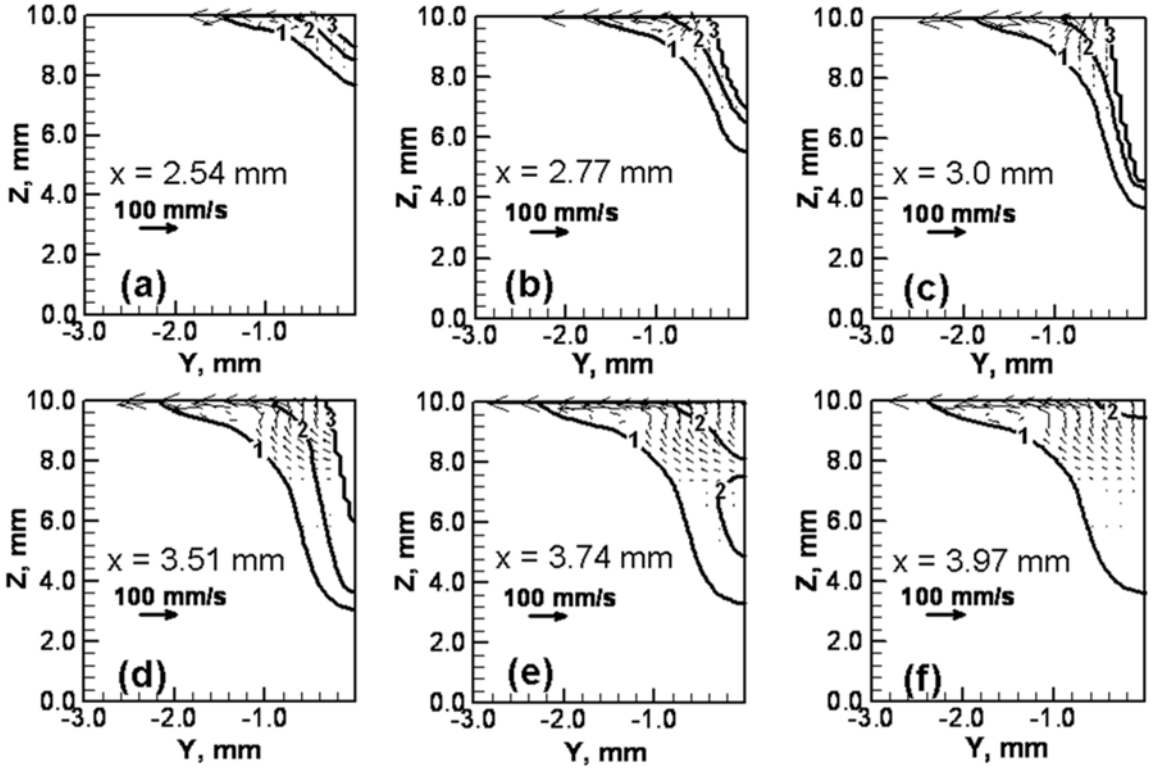

Figure **3.21**: A131 steel weld pool cross sectional geometry for laser power 5.0 kW and welding speed of 12.7 mm/s, at different locations along the welding direction, a) x = 2.54 mm, b) x = 2.77 mm, c) x = 3.0 mm, d) x = 3.51 mm, e) x = 3.74 mm, f) x = 3.97 mm. Levels 1, 2 and 3 correspond to 1745 K, 2500 K and 3100 K, respectively. Laser beam is located at x = 3 mm.

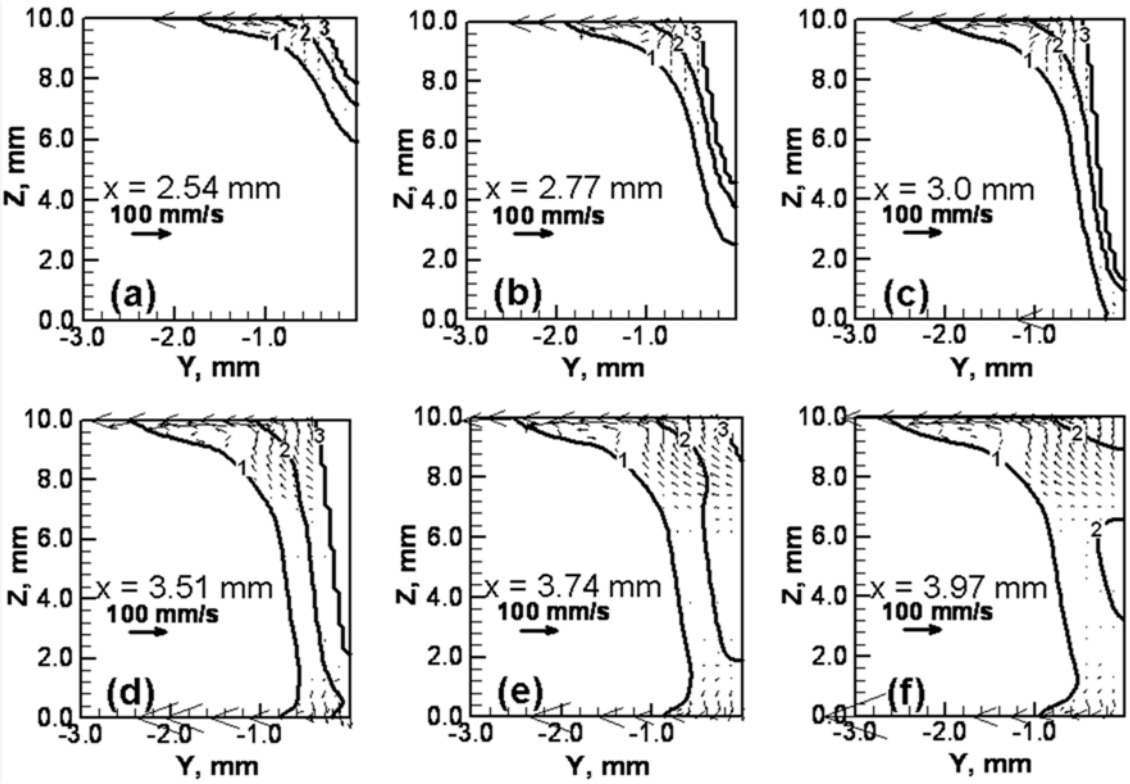

Figure **3.22**: A131 steel weld pool cross sectional geometry for laser power 5.0 kW and welding speed of 12.7 mm/s, at different locations along the welding direction, a) x = 2.54 mm, b) x = 2.77 mm, c) x = 3.0 mm, d) x = 3.51 mm, e) x = 3.74 mm, f) x = 3.97 mm. Levels 1, 2 and 3 correspond to 1745 K, 2500 K and 3100 K, respectively. Laser beam is located at x = 3 mm.

3.5.3.2 Turbulence

Figure **3.23** shows the effective viscosity contours for different transverse sections along the welding direction for partial penetration welding of A131 steel for an input laser power of 5.0 kW at a welding speed of 12.7 mm/s. Figure **3.24** is a similar plot for full penetration laser welding of A131 for an input laser power of 9.6 kW at a welding speed of 12.7 mm/s. Highest viscosity values are obtained near the surfaces of the weld pool due to high turbulent contribution arising from very high surface tension driven

velocities. Viscosity is lower near the solid-liquid boundary and increases towards the center before decreasing at the liquid - vapor interface in the keyhole.

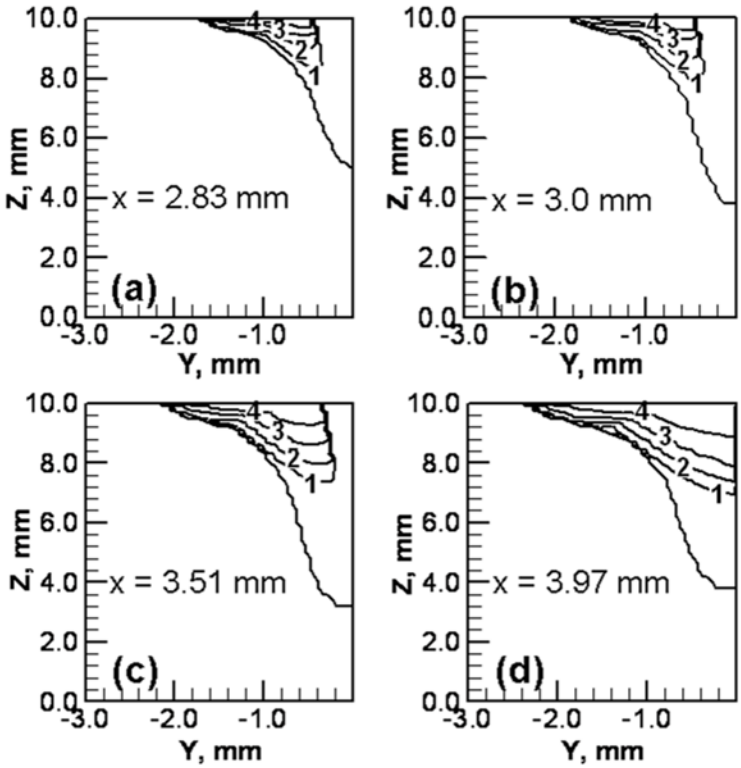

Figure **3.23**: Viscosity contours for the partial penetration A131 steel weld done with 5.0 kW laser power at a welding speed of 12.7 mm/s, for the y-z cross-sections at different locations along the welding direction, a) x = 2.83, b) x = 3.0 mm, c) x = 3.51 mm, and d) x = 3.97. Levels 1, 2, 3 and 4 correspond to 0.02 Pa-s, 0.05 Pa-s, 0.1 Pa-s and 0.2 Pa-s, respectively. Laser beam is located at x = 3 mm.

The fluid flow in the weld pool is turbulent because the flow satisfies Atthey's criteria [50] for turbulence in the weld pool: Reynolds number, $Re = (\rho u_m d/\mu) > 600$ where ρ is density, u_m is maximum velocity, d is pool width and μ is viscosity. Taking $\rho = 7200$ kg/m^3, $u_m = 0.4$ m/s, d = 0.004 m and $\mu = 0.006$ Pa-s, the value of Re is 3840. The turbulence in the weld pool is also evident, post-priori, from the results in Figure **3.23**. It is observed that the maximum value of the effective viscosity, μ_{eff} (= μ_t + μ), is about 30 times the laminar viscosity, μ. The symbol μ_t represents turbulent viscosity. The Turbulence Reynolds Number (TRN), defined as the ratio μ_t/μ is an

indicator of turbulence in the weld pool. Hong et al. [51] found the weld pool to be turbulent for a local value of TRN of 7.9. Since Figure **3.23** shows a maximum value of TRN of about 29, the weld pool is certainly turbulent.

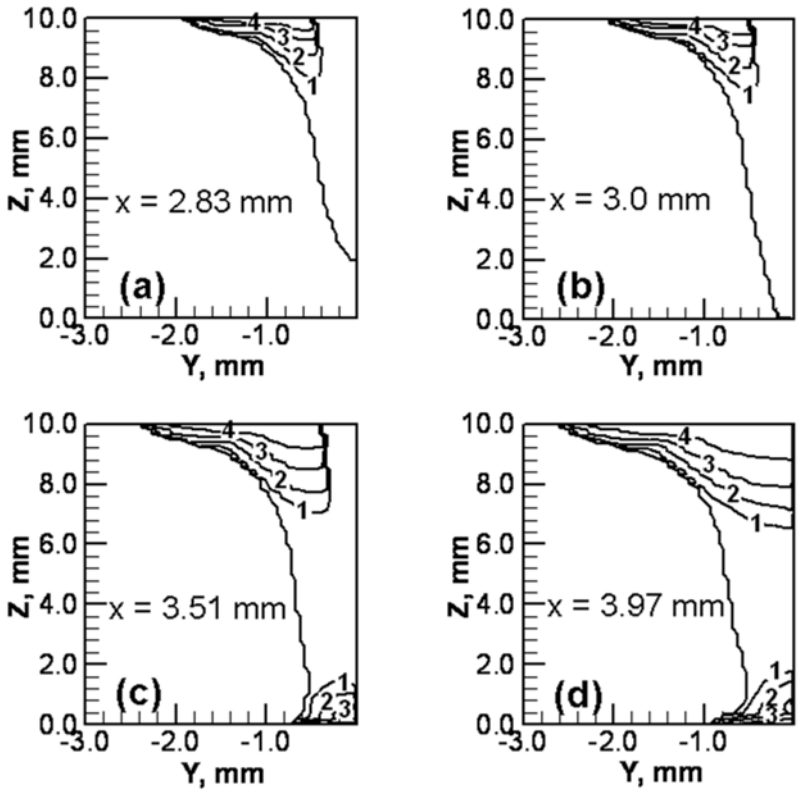

Figure **3.24**: Viscosity contours for the full penetration A131 weld done with 9.6 kW laser power at a welding speed of 12.7 mm/s, for the y-z cross-sections at different locations along the welding direction, a) x = 2.83, b) x = 3.0 mm, c) x = 3.51 mm, and d) x = 3.97 mm. Levels 1, 2, 3 and 4 correspond to 0.02 Pa-s, 0.05 Pa-s, 0.1 Pa-s and 0.2 Pa-s, respectively. Laser beam is located at x = 3 mm.

3.5.3.3 Solidification parameters

The solidification microstructure is affected by the solidification rate, R, thermal gradient, G, undercooling, ΔT, and the alloy composition. In this study, possible undercooling has been ignored and the solidification characteristics have been calculated

considering heat transfer and fluid flow in the weld pool. While G/R determines the solidification morphology, GR determines the scale of the solidification sub-structure. The values of these parameters have been used to understand the solidification structure. The solidification rate (R) under steady state conditions for linear laser welding is defined in terms of welding velocity (v) as follows [28]:

$$R = v \cos \beta \qquad (\mathbf{3.23})$$

where β is the angle between the welding direction and the normal at the solid-liquid boundary.

Figure **3.25** (a) shows the calculated temperature gradients for various laser powers. An increase in the laser power increases the weld pool length and the distance over which the temperature drops from the boiling point (at keyhole walls) to the solidus temperature. As a result, the average temperature gradient in the weld pool decreases as the laser power is increased. Figure **3.25** (b) shows the variation of the calculated temperature gradient with welding speed.

When the welding speed is varied, the temperature gradient in the weld pool is affected by two factors. First, with the increase in the welding speed the weld pool becomes more elongated resulting in lower average spatial temperature gradient. Second, due to the decrease in heat input per unit length with an increase in welding speed, the size of the weld pool decreases and the temperature gradient increases. For the conditions of the welding considered for Figure **3.25** (b), and the properties of A131 steel, the latter effect dominates and the temperature gradient increases with increase in welding speed.

The G/R ratio can be used to understand the nature of the solidification front. The criterion for plane front instability based on constitutional super-cooling is given by the following relation [52]:

$$G/R < \Delta T_E/D_L \qquad (\mathbf{3.24})$$

where ΔT_E represents the temperature difference between the solidus and liquidus temperatures of the alloy and D_L is the diffusivity of a solute in the liquid weld metal.

When this condition is not satisfied, a planar solidification front is obtained. For A131 steel, ΔT_E is 40 K, and D_L is the solute diffusion coefficient in pure liquid iron, which is of the order of 10^{-7} m^2/s for the diffusion of carbon [53]. Thus, $\Delta T/D_L$ is equal to 4×10^2 Ks/mm^2 for solute diffusion in A131 steel. Figure **3.26** (a) and (b) show the variation of G/R with the input power and welding speed respectively. The magnitude of G/R varies from 1.5 to 3.5 $K\text{-}s/mm^2$ and therefore the condition of plane front stability is not satisfied at the trailing edge of the weld pool for the range of process parameters considered. G/R decreases with an increase in input power (Figure **3.26** (a)) due to the increase in G, the temperature gradient at the trailing edge of the weld pool. The values of G/R do not vary significantly with the increase in welding speed (Figure **3.26** (b)) because the temperature gradient G and the solidification rate R increase with increase in welding speed. Thus, the solidification microstructure will become more dendritic with an increase in laser power. On the other hand, the change in welding speed will not have a significant effect over the range of experiments considered.

Figure **3.27** shows the variation of cooling rate, GR, with input laser power and welding speed. The cooling rate at the trailing edge of the weld pool is on the order of 1 K/ms for the range of experiments done. Moreover, the cooling rate decreases with an increase in laser power or decrease in welding speed. With an increase in welding speed, the temperature gradient G, as well as the solidification rate R at the trailing edge of the weld pool increase. However, with an increase in laser power, only the temperature gradient at the end of the weld pool decreases whereas the solidification rate remains same. Thus, the cooling rate GR changes more significantly with variation in welding speed than with variation in laser power. If the input laser power increases or the welding speed decreases, the heat input per unit length decreases in the work-piece. Thus, the microstructure will become coarser with an increase in the heat input per unit length.

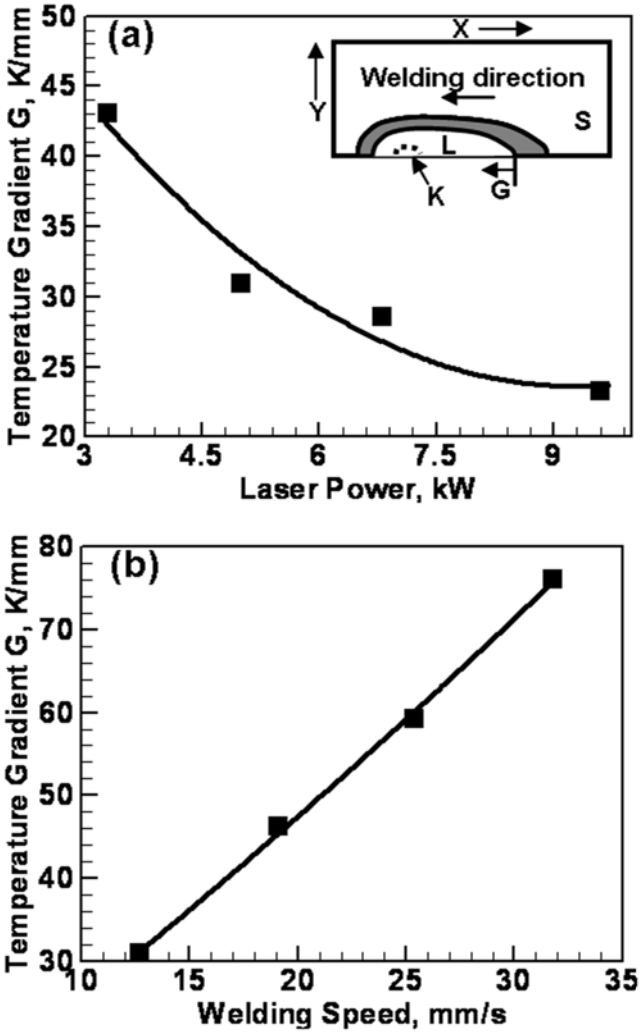

Figure **3.25**: Calculated values of G for A131 steel at the trailing edge on the weld center line at the surface for a) different input powers, at 12.7 mm/s welding speed and b) different welding speeds, at 5.0 kW input power. The symbols indicate the data from numerical simulation, while the solid line indicates the best fit line. The symbols K, L, S represent the keyhole, liquid, and solid regions respectively, and shaded region between L and S is the two phase solid-liquid region.

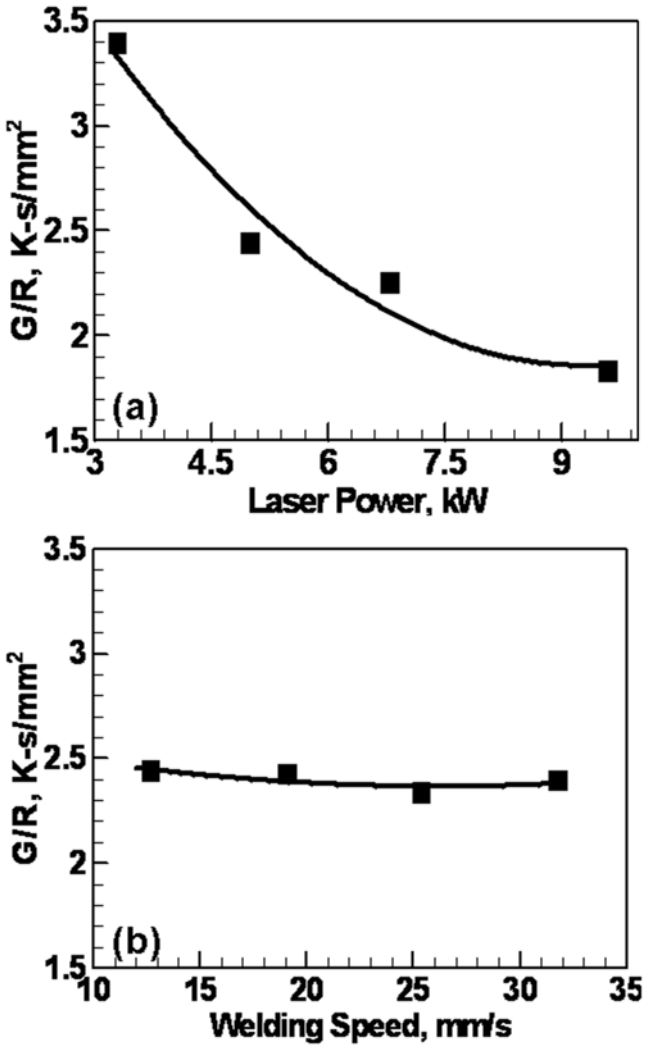

Figure **3.26**: Calculated values of G/R for A131 steel at the trailing edge on the weld center line for a) different input powers, at 12.7 mm/s welding speed and b) different welding speeds, at 5.0 kW input power. The symbols indicate the data from numerical simulation, while the solid line indicates the best fit line.

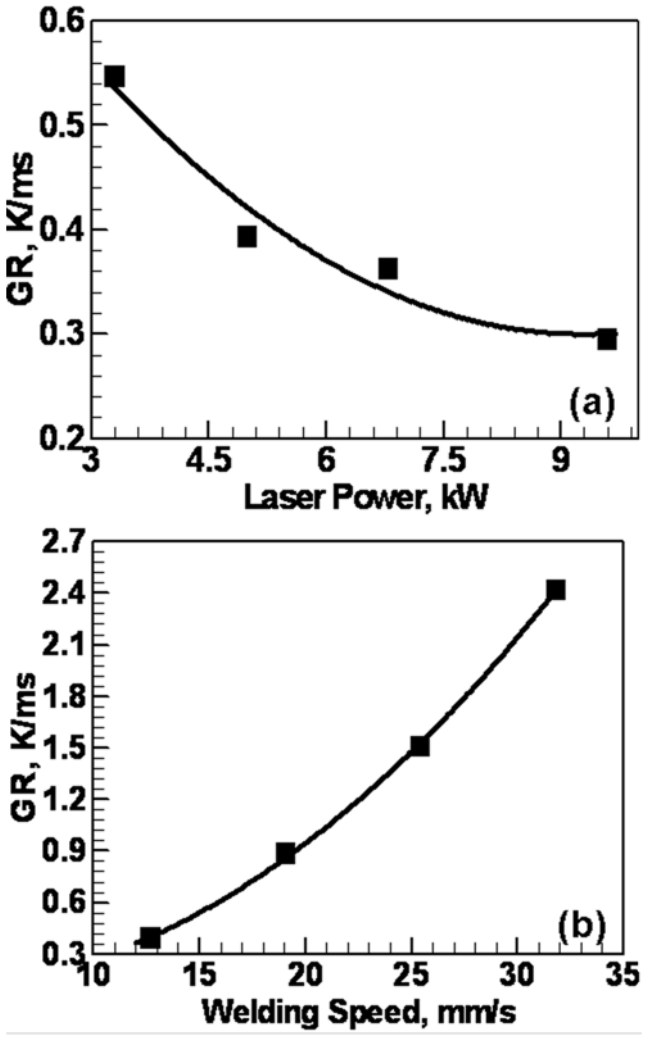

Figure **3.27**: Calculated values of GR for A131 steel at the trailing edge on the weld center line for a) different input powers, at 12.7 mm/s welding speed and b) different welding speeds, at 5.0 kW input power. The symbols indicate the data from numerical simulation, while the solid line indicates the best fit line.

3.5.3.4 Cooling rates

For partial penetration welds, the temperature contours converge towards the bottom of the keyhole. As shown in Figure **3.28** (a), the separation between any two temperature contours decreases with increasing depth. Thus, the cooling time from 1073

K to 773 K becomes small and the cooling rate becomes high near the bottom of the weld pool. On the other hand, the temperature contours are spread out near the bottom for a full penetration weld as shown in Figure **3.28** (b). Therefore, the cooling time from 1073 K to 773 K does not decrease significantly near the bottom of a full penetration weld and a much lower cooling rate is obtained. Figure **3.29** shows the average cooling rates from 1073 K to 773 K for a partial penetration and a full penetration weld at the symmetry plane at different z-locations.

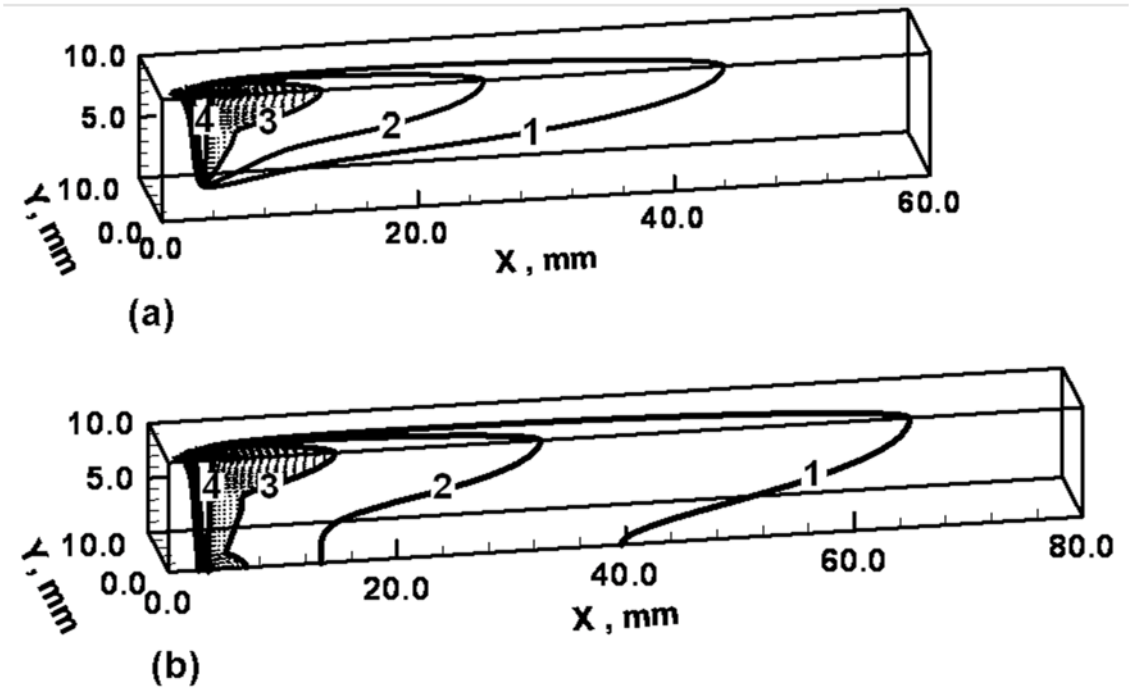

Figure **3.28**: Temperature contours for A131 steel welds a) partial penetration, 5000 W, 12.7 mm/s and b) full penetration, 9600 W, 12.7 mm/s. Levels 1, 2, 3 and 4 correspond to 773 K, 1073 K, 1745 K and 3100 K respectively.

The cooling rate is very high at the lower part of the partial penetration weld compared to the full penetration weld because of the difference in the shapes of temperature contours near the keyhole bottom. The lower cooling rates in the full penetration weld compared to the partial penetration weld can be attributed also to the larger heat input in the former. The trends for the variation of cooling rates with z-distance are also different for the two cases. For full penetration weld shown in

Figure **3.29** (a), the cooling rate reaches a minima somewhere between the top and the bottom surfaces. Therefore, the microstructure for the full penetration weld is expected to be coarser in the interior of the work-piece than near the top and the bottom surfaces. In the case of partial penetration welds, as shown in Figure **3.29** (b), the cooling rates monotonically increase with increasing distance from the top surface.

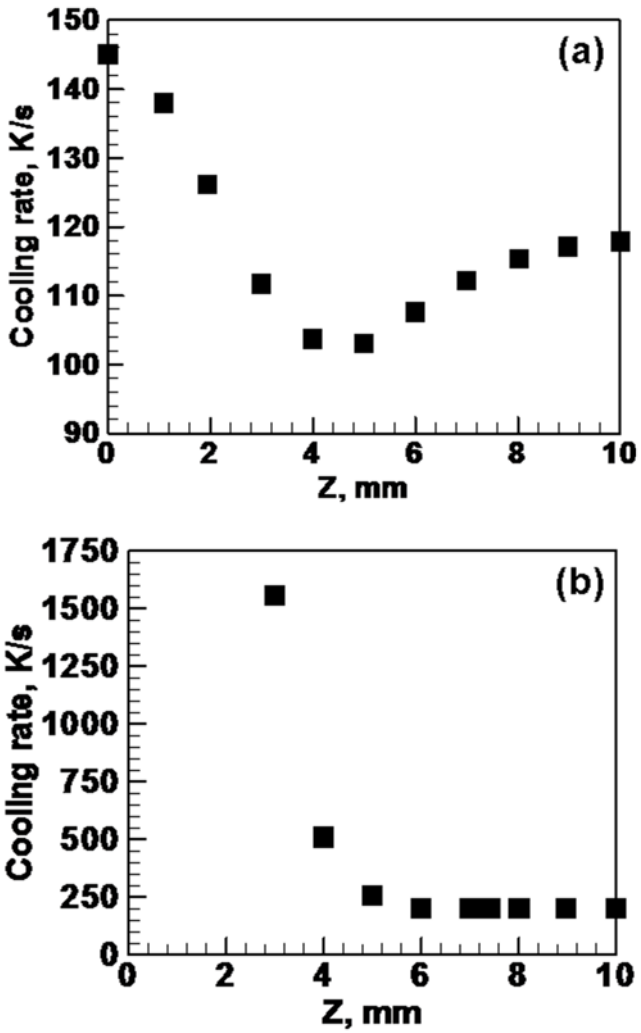

Figure **3.29**: Variation of the 1073 K to 773 K cooling rate at the symmetry plane with distance from the bottom surface, for A131 steel welds made at 12.7 mm/s welding speed and (a) 9600 W, full penetration weld b) 5000 W, partial penetration weld. z = 10 mm for the top surface.

3.5.3.5 Solidification microstructure

The cooling rates give an indication of the scale of microstructure of the welds. A higher cooling rate at the trailing edge of the weld pool, GR, indicates faster cooling at all location of the weldment. Relatively higher cooling rates result in finer microstructures as can be observed by comparing Figure **3.30** (a) with Figures **3.30** (b) and **3.31** (a). Figure **3.30** shows the microstructures for the highest (756 J/mm) and the lowest (157 J/mm) heat input per unit length used to make the welds. The heat input per unit length for Figure **3.30** (a) is 756 J/mm (9.6 kW laser power at 12.7 mm/s welding speed) and is several times higher than that for Figure **3.30** (b), which is 157 J/mm (5.0 kW laser power and 31.8 mm/s). Consequently, the cooling rate for the higher heat input weld was much slower than that for the lower heat input weld. This difference is apparent in the scale of the microstructures of the two cases.

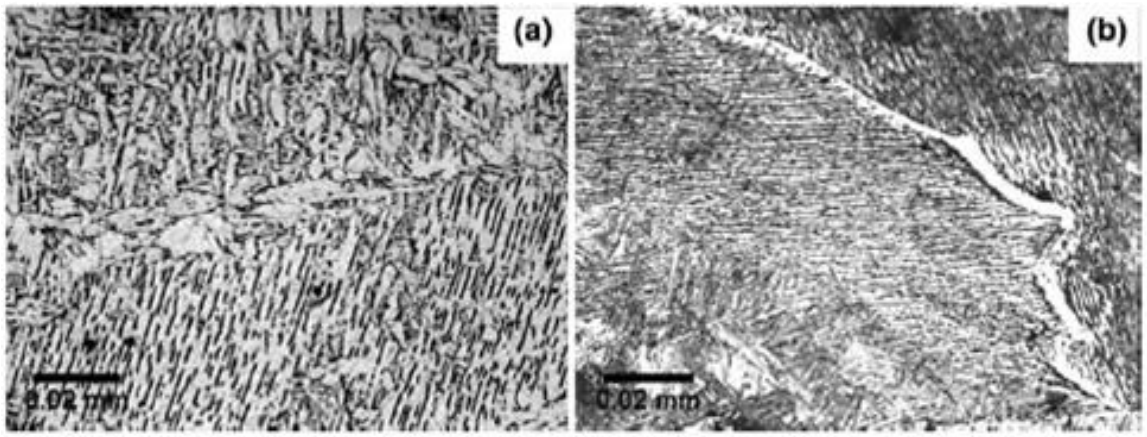

Figure **3.30**: Microstructural scale at the weld center line near the top surface for A131 steel welds made at a) 9.6 kW, 12.7 mm/s and b) 5.0 kW, 31.8 mm/s.

Figure **3.31** (a) and (b) show the microstructures near the bottom of a partial penetration weld (5 kW, 12.7 mm/s) and a full penetration weld (9.6 kW, 12.7 mm/s), respectively. The microstructure for the full penetration weld in Figure **3.31** (b) is much coarser than that for the partial penetration weld shown in Figure **3.31** (a). This difference in microstructure is due to the higher heat input per unit length and consequently much slower cooling in the full penetration case.

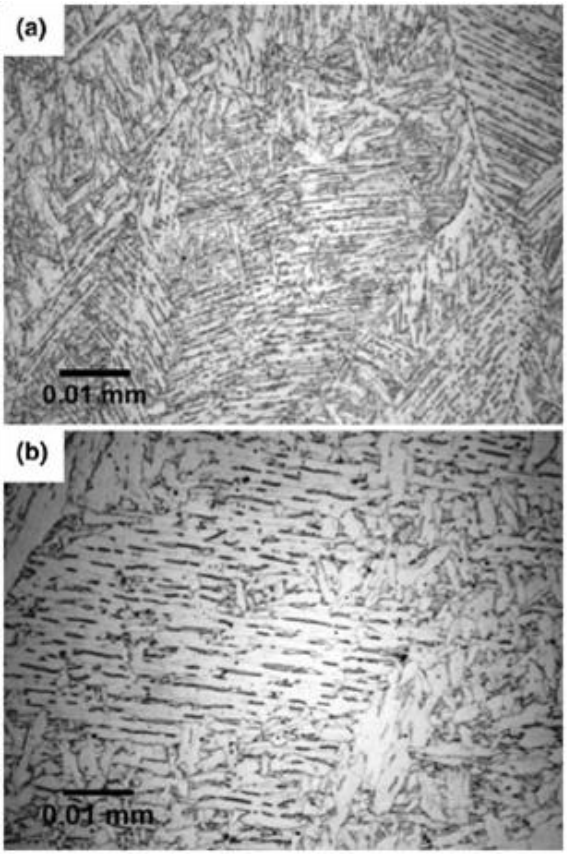

Figure **3.31**: A131 steel microstructure along the weld center-line a) near the bottom of a partial-penetration weld (5.0 kW, 12.7 mm/s) and b) near the bottom of a full-penetration weld (9.6 kW, 12.7 mm/s).

A continuous cooling transformation (CCT) diagram for a low alloy 0.2 % carbon steel, such as that shown in Figure **3.32**, can be used to predict the phases present in the microstructure [54]. From the figure, it can be seen that cooling rates greater than 100 K/s and less than about 600 K/s would result in ferrite plus martensite. Cooling rates higher than 600 K/s would result in mostly martensitic microstructure. Since the cooling rates at the weld center line in the full penetration A131 steel weld varied between 100 and 150 K/s with depth (Figure **3.29** (a)), the microstructure is expected to contain ferrite and martensite. The cooling rates at the weld center line in the partial penetration A131 steel weld varied from around 200 K/s near the top of the weld to around 1550 K/s near the bottom of the weld. Therefore, the microstructure near the weld center line is expected to contain ferrite and martensite near the top of the weld with the amount of

ferrite decreasing as the depth increases. Near the bottom of the partial penetration weld, where the cooling rates are very high, the microstructure is expected to be primarily martensitic.

The actual CCT diagram for A131 steel may differ from the diagram shown in Figure **3.32** because of slight differences in the carbon and alloy contents between the A131 steel and the low alloy carbon steel shown in the figure.

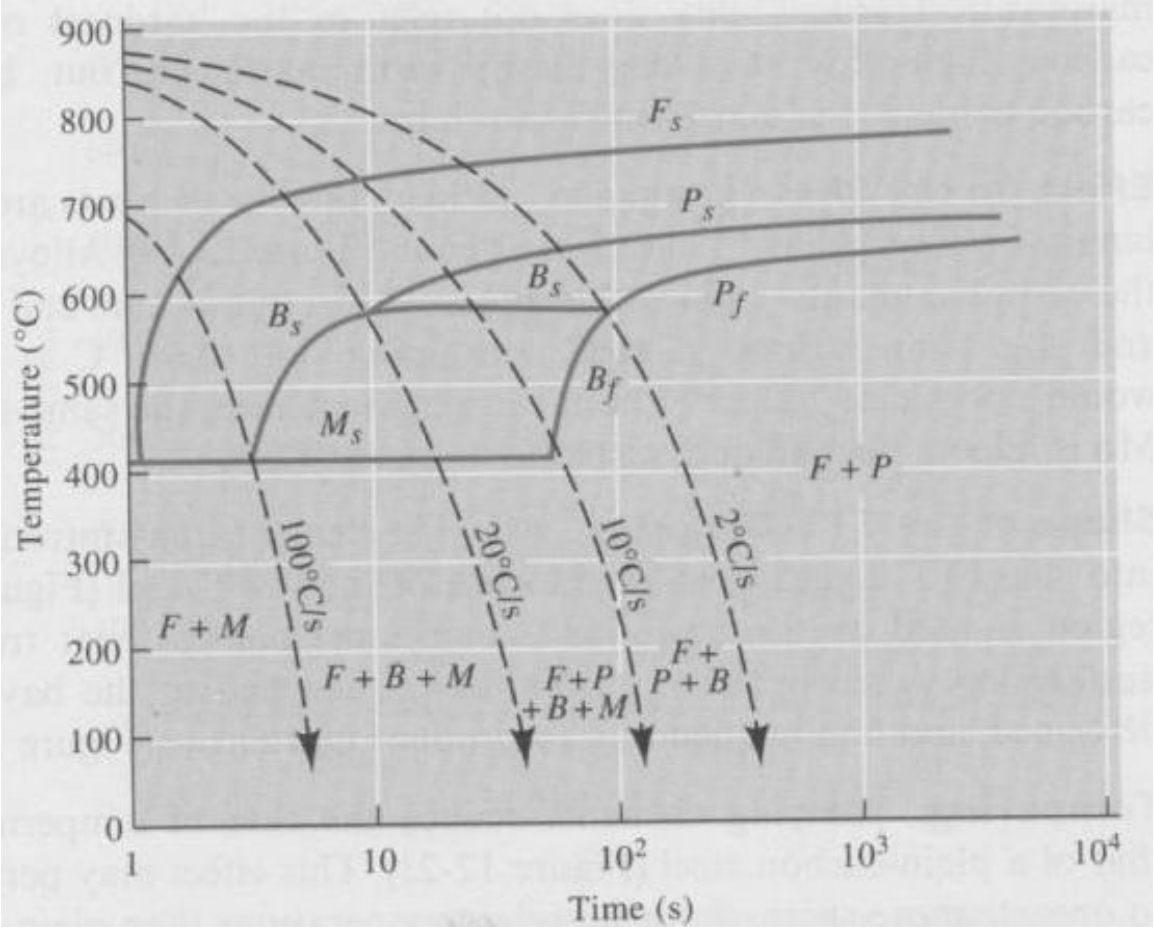

Figure **3.32**: Continuous cooling transformation diagram for a low alloy 0.2 % carbon steel. [54]

3.5.4 Free Surface Calculation

Figure **3.33** shows a transverse cross section of the weld pool located 1.6 mm behind the laser beam for A131 steel welds made with 9.6 kW laser power and 12.7 mm/s welding speed. A detailed description of the experiment is given in **3.2.1**, and the input process parameters are given in Tables **3.7** and **3.8**. The figure shows deformation of the weld pool surfaces under the action of recoil pressure of the metal vapors, surface tension forces, and the pressure due to metal column. The figure shows very little deformation of the top surface for the welding conditions considered. In contrast, there is a noticeable hump at the bottom surface where the melt pool area is much smaller and the hump forms because of the recoil pressure and the metallostatic head. Because of the much larger area of the top surface a small depression at the top surface provides enough metal to form the hump at the bottom surface. The free surface in the keyhole region is governed mainly by the instantaneous vaporization of the metal and the consequent energy balance at the keyhole walls. The free surface calculation here neglects the keyhole region and considers the much larger weld pool surface outside the keyhole. The change in density of material before and after the welding process due to phase changes was also neglected.

For an input laser power of 9.6 kW and absorption coefficient of 0.16, the power absorbed by a single reflection on the flat surface of the work piece is 1536 W. For the sake of comparison, this power is equivalent to an arc source of 10 V and 220 A with an arc efficiency of about 0.7. The arc pressure at a point (x,y) is given as [21, 55]:

$$P_{arc} = \frac{F}{2\pi\sigma^2}\exp\left(-\frac{x^2+y^2}{2\sigma^2}\right) \quad (N/mm^2) \qquad (\mathbf{3.25})$$

$$F = -0.04791 + 0.0002447 \times I \quad (N) \qquad (\mathbf{3.26})$$

$$\sigma = 1.4875 + 0.00123 \times I \quad (mm) \qquad (\mathbf{3.27})$$

where F is the total arc force, I = 220 A is the arc current and σ is the distribution parameter in mm. Figure **3.34** shows a comparison of the recoil pressure calculated for the laser welding with input laser power of 9.6 kW at 12.7 mm/s welding speed with the arc pressure due to an arc current of 220 A. For the conditions described above, the total

recoil force for laser welding process is much smaller than the arc force during arc welding process. For I = 220 A, σ = 1.758 mm and F = 0.005924 N. At the center of the arc spot, i.e. for x = y = 0, P_{arc} = 3.051 X 10^{-4} N/mm^2 or 305.1 Pa. As shown in Figure **3.34**, the recoil pressure for the laser welding process is smaller than the arc pressure. Moreover, considering enhanced absorption of the laser by the work-piece due to multiple reflections, higher arc current will be needed to produce an equivalent heat input during the arc welding process, resulting in higher arc pressure. This explains the relatively smaller top surface deformation during laser welding process as compared to an arc welding process with roughly the same heat input.

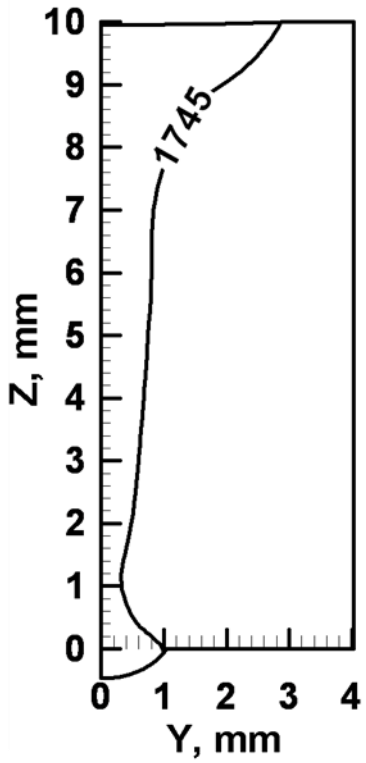

Figure **3.33**: Deformations of the top and bottom surfaces for A131 steel welds made at 9.6 kW laser power, 12.7 mm/s welding speed at a transverse section 1.6 mm behind the laser beam. The 1745 K contour marks the weld pool boundary.

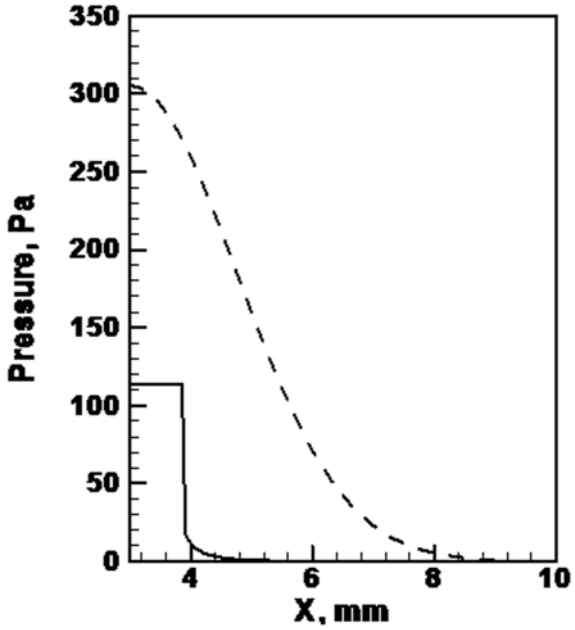

Figure **3.34**: Calculated pressure variation along the weld center line. The solid line is for laser welding with input laser power of 9600 W at 12.7 mm/s welding. The dotted line is the arc pressure for a welding current of 220 A. 3 mm is the starting location of the laser or arc.

3.6 Summary and Conclusions

A computationally efficient model of heat and fluid flow in keyhole mode laser welding was tested for a range of welding velocities and laser powers in partial and full penetration welds. The model was also tested for a range of materials including Al 5754 alloy, A131 structural steel, vanadium, tantalum, 304L stainless steel, and Ti-6Al-4V. The properties of these materials including the density, surface tension, and thermal conductivity display a range of values. For the calculation of turbulent viscosity, a model based on Prandtl's mixing length hypothesis was used under the assumption that the turbulent kinetic energy is a certain fraction of the mean kinetic energy. The model was used to predict weld geometry, temperature and velocity fields for partial and full penetration welds covering a wide range of welding variables.

Keyhole mode welding of the various materials considered in this study involved both low and high Peclet number systems representing different mechanisms of heat transfer in the weld pool. Convection was found to be the main mechanism of heat transfer in the laser welding of low thermal conductivity alloys like steels. The contribution of convection relative to conduction in the overall heat transfer was highest for 304L stainless steel and lowest for aluminum. The relative importance of these two mechanisms in the overall heat transfer depended on the thermal diffusivity and temperature coefficient of surface tension of the metals and alloys studied. Compared to 304L stainless steel, heat transfer by conduction was more significant for aluminum due to its high thermal diffusivity and lower temperature coefficient of surface tension.

The thermo-physical properties of the metals/alloys have a significant impact on both the weld penetration and shape. These properties, including the temperature coefficient of surface tension, affected the weld pool shape through their influence on the heat transport process. Convective heat transfer was more important in the low thermal conductivity materials like steel. These welds tend to have a fusion zone with a pronounced spread near the weld pool surfaces due to surface tension driven convective currents. On the other hand, for high thermal conductivity Al 5754 alloy, convective heat transfer was less important. Therefore, the weld pool width gradually decreased from the top surface to the bottom. High boiling and melting points, and high solid state thermal diffusivity of tantalum resulted in smaller weld pools compared to the other materials studied. The computed weld geometries were in good agreement with the corresponding experimentally determined values for the welding of both the alloys.

Turbulence was found to be more important in regions near the top surface for partial penetration welds and for both the top and bottom surfaces for the full penetration welds, as indicated by the high turbulent viscosity values. Free surface calculations showed a hump at the bottom surface of the full penetration weld. The calculated top surface deformation was very small.

The calculation of solidification parameters indicated that plane front solidification criterion was not satisfied at the trailing edge of the weld pool for the alloys and the experimental conditions considered in the present study. The values of the solidification

parameters depend on the physical properties of the material and varied with the input power and welding speed. The calculated solidification parameters and cooling rates were related to the weld microstructure for partial and full penetration welds. Cooling rates were lower at the bottom of the full penetration weld compared to the bottom of the partial penetration weld.

The model was computationally efficient and could be applied to the calculation of temperatures, and velocities, weld pool geometry and solidification parameters for materials with wide ranging properties and under varying process conditions. The results show that a computationally efficient 3D convective heat transfer model of keyhole mode laser welding, embodying a keyhole geometry sub-model and a methodology of convective heat transfer calculations perfected over decades in fusion welding, can significantly improve the current understanding of keyhole welding of different materials with widely different thermo-physical properties.

3.7 References

[1] Andrews JG, Atthey DR. Hydrodynamic Limit to Penetration of a Material by a High-Power Beam. J. Phys. D-Appl. Phys. 1976;9:2181.
[2] Mazumder J, Steen WM. Heat-Transfer Model for Cw Laser Material Processing. J. Appl. Phys. 1980;51:941.
[3] Postacioglu N, Kapadia P, Davis M, Dowden J. Upwelling in the Liquid Region Surrounding the Keyhole in Penetration Welding with a Laser. J. Phys. D-Appl. Phys. 1987;20:340.
[4] Dowden J, Postacioglu N, Davis M, Kapadia P. A Keyhole Model in Penetration Welding with a Laser. J. Phys. D-Appl. Phys. 1987;20:36.
[5] Kroos J, Gratzke U, Simon G. Towards a Self-Consistent Model of the Keyhole in Penetration Laser-Beam Welding. J. Phys. D-Appl. Phys. 1993;26:474.
[6] Kroos J, Gratzke U, Vicanek M, Simon G. Dynamic Behavior of the Keyhole in Laser-Welding. J. Phys. D-Appl. Phys. 1993;26:481.
[7] Kaplan A. A Model of Deep Penetration Laser-Welding Based on Calculation of the Keyhole Profile. J. Phys. D-Appl. Phys. 1994;27:1805.
[8] Trappe J, Kroos J, Tix C, Simon G. On the Shape and Location of the Keyhole in Penetration Laser-Welding. J. Phys. D-Appl. Phys. 1994;27:2152.
[9] Sudnik W, Radaj D, Erofeew W. Computerized simulation of laser beam welding, modelling and verification. J. Phys. D-Appl. Phys. 1996;29:2811.

[10] Solana P, Ocana JL. A mathematical model for penetration laser welding as a free-boundary problem. J. Phys. D-Appl. Phys. 1997;30:1300.
[11] Zhao H, DebRoy T. Macroporosity free aluminum alloy weldments through numerical simulation of keyhole mode laser welding. J. Appl. Phys. 2003;93:10089.
[12] Ki H, Mohanty PS, Mazumder J. Modeling of laser keyhole welding: Part I. Mathematical modeling, numerical methodology, role of recoil pressure, multiple reflections, and free surface evolution. Metallurgical and Materials Transactions a-Physical Metallurgy and Materials Science 2002;33:1817.
[13] Ki H, Mohanty PS, Mazumder J. Modeling of laser keyhole welding: Part II. Simulation of keyhole evolution, velocity, temperature profile, and experimental verification. Metallurgical and Materials Transactions A-Physical Metallurgy and Materials Science 2002;33:1831.
[14] Ki H, Mohanty PS, Mazumder J. Multiple reflection and its influence on keyhole evolution. J. Laser Appl. 2002;14:39.
[15] Lee JY, Ko SH, Farson DF, Yoo CD. Mechanism of keyhole formation and stability in stationary laser welding. J. Phys. D-Appl. Phys. 2002;35:1570.
[16] Zhou J, Tsai HL, Lehnhoff TF. Investigation of transport phenomena and defect formation in pulsed laser keyhole welding of zinc-coated steels. J. Phys. D-Appl. Phys. 2006;39:5338.
[17] Zhou J, Tsai HL, Wang PC. Transport phenomena and keyhole dynamics during pulsed laser welding. Journal of Heat Transfer-Transactions of the ASME 2006;128:680.
[18] Palmer TA, Elmer JW, Pong R, Gauthier MD. Welding of Vanadium, Tantalum, 304L and 21-6-9 Stainless Steels, and Titanium alloys at Lawrence Livermore National Laboratory using a fiber delivered 2.2 kW diode pumped CW Nd:YAG Laser. Livermore, CA: Lawrence Livermore National Laboratory 2004.
[19] Patankar SV. Numerical Heat Transfer and Fluid Flow. New York: Hemisphere Publishing Corporation, 1980.
[20] Bird RB, Stewart WE, Lightfoot EN. Transport Phenomena. New York: Wiley, 1960.
[21] Zhang W, Kim CH, DebRoy T. Heat and fluid flow in complex joints during gas metal arc welding - Part I: Numerical model of fillet welding. J. Appl. Phys. 2004;95:5210.
[22] Zhang W, Kim CH, DebRoy T. Heat and fluid flow in complex joints during gas metal arc welding - Part II: Application to fillet welding of mild steel. J. Appl. Phys. 2004;95:5220.
[23] Kim CH, Zhang W, DebRoy T. Modeling of temperature field and solidified surface profile during gas-metal arc fillet welding. J. Appl. Phys. 2003;94:2667.
[24] Kou S, Sun DK. Fluid-Flow and Weld Penetration in Stationary Arc Welds. Metallurgical Transactions A-Physical Metallurgy and Materials Science 1985;16:203.
[25] Kumar A, DebRoy T. Calculation of three-dimensional electromagnetic force field during arc welding. J. Appl. Phys. 2003;94:1267.
[26] Voller VR, Prakash C. A Fixed Grid Numerical Modeling Methodology for Convection Diffusion Mushy Region Phase-Change Problems. International Journal of Heat and Mass Transfer 1987;30:1709.

[27] Brent AD, Voller VR, Reid KJ. Enthalpy-Porosity Technique for Modeling Convection-Diffusion Phase-Change - Application to the Melting of a Pure Metal. Numerical Heat Transfer 1988;13:297.
[28] He X, Elmer JW, DebRoy T. Heat transfer and fluid flow in laser microwelding. J. Appl. Phys. 2005;97:9.
[29] He X, DebRoy T, Fuerschbach PW. Probing temperature during laser spot welding from vapor composition and modeling. J. Appl. Phys. 2003;94:6949.
[30] De A, DebRoy T. A smart model to estimate effective thermal conductivity and viscosity in the weld pool. J. Appl. Phys. 2004;95:5230.
[31] De A, DebRoy T. Probing unknown welding parameters from convective heat transfer calculation and multivariable optimization. J. Phys. D-Appl. Phys. 2004;37:140.
[32] Elmer JW, Palmer TA, Zhang W, Wood B, DebRoy T. Kinetic modeling of phase transformations occurring in the HAZ of C-Mn steel welds based on direct observations. Acta Mater. 2003;51:3333.
[33] Wilcox DC. Turbulence Modeling for CFD. California: DCW Industries, 1993.
[34] Launder BE, Spalding DE. Lectures in Mathematical Models of Turbulence. NY: Academic Press, 1972.
[35] Hong K. Ph.D. dissertation. Waterloo: University of Waterloo, 1996. p.145.
[36] Yang Z, Debroy T. Modeling macro-and microstructures of gas-metal-arc welded HSLA-100 steel. Metallurgical and Materials Transactions B-Process Metallurgy and Materials Processing Science 1999;30:483.
[37] Ketter RL, Prawel SP. Modern Methods of Engineering Computation. New York: McGraw Hill, 1969.
[38] Brandes EA, Brook GB, editors. Smithells Metals Reference Book. MA: Butterworth Heinemann, 1992.
[39] Lide DR, editor CRC Book of Chemistry and Physics. FL: CRC Press, 2000.
[40] Mills KC. Recommended Values of Thermophysical Properties of Selected Commercial Alloys. Materials Park, OH: ASM, 2002.
[41] Iida T, Guthrie RIL. The Physical Properties of Liquid Metals Oxford: Clarendon Press, 1988.
[42] Ho CY, Touloukian YS, editors. Thermophysical Properties of Matter: Specific Heat. New York: IFI/Plenum: Purdue University, 1977.
[43] Chase MW, editor Thermochemical Tables: NIST-JANAF. Melville, NY: American Institute of Physics, 1998.
[44] Kaye GWC, Laby TB, editors. Tables of Physical and Chemical Constants. London: Longman, 1995.
[45] Yaws CL. Handbook of Thermal Conductivity. Houston: Gulf Publishing, 1997.
[46] Ho CY, Touloukian YS, editors. Thermophysical Properties of Matter: Thermal Conductivity. New York: IFI/Plenum: Purdue University, 1977.
[47] Ho CY, Liley PE, Power RW, editors. National Standard Reference Data Series: No. 16: Thermal Conductivity of Selected Materials, Pt. 2, USGPO. Washington D.C.: National Bureau of Standards, 1968.
[48] Mishra S, DebRoy T. Measurements and Monte Carlo simulation of grain growth in the heat-affected zone of Ti-6Al-4V welds. Acta Mater. 2004;52:1183.

[49] Turkdogan ET. Physical Chemistry of High Temperature Technology. New York: Academic Press, 1980.
[50] Atthey DR. A Mathematical-Model for Fluid-Flow in a Weld Pool at High Currents. Journal of Fluid Mechanics 1980;98:787.
[51] Hong K, Weckman DC, Strong AB, Zheng W. Modelling turbulent thermofluid flow in stationary gas tungsten arc weld pools. Science and Technology of Welding and Joining 2002;7:125.
[52] Debroy T, David SA. Physical Processes in Fusion-Welding. Reviews of Modern Physics 1995;67:85.
[53] Geiger H, Poirier DR. Transport Phenomena in Metallurgy. London: Addison Wesley, 1973.
[54] Askeland DR. The Science and Engineering of Materials. Boston: PWS Publishing Company, 1994.
[55] Lin ML, Eagar TW. Pressures Produced by Gas Tungsten Arcs. Metallurgical Transactions B-Process Metallurgy 1986;17:601.

Chapter 4

Heat Transfer and Fluid Flow in Electron Beam Welding

4.1 Introduction

Although both laser and electron beams (EB) are used for deep penetration welds, there are some important differences in the two welding processes. Laser beam welding (LBW) is generally conducted at atmospheric pressure, whereas electron beam welding (EBW) is commonly conducted under vacuum levels of about 10^{-5} torr. Within the keyhole, the pressure exerted by metal vapors on the wall balances the pressure due to surface tension and hydrostatic force. The wall temperatures can be evaluated from the pressure of metal vapors in the keyhole and the equilibrium pressure versus temperature relationship for the given alloy. As these forces vary with depth, the equilibrium wall temperature also varies with depth.

Assuming that the keyhole is filled with metal vapors, the variation of wall temperature with depth in LBW is likely to be small compared to the variation in EBW (see Appendix A). In LBW, the keyhole wall temperatures can be assumed to be equal to the normal boiling point of the alloy at all depths [1-5]. On the other hand, during EBW conducted under vacuum, there can be significant variation of wall temperatures with depth [6, 7]. The variation of temperature on the keyhole walls in EBW may result in significant Marangoni convection currents along the keyhole walls and affect the convective heat transfer within the weld pool.

As discussed in Chapter 2, several of the numerical models available for keyhole mode welding often include simplifications to minimize the computational effort [1, 2, 5, 8-15]. These simplifications include, but are not limited to, the assumption of a pre-defined axi-symmetric keyhole geometry, ignoring convective heat transfer, and two dimensional (2D) approximation to the three dimensional (3D) problem. The simplifications limit the applicability of a numerical model in terms of the range of process parameters (low welding speeds) or the range of thermo-physical properties of

the materials (low thermal conductivity). On the other hand, the comprehensive 3D models of keyhole mode welding are computationally intensive and require a lot of time to complete the calculations [16-21]. Furthermore, most of the available models have been designed for LBW.

Very few models are available in literature that specifically address keyhole mode EBW [7, 14, 22-26]. Therefore, there is a need for a 3D heat transfer and fluid flow model for EBW that is widely applicable in terms of welding conditions and work-piece materials. In the previous chapter, a computationally efficient model of keyhole mode laser welding was developed that can be applied to materials with wide ranging properties and under wide ranging process conditions. Here, a computationally efficient 3D numerical model of heat transfer and fluid flow in keyhole mode EBW has been developed and validated. The model takes into account the variation of wall temperature with depth and the resulting surface tension gradient driven fluid flow on keyhole walls. Enhancement of EB absorption due to multiple reflections has been treated by calculating an average location independent enhanced absorption coefficient based on the keyhole geometry [2, 5].

Experimental work involving Ti-6Al-4V, 21Cr-6Ni-9Mn stainless steel, and 304L stainless steel was performed at both Los Alamos National Laboratory (LANL) and Lawrence Livermore National Laboratory (LLNL). Ti-6Al-4V and 21Cr-6Ni-9Mn stainless steel welds were made at two different input powers. Since the power density distribution is a very important parameter in the EBW process, the model was applied to 304L stainless steel welds made with fixed input power and welding speed but different power density distributions. The power density distribution was varied by changing the focal spot radius which was, in turn, varied by changing the work distance and then refocusing the EB to a sharp spot on the work-piece surface. The increase in the focal spot diameter with increasing work distance affects the geometry of the weld pool [27].

The numerically computed fusion zone geometries were compared with the corresponding experimentally determined values for each weld. For the Ti-6Al-4V and 21Cr-6Ni-9Mn steel welds, temperatures at several monitoring locations in the specimens were measured as a function of time during welding. The computed thermal cycles were

compared with the experimentally observed thermal cycles for these two alloys. Weld geometries were calculated for EB and LB welds for similar process parameters except for the difference in ambient pressure conditions.

4.2 Experiments

4.2.1 Power variation: 21Cr-6Ni-9Mn steel and Ti-6Al-4V welds

EB welds were made on 21Cr-6Ni-9Mn stainless steel and Ti-6Al-4V samples at 17 mm/s welding speed and two different power levels each at LANL. The sample thickness was 6.45 mm for 21Cr-6Ni-9Mn stainless steel and 7.13 mm for Ti-6Al-4V. The composition of 21Cr-6Ni-9Mn stainless steel was 0.044 % C, 19.77 % Cr, 7.06 % Ni, 9.53 % Mn, 0.39 % Si, 0.29 % N, 0.16 %, Mo, 0.022 % P, 0.001 % S, and balance Fe. The composition of Ti-6Al-4V alloy was 5.8 % Al, 4.04 % V, 0.0077 % C, 0.096 % O, 0.0036 % N, 0.12 % Fe, 0.0048 % H, and 89.9 % Ti.

For these welds, the work distance was 244.5 mm and chamber pressure was approximately 4×10^{-5} torr. The EB currents were 3.7 mA and 7.4 mA for 21Cr-6Ni-9Mn stainless steel, and 5.0 mA and 10.0 mA for Ti-6Al-4V, at 110 kV. Four 0.02 mm diameter type K thermocouples, made of positive Chromel (90 % Ni, 10 % Cr) wire and negative Alumel (95 % Ni, 2 % Mn, 2 % Al, and 1 % Si) wire, were used to record thermal cycles. The thin thermocouples were chosen to accurately record the rapid temperature changes. The thermocouples were spot-welded at (i) y = +1.5 mm, top surface, (ii) y = -1.5 mm, top surface, (iii) y = 2.5 mm, top surface, and (iv) y = 0 mm, bottom surface where y indicates the distance from the weld center line. The plate was clamped on the four corners with 6.35 mm space under each corner in order to thermally isolate the bottom of the plate from the holding fixture. The EB radius at sharp focus was measured to be about 0.12 mm for 21Cr-6Ni-9Mn stainless steel welds and 0.13 mm for Ti-6Al-4V alloy welds.

4.2.2 Power density variation: 304L stainless steel welds

Autogenous EB welds were made for us on 9.5 mm thick 304L stainless steel samples at a power of 1000 W (100 kV, 10 mA) and a welding speed of 17 mm/s at LLNL. The stainless steel work-piece had a composition of 18.2 % Cr, 8.16 % Ni, 1.71 % Mn, 0.02 % C, 0.082 % N, 0.47 % Mo, 0.44 % Si, 0.14 % Co, 0.35 % Cu, 0.0004 % S, 0.03 % P, and balance Fe. Six welds were made using a sharply focused beam at different work distances. The resulting weld pool cross-sections were polished and etched with electrolytic oxalic acid solution to provide the outline of the fusion zone boundary. Image Pro, Version 4.1 was then used to measure the weld dimensions [27].

The sharp focus condition was determined at LLNL using an Enhanced Modified Faraday Cup (EMFC) device to ensure a more consistent and quantified beam focus than is possible using conventional manual techniques [27]. The EMFC device samples the beam as it passes through 17 linear slits placed radially around a tungsten slit disk and converts them into voltage drops across a known resistor. A computer assisted tomographic (CT) imaging algorithm is then used to reconstruct the power density distribution of the beam using the data from the 17 linear slits. From the reconstructed beam, the peak power density, full width of the beam at half of its peak intensity (FWHM), and the full width of the beam at $1/e^2$ of the peak intensity (FWe2) are measured. The beam radius was taken to be ½ of the FWe2 value measured by the EMFC. Figure **4.1** shows the beam shape obtained at sharp focus and 229 mm work distance from EB welder model number SN/175 manufactured by Hamilton Standard [27]. Since the beam has an elliptical shape, the effective value of the beam radius was taken as the radius of a circle with an area equal to the actual beam spot. The beam shape and radius may vary with distance from the focal plane which can affect the weld geometry. The beam divergence depends on the work-distance and is likely to be small for large work-distances. Due to lack of data on the divergence of beam near the focal plane, its effect has been neglected in this work.

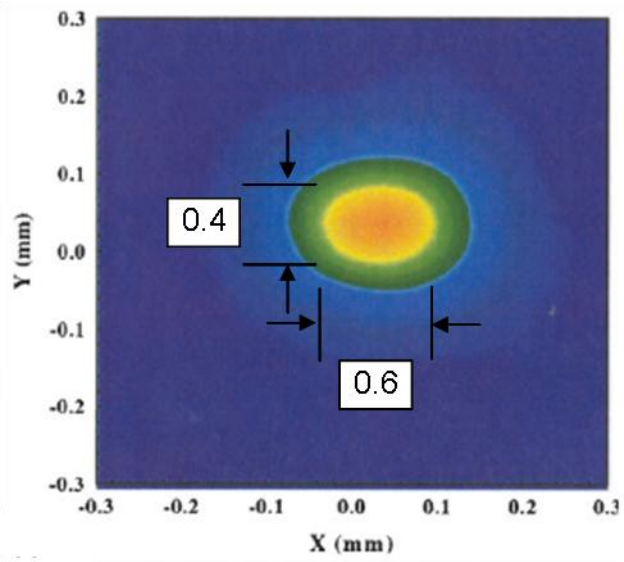

Figure **4.1**: Beam shape for 0.17 mm beam radius produced at sharp focus settings for 1000 W power at work distance of 229 mm.

4.3 Mathematical model

Quasi-steady state has been assumed for the welding process. The transient fluctuations of the vapor cavity have been neglected.

4.3.1 Calculation of keyhole geometry

The calculation of keyhole geometry for EBW is based on an energy balance at the keyhole walls similar to LBW model described in Chapter 3. However, instead of assuming constant keyhole wall temperature, the wall temperatures in the EBW model are iteratively calculated at each depth. The temperature gradient in the vertical direction is small compared to that along any direction in the horizontal plane. Therefore, the heat transfer in the vertical direction is small. In other words, for the purpose of calculating the keyhole geometry, it is assumed that heat transfer takes place mainly along horizontal

planes. However, the temperature gradient on the keyhole walls along the vertical direction is still sufficient to generate surface tension driven flow along the keyhole walls in the vertical direction.

A balance between the surface tension force $\gamma(T)/r(z)$, the hydrostatic force due to the liquid head ρgz, and the pressure of metal vapors 'p' keeps the keyhole open. The force balance at the vapor/liquid interface is given as follows:

$$p = \rho gz + \gamma(T)/r(z) \qquad (\mathbf{4.1})$$

where ρ is the density, g is the acceleration due to gravity, $\gamma(T)$ is the temperature dependent surface tension and r(z) is the keyhole radius at distance z from the top surface. The decrease in r(z) with increasing depth in the keyhole results in an increase in the surface tension force. As a result, the vapor pressure required to keep the keyhole open increases with depth. Thus, the vapor pressure at various depths in the keyhole can be calculated from the above equation. The temperature at the keyhole wall at any depth can then be calculated from the equilibrium temperature versus pressure relation for the liquid-vapor interface.

The keyhole geometry is iteratively calculated by first assuming a constant temperature equal to the normal boiling point of the alloy at 1 atmosphere on the keyhole walls. The wall temperature is modified in subsequent iterations by calculating the vapor pressure required to balance the surface tension and the hydrostatic force at the keyhole wall at all depths. Using this calculated vapor pressure, the wall temperature is then determined through equilibrium temperature versus pressure relation. Thus, the wall temperatures are corrected with each iteration, and the calculations continue until the change in keyhole depth with each additional iteration becomes less than 10^{-4} mm, at which point the calculations are assumed to have converged.

During calculation of the keyhole geometry, all temperatures inside the keyhole were assigned the wall temperature at that depth, for the identification of the keyhole. At each horizontal *xy* plane, where x is the direction of welding, the keyhole boundary was identified by both minimum and maximum *x* values for any given *y* value. The steps in the calculation of keyhole geometry are summarized as follows:

1. The keyhole geometry is calculated based on an energy balance at the liquid-vapor interface and the assumption of planar heat conduction. For the first iteration, the keyhole wall temperature at all locations is taken as the normal boiling point of the alloy at 1 atm.
2. After calculating the keyhole geometry, the vapor pressure at any depth inside the keyhole is calculated from a force balance (Eq. **4.1**) involving the vapor pressure, hydrostatic force, and surface tension force at the liquid-vapor interface. The keyhole radius r(z) is taken as half of the distance between the front and rear keyhole walls (the two keyhole locations on the vertical plane containing the welding direction) at distance 'z' from the top surface.
3. Equilibrium pressure versus temperature relation for the given alloy is used to calculate the wall temperatures at all depths.
4. Steps 1-3 are repeated a few times with improved values of wall temperatures. The iterations are stopped when the keyhole depth becomes constant with iterations.

4.3.2 Fluid flow and heat transfer

The fluid flow and heat transfer model is described in Chapter 3. Since the temperature difference between the top and the bottom of the keyhole can be a few hundred degrees, the Marangoni stress boundary condition has been applied. The w-velocity boundary condition along the keyhole walls is therefore given as:

$$\mu \frac{\partial w}{\partial n} = \frac{d\gamma}{dT} \frac{\partial T}{\partial z} \qquad (\mathbf{4.2})$$

where n is the direction vector normal to the keyhole surface into the vapor region.

4.3.3 Calculation methodology

1. Keyhole geometry is calculated iteratively based on energy and pressure balance at keyhole walls.
2. The calculated keyhole geometry is mapped onto a coarser mesh for the solution of 3D heat transfer and fluid flow. Temperatures within the keyhole at any depth are assigned the final wall temperature value calculated at that depth during keyhole geometry calculations.
3. The mass, momentum and energy conservation equations are solved assuming fixed wall temperatures and zero mass flux across the keyhole walls. A turbulence model is used to enhance the viscosity and thermal conductivity in the liquid region.

4.4 Results and Discussion

4.4.1 Model Validation

The 3D EB heat transfer and fluid flow model has been validated with 21Cr-6Ni-9Mn stainless steel, 304L stainless steel, and Ti-6Al-4V alloy welds. Calculated weld geometries and thermal cycles at specific locations were compared with experimental results for 21Cr-6Ni-9Mn stainless steel and Ti-6Al-4V alloy welds made with different power levels. The calculated and experimental weld geometries were also compared for 304L stainless steel welds made with the same heat input but different power density distributions. The experimental conditions are described in section **4.2**. The data used for calculations is given is Tables **4.1** and **4.2**. Constant temperature-independent thermal conductivities of solid and liquid phases were used for 21Cr-6Ni-9Mn stainless steel and Ti-6Al-4V. For the 304L stainless steel calculations, temperature-dependent thermal conductivity values were used for the calculations. Thermal conductivity data for the solid phase were available up to a temperature of 1273 K. Above this temperature,

thermal conductivity values for the solid phase were estimated based on linear extrapolation of the experimental data for 304L stainless steel [28]. For the liquid phase, thermal conductivity was calculated based on Wiedemann-Franz relation, which states that the ratio of thermal conductivity to the product of temperature and electrical conductivity is a constant [29]. The electrical conductivity of liquid stainless steel was taken as the electrical conductivity of liquid iron at its theoretical melting point, which was close to the value obtained by extrapolating the data for electrical resistivity of 18Cr-8Ni steel between 300 K and 1273 K to the liquidus temperature [30].

Table **4.1**: Data used for keyhole calculations.

Physical Property	21-6-9 SS	304L SS	Ti-6Al-4V
Boiling point at 1 atm, (K) [30]	2881	3100	3315
Density of liquid at boiling point, (kg/m^3) [30-33]	5800	5800	3780
Specific heat of liquid at boiling point, (J/kg K) [30, 31, 34-36]	800	800	730
Thermal conductivity of liquid at boiling point, (W/m-K) [28, 31, 35, 37, 38]	32	--	37
Laser beam absorption coefficient, η	0.24	--	0.24
EB absorption coefficient, η [39]	0.25	0.2	0.25
Laser beam radius, mm	0.23	--	0.23
Electron beam radius, mm	0.15	*	0.17
Change in laser beam radius with depth, (mm/mm)	0.045	--	0.045
Change in electron beam radius with depth, (mm/mm)	0.00	0.00	0.00
Plasma attenuation coefficient for laser, (m^{-1})	100	--	100
Plasma attenuation coefficient for e-beam, (m^{-1})	10	10	10

* Values depended on work-distance.

Table **4.2**: Data used for fluid flow calculations.

Physical Property	21-6-9 SS	304L SS	Ti-6Al-4V
Solidus temperature, (K) [34, 40]	1697	1697	1878
Liquidus temperature, (K) [34, 40]	1727	1727	1928
Density of liquid (kg/m^3) [30, 40]	7000	7000	4000
Specific heat of solid, (J/kg K) [34, 40]	712	712	670
Specific heat of liquid, (J/kg K) [34, 40]	800	800	730
Thermal conductivity of liquid, (W/m-K)[28, 31, 35, 37, 38]	29	---	29
Thermal conductivity of solid, (W/m-K) [28, 31, 35, 37, 38]	29	---	21
Viscosity, (Pa-s) [34, 40]	0.007	0.007	0.005
Coefficient of thermal expansion, (1/K) [30]	1.96×10^{-5}	1.96×10^{-5}	8×10^{-6}
Temperature coefficient of surface tension, (N/m K) [34, 40]	-0.43×10^{-3}	-0.43×10^{-3}	-0.26×10^{-3}
Enthalpy of solid at melting point, (J/kg) [34, 40]	1.20×10^{6}	1.20×10^{6}	1.12×10^{6}
Enthalpy of liquid at melting point, (J/kg) [34, 40]	1.26×10^{6}	1.26×10^{6}	1.49×10^{6}
Emissivity	0.3	0.3	0.3
Heat transfer coefficient, W/m^2-K	210	210	210

* Values depended on work-distance.

4.4.1.1 Weld geometry

4.4.1.1.1 Power variation: 21Cr-6Ni-9Mn steel and Ti-6Al-4V

Figure **4.2** shows a comparison of computed and experimentally observed weld cross-sections of two EB welds of 21Cr-6Ni-9Mn stainless steel for two input powers (407 W and 814 W). The computed cross-sections of the fusion zone geometry, shown by solid lines, are in good agreement with the corresponding experimental results. Both welds show narrow and deep fusion zone geometry characteristic of EB welds.

Figure **4.3** (a) and (b) show a similar comparison of weld cross-sections for Ti-6Al-4V welds at two different input powers. Solid lines mark the calculated fusion zone boundary given by the projections of solidus temperature contours on a vertical plane perpendicular to the welding direction. The fusion zones of Ti-6Al-4V welds have a martensitic microstructure with columnar grains. The microstructure also shows a light etching inner heat affected zone and a dark etching outer heat affected zone. The location of the fusion zone boundary at the top surface can be discerned from the deformation of the top surface. The computed and the experimental weld geometries are in very good agreement.

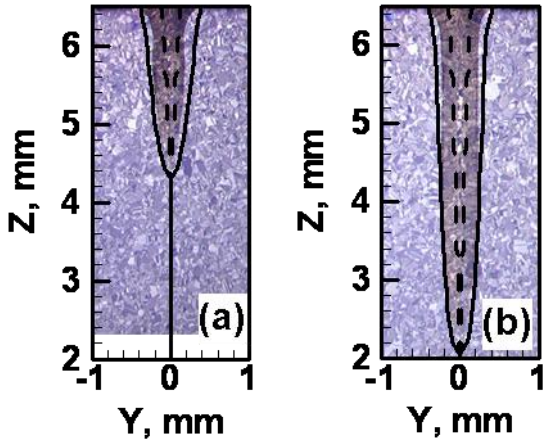

Figure **4.2**: Comparison of EB weld cross-section for 21Cr-6Ni-9Mn stainless steel at 17 mm/s welding speed and at input powers a) 407 W and b) 814 W. The computed weld pool and keyhole geometries are shown by solid lines and dashed lines respectively.

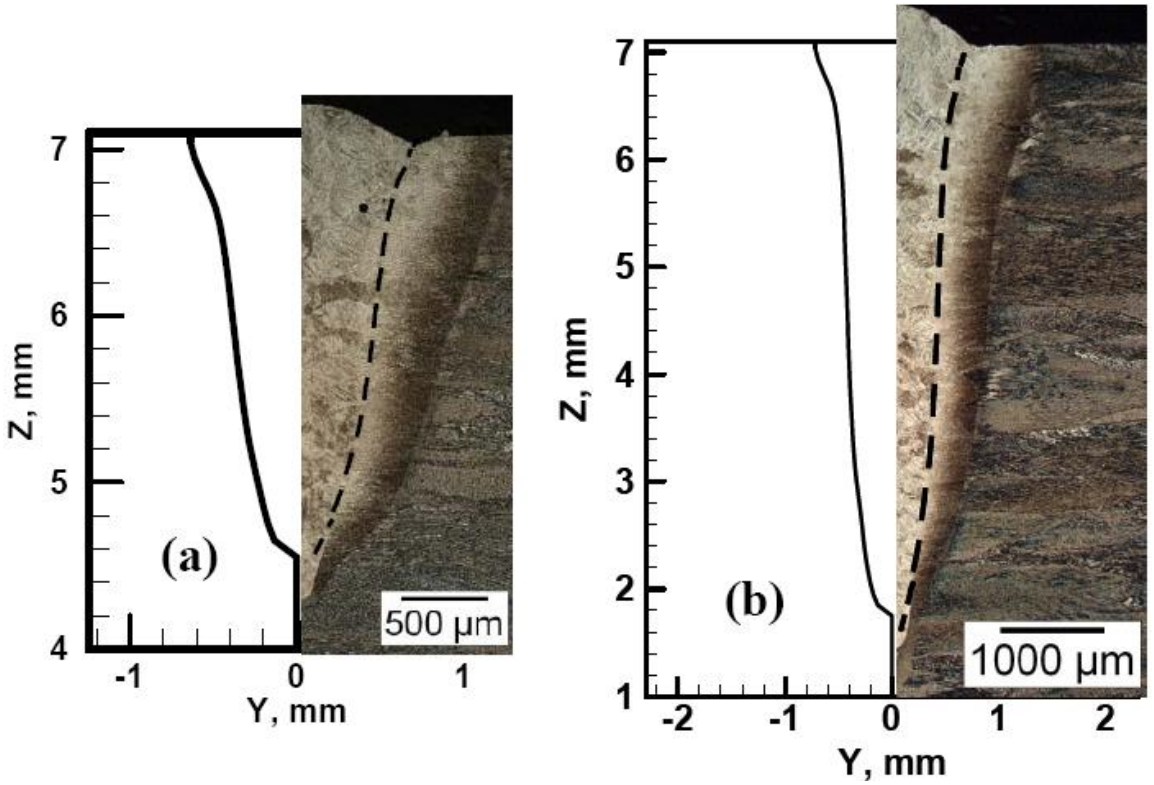

Figure **4.3**: Comparison of computed (solid lines) and experimentally determined EB weld cross-section for Ti-6Al-4V weld made at 17 mm/s welding speed with a) 550 W input power and b) 1114 W input power. The dashed line marks the experimentally observed fusion zone boundary.

The fusion zone volume for the two materials can be compared by examining their properties from the following approximate analysis. Amount of heat required to raise the temperature of a certain volume of the material to its melting point is equal to $V\rho[C_p(T_m - T_{amb}) + H_f]$, where V is the volume, ρ is the density, C_p is the specific heat, T_m is the melting point, and T_{amb} is the ambient temperature. For the same heat input, the approximate ratio of the fusion zone volumes can be found from the ratio of the above terms. Using the values given in Table **4.2**, the ratio of melt pool volume of the stainless steel to the melt pool volume of Ti-6Al-4V is about 0.77. In other words, we should expect a larger melt pool volume for Ti-6Al-4V as compared to 21Cr-6Ni-9Mn steel under similar heat input conditions. For heat inputs of 407 W for 21Cr-6Ni-9Mn stainless steel and 550 W for Ti-6Al-4V, the ratio of fusion zone volumes should be

approximately 0.57, if equal proportion of the beam energy was used for melting in the welding of the two materials. Since the weld pool temperatures vary with location and the melting efficiencies depend on process and material properties, this number can be used only for qualitative purpose. The experimentally observed ratio of melt pool volumes can be approximately compared from the melt pool cross-sections of the welds of the two materials. Approximating the fusion zones with triangles and using weld depth and half-width of 2.1 mm and 0.6 mm, respectively, for Ti-6Al-4V weld at 550 W, and using weld depth and half-width of 2.5 mm and 0.36 mm, respectively, for Ti-6Al-4V weld made at 407 W, the approximate ratio of melt pool volumes is 0.5. Therefore the Ti-6Al-4V weld is larger than the 21Cr-6Ni-9Mn weld.

4.4.1.1.2 Power density variation: 304L stainless steel welds

As shown in Table **4.3**, an increase in work distance from 127 mm to 457 mm resulted in more than a two-fold increase in the beam focal spot radius (R_f). With a larger focal spot radius, the beam is more diffuse and the peak power density is lower, decreasing from 34.9 kW/mm^2 for 127 mm work-distance (focal radius = 0.13 mm) to 7.79 kW/mm^2 for 457 mm work-distance (focal radius = 0.28 mm) [27]. As a result, the weld characteristics are likely to be strongly affected by the variation in beam radius.

With an increase in beam radius, the input energy distribution is more diffuse and the peak power density decreases, thus decreasing the weld penetration. However, a larger focal spot radius increases melting on the top surface, resulting in a wider weld pool. Thus, the ratio of weld pool depth to width decreases with increasing beam radii, as shown in Table **4.3**. The calculated and experimental depth and width were in reasonable agreement. The difference in calculated and experimental values was less than 9 % for depth and less than 16 % for width. The area of calculated weld cross-section is nearly constant with variation in the beam radius. Figure **4.4** shows the variation of weld pool depth and width at the top surface with the variation in the focal spot radius. Trend lines are also plotted for the calculated and measured weld depth and width. The calculated weld width and depth display trends similar to the measured values.

Table **4.3**: Data used for fluid flow calculations.

WD, mm	R_f, mm	PPD, kW/mm^2	d_m, mm	d_c, mm	% error	w_m, mm	w_c, mm	% error	MA, mm^2	AR
127	0.131	34.9	4.46	4.20	-6.19	1.27	1.38	7.97	2.40	3.52
184	0.166	21.6	4.21	3.87	-8.79	1.29	1.52	15.13	2.55	3.27
229	0.173	20.0	3.97	3.80	-4.47	1.48	1.58	6.33	2.63	2.65
305	0.207	14.1	3.69	3.56	-3.65	1.48	1.68	11.90	2.58	2.49
381	0.243	10.2	3.39	3.33	-1.80	1.55	1.76	11.93	2.56	2.19
457	0.279	7.8	2.96	2.97	0.34	1.71	1.90	10.00	2.62	1.73

* Values depended on work-distance.

WD: work distance, R_f: focal spot radius, PPD: peak power density, d_m: measured weld depth, d_c: calculated weld depth, w_m: measured weld width, w_c: calculated weld width, MA: measured cross-sectional area, AR: aspect ratio. % error is the difference between the calculated and experimental values divided by the calculated value. All the measurements were made at LLNL.

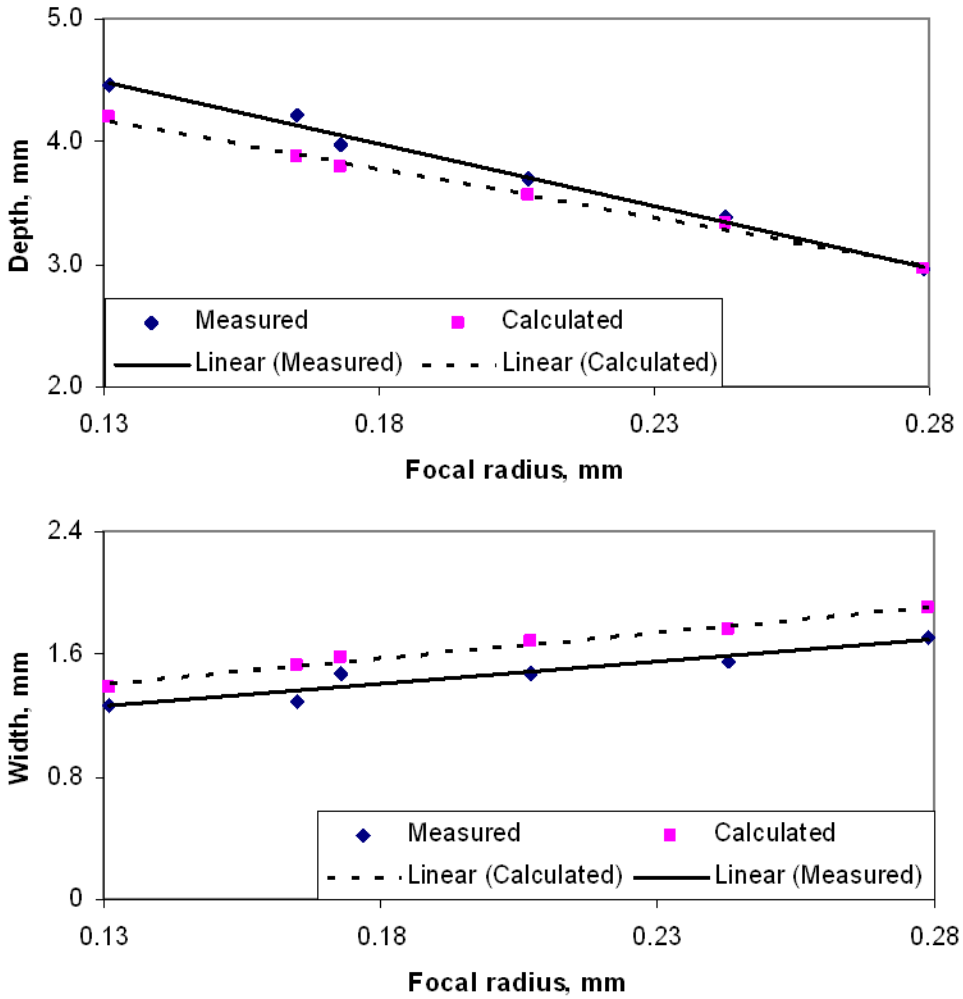

Figure **4.4**: Variation of weld depth and weld width with spot radius.

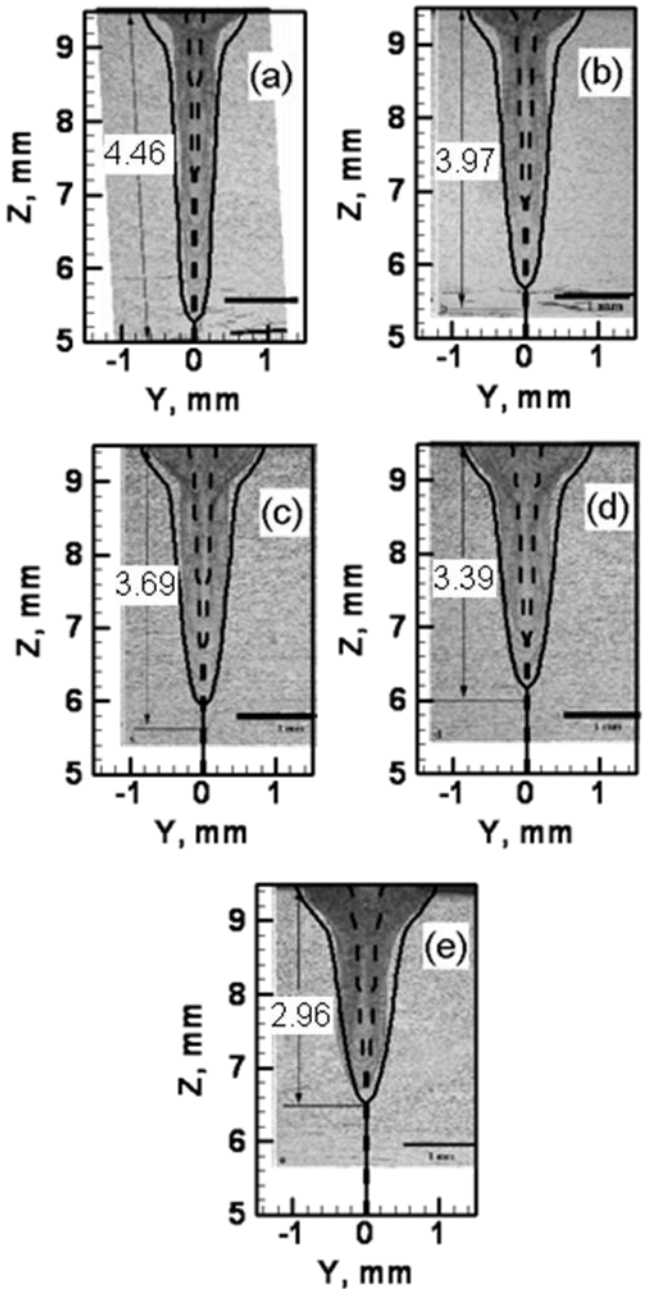

Figure **4.5**: Comparison of experimental and calculated weld geometries for 304 L stainless steel welds made with focal spot radii a) 0.131 mm, b) 0.173 mm, c) 0.207 mm, d) 0.243 mm, and e) 0.279 mm. Input power: 1000 W. Welding speed 17 mm/s. Weld penetration is in mm.

4.4.1.2 Thermal cycle

Thermal cycles were computed for 21Cr-6Ni-9Mn stainless steel welds (407 W and 814 W input power, 17 mm/s welding speed) and Ti-6Al-4V welds (550 W and 1114 W input power, 17 mm/s welding speed). The computed thermal cycles were compared with experimental measurements in Figures **4.6** and **4.7** at three monitoring locations for 21Cr-6Ni-9Mn stainless steel welds made at 407 W and 814 W, respectively. The time scales in the computed temperature versus time plots were constructed by dividing the distance with the welding velocity. The experimental and the calculated time scales were synchronized by taking the same time to reach peak temperature for both plots. Locations of the thermocouples and the welding conditions are described in section **4.2.1**. The computed thermal cycles agreed well with the corresponding experimentally determined values at all three locations for both powers. A comparison of the data in Figures **4.6** and **4.7** indicates that at any given monitoring location the peak temperature increases with an increase in heat input.

Figures **4.8** and **4.9** show the comparison of the computed and the experimentally determined temperature versus time plots at three monitoring locations for Ti-6Al-4V welds made at 550 W and 1114 W input power, respectively. The computed thermal cycles agreed well with the corresponding experimentally determined values at all three monitoring locations for both input powers. The peak temperatures obtained at the top surface for Ti-6Al-4V made at 550 W were higher than the peak temperatures obtained at similar locations for 21Cr-6Ni-9Mn stainless steel made at the higher input power of 814 W. This difference in peak temperatures can be attributed to the higher boiling point and lower solid state thermal conductivity of Ti-6Al-4V compared to 21Cr-6Ni-9Mn stainless steel.

Because of the lower heat input and higher welding speeds compared to arc welding, cooling rates are higher in EBW. For a 2 mm deep 21Cr-6Ni-9Mn steel weld made at 407 W input power and 17 mm/s welding speed, the calculated time to cool from 1073 K to 773 K (800 ^{0}C to 500 ^{0}C) at the weld center line on the top surface of the work-piece was 0.128 s. That is, the cooling rate from 1073 K to 773 K was 2343.7 K/s.

Larger heat inputs and lower welding speeds required to produce similar weld penetration in arc welding (due to more diffused energy distribution) result in higher cooling times. For the welding conditions considered by Kumar et al. [41], penetration depths between 1 to 6 mm were obtained and the time to cool from 1073 K to 773 K was between 1 to 21 s. Therefore, the cooling rates in gas metal arc fillet welding were much lower compared to EBW.

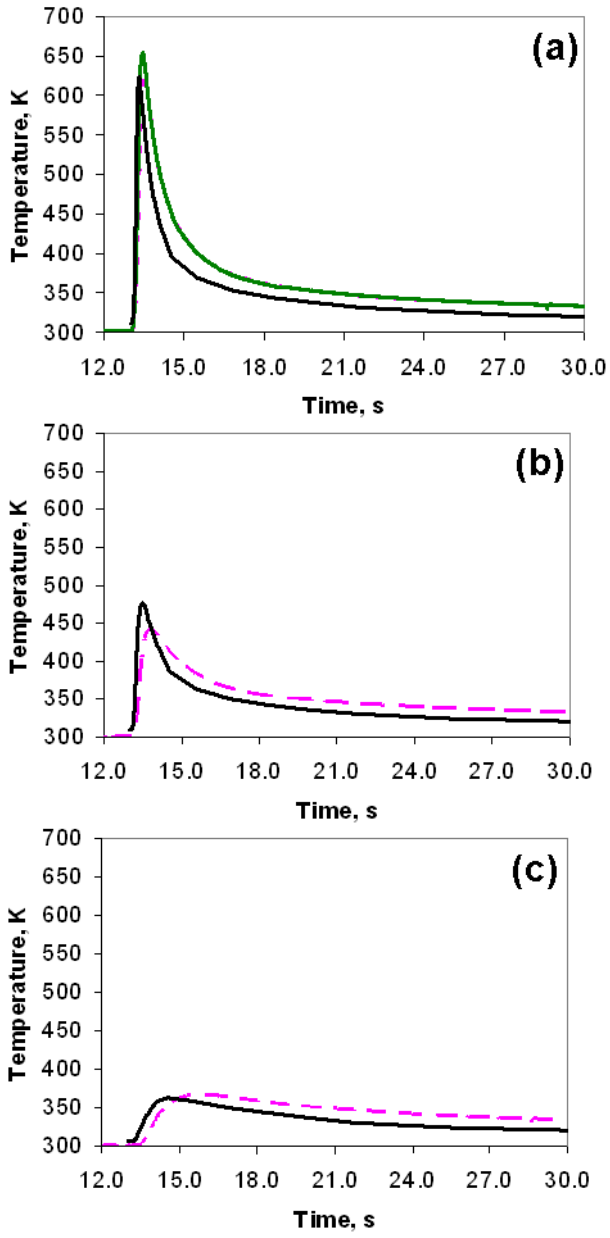

Figure **4.6**: Experimental and computed thermal cycles for EB welds made on 21Cr-6Ni-9Mn stainless steel at 407 W input power and 17 mm/s welding speed at (a) y = 1.5 mm at the top surface, (b) y = 2.5 mm at the top surface, and (c) y = 0 mm at the bottom surface. y is the distance from the weld center line. Solid line shows the computed thermal cycle.

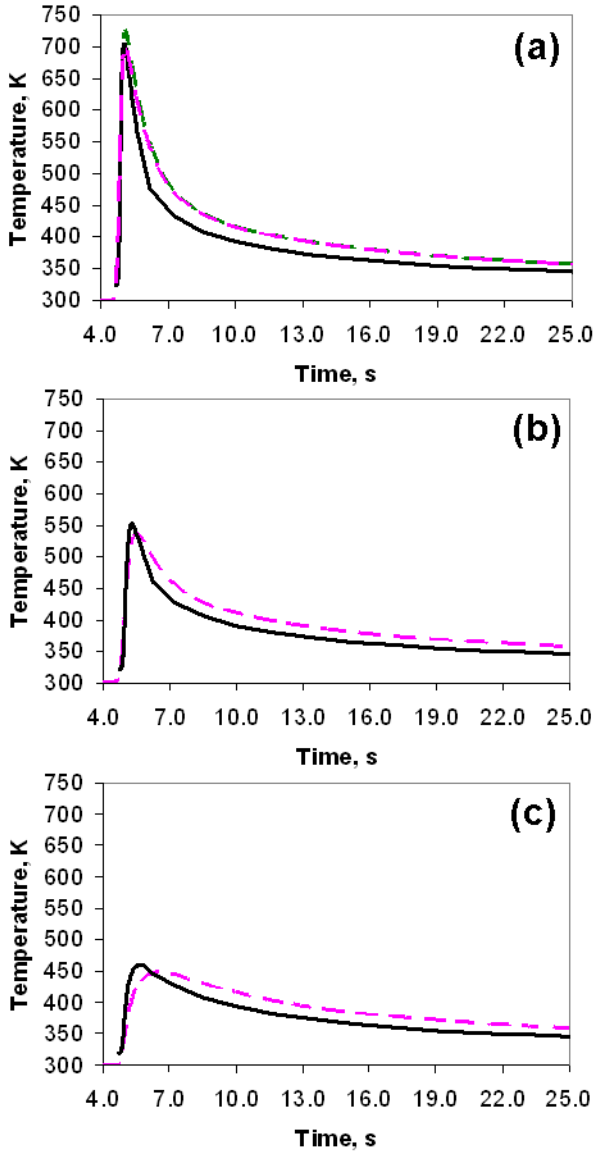

Figure **4.7**: Experimental and computed thermal cycles for EB welds made on 21Cr-6Ni-9Mn stainless steel at 814 W input power and 17 mm/s welding speed at (a) y = 1.5 mm at the top surface, (b) y = 2.5 mm at the top surface, and (c) y = 0 mm at the bottom surface. y is the distance from the weld center line. Solid line shows the computed thermal cycle.

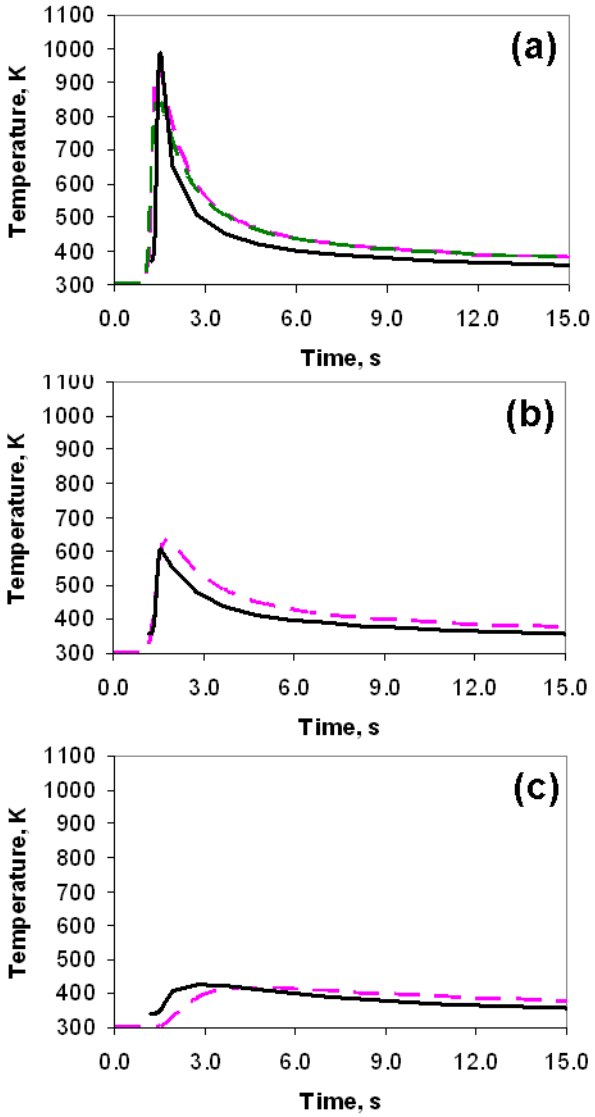

Figure **4.8**: Experimental and computed thermal cycles for EB welds made on Ti-6Al-4V at 550 W input power and 17 mm/s welding speed at (a) y = 1.5 mm at the top surface, (b) y = 2.5 mm at the top surface, and (c) y = 0 mm at the bottom surface. y is the distance from the weld center line. Solid line shows the computed thermal cycle.

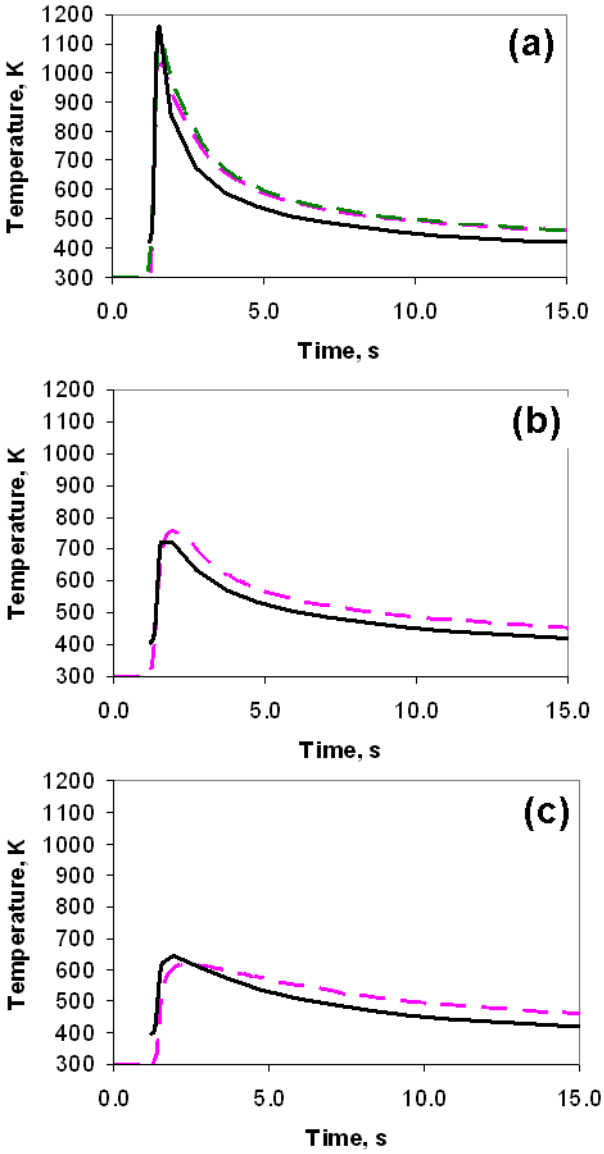

Figure **4.9**: Experimental and computed thermal cycles for EB welds made on Ti-6Al-4V at 1114 W input power and 17 mm/s welding speed at (a) y = 1.5 mm at the top surface, (b) y = 2.5 mm at the top surface, and (c) y = 0 mm at the bottom surface. y is the distance from the weld center line. Solid line shows the computed thermal cycle.

4.4.2 Fluid flow

Figures **4.10** and **4.11** show the computed fluid flow during EBW of 21Cr-6Ni-9Mn stainless steel and Ti-6Al-4V welds, respectively. The experimental conditions for these welds are described in section **4.2.1**. The fluid moving out from the center of the weld pool carries heat and enhances the heat transfer. The region within the weld pool with no velocity vectors is the keyhole. On the keyhole walls, the velocity vectors due to Marangoni convection can be observed. These Marangoni convection currents bring heat from the keyhole bottom, where the wall temperature is relatively higher, to the top surface and then outwards, thus enhancing the heat transfer within the weld pool. Such re-circulatory flow of hot liquid from the bottom to the top and then radially outwards, can result in increased weld pool width near the top surface.

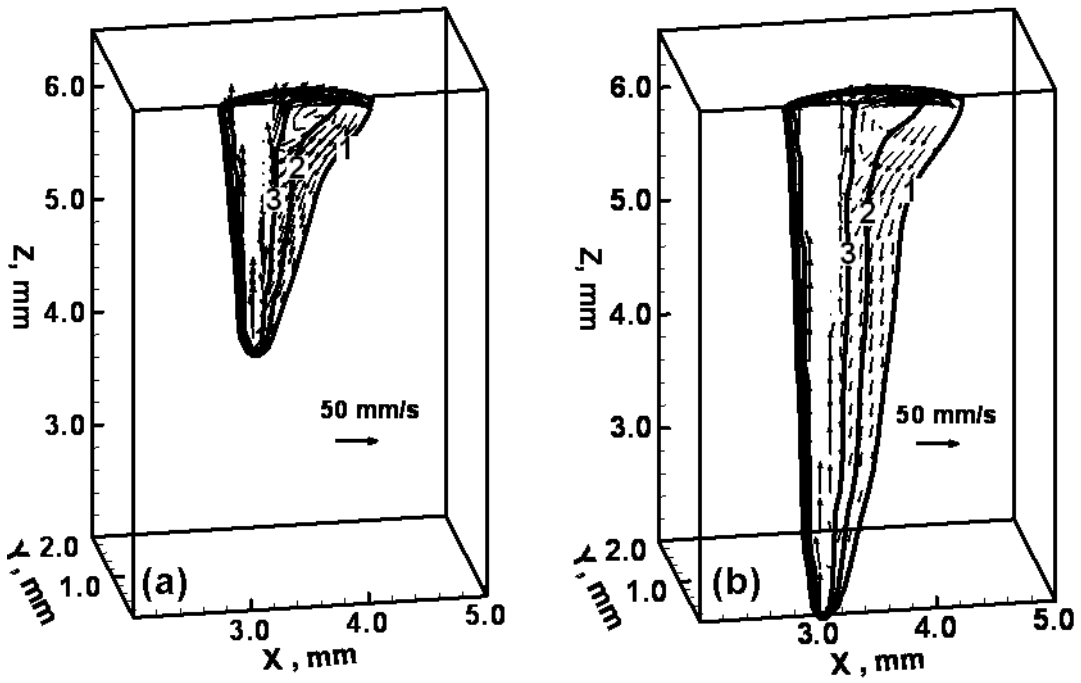

Figure **4.10**: Fluid flow in 21Cr-6Ni-9Mn stainless steel EB weld pool at 17 mm/s welding speed and at input powers a) 407 W and b) 814 W. Levels 1, 2 and 3 correspond to temperatures 1697 K, 1900 K and 2200 K.

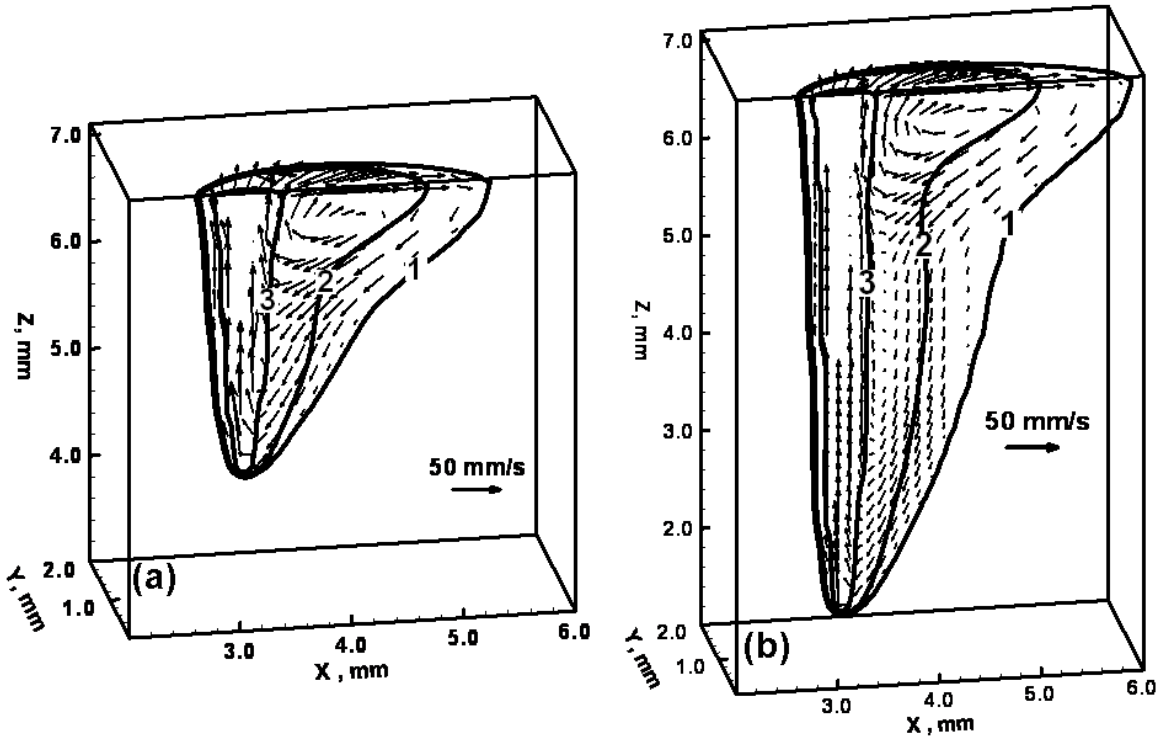

Figure **4.11**: Fluid flow in a Ti-6Al-4V EB weld pool made at 17 mm/s welding speed at input power of a) 550 W and b) 1114 W. Levels 1, 2 and 3 correspond to temperatures 1878 K, 2000 K and 2500 K.

Figure **4.12** shows the temperature contours and velocity vectors for the 304L stainless steel welds for the welds made with the smallest (0.13 mm) and the largest (0.28 mm) focal spot radius. In this figure, there is a strong circulation of liquid near the top surface of the weld pool and the fluid moves at high velocities from the hot region near the keyhole carrying heat outward. The enhanced heat transfer due to Marangoni convection results in the widening of the weld pool near the top of the surface. Since Marangoni convection cannot directly enhance the heat transfer in horizontal planes at large distances from the top surface, the weld pool is narrow. The result is a weld pool that is widened near the top surface.

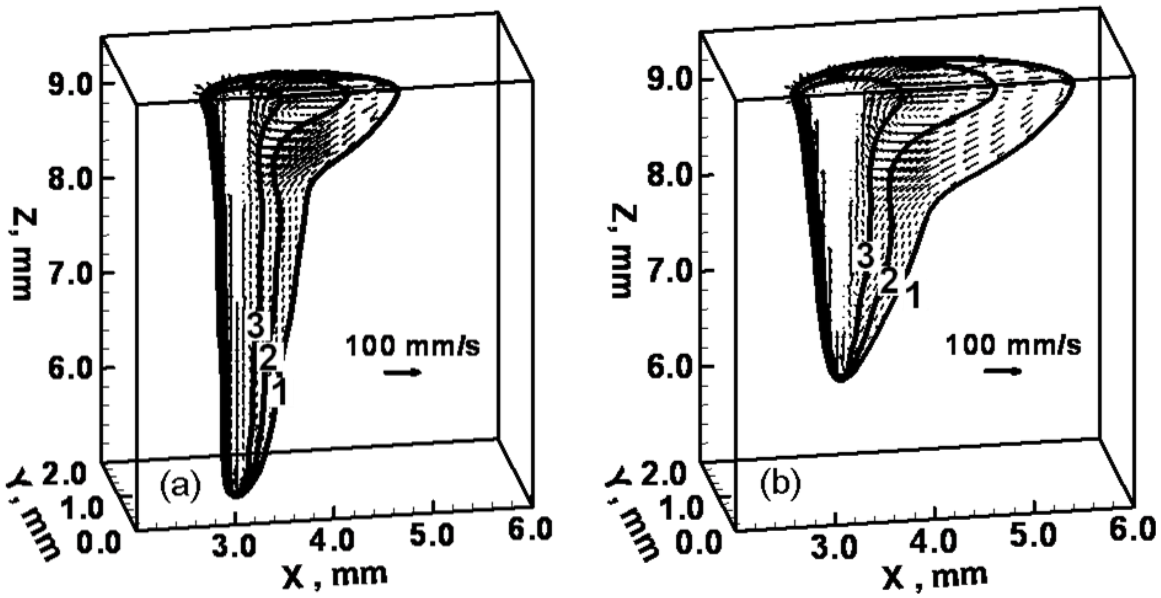

Figure **4.12**: Fluid flow pattern in EB weld on 304L stainless steel for focal spot radius of a) 0.13 mm and b) 0.28 mm. Levels 1, 2, and 3 represent 1697 K, 1900 K and 2200 K, respectively.

Figure **4.13** shows the fluid flow in transverse planes perpendicular to welding direction at selected distances from the heat source. Plane 'a' is the closest to the EB axis (located 0.11 mm behind EB axis) and plane 'f' is the farthest behind the EB axis (located 0.95 mm behind EB axis). The keyhole region, which is characterized by the absence of velocity vectors at the center of the weld pool, is present only in Figure **4.13** (a). Under the influence of surface tension gradients at the vapor-liquid interface, the fluid near the keyhole wall moves from the bottom to the top. The fluid velocities in the vertical direction are highest near the vapor-liquid interface and decrease to zero at the solid-liquid boundary. As the distance from the heat source increases, fluid gradually starts to move downwards and the reversal of the direction of fluid velocity from upwards to downwards happens at shorter distances from the top surface. In short, fluid moves upwards and outwards near the keyhole region, and comes downwards and inwards away from it. The study of fluid flow patterns gives insight into the convective heat transport process and its effect on weld geometry and cooling rates. Fluid moving from hotter region to cooler region will enhance the heat transfer to the cooler region and increase the

weld pool size. Furthermore, when coupled with species transport equations, calculation of fluid velocities can help in understanding and predicting the solute distribution in the fusion zone.

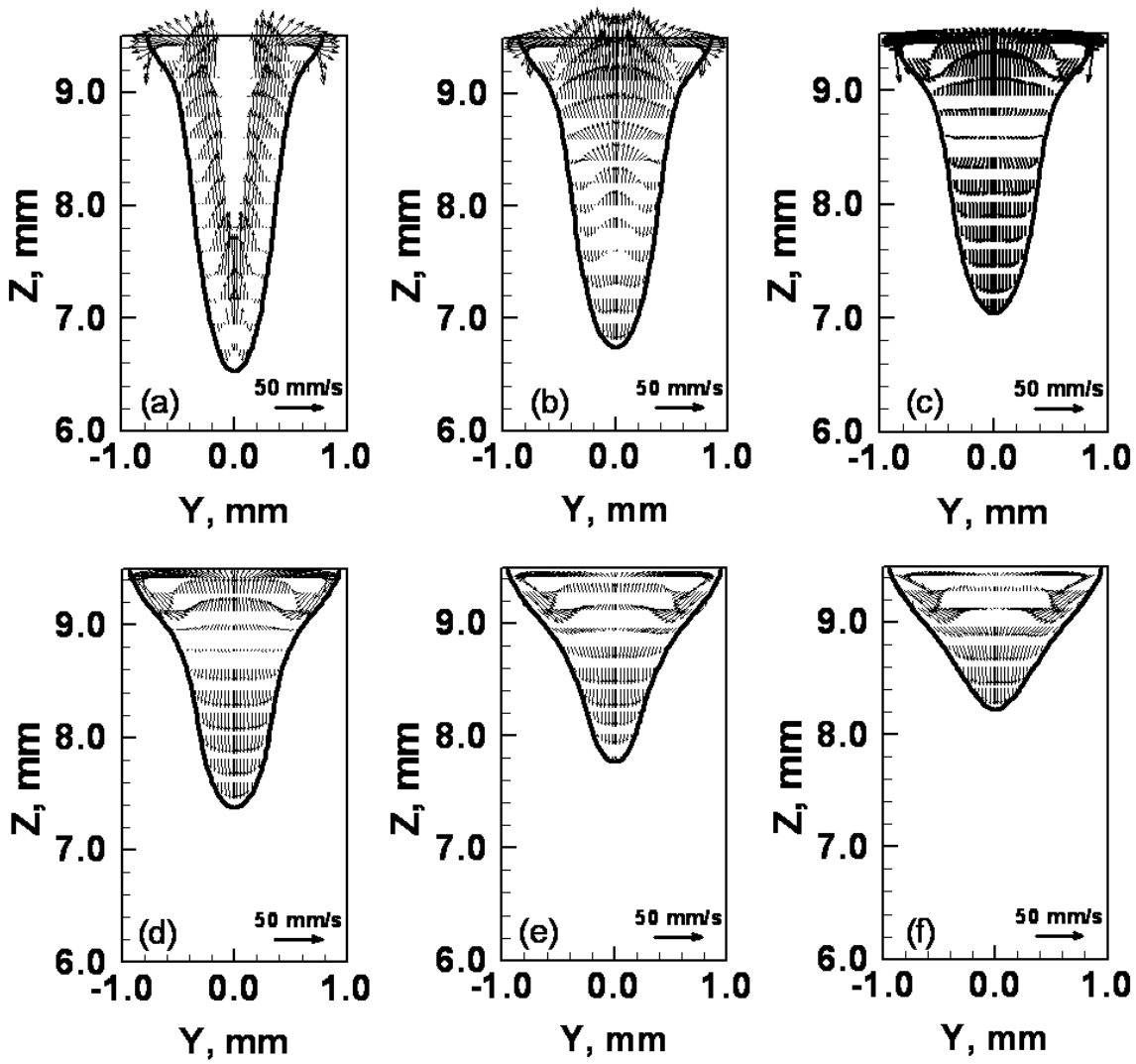

Figure **4.13**: Fluid flow in the weld made with 0.28 mm beam radius in transverse planes located at (a) 0.11 mm, (b) 0.28 mm, (c) 0.45 mm, (d) 0.62 mm, (e) 0.78 mm and (f) 0.95 mm behind the EB. Only the top 3.5 mm of the total plate thickness of 9.5 mm is shown.

4.4.2.1 Convective heat transfer

The significance of convective heat transfer relative to conductive heat transfer can be measured in terms of the Peclet number. Using ρ = 7000 kg/m^3, u = 0.1 m/s (the value of the reference velocity vector in Figure **4.12**), C_p = 800 J/kg-K, half-width of the weld pool, w/2 = 8.0 X 10^{-4} m, and k = 30 W/m-K, for the welding of 304L stainless steel, the calculated Peclet number ($\rho u C_p (w/2)/k$) is 14.9, meaning that convective heat transfer is very important for these welding conditions.

To further illustrate the significance of convection on the weld pool geometry, the temperature field in the work-piece was calculated by considering only conductive heat transfer and ignoring fluid flow. Figure **4.14** shows the calculated weld pool cross-sections for 304L stainless steel welds with and without consideration of convective heat transfer for the lowest and highest focal spot radius cases described in section **4.2.2**. Figures **4.14** (a) and (c) show the calculated weld pool cross-sections for the case of 0.13 mm and 0.28 mm focal spot radius, respectively, with convection, and Figure **4.14** (b) and (d) show the corresponding weld cross-sections in the absence of convection. In the absence of convection, heat transfer is significantly reduced resulting in much narrower weld pools. The calculated weld pool in the absence of convection also lacks the nail head shape usually observed in experiments because of the absence of enhanced outward heat transfer at the top surface of the work-piece. The differences in shape and size of the calculated weld pools in the absence of and in the presence of convection indicate the significance of convective heat transfer under the conditions considered.

4.4.3 Non-dimensional analysis

Table **4.4** shows various dimensionless numbers calculated for the EBW of 21Cr-6Ni-9Mn stainless steel, 304L stainless steel and Ti-6Al-4V alloy. Since the Peclet number is much higher than 1 for all the three alloys, convection plays a very significant role in the heat transfer compared to conduction. The surface tension Reynold's number for all the three alloys is of the order of 10^4, indicating a strong effect of the surface

tension gradient on the fluid flow in comparison with the viscous force. According to Atthey's criteria [42], the weld pools are turbulent when the Reynold's number, Re ($\rho u_m w/\mu$) is greater than 600. This condition is satisfied for the welding of all the three materials indicating a turbulent weld pool. The very low values of the Magnetic Reynolds numbers indicate that the Lorentz force is insignificant compared to the viscous force.

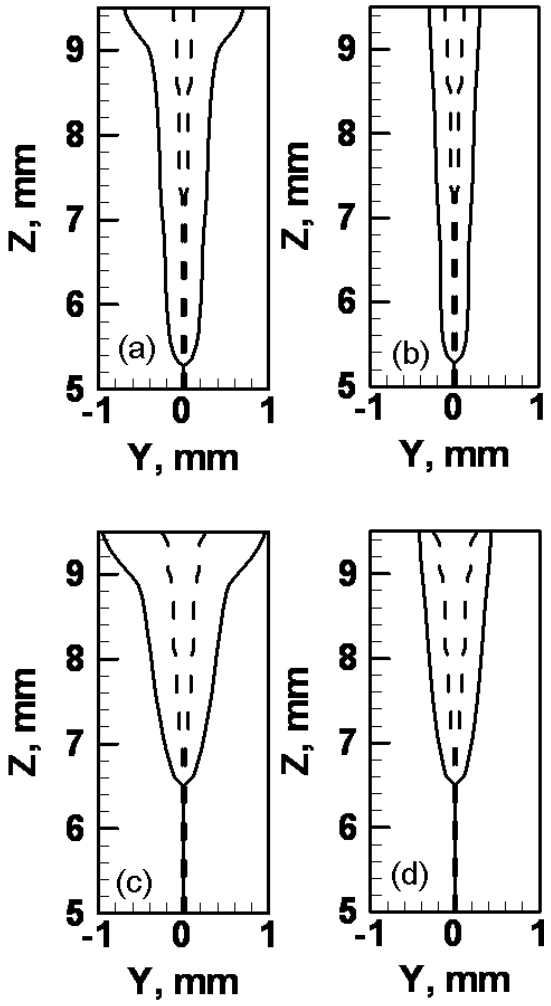

Figure **4.14**: 304L weld pool cross-sections for focal spot radius of 0.13 mm (a) with convection, (b) without convection, and 0.28 mm (c) with convection, and (d) without convection. Input power: 1000 W, welding speed: 17 mm/s.

Table **4.4**: Dimensionless numbers for EBW of 21Cr-6Ni-9Mn stainless steel at 814 W, 304L stainless steel at 1000 W, and Ti-6Al-4V at 1114 W, and the values used in calculations.

Values used for calculation of dimensionless numbers				
		21-6-9 SS 814 W	304L SS 1000 W	Ti-6Al-4V, 1114 W
Characteristic flow velocity, m/s	u	0.1	0.1	0.1
Maximum flow velocity, m/s	u_m	1.0	1.0	0.6
Weld pool width, m	w	9.0×10^{-4}	1.7×10^{-3}	1.5×10^{-3}
*Temperature difference, K	ΔT	550	800	700
Density, kg/m^3 [30, 40]	ρ	7000	7000	4000
Viscosity, kg/m-s [34, 40]	μ	0.007	0.007	0.005
Thermal conductivity, W/m-K [28, 31, 35, 37, 38]	k	30	30	30
Specific heat, J/kg-K [34, 40]	C_p	800	800	730
Surface Tension, N/m-K [30]	γ	1.87	1.87	1.65
Temperature coefficient of surface tension, (N/m K) [34, 40]	$\frac{d\gamma}{dT}$	-0.43×10^{-3}	-0.43×10^{-3}	-0.26×10^{-3}
Current, A	I	7.4×10^{-3}	10.0×10^{-3}	10.4×10^{-3}
Magnetic permeability of free space, N/A^2[30]	μ_m	$4\pi \times 10^{-7}$	$4\pi \times 10^{-7}$	$4\pi \times 10^{-7}$
Dimensionless number	Definition	21-6-9 SS 814 W	304L SS 1000 W	Ti-6Al-4V, 1114 W
Peclet Number, Pe	$= \frac{u\rho C_p\left(\frac{w}{2}\right)}{k}$	8.4	15.9	7.3
Surface tension Reynold's number, Ma	$= \frac{\rho\left(\frac{w}{2}\right)\left\|\frac{d\gamma}{dT}\right\|\Delta T}{\mu^2}$	1.5×10^4	4.2×10^4	2.2×10^4
Reynold's Number, Re	$= \frac{\rho u_m w}{\mu}$	900	1700	720
Magnetic Reynold's Number, R_m	$= \frac{\rho\mu_m I^2}{4\pi^2\mu^2}$	2.5×10^{-4}	4.5×10^{-4}	5.5×10^{-4}

*Difference between the calculated keyhole wall temperature near the top surface and solidus temperature.

4.4.4 Vapor pressure and wall temperature

Figure **4.15** (a) shows the variation of vapor pressure with depth in the keyhole for the 21Cr-6Ni-9Mn stainless steel weld made with an input power of 407 W at welding speed of 17 mm/s. The values given in the plot represent the pressure required to balance the surface tension force and the hydrostatic force of the liquid metal at the keyhole walls in order to keep the keyhole open. The metal vapor pressure in the keyhole increases with depth and it can become very high near the keyhole bottom. As the keyhole radius becomes smaller with increasing depth, the pressure increases at a higher rate. In the calculation of the keyhole profile, the radius of the keyhole decreases from a maximum value at the top to zero at the bottom. In reality, the keyhole bottom is likely to be rounded and the radius of curvature is likely to have a finite value. Thus, calculated vapor pressures near the keyhole bottom may be somewhat higher than their true values.

Figure **4.15** (b) shows the variation of wall temperature with depth and is calculated from the equilibrium pressure versus temperature relationship for 21Cr-6Ni-9Mn stainless steel. The equilibrium vapor pressures over the alloys were calculated assuming ideal solution behavior. For example, for stainless steel, the equilibrium vapor pressure was taken as the sum of the products of the mole fraction and the equilibrium vapor pressure of pure Fe, Cr, Ni and Mn. The wall temperatures varied by about 400 K from about 2308 K to about 2734 K.

Figure **4.16** (a) and (b) show the variation of keyhole pressure and wall temperature with depth for Ti-6Al-4V weld made with an input power of 550 W at a welding speed of 17 mm/s. The wall temperatures varied by about 400 K from 2632 K near the top surface to 3034 K near the keyhole bottom. Schauer and Giedt [6] measured the wall temperatures in an EB cavity for various alloys and found a similar variation with depth. Measurements for variation of wall temperature along the depth of a vapor cavity in laser welding are not available.

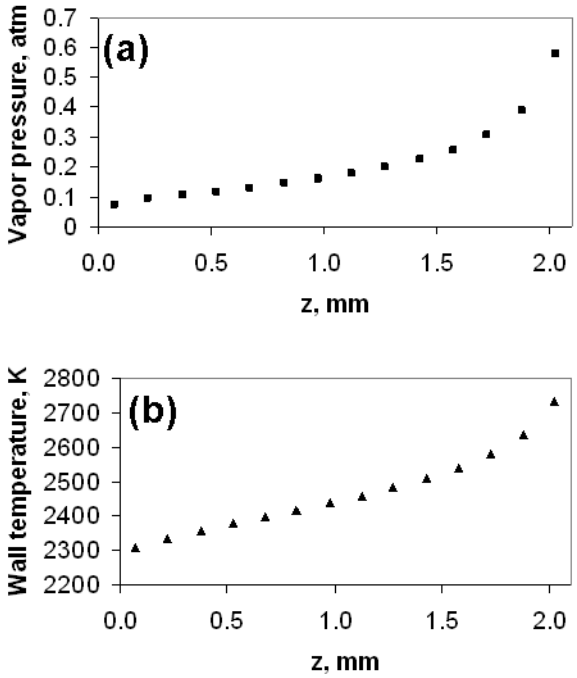

Figure **4.15**: Variation of (a) vapor pressure in the keyhole and (b) keyhole wall temperature, with depth for electron beam welding of 21Cr-6Ni-9Mn stainless steel at 407 W input power and 17 mm/s welding speed. z = 0 at the surface of the work piece. Equilibrium pressure versus temperature relation for the alloy was calculated assuming ideal solution behavior from the pressure versus temperature relation for the constituting metals.

The temperature versus pressure relations for various metals that constitute the three alloys used in this study are as given in Eqs. **4.3** to **4.12**. In these equations, p_i is the pressure in mm of mercury and T is the temperature in K.

Temperature versus pressure relation for Fe [30]:

$$\log_{10}(p_{Fe}) = 13.27 - 19710.0/T - 1.27 \log_{10}(T) \qquad (\mathbf{4.3})$$

Temperature versus pressure relation for Cr [30]:

$$\log_{10}(p_{Cr}) = 14.56 - 20680.0/T - 1.31 \log_{10}(T) \qquad (\mathbf{4.4})$$

Temperature versus pressure relation for Ni [30]:

$$\log_{10}(p_{Ni}) = 16.95 - 22400.0/T - 2.0\log_{10}(T) \quad (\mathbf{4.5})$$

Temperature versus pressure relation for Mn [30]:

For T < 2333 K,

$$\log_{10}(p_{Mn}) = 17.27 - 13900.0/T - 2.52\log_{10}(T) \quad (\mathbf{4.6})$$

For T > 2333 K,

$$p_{Mn} = 760 \text{ X } 2.718^{(27796.50(-1/T+1/2333.)} \quad (\mathbf{4.7})$$

Temperature versus pressure relation for Ti [30]:

$$\log_{10}(p_{Ti}) = 11.74 - 23200.0/T - 0.66\log_{10}(T) \quad (\mathbf{4.8})$$

Temperature versus pressure relation for V [30]:

For T < 2175 K,

$$\log_{10}(p_V) = 10.12 - 26900.0/T + 0.33\log_{10}(T) - 0.000265\ T \quad (\mathbf{4.9})$$

For T > 2175 K,

$$p_V = 760.0 \text{ X } 2.718^{(54991.6\ (-1/T+1/3683.0)} \quad (\mathbf{4.10})$$

Temperature versus pressure relation for Al [30]:

For T < 2800 K,

$$p_{Al} = 12.36 - 16450.0/T - 1.023\log_{10}(T) \quad (\mathbf{4.11})$$

For T > 2800 K,

$$p_{Al} = 760.0 \text{ X } 2.718^{(34989.2\ (-1/T+1/2760.6)} \quad (\mathbf{4.12})$$

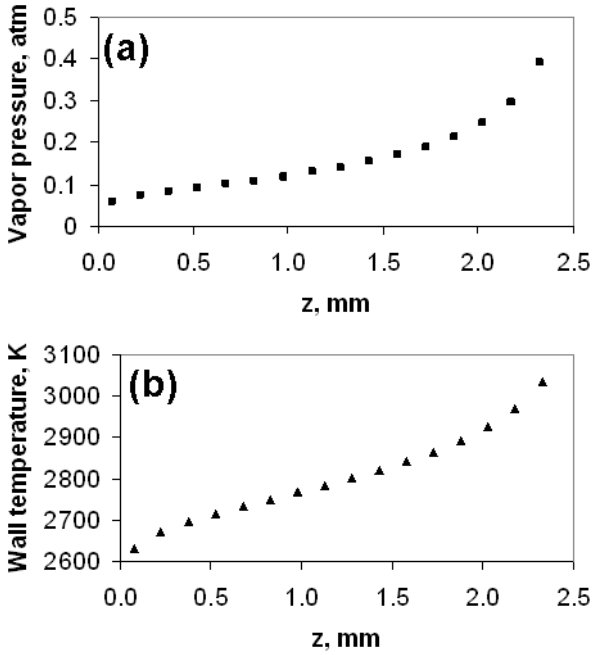

Figure **4.16**: Variation of vapor pressure in the keyhole with depth for EBW of Ti-6Al-4V at 550 W input power and 17 mm/s welding speed. z = 0 at the surface of the work piece. Equilibrium pressure versus temperature relation for the alloy was calculated assuming ideal solution behavior from the pressure versus temperature relation for the constituting metals.

Figure **4.17** shows the variation of vapor pressure with depth for beam radii of 0.13 mm and 0.28 mm. As shown in Figure **4.5**, the keyhole becomes narrower and deeper as the beam radius is decreased. The narrower keyhole for lower focal spot radius requires a larger vapor pressure to balance the surface tension force that tends to close the keyhole. Therefore, vapor pressures are higher for the higher peak power densities obtained with the smaller focal spot radii. In accordance with higher vapor pressures in the keyhole for the smaller beam radius, equilibrium wall temperatures at the keyhole walls are higher for the beam radius of 0.13 mm as compared to the larger beam radius of 0.28 mm as shown in Figure **4.18**.

The higher keyhole wall temperatures for smaller focal spot radius are consistent with more intense heating. The average temperature gradient in perpendicular-to-welding direction was always significantly higher than that along the keyhole wall in the vertical direction. For example, for the weld made with the beam radius of 0.28 mm the

average temperature gradient in the weld pool at mid-height of the keyhole in the horizontal direction was about 26 times that in the vertical direction. Thus, the assumption that the temperature gradient in the vertical direction is small compared to that in the horizontal plane is justified. Since the variation of vapor pressure from the bottom to the top of the keyhole results in only 3 to 5 % variation in the wall temperature, any errors in vapor pressure calculation are likely to result in much smaller errors in the computed wall temperatures.

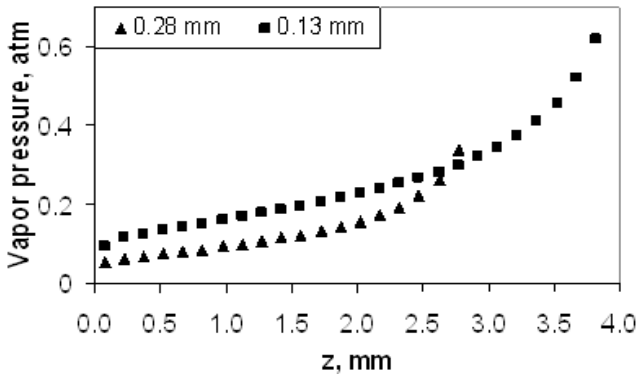

Figure **4.17**: Variation of vapor pressure in the keyhole with depth for radius of 0.13 mm and 0.28 mm. z = 0 at the surface of the work-piece.

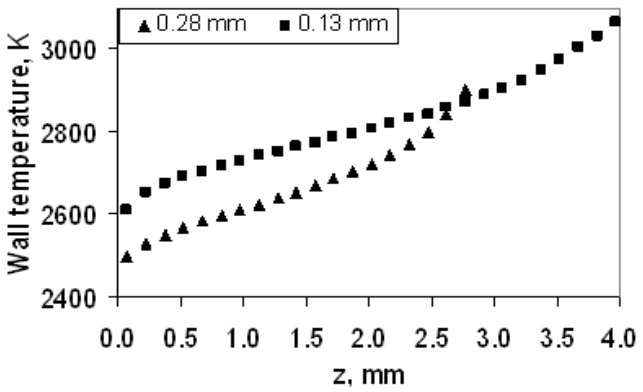

Figure **4.18**: Variation of keyhole wall temperature with depth for radius of 0.13 mm and 0.28 mm. z = 0 at the surface of the work-piece. Equilibrium pressure versus temperature relation for the alloy was calculated assuming ideal solution behavior from the pressure versus temperature relation for the constituting metals.

4.4.5 Effect of wall temperature on weld: EBW versus LBW

As discussed earlier, the keyhole wall temperatures are lower in EB welds as compared to LB welds due to the lower ambient pressure in electron beam welding. The differences in keyhole temperatures in EBW compared to LBW can result in different weld geometries for the two welding processes. Heat transfer and fluid flow calculations for laser and electron beam welding were performed for same process parameters for Ti-6Al-4V and 21Cr-6Ni-9Mn stainless steel. That is, the input power, power distribution, welding speed, focal spot radius, beam divergence, beam attenuation by plasma, and material absorption coefficient were taken to be same for both laser and electron beam welding. The calculated weld geometries for 21Cr-6Ni-9Mn stainless steel and Ti-6Al-4V are shown in Figures **4.19** and **4.20**, respectively. Since laser beam welds operate at higher keyhole surface temperatures, more energy is required to raise the temperature of the material to the higher keyhole wall temperatures in LBW compared to EBW. Therefore, for a given heat input, penetration in LBW is likely to be lower compared to EBW if all other process parameters are the same. However, since the higher keyhole surface temperatures result in greater heat transport in the horizontal plane, the LB welds are wider compared to the EB welds for 21Cr-6Ni-9Mn stainless steel and Ti-6Al-4V. Figures **4.19** and **4.20** show that even the difference of wall temperatures in LBW and EBW can affect the keyhole geometry appreciably.

4.5 Summary and Conclusions

A numerical model was developed and tested to calculate the fluid flow and heat transfer in 3D during keyhole mode EBW for the first time. An energy balance based model was used to calculate the keyhole shape in EBW by considering the variation of keyhole wall temperature as a function of keyhole depth. The model was tested for the welding of 21Cr-6Ni-9Mn stainless steel, 304L stainless steel, and Ti-6Al-4V alloy. The model was used to calculate temperature fields, thermal cycles, weld geometry, and fluid flow. A turbulence model based on Prandtl's mixing length hypothesis was used to

estimate the effective viscosity and effective thermal conductivity values. Temperatures on keyhole walls in EBW were calculated from the equilibrium temperature-pressure relations for the metal-vapor interface. The vapor pressure, in turn, was calculated from a force balance at the keyhole walls.

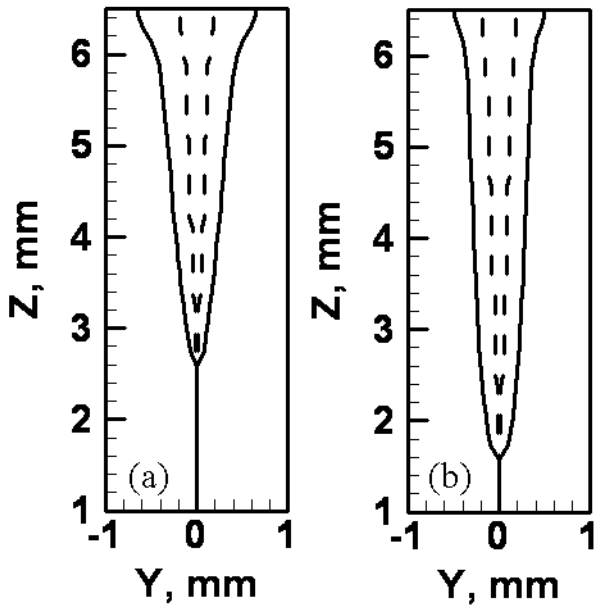

Figure **4.19**: Computed weld cross-sections for 21Cr-6Ni-9Mn stainless steel welds made with 1000 W input power at 17 mm/s welding speed by (a) LBW and (b) EBW.

The volume of the fusion zones could be related to the material properties like density, specific heat and melting point. As expected, welding parameters such as the beam radius, input power, and welding speed affected the weld pool geometry. Relatively low keyhole wall temperature in EBW compared with that during LBW was a contributing factor in the formation of narrower EB welds for the experimental conditions considered here. The presence of surface tension driven vertical flow along the keyhole walls in EBW enhanced the heat transfer. Convective heat transfer was very significant in determining the weld geometry, as shown by Peclet number calculations. In the absence of convection, the calculated nail head shape of the weld pool was not obtained. The reduced heat transfer near the top surface in the absence of convection resulted in a

much narrower calculated weld pool, further illustrating the significance of convective heat transfer for the welding conditions.

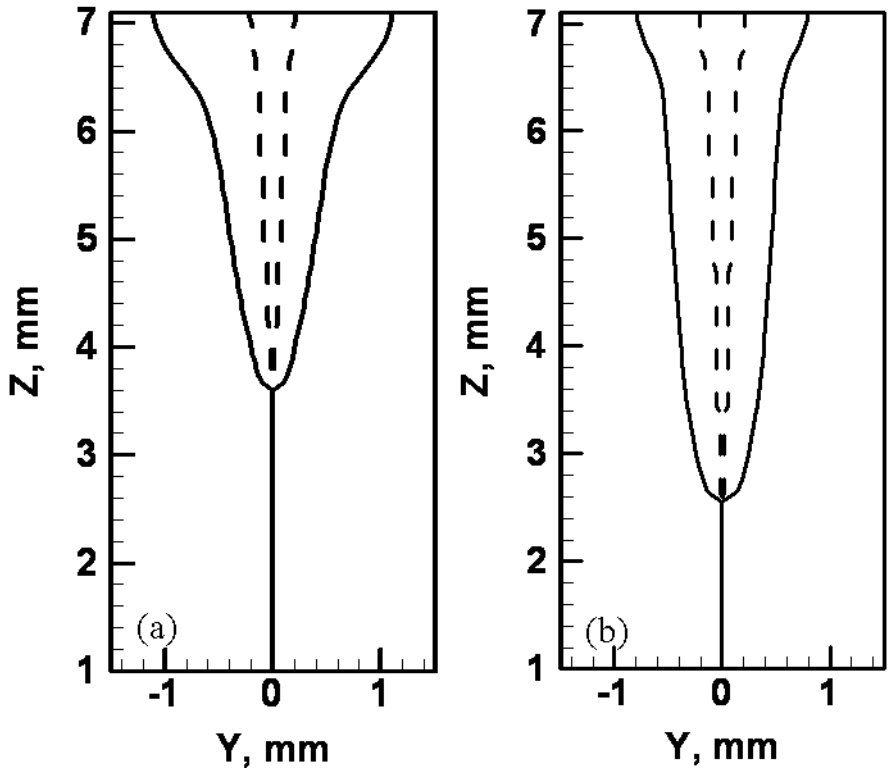

Figure **4.20**: Computed weld cross-sections for Ti-6Al-4V welds made with 1000 W input power at 17 mm/s welding speed by (a) LBW and (b) EBW.

The calculation of dimensionless numbers showed that convection was the dominant mechanism of heat transfer in the weld pool, and the gradient of surface tension played an important role in the fluid flow. The Lorentz force was insignificant compared with the Marangoni force. Higher peak temperatures found in Ti-6Al-4V welds compared to similar locations in 21Cr-6Ni-9Mn stainless steel welds was attributed to higher boiling point and lower solid state thermal conductivity of Ti-6Al-4V.

The effect of variations in the power density distribution was also studied for 304L stainless steel by changing the focal spot radius at a fixed input power. With an increase in the focal spot size, the power distribution became progressively diffused, the penetration depth decreased and the weld width increased. The total weld cross-sectional

area remained constant with the power density variation for the fixed input power. Higher peak power density with the same input power, resulted in higher peak temperature and vapor pressure at the keyhole bottom. Keyhole wall temperatures calculated for EBW from pressure balance at keyhole walls and using the equilibrium pressure versus temperature relation were lower than the keyhole wall temperatures in LBW. Heat transfer and fluid flow calculations for EBW and LBW for similar process parameters showed that the lower keyhole wall temperatures in EBW tend to increase the weld penetration and decrease the weld width compared to LBW.

4.6 References

[1] Dowden J, Postacioglu N, Davis M, Kapadia P. A Keyhole Model in Penetration Welding with a Laser. J. Phys. D-Appl. Phys. 1987;20:36.
[2] Kaplan A. A Model of Deep Penetration Laser-Welding Based on Calculation of the Keyhole Profile. J. Phys. D-Appl. Phys. 1994;27:1805.
[3] Matsunawa A, Semak V. The simulation of front keyhole wall dynamics during laser welding. J. Phys. D-Appl. Phys. 1997;30:798.
[4] Ye XH, Chen X. Three-dimensional modelling of heat transfer and fluid flow in laser full-penetration welding. J. Phys. D-Appl. Phys. 2002;35:1049.
[5] Zhao H, DebRoy T. Macroporosity free aluminum alloy weldments through numerical simulation of keyhole mode laser welding. J. Appl. Phys. 2003;93:10089.
[6] Schauer DA, Giedt WH, Shintaku SM. Electron-Beam Welding Cavity Temperature Distributions in Pure Metals and Alloys. Weld. J. 1978;57:S127.
[7] Wei PS, Chow YT. Beam Focusing Characteristics and Alloying Element Effects on High-Intensity Electron-Beam Welding. Metallurgical Transactions B-Process Metallurgy 1992;23:81.
[8] Andrews JG, Atthey DR. Hydrodynamic Limit to Penetration of a Material by a High-Power Beam. J. Phys. D-Appl. Phys. 1976;9:2181.
[9] Postacioglu N, Kapadia P, Davis M, Dowden J. Upwelling in the Liquid Region Surrounding the Keyhole in Penetration Welding with a Laser. J. Phys. D-Appl. Phys. 1987;20:340.
[10] Mazumder J, Steen WM. Heat-Transfer Model for Cw Laser Material Processing. J. Appl. Phys. 1980;51:941.
[11] Kroos J, Gratzke U, Simon G. Towards a Self-Consistent Model of the Keyhole in Penetration Laser-Beam Welding. J. Phys. D-Appl. Phys. 1993;26:474.
[12] Kroos J, Gratzke U, Vicanek M, Simon G. Dynamic Behavior of the Keyhole in Laser-Welding. J. Phys. D-Appl. Phys. 1993;26:481.
[13] Trappe J, Kroos J, Tix C, Simon G. On the Shape and Location of the Keyhole in Penetration Laser-Welding. J. Phys. D-Appl. Phys. 1994;27:2152.

[14] Sudnik W, Radaj D, Erofeew W. Computerized simulation of laser beam welding, modelling and verification. J. Phys. D-Appl. Phys. 1996;29:2811.
[15] Solana P, Ocana JL. A mathematical model for penetration laser welding as a free-boundary problem. J. Phys. D-Appl. Phys. 1997;30:1300.
[16] Ki H, Mohanty PS, Mazumder J. Modeling of laser keyhole welding: Part I. Mathematical modeling, numerical methodology, role of recoil pressure, multiple reflections, and free surface evolution. Metallurgical and Materials Transactions a-Physical Metallurgy and Materials Science 2002;33:1817.
[17] Ki H, Mohanty PS, Mazumder J. Modeling of laser keyhole welding: Part II. Simulation of keyhole evolution, velocity, temperature profile, and experimental verification. Metallurgical and Materials Transactions a-Physical Metallurgy and Materials Science 2002;33:1831.
[18] Ki H, Mohanty PS, Mazumder J. Multiple reflection and its influence on keyhole evolution. J. Laser Appl. 2002;14:39.
[19] Lee JY, Ko SH, Farson DF, Yoo CD. Mechanism of keyhole formation and stability in stationary laser welding. J. Phys. D-Appl. Phys. 2002;35:1570.
[20] Zhou J, Tsai HL, Lehnhoff TF. Investigation of transport phenomena and defect formation in pulsed laser keyhole welding of zinc-coated steels. J. Phys. D-Appl. Phys. 2006;39:5338.
[21] Zhou J, Tsai HL, Wang PC. Transport phenomena and keyhole dynamics during pulsed laser welding. Journal of Heat Transfer-Transactions of the ASME 2006;128:680.
[22] Elmer JW, Giedt WH, Eagar TW. The Transition from Shallow to Deep Penetration During Electron-Beam Welding. Weld. J. 1990;69:S167.
[23] Hemmer H, Grong O. Prediction of penetration depths during electron beam welding. Science and Technology of Welding and Joining 1999;4:219.
[24] Klemens PG. Heat Balance and Flow Conditions for Electron-Beam and Laser-Welding. J. Appl. Phys. 1976;47:2165.
[25] Wei PS, Giedt WH. Surface-Tension Gradient-Driven Flow around an Electron-Beam Welding Cavity. Weld. J. 1985;64:S251.
[26] Wei PS, Kuo YK, Ku JS. Fusion zone shapes in electron-beam welding dissimilar metals. Journal of Heat Transfer-Transactions of the ASME 2000;122:626.
[27] Palmer TA, Elmer JW. Characterisation of electron beams at different focus settings and work distances in multiple welders using the enhanced modified Faraday cup. Science and Technology of Welding and Joining 2007;12:161.
[28] Kaye GWC, Laby TB, editors. Tables of Physical and Chemical Constants. London: Longman, 1995.
[29] Lancaster JF. The Physics of Welding. Oxford: Pergamon Press, 1986.
[30] Brandes EA, Brook GB, editors. Smithells Metals Reference Book. MA: Butterworth Heinemann, 1992.
[31] Turkdogan ET. Physical Chemistry of High Temperature Technology. New York: Academic Press, 1980.
[32] Ho CY, Liley PE, Power RW, editors. National Standard Reference Data Series: No. 16: Thermal Conductivity of Selected Materials, Pt. 2, USGPO. Washington D.C.: National Bureau of Standards, 1968.
[33] Lide DR, editor CRC Book of Chemistry and Physics. FL: CRC Press, 2000.

[34] He X, Elmer JW, DebRoy T. Heat transfer and fluid flow in laser microwelding. J. Appl. Phys. 2005;97:9.
[35] Yaws CL. Handbook of Thermal Conductivity. Houston: Gulf Publishing, 1997.
[36] Iida T, Guthrie RIL. The Physical Properties of Liquid Metals Oxford: Clarendon Press, 1988.
[37] Mills KC. Recommended Values of Thermophysical Properties of Selected Commercial Alloys. Materials Park, OH: ASM, 2002.
[38] Ho CY, Touloukian YS, editors. Thermophysical Properties of Matter: Thermal Conductivity. New York: IFI/Plenum: Purdue University, 1977.
[39] Schiller S, Heisig U, Panzer S. Electron Beam Technology. Berlin: John Wiley and Sons, 1982.
[40] Mishra S, DebRoy T. Measurements and Monte Carlo simulation of grain growth in the heat-affected zone of Ti-6Al-4V welds. Acta Mater. 2004;52:1183.
[41] Kumar A, DebRoy T. Neural network model of heat and fluid flow in gas metal arc fillet welding based on genetic algorithm and conjugate gradient optimisation. Science and Technology of Welding and Joining 2006;11:106.
[42] Atthey DR. A mathematical model for fluid flow in a weld pool at high currents. J. Fluid Mech. 1980;98:787.

Chapter 5

Reliability and Tailoring Weld Geometry

5.1 Introduction

There are two main difficulties associated with the widespread use of numerical models of welding processes. First, the model results do not always agree with the experimental results because of uncertainties in the values of several model input parameters that cannot be estimated from the fundamental principles. For example, laser beam absorptivity depends on various factors like surface temperature, presence of oxide layer on the surface, angle of incidence, etc. As such, it is very difficult to estimate the value of absorption coefficient. There can also be uncertainty regarding the measured focal spot size of the laser or electron beam because the focal spot size is often measured by irradiating a thin metal foil by the energy beam for a limited time and taking the radius of the evaporated region as the beam radius. However, this method is not very accurate. For low power beams and low heating times, the evaporated region may be smaller than the beam radius. For high heating times, on the other hand, region outside the direct impact of the energy beam may be evaporated because of conductive heat transfer from the hotter regions. Thus the 'measured' beam radius may be larger than the actual beam radius. Furthermore, scattering of the beam by the gas or metal vapors present in the keyhole can result in a change in the beam radius. It is very difficult to calculate the effective values of beam radius in the presence of a cloud of metal vapors that scatter radiation. Finally, there may also be uncertainties in thermo-physical properties of the material.

Second, the numerical heat transfer and fluid flow models of welding processes are unidirectional in nature and designed to calculate weld characteristics from the welding variables. However, the ability to prescribe a set of welding process conditions to attain a particular set of weld characteristics (weld geometry, cooling rate) is often

needed but not currently possible. Moreover, since the keyhole mode welding process is very complicated and involves non-linear interactions of several welding variables, a particular weld attribute may be obtained via multiple paths. The unidirectional numerical models for keyhole mode laser welding cannot prescribe these multiple sets of welding variables.

These major problems can be solved by combining the numerical models with a suitable optimization algorithm. First, the reliability of the calculated results can be improved by estimating uncertain input parameters from a limited volume of experimental data. By coupling a genetic algorithm (GA) based optimization method [1-4] with a three dimensional (3D) heat transfer model [5, 6], the optimized values of these uncertain parameters can be determined so that the computed weld geometry agrees well with the experimental data. Second, the GA can systematically search for multiple solution sets of welding variables [7, 8], each of which can result in a specific weld geometry. Since the search involves a well tested forward heat transfer model for keyhole mode welding [5, 6], the estimation of uncertain parameters and multiple sets of welding variables comply with the phenomenological laws of welding physics.

5.2 Mathematical model

5.2.1 Heat transfer model

Welds were made on 1.0 mm thick 5182 Al-Mg alloy plates with 2.6 kW Nd:YAG laser at welding speeds varying from 63.5 mm/s to 105.8 mm/s [9]. A 3D heat transfer model [5, 6] is used for the calculation of temperature fields from a set of specified welding conditions and materials properties. Since the main goal here was to establish a methodology to estimate uncertain parameters and provide an inverse modeling capability for tailoring weld attributes, a simple forward model was selected. Aluminum alloy was chosen because of its high thermal conductivity because of which convection is not very important. The main assumptions of the model are the following:

1. A constant temperature equal to the boiling point of the alloy is assumed on the keyhole walls. Since the keyhole is exposed to the atmosphere, the equilibrium pressures of all the alloying elements add up to one atmosphere.
2. Furthermore, since the orientation of the keyhole is almost vertical, and the temperature everywhere at the keyhole wall is the boiling point of the alloy, the heat transfer takes place mainly along the horizontal plane.
3. The laser beam absorption coefficient and plasma absorption coefficient are assumed to have constant, location independent values.

The model calculates weld geometry based on several parameters which include material properties, welding process parameters and geometrical parameters. Table **5.1** lists the values used for the input parameters.

Table **5.1**: Data used in the calculations.

Physical Property	Value
Boiling point, (K) [6]	1930
Solidus temperature, (K) [6]	850
Density, (kg/m^3) [6]	2300
Specific heat, (J/kg-K) [6]	1200
Thermal conductivity, (W/m-K) [6]	108
Beam diameter at the end of the focusing lens, (mm)	28
Focal length of lens, (mm)	78
Heat of evaporation of Al, (J/kg) [10]	1.08×10^7
Heat of evaporation of Mg, (J/kg) [10]	5.25×10^7
Inverse Bremsstrahlung absorption coefficient, (m^{-1})	100
Heat transfer coefficient, (W/m^2-K)	15

The two-dimensional temperature field in an infinite plate can be calculated considering heat conduction from the keyhole wall into the plate as [11]:

$$T(r,\varphi) = T_a + \frac{P'}{2\pi\lambda} K_0(\Omega r) e^{-\Omega r \cos\varphi} \qquad (\mathbf{5.1})$$

where (r, φ) designates the location in the plate with the line source as the origin, T_a is the ambient temperature, P' is the power per unit depth, λ is the thermal conductivity, K_0 is the solution of the second kind and zero-order modified Bessel function and, $\Omega = \nu/2\kappa$, where ν is the welding speed and κ is the thermal diffusivity.

The radial heat flux conducted into the keyhole wall, I_c can be obtained from the relation:

$$I_c(r,\varphi) = -\lambda \frac{\partial T(r,\varphi)}{\partial r} \qquad (5.2)$$

The locally absorbed beam energy flux, I_a, on the keyhole wall taking into account the absorption by the work-piece during multiple reflections and the plasma absorption is calculated as [5, 6]:

$$I_a = e^{-\beta l}\left(1-(1-\alpha)^{1+\pi/4\theta}\right)I_0 \qquad (5.3)$$

where β is the inverse Bremsstrahlung absorption coefficient of plasma, 'l' is the average path of the laser beam in plasma before it reaches the keyhole wall, α is the absorption coefficient of the work piece, θ is the average angle between the keyhole wall and the initial incident beam axis, and I_0 is the local incident beam intensity.

The evaporative heat flux, I_v on the keyhole wall is given as:

$$I_v = \sum_{i=1}^{n} J_i \Delta H_i \qquad (5.4)$$

where n is the total number of alloying elements in the alloy, ΔH_i is the heat of evaporation of element 'i', and J_i is the evaporation flux of element 'i' given by the modified Langmuir equation [12-14]:

$$J_i = \frac{a_i P_i^0}{7.5}\sqrt{\frac{M_i}{2\pi R T_b}} \qquad (5.5)$$

where a_i is the activity of element 'i', P_i^0 is the equilibrium vapor pressure of element i over pure liquid at the boiling point T_b, and M_i is the molecular weight of element 'i'. The factor 7.5 is used to account for the diminished evaporation rate at one atmosphere

pressure compared to the vaporization rate in vacuum and is based on previous experimental results [13, 14].

A simple heat flux balance on the keyhole wall gives the following relation for local keyhole wall angle θ:

$$\tan(\theta) = \frac{I_c}{I_a - I_v} \qquad (\mathbf{5.6})$$

The keyhole model solves these equations to calculate the temperature distribution in the work-piece from the top surface of the sample up to the bottom of the keyhole. To calculate the temperature profile below the keyhole and hence to calculate the total weld pool depth, the model is combined to another computer code which solves the following heat conduction equation:

$$\frac{\partial^2 T}{\partial x^2} + \frac{\partial^2 T}{\partial y^2} + \frac{\partial^2 T}{\partial z^2} - \frac{\nu}{\kappa}\frac{\partial T}{\partial x} = 0 \qquad (\mathbf{5.7})$$

where ν is the welding speed and κ is the thermal diffusivity of the work-piece. The other boundary conditions are as follows:

The boundary condition for the bottom surface is given by:

$$J(x, y, z)\big|_{z=max} = h[T_a - T(x, y, z)\big|_{z=max}] \qquad (\mathbf{5.8})$$

where $J(x, y, z)$ is the heat flux, h is the heat transfer coefficient, T_a is the ambient temperature, and $T(x, y, z)$ is the local temperature.

The temperatures at the surfaces far from the heat source are assumed to be equal to the ambient temperature. The 3D numerical model for the solution of the above equations, henceforth referred to as the forward numerical model, gives the temperature distribution in the work-piece.

5.2.2 Genetic Algorithm as an optimization model

The first step in the computational procedure is to optimize the values of the uncertain parameters in the model namely, the beam radius at the focal plane (r) and the laser beam absorption coefficient (α). A population of randomly generated sets of uncertain parameters is initially formed by the GA [1, 2, 15]. The weld pool depth and width are calculated using the forward numerical model for each of the sets of uncertain parameters for each of the welding conditions in the experimental data set [9]. Table **5.2** shows the experimental data set used for this study, consisting of five welding conditions and the corresponding weld pool dimensions, i.e. depth and width. The deviation of computed depth and width from the corresponding experimentally observed results can be quantified by the following objective function:

$$O1(f) = \sum_{k=1}^{5}\left[\left|\frac{d^c}{d^e} - 1\right|_k + \left|\frac{w_t^c}{w_t^e} - 1\right|_k + \left|\frac{w_b^c}{w_b^e} - 1\right|_k\right] \qquad (\mathbf{5.9})$$

where 'k' designates the specific set of welding conditions given in Table **5.2**, d^c, w_t^c and w_b^c are the computed weld pool depth, width at top of the work-piece, and width at bottom of the work-piece, respectively, and d^e, w_t^e, and w_b^e are the corresponding experimental weld pool depth, width at top of the work-piece, and width at bottom of the work-piece for these sets of welding conditions. Note that for each of the five welding conditions the experimental weld depth was equal to the work-piece thickness. Two values of width have been specified for the weld pool cross-section, i.e. at the top and at the bottom of the work-piece to ensure a better correspondence between a low objective function O1(f) and a good agreement between the calculated and the experimental weld pool geometry.

Table **5.2**: Welding conditions and weld dimensions

Data set	Power (W)	Welding speed (mm/s)	Defocus (mm)	Experimental value		
				Weld pool depth (mm)	Weld pool width (mm)	
(a)	2600	63.5	0.0	1.0	2.35	1.67
(b)	2600	74.1	0.0	1.0	2.27	1.83
(c)	2600	84.7	0.0	1.0	1.96	1.23
(d)	2600	93.5	0.0	1.0	1.73	0.73
(e)	2600	105.8	0.0	1.0	1.63	0.56

The objective function O1(f) depends on the beam radius at the focal plane 'r', and the absorption coefficient α.

$$O1(f) = f\left(\frac{r}{r_0}, \alpha\right) \qquad (\mathbf{5.10})$$

where $r_0 = 0.3$ mm is a reference value of the radius of the beam experimentally measured at the focal point. The random values of 'r' are generated by the following scheme. The value of the relative error 'e' in beam radius is randomly generated within a negative lower limit and a positive upper limit. The upper and the lower limits are the specified maximum positive and negative errors, respectively, in the measurement of radius. The relative error in beam radius, 'e', can be either positive or negative. The value of 'r' is then calculated as:

$$r = (1+e)r_0 \qquad (\mathbf{5.11})$$

The values of absorption coefficient are also randomly generated within an upper and a lower limit. A systematic global search is then undertaken by the GA to find the set of uncertain parameters which result in least value of the objective function, i.e. which give weld pool depth and width values very close to the experimental values. The effectiveness of the search for optimized values of the two parameters is enhanced by using dimensionless values of radius which is comparable in magnitude with the absorption coefficient. The sets of unknown input parameters commonly referred as population in GA, changes with every iteration following the rules of GA [1-4]. The GA

used in the present study is a parent-centric recombination (PCX) operator-based generalized generation gap (G3) model [1, 2]. This particular GA was chosen because it has a faster convergence rate on standard test functions compared to other evolutionary algorithms [16, 17].

After obtaining the optimized values of uncertain parameters using GA, the next step is to search for multiple pathways or different sets of welding variables, i.e. laser power, welding speed and beam defocusing to obtain pre-defined specific weld geometry. Since multiple solutions are needed, it is important to prevent premature convergence of the PCX G3 GA population. The tendency to converge prematurely was reduced by replacing sets of welding variables similar to the current best solution with randomly generated sets of welding variables after a fixed number of iterations. An initial population of randomly selected welding variables is formed by the PCX- G3 GA. For each set of the welding variables, the forward numerical model calculates the weld pool dimensions, i.e. depth and width at top and bottom of the work-piece. Not all sets of welding variables result in the desired weld pool geometry. The deviation between the weld pool geometry for any set of welding variables and the target geometry is obtained as:

$$O2(f) = \left|\frac{d^c}{d^e} - 1\right| + \left|\frac{w_t^c}{w_t^e} - 1\right| + \left|\frac{w_b^c}{w_b^e} - 1\right| \qquad (\mathbf{5.12})$$

where d^c, w_t^c and w_t^c are the computed weld pool depth, width at top of the work-piece, and width at bottom of the work-piece, respectively, and d^e, w_t^e, and w_b^e are the corresponding experimental weld pool depth, width at top of the work-piece, and width at bottom of the work-piece for the target geometry chosen for the study. The objective function depends on the three welding variables: laser power 'P', welding speed ν, and beam defocusing δ.

$$O2(f) = O2\left(\frac{P}{P^0}, \frac{\nu}{\nu^0}, \frac{\delta}{\delta^0}\right) \qquad (\mathbf{5.13})$$

where P^0, ν^0, and δ^0 are the reference values of the variables that represent the order of magnitude of the respective variables. The non-dimensional values of different welding

variables are comparable in magnitude. Thus, the importance of each welding variable is preserved by their non-dimensional values. The actual values of the welding variables are calculated by multiplying the non-dimensional value with the corresponding reference value. The GA then systematically searches for sets of welding variables that produce weld dimensions that are close to the target dimensions. The search involves improvement in the values of the GA population with iterations following certain laws of GA [1-4].

The specific application for using this model for optimizing sets of unknown input parameters is explained in the Appendix C and a similar methodology is followed for obtaining multiple sets of welding variables.

5.3 Results and Discussion

5.3.1 Improving reliability of calculated results

Since the model is based on well-tested equations of heat transfer the mismatch between the computed and the experimental results may be attributed primarily to uncertainties in some of the input parameters. Values of the beam radius at the focal plane and absorption coefficient were identified as the important uncertain parameters and their values were estimated from a limited volume of experimental data. Assuming that energy absorption is due to photon-electron interaction, the absorption coefficient for clean flat surfaces can be estimated from the following relation [18]:

$$\alpha = 0.365\left(\frac{\rho}{\lambda}\right)^{1/2} - 0.0667\left(\frac{\rho}{\lambda}\right) + 0.006\left(\frac{\rho}{\lambda}\right)^{3/2} \qquad \textbf{(5.14)}$$

where ρ is the electrical resistivity (ohm-cm) of the liquid metal at the boiling point, and λ is the wavelength (cm) of the incident laser beam. However, the estimated absorption coefficient may differ from the actual value owing to naturally occurring oxide layers and other surface imperfections. Significant errors may also exist in the measured value of beam radius at the focal plane. Using GA and the five sets of welding conditions given in

Table **5.2**, the value of the beam radius was estimated to be 0.232 mm and the value of absorption coefficient was estimated to be 0.096.

Figure **5.1** shows the 3D temperature fields calculated using the estimated values of beam radius and absorption coefficient for the welding conditions corresponding to data set (e) listed in Table **5.2**. Welding direction is the positive x direction. The keyhole boundary is marked by the boiling point of the alloy (1930 K) whereas the region between the boiling point and solidus temperature (850 K) indicates the weld pool. As seen in Figure **5.1**, the weld pool is highly elongated at the rear and compressed at the front. This is due to the high welding speed.

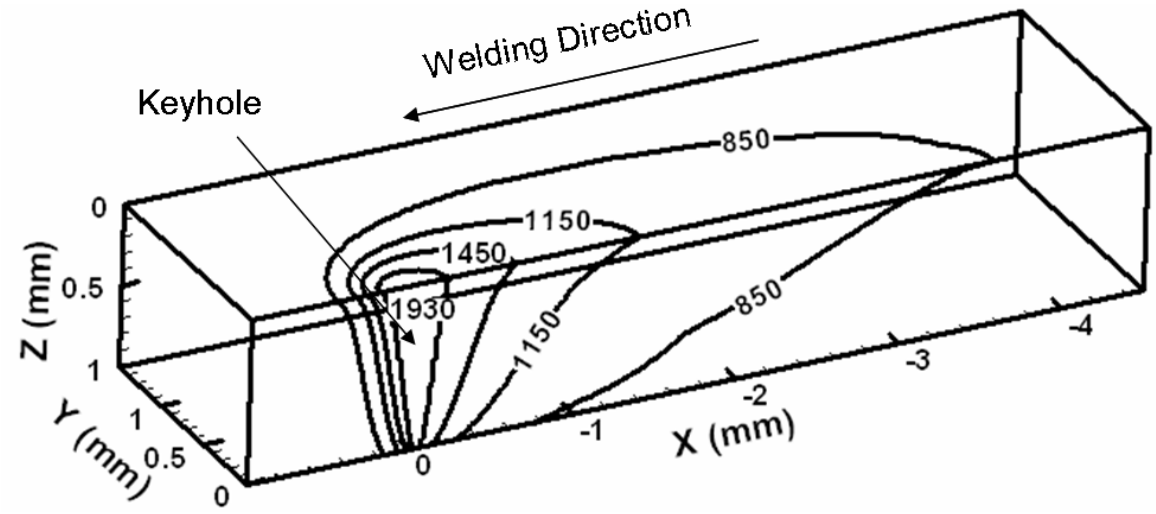

Figure **5.1**: Computed temperature fields: 5182 Al alloy, power: 2600 W, speed: 106 mm/s, defocus: 0 mm. Temperatures on isotherms are in K.

Figure **5.2** shows the weld geometries calculated using the optimized values of uncertain parameters for the five sets of welding conditions given in Table **5.2**. The equilibrium solidus temperature of the 5182 Al alloy (850 K) marks the calculated weld pool boundary. Figure **5.2** (a)-(e) show a reasonable agreement between the calculated and the experimentally measured weld pool dimensions indicating that the computed values of the laser beam absorption coefficient and the beam radius are appropriate.

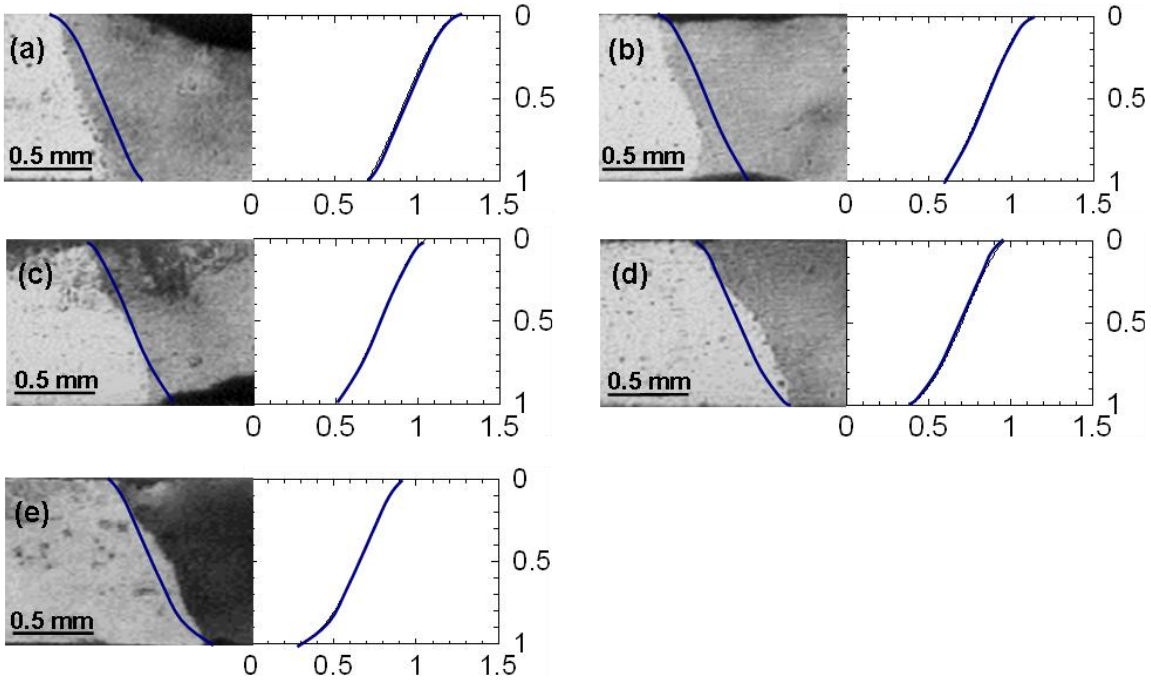

Figure **5.2**: Experimental and calculated weld pool dimensions for the five sets of welding conditions given in Table **5.2**, i.e., 2600 W power, 0 mm defocus, and (a) 63.5 mm/s, (b) 74.1 mm/s, (c) 84.7 mm/s, (d) 93.5 mm/s, and (e) 105.8 mm/s. The solid lines are the calculated weld pool boundaries.

5.3.2 Multiple sets of process variables

The first step towards obtaining multiple solution sets of welding variables for specified weld geometry is to define the desired weld geometry. As described previously, three parameters, i.e. depth, width at the top of the work-piece, and width at the bottom of the work-piece define the weld geometry. Weld geometry corresponding to experimental data set (c) in Table **5.2** was chosen as the target weld geometry in this study. Thus, one or more solution(s) in the GA population with acceptable low objective function value is likely to have welding variables with values very close to the corresponding welding variables of data set (c).

After identifying the target geometry, the GA was used to calculate multiple sets of welding variables, i.e., laser power, welding speed, and beam defocusing combinations

that would result in the specified weld geometry. To ensure a diverse initial set of welding variables, the values of these welding variables were generated randomly within their specified ranges. The goal was to minimize chances of premature convergence. In other words, diverse initial sets of welding variables reduce the chances of the population becoming similar without much improvement in the objective function value, and/or in case of a requirement of multiple solutions, most of the low objective function members have almost similar values. A GA population size of 200 was chosen for this study. This number of variable sets was chosen based on how the population size influenced the effectiveness of GA using standard test functions [1, 2] and the spread of GA variables for this problem.

Figure **5.3** (a) shows the initial GA population, which include the sets of laser power, welding speed, and beam defocus. The values of input power were chosen in the range of 2300 to 2800 W, welding speed in the range of 95 to 130 mm/s, and beam defocus in the range of -1.0 to +0.5 mm. The variable sets were then improved iteratively. Iterations were stopped when the objective function values for a sufficient percentage of the GA population were below a prescribed limit. Values of the welding variables for the initial GA population are shown in Figure **5.3** (a) and their objective function values are plotted in Figure **5.3** (b). For several sets of the welding variables the objective function value is very low when compared to the general population, indicating the possibility of finding solution sets near these 'peaks' with sufficiently low objective function values.

Figure **5.4** (a) shows that the average value of objective function decreases with the number of iterations. However, the figure also shows that the average objective function sometimes changes abruptly. For example, a sudden increase in the objective function value was observed after 75 iterations. Sometimes several individuals form a cluster around a single solution during iterations. To promote diversity, the crowding was reduced every twenty five iteration by replacing all individuals in the cluster, except the best individual, with randomly generated individuals. The new members affected the average fitness values significantly after 75 iterations as seen in Figure **5.4** (a). The objective function for the best member of the population also decreased, although not

continuously, with iterations as shown in Figure **5.4** (b). The creation of new members clearly affects the minimum values of the objective function with iterations and the variation is not continuous because of the uncertain nature of the fitness changes with iterations. Figure **5.4** (c) shows almost a gradual increase in the number of qualified low objective function individuals with iterations. Abrupt changes in the behavior occur when individuals in a cluster are deliberately replaced by randomly selected individuals to reduce the elite preserving nature of the GA.

The individuals with low objective function values obtained after the final iteration represent the alternative pathways for obtaining the target weld geometry. Table **5.3** lists the solutions, i.e., some of the many sets of welding variables that will result in the target weld geometry. The solutions are spread over a wide range for all the three welding variables. The results show a variation of about 35 % above the minimum value of power. Similarly, there is a variation of about 58 % in speed and significant variation, between -1.31 mm and 0.49 mm, in the defocus values among various combinations of solutions. Although the GA recommends many solution sets, these solutions are not exhaustive and many more welding variable sets may exist for the same target geometry.

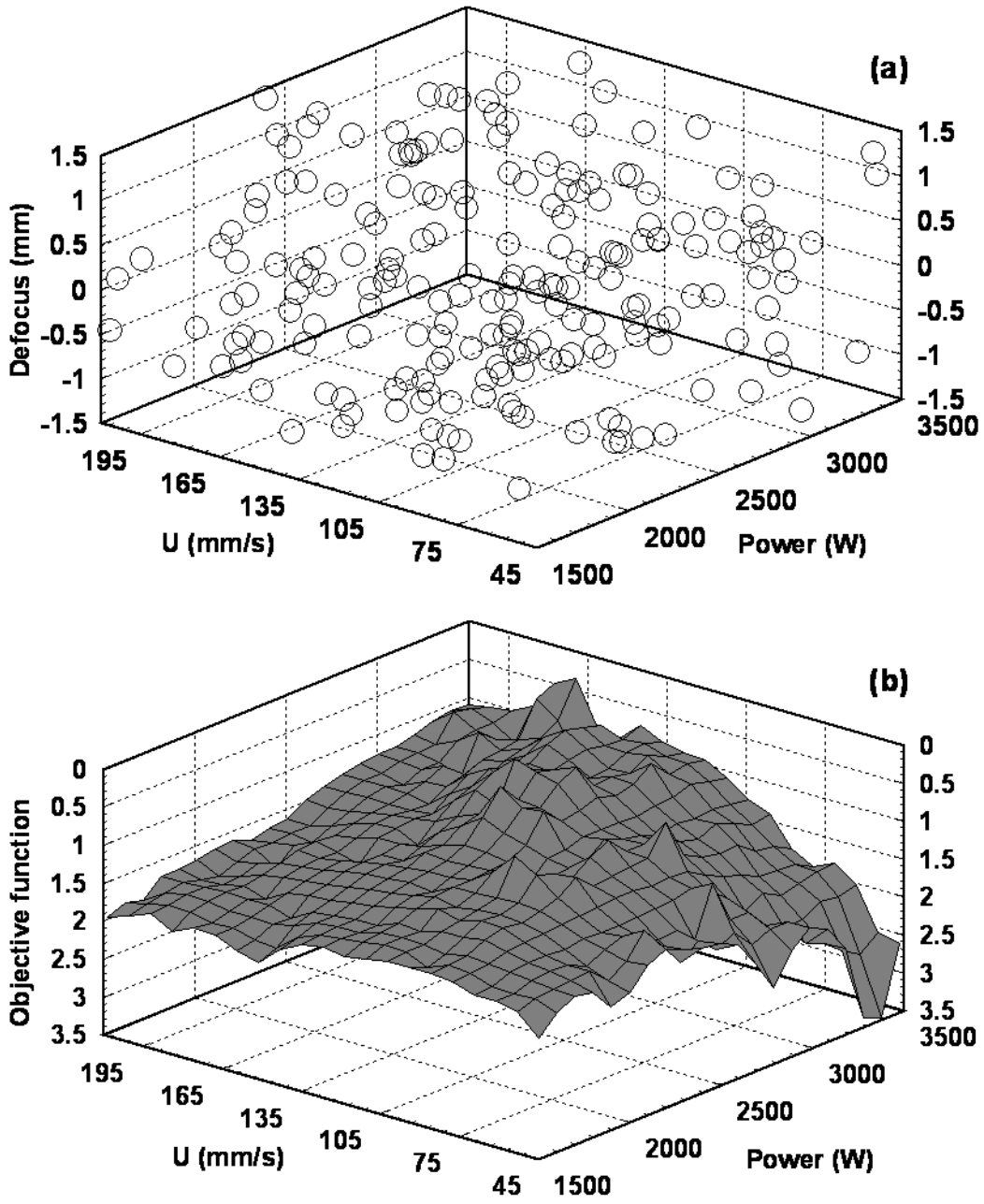

Figure **5.3**: Initial population of randomly chosen values of welding variable sets and their objective function values. (a) A large space of variables was searched to find optimum solutions (b) Low values of objective function for several sets of welding variables suggest presence of multiple optimal solutions.

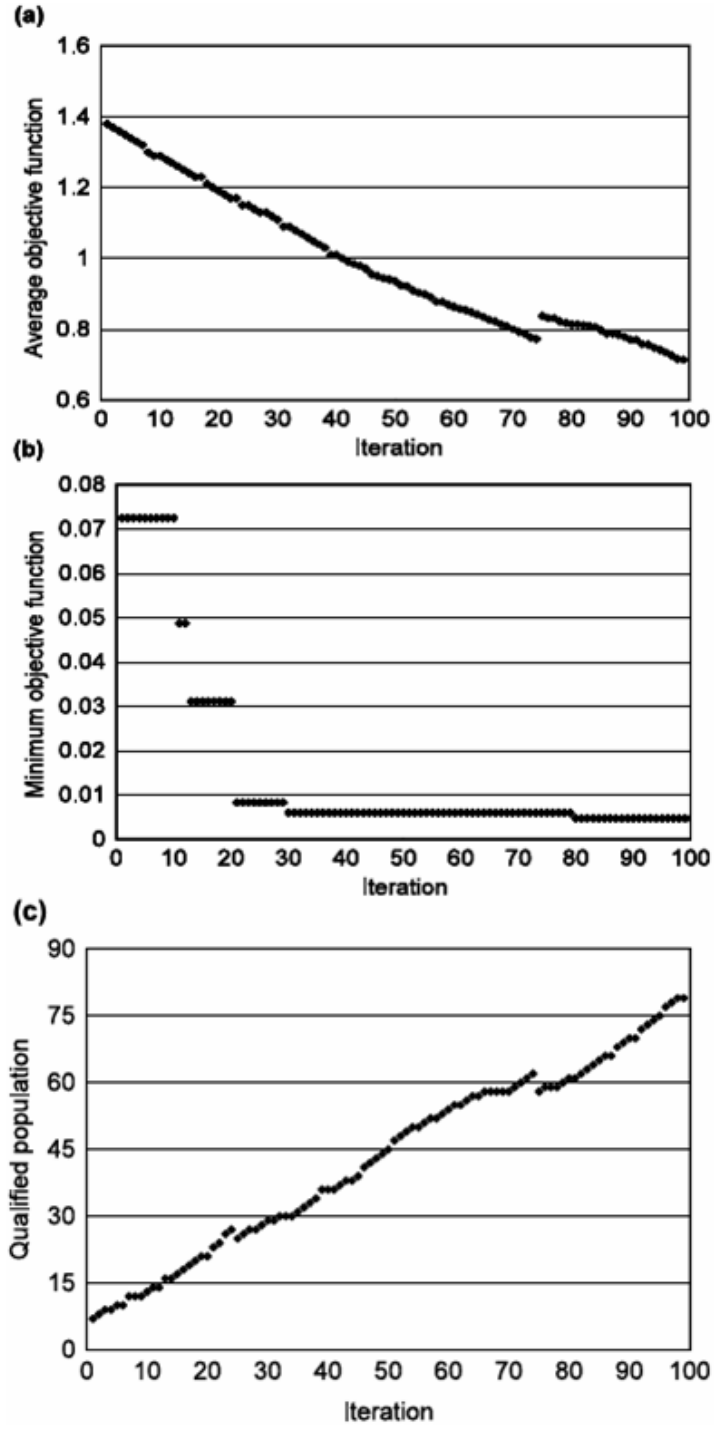

Figure **5.4**: Plots show the (a) variation of population averaged objective function with iterations, (b) variation of minimum objective function value with iterations, and (c) number of individuals whose objective function values defined by equation (12) are lower than 0.2.

Figure **5.5** shows the transverse section keyhole profile, along with the weld pool boundary, for each of the six solution sets of welding variables given in Table **5.3**. We see that sets of welding variables very different from each other can result in similar keyhole profiles and weld pools. Figure **5.6** shows the comparison of weld geometries calculated for the different sets of welding conditions (values of input power, welding speed, and beam defocus given in Table **5.3**) using the 3D heat transfer model with the specified weld geometry. The calculated weld pool boundary is marked by the solidus temperature of the 5182 Al alloy (850 K). The calculated geometry agreed reasonably well with the target geometry in each case as seen in Figure **5.6**. Thus, each set of welding variables listed in Table **5.3** results in weld geometry close to the target geometry. Any one of the six sets of welding conditions may be chosen to obtain the specified geometry. A higher welding speed may be desired if the production rate is an important consideration. On the other hand, system limitations may require use of a lower power laser. Note that the first set of welding conditions in Table **5.3** is very close to the experimental welding conditions for our target geometry.

Table **5.3**: Optimized sets of laser power, welding speed, and beam defocus to achieve the following weld pool dimensions: weld pool depth = 1.0 mm, weld pool width at the top surface = 1.63 mm, and weld pool width at the bottom surface = 0.56 mm.

	Power (W)	Speed (mm/s)	Defocus (mm)
(a)	2586	108	0.06
(b)	2843	157	-0.87
(c)	2947	133	0.34
(d)	3278	133	0.49
(e)	3354	162	0.22
(f)	3488	171	-1.31

5.4 Summary and conclusions

Values of certain parameters like the focal spot radius of laser beam and absorption coefficient are often not known accurately. Therefore, a real number based GA was combined with a 3D heat transfer model for keyhole mode laser welding to estimate the values of these parameters by minimizing the difference between the calculated and the measured weld dimensions for keyhole mode laser welding of 5182 Al-Mg alloy for five sets of welding conditions. Using these values of focal spot radius and absorption coefficient, the computed weld geometries were found to be in good agreement with the experimentally observed weld geometry for all the five experimental conditions. Numerical models of heat transfer can thus be combined with a GA and a limited volume of experimental data of weld geometry during keyhole mode laser welding to improve reliability of predictions of temperature fields and weld geometry. Even though only two uncertain parameters were optimized using GA in this work, other parameters like effective thermal conductivity and viscosity in a turbulent weld pool and effective values of temperature dependent thermo-physical properties can also be optimized using this methodology.

The GA was also combined with the 3D heat transfer model of keyhole mode laser welding to find welding conditions which could result in a specified weld geometry. Multiple sets of laser power, welding speed, and beam defocus with widely different values were found to meet the specified weld width at the top and the bottom of the plate. Therefore, the weld geometry for keyhole mode welding of 5182 Al-Mg alloy can be tailored based on scientific principles via multiple pathways, i.e., using different combinations of laser power, welding speed and laser beam defocus. Following this methodology, welding conditions to obtain other weld attributes such as a desired cooling rate can also be obtained.

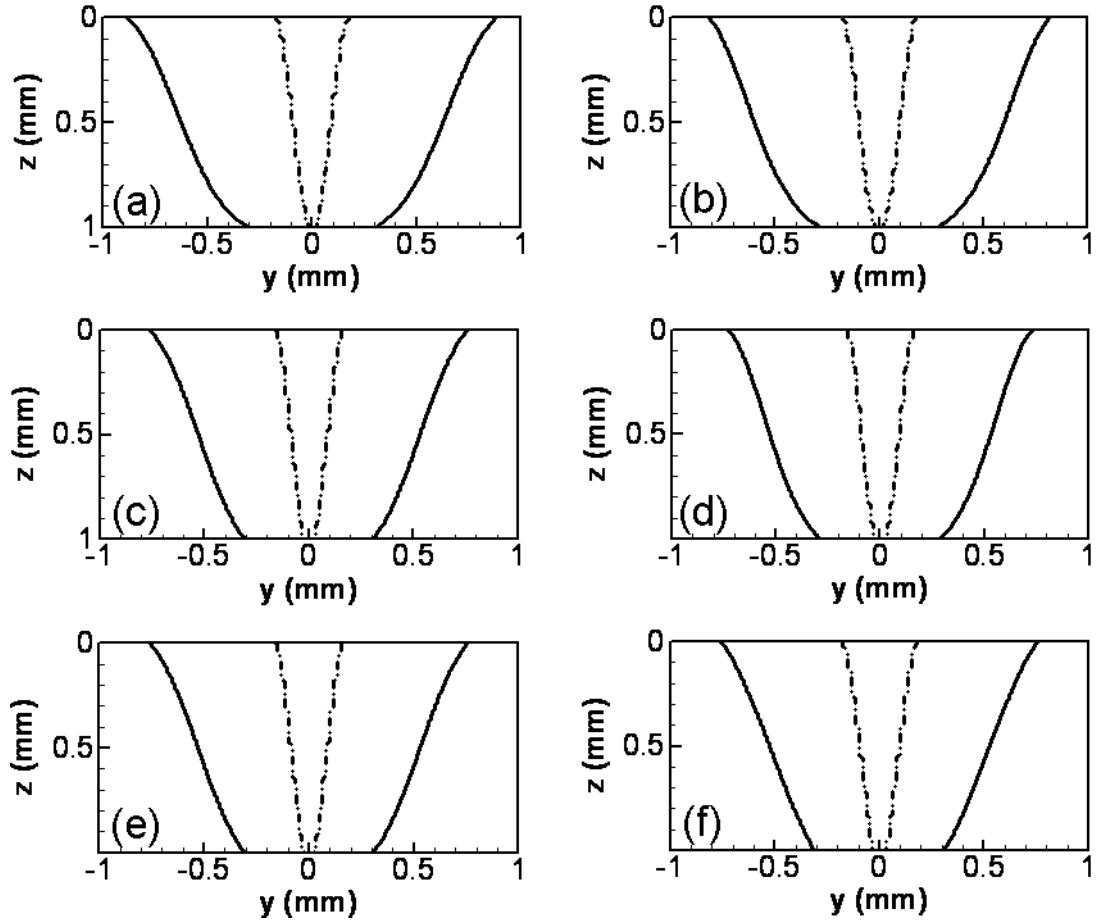

Figure **5.5**: The transverse section keyhole boundary and the weld pool boundary for each of the six solution sets of welding variables in Table **5.3**. Broken lines mark the keyhole boundary and the solid lines indicate the weld pool boundary.

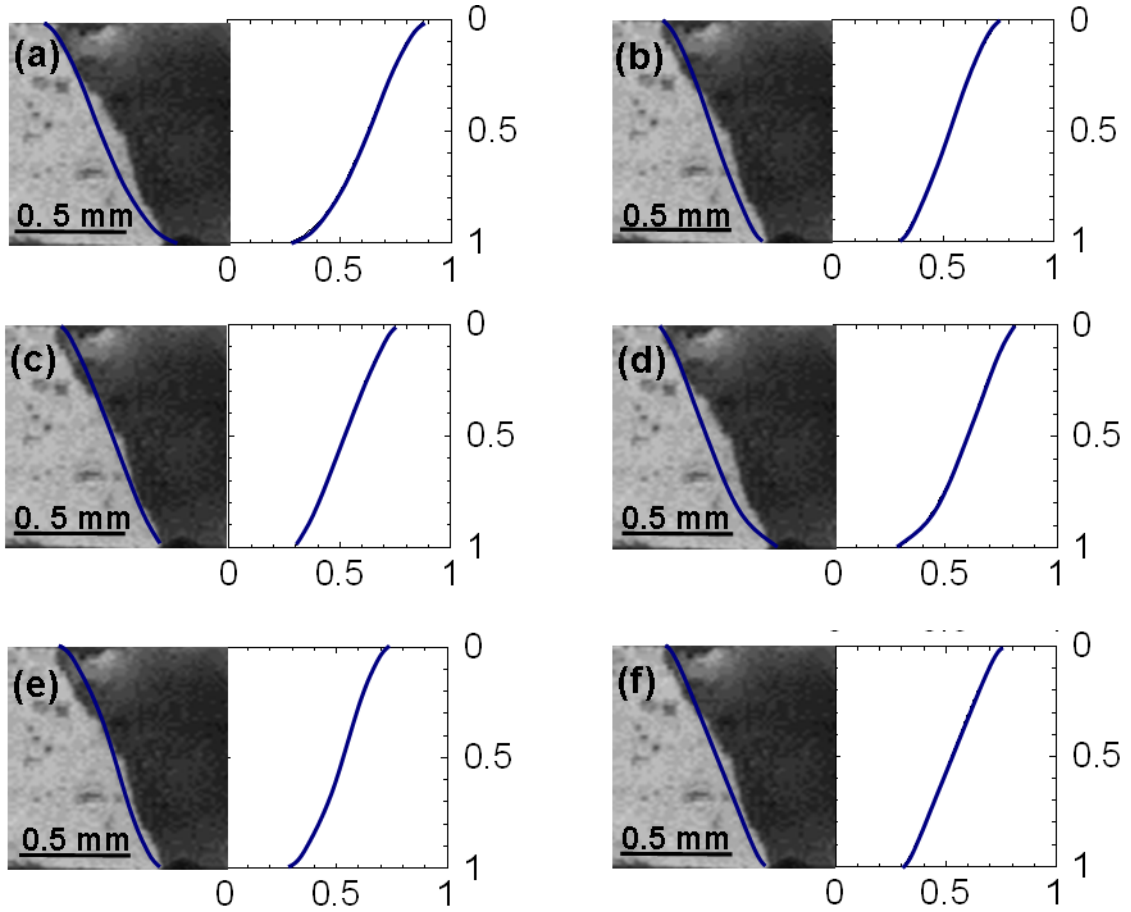

Figure **5.6**: Comparisons between the calculated and the experimental weld pool geometry for different optimized combinations of welding variables given in Table **5.3**. The solid line marks the computed weld pool boundary which represents the equilibrium solidus temperature of 5182 Al alloy.

5.5 References

[1] Deb K. Multi-objective optimization using evolutionary algorithms. New York: Wiley, 2001.
[2] Deb K, Anand A, Joshi D. A computationally efficient evolutionary algorithm for real-parameter optimization. Evolutionary Computation 2002;10:371.
[3] Goldberg DE. Genetic Algorithm in Search, Optimization and Machine Learning. MA:Addison: Wesley, 1989.
[4] Back T, Fogel DB, Michalewicz Z, editors. Handbook of Evolutionary Computations. New York: Oxford University Press, 2000.

[5] Kaplan A. A Model of Deep Penetration Laser-Welding Based on Calculation of the Keyhole Profile. J. Phys. D-Appl. Phys. 1994;27:1805.
[6] Zhao H, DebRoy T. Macroporosity free aluminum alloy weldments through numerical simulation of keyhole mode laser welding. J. Appl. Phys. 2003;93:10089.
[7] Mishra S, Debroy T. A computational procedure for finding multiple solutions of convective heat transfer equations. J. Phys. D-Appl. Phys. 2005;38:2977.
[8] Mishra S, DebRoy T. A heat-transfer and fluid-flow-based model to obtain a specific weld geometry using various combinations of welding variables. J. Appl. Phys. 2005;98.
[9] Pastor M, Zhao H, Martukanitz RP, Debroy T. Porosity, underfill and magnesium loss during continuous wave Nd : YAG laser welding of thin plates of aluminum alloys 5182 and 5754. Weld. J. 1999;78:207S.
[10] Brandes EA, Brook GB, editors. Smithells Metals Reference Book. MA: Butterworth Heinemann, 1992.
[11] Rosenthal D. Trans. ASME 1946;48:848.
[12] Block-bolten A, Eagar TW. Metal Vaporization from Weld Pools. Metallurgical Transactions B-Process Metallurgy 1984;15:461.
[13] Collur MM, Paul A, Debroy T. Mechanism of Alloying Element Vaporization During Laser-Welding. Metallurgical Transactions B-Process Metallurgy 1987;18:733.
[14] Sahoo P, Collur MM, Debroy T. Effects of Oxygen and Sulfur on Alloying Element Vaporization Rates During Laser-Welding. Metallurgical Transactions B-Process Metallurgy 1988;19:967.
[15] Kumar A, Mishra S, Elmer JW, Debroy T. Optimization of the Johnson-Mehl-Avarami equation parameters for alpha-ferrite to gamma-austenite transformation in steel welds using a genetic algorithm. Metallurgical and Materials Transactions A-Physical Metallurgy and Materials Science 2005;36A:15.
[16] Deb K, Anand A, Joshi D. Report No. 2002003. KanGAL, Indian Institute of Technology (Kanpur, India), 2002.
[17] Deb K. Report No. 2003003. KanGAL, Indian Institute of Technology (Kanpur, India), 2003.
[18] Bramson MA. Infrared Radiation: A Handbook for Applications New York: Plenum, 1968.

Chapter 6

Concluding Remarks

6.1 Summary and Conclusions

Three dimensional (3D) heat transfer and fluid flow models for keyhole mode laser beam and electron beam welding (EBW) were developed. A turbulence model based on Prandtl's mixing length hypothesis was used to estimate the effective thermal conductivity and viscosity values. Temperatures on keyhole walls were assumed to be constant in laser beam welding (LBW). In EBW, keyhole wall temperatures were calculated from the equilibrium temperature versus pressure relation for the material and the vapor pressures in the keyhole. The vapor pressure in the keyhole was calculated from a balance between the hydrostatic force, the surface tension force and the vapor pressure. The following are the main conclusions:

1. The numerical heat transfer and fluid flow model for keyhole mode LBW was applied to materials with wide ranging thermo-physical properties like density, thermal conductivity and boiling point, and under varying input power and welding speeds. The tested materials included important engineering alloys like 5754 aluminum alloy, A131 structural steel, 304L stainless steel, Ti-6Al-4V alloy, vanadium, and tantalum.
    a. The computed cross-sectional geometry agreed reasonably well with the experimental observations for all the materials over a wide range of welding conditions considered. The weld pool geometry was related to the material properties. Tantalum welds were smaller compared to steel welds under similar welding conditions due to its higher boiling point. The weld cross-sectional width of high thermal conductivity alloys like aluminum gradually decreases from the top to the bottom of the weld. As opposed to that, the low thermal conductivity alloys like steel have nail-

head shaped geometry. This widening of the weld pool near the top surface of the weld pool is due to the surface tension gradient driven fluid flow that carries heat outwards from the hot keyhole region.

b. Convective heat transfer was important for all the materials investigated. However, as shown by the calculation of Peclet number, convective heat transfer was more significant for materials with lower thermal diffusivity (steel) than those with higher thermal diffusivity (aluminum). This difference in the importance of convective heat transport resulted in different weld shapes for low and high thermal diffusivity alloys.

c. Turbulence was more important for locations near the weld pool surfaces.

d. The free-surface calculations showed significant deformation of the bottom surface of the full penetration weld under the effect of recoil pressure and weight of the liquid melt pool.

e. The calculation of solidification parameters for alloys showed that the plane front stability criterion under the theory of constitutional supercooling was not satisfied. Solidification structure was related to the solidification parameters.

f. Cooling rates were studied for both partial and full penetration welds and related to the observed microstructure. In particular, cooling rates were much higher at the bottom of partial penetration welds compared to the bottom of partial penetration welds. This was reflected in finer observed microstructure for partial penetration welds.

2. For EBW, the numerical model considered the variation of keyhole wall temperatures with depth and its effect on the heat transfer and fluid flow in the weld pool. The model was tested for 21Cr-6Ni-9Mn stainless steel and Ti-6Al-4V welds made with different input powers, and 304L stainless steel welds made with same input power but different power density distributions. The power density distributions were varied at fixed input power by varying the focal spot size.

a. The calculated and experimental weld geometries and thermal cycles agreed reasonably well for the work-piece materials and welding conditions considered. The volume of the fusion zones depended on the material properties like density, specific heat and melting point. Due to the higher boiling point and lower solid state thermal conductivity of Ti-6Al-4V, higher peak temperatures were obtained in Ti-6Al-4V compared to similar locations in 21Cr-6Ni-9Mn steel.
b. Increase in the focal spot size resulted in more diffused power distribution which led to a decrease in penetration depth and the increase in weld width. Higher peak power density with the same input power, resulted in higher keyhole wall temperatures and vapor pressure in the keyhole.
c. From the calculation of dimensionless numbers, it was found that convection was the dominant mechanism of heat transfer in the weld pool, and the gradient of surface tension played an important role in the fluid flow. Calculated weld pool was much narrower in absence of convection compared to when convection was present. The calculated weld pool also lacked the nail-head shape when convection was not considered. The Lorentz force was insignificant compared with the Marangoni force.

3. Calculation of temperatures and fluid velocities for EBW and LBW for similar process parameters (except the lower ambient pressure in EBW) showed that lower equilibrium wall temperatures enable easier (deeper) keyhole penetration, and hence, deeper welds. However, as a result of lower keyhole wall temperatures, the weld pool in EBW is narrower compared to LBW since less heat is conducted from the keyhole walls into the work-piece.
4. The numerical models for keyhole mode welding could be applied to materials with wide ranging thermo-physical properties. The results show that a computationally efficient model combining 3D heat transfer and fluid flow calculations with a keyhole geometry sub-model can significantly improve the understanding of keyhole welding of different materials.

5. Uncertain parameters involved in LBW (laser beam radius and absorption coefficient) could be estimated using genetic algorithm with the numerical model and limited volume of experimental data. The results show that the reliability of calculations can be improved by combining numerical models with an optimization algorithm.
6. Genetic algorithm was used to find various welding conditions that would result in a specified weld geometry. It was found that significantly different sets of welding conditions can result in similar weld geometries.

6.2 Future work

During the course of this research, several areas were identified that required future research.

First, the keyhole calculation model in this study considers multiple reflections by using an average location independent enhanced absorption coefficient based on averaged conical keyhole geometry. However, in reality the enhancement in absorption may be non-uniform depending on the shape of the keyhole. A ray tracing procedure for estimating the enhancement in absorption coefficient at all locations on the keyhole wall due to multiple reflections for the calculated keyhole profile will require calculations of surface normal at each point on the keyhole wall. This task will significantly increase the computational work involved in the keyhole geometry calculation. An alternative is to follow a ray-tracing procedure assuming a conical keyhole shape. For such a keyhole shape, simple geometric relations will apply. However, calculation of local temperature on the three dimensional keyhole surface has to be undertaken simultaneously with the heat transfer and fluid flow calculations in the weld pool. As a result, the computational task will be significantly more intensive than the model demonstrated in this thesis. However, the main merit of undertaking such a project would be to examine the extent of temperature variation on the keyhole surface.

Secondly, the temperatures everywhere on the keyhole walls in LBW have been assumed to be equal to the boiling point of the alloy at 1 atm pressure. Since the

variation in keyhole wall temperatures with depth is small and not likely to effect the keyhole penetration significantly, this assumption is reasonable. However, as discussed in Chapter 3, assumption of constant keyhole wall temperatures may result in calculated weld geometry that has a tapered lower part whereas the observed lower part of fusion zone is usually parallel-sided. Therefore, the procedure for calculating the keyhole wall temperatures in EBW can also be followed for LBW. However, except near the tip of the keyhole, the procedure is not likely to have any impact.

Thirdly, the calculated temperature fields and thermal cycles can be used to calculate the expected microstructure and the stress in the work-piece. This will require use of phenomenological models for the respective tasks.

Finally, this methodology of improving the modeling results and tailoring weld attributes involves many runs of the numerical code. This makes the computational task very time taking. To reduce the computational time, a neural network may be used. The neural network can be trained using various sets of input parameters covering the whole range of process conditions expected in the welding process and the results computed for these input parameters using the numerical model.

Appendix A

Variation of Keyhole Wall Temperatures

The keyhole is kept open as a result of a balance between the vapor pressure inside the keyhole, the surface tension and the hydrostatic force at the vapor-liquid interface. The force balance at the keyhole walls is given by Eq. **A.1**:

$$P = P_0 + \gamma(T)/r(z) + \rho g z \qquad (\mathbf{A.1})$$

where P is the vapor pressure inside the keyhole, P_0 is the ambient pressure, $\gamma(T)$ is the surface tension at local wall temperature T, ρ is the density, and g is the acceleration due to gravity. r(z) is the average radius of curvature of the keyhole at distance z from the top surface, and is taken to be half of the keyhole diameter along the welding direction. Variation of vapor pressure with temperature can be given by integrating the Clausius-Clapeyron equation [1]:

$$P = P_0 \exp\left(H_{LV} \frac{T - T_{LV}}{RTT_{LV}} \right) \qquad (\mathbf{A.2})$$

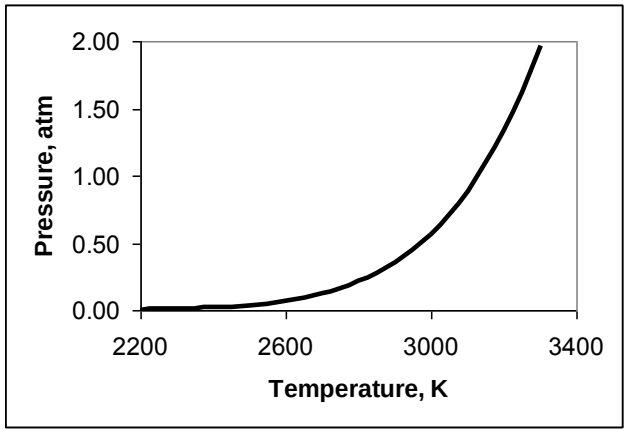

Figure **A.1**: Equilibrium vapor pressure versus temperature variation.

Figure **A.1** shows the variation of pressure for iron according to the Clausius-Clapeyron equation. In typical electron beam welding, $P_0 \sim 0$ atm, while in typical laser welding $P_0 \sim 1$ atm. From Figure **A.1**, an excess pressure (i.e. the pressure difference between the top and the bottom of the keyhole) of say, 0.5 atm, in an electron beam welding cavity will result in temperature difference of several hundred degrees Kelvin. Since there is a continuous flow of metal vapors out of the keyhole, it can be assumed that the vapor cavity in laser beam welding is filled with metal vapors. Thus, for a similar excess pressure of 0.5 atm in the keyhole, the total vapor pressure due to metal atoms from the work-piece varies from 1 atm near the top of the keyhole to 1.5 atm near the keyhole bottom. The temperature difference between the bottom and the top of the keyhole will be much less than the corresponding value for electron beam welds. Temperature at all locations on the keyhole walls in laser beam welding is commonly assumed to be equal to the boiling point of the alloy [2-5]. However, the larger variation of temperature on the keyhole walls for electron beam welding has been considered during the calculation of keyhole geometry and also for the surface tension gradient (resulting from temperature dependence of surface tension) driven Marangoni convection along the keyhole walls.

References

[1] Lee JY, Ko SH, Farson DF, Yoo CD. Mechanism of keyhole formation and stability in stationary laser welding. J. Phys. D-Appl. Phys. 2002;35:1570.
[2] Dowden J, Postacioglu N, Davis M, Kapadia P. A Keyhole Model in Penetration Welding with a Laser. J. Phys. D-Appl. Phys. 1987;20:36.
[3] Matsunawa A, Semak V. The simulation of front keyhole wall dynamics during laser welding. J. Phys. D-Appl. Phys. 1997;30:798.
[4] Kaplan A. A Model of Deep Penetration Laser-Welding Based on Calculation of the Keyhole Profile. J. Phys. D-Appl. Phys. 1994;27:1805.
[5] Ye XH, Chen X. Three-dimensional modelling of heat transfer and fluid flow in laser full-penetration welding. J. Phys. D-Appl. Phys. 2002;35:1049.

Appendix B

Calculation of Recoil Pressure

Recoil pressure exerted by the metal vapors can be given by the difference between the momentum of the vapors leaving the surface and the z-direction momentum of the liquid near the liquid – vapor interface.

$$P_{rec} = \rho_g v_g^2 - \rho_l v_l^2 \quad \textbf{(B.1)}$$

The subscripts ‘g’ and ‘l’ stand for gas and liquid respectively, and the velocities normal to the liquid – vapor interface. Since by mass conservation:

$$\rho_g v_g = \rho_l v_l \quad \textbf{(B.2)}$$

$$\rho_g << \rho_l \quad \textbf{(B.3)}$$

$$v_g >> v_l \quad \textbf{(B.4)}$$

Therefore,

$$P_{rec} = (\rho_g v_g) v_g - (\rho_l v_l) v_l = (\rho_g v_g)(v_g - v_l) \sim \rho_g v_g^2 \quad \textbf{(B.5)}$$

$$P_{rec} \sim J_g v_g \quad \textbf{(B.6)}$$

where J_g is the vaporization flux, which can be calculated from the Langmuir equation given in equation Eq. **B.7**.

$$v_g = J_g / c \quad \textbf{(B.7)}$$

where c is the concentration of the metal vapors and is given by:

$$c = \frac{M p_v}{RT} \quad \textbf{(B.8)}$$

where M is the molecular weight of iron, and p_v is the vapor pressure of iron at temperature T, calculated from an empirical relation [1].

References

[1] Brandes EA, Brook GB, editors. Smithells Metals Reference Book. MA: Butterworth Heinemann, 1992.

Appendix C

Genetic Algorithm

The GA used in the present study to calculate the optimized values of the input variables is a parent centric recombination (PCX) operator based generalized generation gap (G3) model [1, 2]. This model was chosen because it has been shown to have a faster convergence rate on standard test functions as compared to other evolutionary algorithms. The algorithm for the model is as follows:

1. Each individual in a population represents a set of randomly chosen values of the two input variables, i.e., beam radius at focus, and absorption coefficient. A parent refers to an individual in the current population. The individual that has the best fitness, i.e., the one that gives the minimum value of the objective function in the entire population, is the best parent. The best parent and two other randomly selected parents are chosen from the population.
2. A recombination scheme is used to create two new individuals from these three chosen parents. PCX based G3 models are known to converge rapidly when three parents and two offspring are selected [2].
3. Two new parents are randomly chosen from the current population.
4. The two randomly chosen parents in step 3 and the two new offspring generated in step 2A form a subpopulation of four individuals.
5. The two best solutions, i.e., the solutions having the least values of the objective function, are chosen from the subpopulation of four members created in step 4. These two individuals replace the two parents randomly chosen in step 3.
6. The calculations are repeated from step 1 again until convergence is achieved.

Figure **C.1** shows the application of these steps to the present study. Every 25 iterations, all individuals forming a cluster near the best individual were replaced by randomly generated individuals to reduce any tendency of premature convergence of the population. The recombination scheme [step (2)] used in the present model is based on

the parent centric recombination (PCX) operator. A brief description of the PCX operator, as applied to the present problem of three input variables, is described as follows:

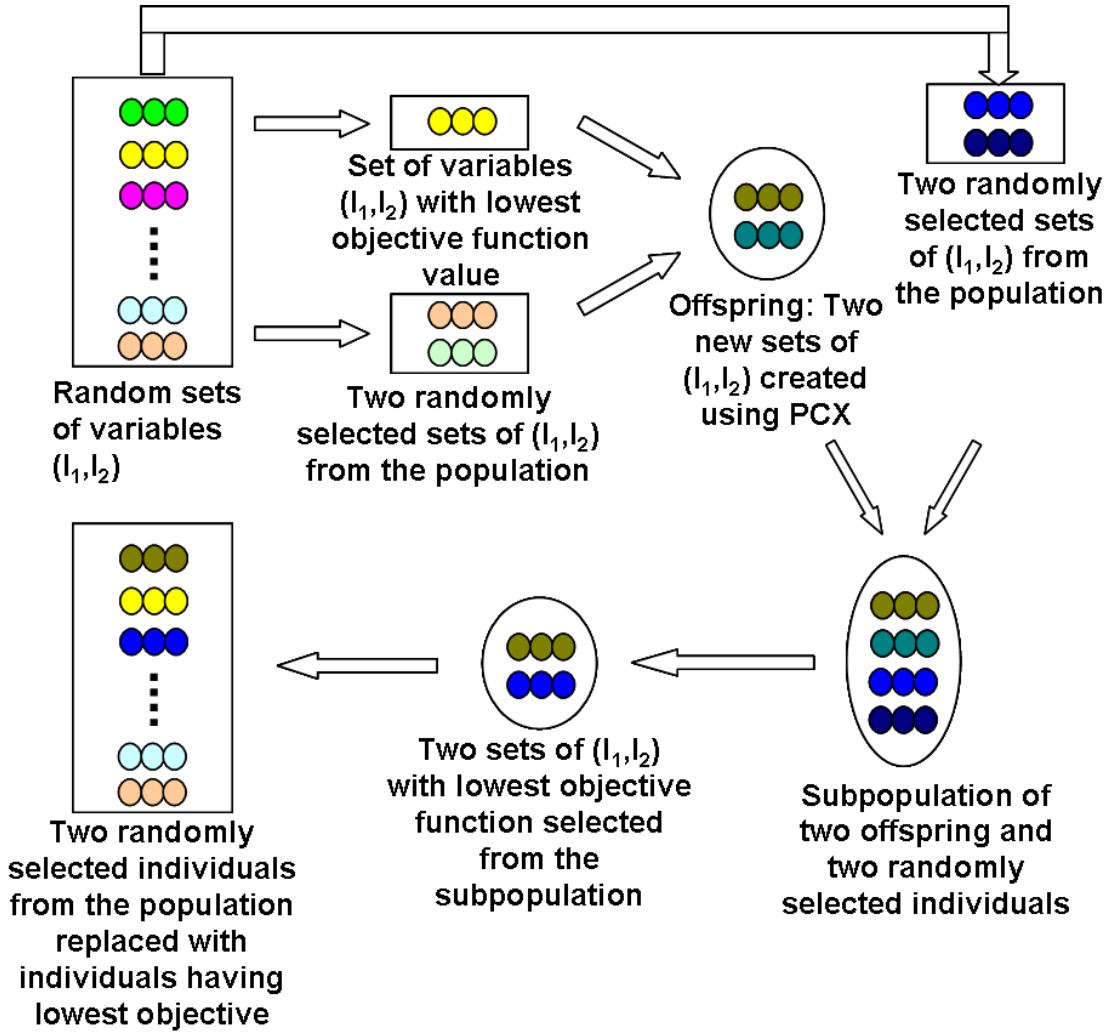

Figure **C.1**: Generalized generation gap (G3) model using parent centric recombination (PCX) operator [3].

First three parents, i.e., $\left(f_1^0, f_2^0\right)$, $\left(f_1^1, f_2^1\right)$, $\left(f_1^2, f_2^2\right)$ are selected from the current population. Here, the subscripts represent the two input variables, while the superscripts denote the parent identification number. The mean vector or

centroid, $\vec{g} = \left(\frac{f_1^0 + f_1^1 + f_1^2}{3}, \frac{f_2^0 + f_2^1 + f_2^2}{3} \right)$, of the three chosen parents is computed. To create an offspring, one of the parents, say $\vec{x}^{(p)} = \left(f_1^0, f_2^0\right)$ is chosen randomly. The direction vector, $\vec{d}^{(p)} = \vec{x}^{(p)} - \vec{g}$, is next calculated from the selected parent to the mean vector or centroid. Thereafter, from each of the other two parents, i.e., $\left(f_1^1, f_2^1\right)$ and $\left(f_1^2, f_2^2\right)$ perpendicular distances, D_i, to the direction vector, $\vec{d}^{(p)}$, are computed and their average, $\bar{D}$, is found. Finally, the offspring, i.e., $\vec{y} = \left(f_1^{'}, f_2^{'}\right)$, is created as follows:

$$\vec{y} = \vec{x}^{(p)} + w_\zeta \left|\vec{d}^{(p)}\right| + \sum_{i=1, i\neq p}^{2} w_\eta \overline{D}\vec{h}^{(i)} \qquad \textbf{(C.1)}$$

where $\vec{h}^{(i)}$ are the orthonormal bases that span the subspace perpendicular to $\vec{d}^{(p)}$, and w_ζ and w_η are randomly calculated zero-mean normally distributed variables. The values of the variables that characterize the offspring, $\vec{y} = \left(f_1^{'}, f_2^{'}\right)$, are calculated as follows:

$$f_1^{'} = f_1^0 + f_{11} + f_{12} \qquad \textbf{(C.2)}$$

$$f_2^{'} = f_2^0 + f_{21} + f_{22} \qquad \textbf{(C.3)}$$

where,

$$f_{11} = w_\zeta \left(\frac{2f_1^0 - f_1^1 - f_1^2}{3} \right) \qquad \textbf{(C.4)}$$

$$f_{21} = w_\zeta \left(\frac{2f_2^0 - f_2^1 - f_2^2}{3} \right) \qquad \textbf{(C.5)}$$

$$f_{12} = w_\eta \left(\frac{a_2 + b_2}{2} \right) \left[1 - \left(\frac{2f_1^0 - f_1^1 - f_1^2}{3d} \right)^2 \right] \qquad \textbf{(C.6)}$$

$$f_{22} = w_\eta \left(\frac{a_2 + b_2}{2} \right) \left[1 - \left(\frac{2f_2^0 - f_2^1 - f_2^2}{3d} \right)^2 \right] \qquad \textbf{(C.7)}$$

The expressions for the variables d, a_2, and b_2, used in Eq. **C.6** and **C.7** are as follows:

$$d = \sqrt{\left(\frac{2f_1^0 - f_1^1 - f_1^2}{3}\right)^2 + \left(\frac{2f_2^0 - f_2^1 - f_2^2}{3}\right)^2} \quad \textbf{(C.8)}$$

$$a_2 = e_1 \times \sqrt{1-(a_1)^2} \quad \textbf{(C.9)}$$

$$b_2 = e_2 \times \sqrt{1-(b_1)^2} \quad \textbf{(C.10)}$$

$$a_1 = \sum_{i=1}^{2} \frac{\left(f_i^1 - f_i^0\right)\left(\frac{2f_i^0 - f_i^1 - f_i^2}{3}\right)}{d \times e_1} \quad \textbf{(C.11)}$$

$$e_1 = \sqrt{\left(f_1^1 - f_1^0\right)^2 + \left(f_2^1 - f_2^0\right)^2} \quad \textbf{(C.12)}$$

$$b_1 = \sum_{i=1}^{2} \frac{\left(f_i^2 - f_i^0\right)\left(\frac{2f_i^0 - f_i^1 - f_i^2}{3}\right)}{d \times e_2} \quad \textbf{(C.13)}$$

$$e_2 = \sqrt{\left(f_1^2 - f_1^0\right)^2 + \left(f_2^2 - f_2^0\right)^2} \quad \textbf{(C.14)}$$

References

[1] Deb K, Anand A, Joshi D. A computationally efficient evolutionary algorithm for real-parameter optimization. Evolutionary Computation 2002;10:371.

[2] Deb K. Multi-objective optimization using evolutionary algorithms. New York: Wiley, 2001.

[3] Kumar A, Debroy T. Tailoring complex weld geometry through reliable heat-transfer and fluid-flow calculations and a genetic algorithm. Metallurgical and Materials Transactions a-Physical Metallurgy and Materials Science 2005;36A:2725.

VITA

Rohit Rai

Rohit Rai was born in Gorakhpur (Uttar Pradesh), India, on 30th June 1982. In August 2000, he joined the Department of Metallurgical and Materials Engineering at Indian Institute of Technology, Kharagpur where he was awarded the degree of Bachelor of Technology (Honors) in May 2004. He joined the Department of Materials Science and Engineering at The Pennsylvania State University in August 2004 to pursue graduate study under the guidance of Professor Tarasankar DebRoy.

A list of his publications in peer reviewed journals is as follows:

1. R. Nandan, R. Rai, R. Jayakanth, S. Moitra, N. Chakraborty, and A. Mukhopadhyay, Materials and Manufacturing Processes, vol. 20 (3), pp. 459-478, 2005.
2. R. Rai and T. DebRoy, Journal of Physics D: Applied Physics, vol. 39, pp. 1257-1266, 2006.
3. R. Rai, G.G. Roy, and T. DebRoy, Journal of Applied Physics, vol. 101, 054909, 2007.
4. R. Rai, J.W. Elmer, T.A. Palmer, and T. DebRoy, Journal of Physics D: Applied Physics, vol. 40, pp. 5753-5766, 2007.
5. R. Rai, S.M. Kelly, R.P. Martukanitz, and T. DebRoy, Metallurgical Transactions A, vol. 39A, pp. 98-112, 2008.
6. R. Rai, P. Burgardt, J. O. Milewski, T. J. Lienert, and T. DebRoy, accepted for publication in Journal of Physics D: Applied Physics.
7. R. Rai, T. A. Palmer, J.W. Elmer, and T. DebRoy, submitted for publication in Welding Journal.
8. B. Ribic, R. Rai, and T. DebRoy, accepted for publication in Science and Technology of Welding and Joining.